MULTISCALE SIMULATION OF MOLECULAR AND CELLULAR BLOOD FLOW AND CLOTTING: FROM NANO-DRUG DELIVERY TO ARTERIAL THROMBOSIS

A Dissertation
Presented to
The Academic Faculty

By

Zixiang Leonardo Liu

In Partial Fulfillment
of the Requirements for the Degree
Doctor of Philosophy in the
School of Mechanical Engineering

Georgia Institute of Technology

December 2020

MULTISCALE SIMULATION OF MOLECULAR AND CELLULAR BLOOD FLOW AND CLOTTING: FROM NANO-DRUG DELIVERY TO ARTERIAL THROMBOSIS

Approved by:

Dr. David N. Ku, Advisor
School of Mechanical Engineering
Georgia Institute of Technology

Dr. Cheng Zhu
School of Mechanical Engineering and Department of Biomedical Engineering
Georgia Institute of Technology

Dr. Jonathan R. Clausen
Fluid and Reactive Processes
Sandia National Laboratories

Dr. Cyrus K. Aidun, Advisor
School of Mechanical Engineering
Georgia Institute of Technology

Dr. Alfredo Alexander-Katz
Department of Materials Science and Engineering
Massachusetts Institute of Technology

Dr. Rekha R. Rao
Fluid and Reactive Processes
Sandia National Laboratories

Date Approved: Oct 1st, 2020

Dedicated to my Mom, Lijuan Huang

With your unconditional love

I was always home

Till we meet again

Dedicated to my Daughter, Elisha Liu

With your first cry

I know I am home

Off we go to explore world

ACKNOWLEDGEMENTS

I would like to thank my advisors, Professor David N. Ku and Professor Cyrus K. Aidun, for their support during my PhD studies at Georgia Tech. I am thankful to Dr. Aidun for providing me the freedom to explore interesting topics on my own, and giving me access to sufficient computational resources that made this thesis possible. I am very grateful to Dr. Ku, for his dedication to educating me to become a good scientist as well as a critical thinker. I appreciate that he offered me the opportunity to work on highly interdisciplinary and meaningful research topics related to human health, and always encouraged me to think out of the box. Also, I always appreciate the life stories and wisdom that he shared with me when I needed them most.

I am also grateful to Professor Cheng Zhu and Professor Alfredo Alexander-Katz for serving on my thesis reading committee, answering my research questions and providing constructive suggestions and critics. I appreciate Dr. Alexander-Katz for providing valuable comments from soft-matter physics perspectives. I thank Dr. Zhu for bringing in more biologically-relevant insights to my research.

Special thanks to the Sandians I worked with or met through the NanoCRISPR project. Especially, Dr. Jonathan Clausen and Dr. Rekha Rao have been great mentors and collaborators to me. I appreciate their patience and time spent with me during those biweekly meetings. I also want to thank Rekha and Jon for hosting my visit to Albuquerque and introducing me to many wonderful scientists and collaborators in Sandia, including Dr. Kimberly S Butler, Dr. Justin L Wagner, Dr. Dan S Bolintineanu, Dr. Jeremy B Lechman, Dr. Kristianto Tjiptowidjojo, Weston Ortiz, Dr. Rich Martin.

My gratitude is also extended to the past and existing group members both in the Lattice-Boltzmann Group at IPST and in the Biofluids and Medical Device Group at IBB. Special thanks to Vincent Lee and Dennis Oztekin, I appreciate the relaxing lunch hours we had over many places primarily in Firehouse and Pacific Grill. To the Ku lab members, Dr.

Michael Griffin, Dr. Patricia Yang, Dongjune Kim, Chris Bressete, Trent Callcott, Gian Carlo Rivera Crespo, Dr. Viviana A. Claveria and Britt van Rooij (visitor from University of Amsterdam), thanks for collectively creating a friendly, inspiring and collaborative environment in the group.

Finally, I want to thank my family for giving me unconditional love. I owe my life to my Mom, Lijuan Huang. I know she is always watching me and being proud of me. I want to thank my Dad, Dejing Liu, for bearing with my absence from home for many years. I want to thank my wife, Wenjuan, for being considerate and supportive of my academic pursuit. Special thanks to my daughter, Elisha, who was born a few months ago in the midst of COVID-19. Her beautiful ”invasion” to my life brought me incredible joy. Last but not the least, I want to thank Him for all the blessings that I have been given.

TABLE OF CONTENTS

LIST OF TABLES

LIST OF FIGURES

SUMMARY

Blood is a biological fluid that transports life-sustaining solutes throughout the body. Separately, blood can clot to stop hemorrhaging or obstruct the arteries to cause heart attacks or strokes. These critical pathophysiological processes rely on the participation of both microscale cells and nanoscale molecules subjected to hydrodynamics. In this thesis, we developed a coupled lattice-Boltzmann and Langevin-dynamics (LB-LD) approach, allowing for simulating blood flow and clotting processes with both cellular and molecular-level biophysical details. The research problems of interest to the thesis range from nano-drug delivery to high-shear thrombosis. For the transport of nano-drugs in microvessels, we demonstrated a particle size-dependent transition from Brownian-motion dominant dispersion to margination in microvessels. To study nanoparticle (NP) partition through microvascular bifurcations, a general particulate suspension inflow/outflow boundary condition is developed and used to discover a heterogeneous partition of the NP in response to the Zweifach-Fung (ZF) effect. To inform macroscale drug delivery applications through constitutive relations, we characterized the diffusion tensor of NP in sheared cellular blood over a wide range of shear rate and hematocrit. The nonlinear hemorheological scaling of the diffusivity was attributed to the red blood cell (RBC) morphology change in principal directions. To elucidate the mechanisms for shear-induced platelet aggregation (SIPA), an $in\ silico$ SIPA simulator informed by the status quo single-molecule measurements is developed. It is found that SIPA is a two-stage process involving in-flow agglomeration and capture of agglomerates to the surface. Transition from the lag time (LT) regime to rapid platelet accumulation (RPA) was attributed to the elevation of local VWF concentration and/or the VWF size. Some contradictory observations in the field of arterial thrombosis were addressed. This thesis provided a novel paradigm for simulating blood flow and clotting at both molecular- and cellular-scales. The multiscale in silico approach offers a cross-scale tool for exploring novel biophysical mechanisms for vascular diseases or other

biophysical processes that are typically inaccessible to only single-molecule measurements, fluidic assays, or single-scale computational methods. Such new perspectives may lead to the discovery of novel therapies for life-threatening vascular diseases.

CHAPTER 1

INTRODUCTION AND BACKGROUND

1.1 Background and significance

1.1.1 Modeling Whole Blood as a Multiscale and Multicomponent Suspension Fluid

Analysis of whole blood flow has been demonstrated through direct numerical simulation (DNS) of the major constituents of blood including the plasma, red blood cells (RBCs) (about 45%), and other cells (about 0.7%) such as white blood cells (WBCs) and platelets [1, 2, 3, 4, 5]. Both single RBC dynamics [1, 3, 6] and rheological properties of dense suspensions of RBCs [7, 8, 9, 10] have been computationally resolved, showing promising agreements with experimental results. Particularly, lattice-Boltzmann (LB) method for the fluid phase coupled with the Spectrin-Link (SL) analysis of the RBC membrane as a hybrid mesoscopic method (LB-SL) has shown to be a suitable cellular blood flow solver [3]. However, whole blood in nature is composed of not only cells but also a large population of functional biomolecules that are nanoscale in size. Analysis of the transport of such nanoscale solutes in cellular blood flow remains challenging due to the large length-scale discrepancy between nanoscale particles (NPs) $\sim$O(10 nm) and cells $\sim$O(10 μm). Further complexities come from the intricate colloidal suspension dynamics, which highly depend on thermal fluctuation, hydrodynamic interactions (HI) mediated through the fluid, and particle-cell interactions. Given the multiscale nature of whole blood flow, developing a hybrid blood flow solver including both cellular and molecular mechanisms is necessary for the study of various blood flow phenomena that are of both biological and clinical relevance.

1.1.2 Particle Transport in Blood Flow: from Nano-Drug Dispersion to Platelet Margination

The rapid advancement of nanotechnology and nanomaterial manufacturing has led to emerging exposure of human cardiovascular systems to nanosized particulate matters ranging from engineered nanocarriers functioning as medicine/imaging agents to aerosol pollutant particulates potentially causing fatal cardiovascular disease. Both the design of optimal nanocarrier systems and the prevention and control of nanoparticle (NP) toxicity rely heavily on the knowledge of NP distribution in vascular systems. Nevertheless, the distribution of NP in micro-vessels, microvascular beds and large-scale blood circulation organs remains elusive to date and limits the bioavailability of NP systems to the human bio-environment. Understanding the dispersive properties of solutes and cells of diverse sizes ranging from nanometer to micrometer in blood flow shows physiological significance. As a relevant example of microscale particle transport in blood, platelets margination has shown to play an important role in affecting the formation of arterial thrombus [11]. Motivated by that, a plethora of studies [12, 13, 14, 15, 16, 17, 18, 19, 20] have dedicated to unravelling the mechanistic mechanisms of margination. The platelet margination is found to be primarily driven by the RBC-enhanced diffusion in the RBC-laden region synergistically accompanied by the sink-like effect of the cell free layer (CFL). Nanoscale particle (NP) dispersion in blood flow, on the other end of the spectrum, has recently received considerable attention [21, 22, 23, 24] due to the fast development of nano-drug delivery techniques that have the potential to revolutionize the traditional therapeutics due to its ability to overcome various biological barriers [25]. Although the transport of nanoscale and microscale particles in blood have been investigated separately and understood to a great extent, there is a need of a systematic interrogation of the particle dispersion mechanisms across nano-to-microscale sizes using a unified computational framework within a variety of flow structures (such as simple shear flows, tubular flows and branching flows, etc.).

1.1.3 Shear-Induced Platelet Aggregation Mediated by von Willebrand Factor

Acute myocardial infarction and ischemic stroke are the leading causes of morbidity and mortality worldwide, which are induced by the formation of occlusive thrombus at the site of atherosclerotic plaque rupture under very high shear rates ranging from 5000 to 40 000 s^{-1} [26, 27]. Different from the coagulation process that is explained by the classic Virchow's triad [28], arterial thrombosis is induced by an alternative high-shear thrombosis triad composed of a pathophysiological high-shear environment, a thrombogenic surface, and pro-thrombotic blood constituents that primarily include the platelet and the von Willebrand factor (VWF) [29, 11]. Pathologically, the formation of atherosclerotic plaque leads to a vascular stenosis, causing pathologically high wall shear rates. Such high shear rate condition causes coagulation factors such as thrombin to be generally washed out of the clot. When the atherosclerotic plaque cap ruptures to expose the subendothelial collagen, it provides a thrombogenic surface. The subsequent accumulation of VWF-platelet aggregates on the thrombogenic surface leads to the arterial thrombosis and occlusion. Although coagulation may stabilize a thrombus after occlusion, these coagulation factors have a kinetic activation rate that is much too slow to cause the occlusive thrombus. Based on the high-shear triad, we have successfully created arterial thrombosis $in\ vitro$ using a stenotic glass capillary tube coated with fibrillar collagen [30]. The occlusion time measured with our system matches well with pathological timescales [31, 32]. The thrombus accumulation process was found to have two phases of growth [11, 30]. The initial phase, termed the lag time (LT), features a slow accumulation of the first-layer thrombus that typically lasts for several minutes. The subsequent phase, termed as rapid platelet accumulation (RPA), shows a thrombus growth rate that is 4×6 times the rates at LT phase [30, 33]. Understanding the biophysical mechanisms for RPA is essential as it directly leads to occlusive thrombus, causing clinical events such as ST-segment Elevation Myocardial Infarction (STEMI).

1.2 Specific Aims

The objective of this thesis is to develop a multiscale and multicomponent blood flow computational framework for simulating whole blood flow and clotting at cellular and molecular scales. This high-fidelity computational framework will combine the advantages of the state-of-the-art complex fluid solver technique based on the lattice-Boltzmann (LB) method coupled with multiscale particulate suspension dynamics. The method is applied to a series of blood flow and clotting problems involving particle dispersion in blood and high-shear induced thrombosis to both gain novel, fundamental understanding of blood as a complex biological fluid and provide clinically relevant suggestions to blood pathology. Specifically, the following specific aims are proposed:

1. **Develop a lattice Boltzmann-Langevin dynamics (LB-LD) approach for multiscale and multicomponent blood suspension flow applications incorporating both cellular and molecular biophysics.** Aim 1 will develop a two-way coupled LB-Langevin dynamics (LB-LD) approach to resolve the multiscale particle and polymer suspension dynamics.

2. **Characterize the dispersion and distribution of nano-to-microscale particles in cellular blood flow through micro-vessels.** Aim 2 will attempt to quantitatively show how the transport mechanism varies with particle size from the nano- to microscale.

3. **Predict the partitioning of blood-borne nanoparticles through physiologic microvascular bifurcations.** Aim 3 attempts to understand how NPs partition through a single microvascular bifurcation. Incorporating RBC-NP interaction is paramount to the predictions of NP distribution and delivery efficiency.

4. **Quantify the RBC-enhanced shear-induced diffusivity of nanoparticles in a viscometric blood flow as a function of shear rate and hematocrit.** Aim 4 will

develop a NP diffusivity tensor, as an accurate constitutive law, to link the local hemorheological properties and the NP diffusion property.

5. **Interrogate the biophysical mechanisms of the shear-induced platelet aggregation (SIPA) through VWF entanglement under elevated shear.** Aim 5 is to understand the molecule- and cell-level biophysical mechanisms of SIPA and the rapid platelet accumulation (RPA) that causes occlusive thrombosis, providing testable hypotheses to direct future experimental work to discover potential VWF-targeting therapies for high-shear thrombosis.

With regard to expected outcomes, this thesis will deliver a multiscale blood flow solver for studying general blood flow and clotting events. This work will elucidate the dispersion and diffusion mechanisms of nanoparticles in cellular blood flow within microcirculations by showing: the particle size-induced transition from Brownian dispersion to margination, the Zweifach-Fung effect-induced heterogeneous partition of nanoparticles through microvascular bifurcations, and the anisotropic nanoparticle diffusion tensor in sheared blood as a constitutive relation for large scale nanoparticle biotransport applications. The biophysics of SIPA will be demonstrated to explain the RPA that causes occlusive thrombosis, pointing towards testable hypotheses for potential VWF-targeting antithrombotic therapies specific to elevated shear.

CHAPTER 2

DEVELOPMENT OF A COUPLED LATTICE BOLTZMANN/LANGEVIN DYNAMICS METHOD FOR MULTISCALE AND MULTICOMPONENT BLOOD SUSPENSION FLOWS

In this chapter, a hybrid computational method coupling the lattice-Boltzmann (LB) method and a Langevin-dynamics (LD) method is developed to simulate nanoscale particle and polymer (NPP) suspensions in the presence of both thermal fluctuation and long-range many-body hydrodynamic interactions (HI). Brownian motion of the NPP is explicitly captured by a stochastic forcing term in the LD method. The LD method is two-way coupled to the non-fluctuating LB fluid through a discrete LB forcing source distribution to capture the long-range HI. To ensure intrinsically linear scalability with respect to the number of particles, an Eulerian-host algorithm for short-distance particle neighbor search and interaction is developed and embedded to LB-LD framework. The validity and accuracy of the LB-LD approach are demonstrated through several sample problems. The simulation results show good agreements with theory and experiment. The LB-LD approach can be favorably incorporated into complex multiscale computational frameworks for efficiently simulating multiscale, multicomponent particulate suspension systems such as complex blood suspensions.

2.1 Introduction

Simulating suspensions of nanoscale particles or polymers is a challenging task that involves resolving particle-particle interaction, thermal fluctuation and long-range many-body hydrodynamic interactions (HI) that contribute to complex suspension microstructures [34, 35]. Conventional particle-based methods such as Molecular dynamics (MD) [36], dissipative particle dynamics (DPD) [37], Brownian dynamics (BD) [38] and Stoke-

sian dynamics (SD) [39] have advanced this field considerably. The MD and DPD approaches resolve the fluid particles explicitly and are often suitable for problem with relatively small length and time scales. The conventional BD neglects the particle inertia the HI effect to accommodate for computational efficiency [38]. The SD method has been a successful computational tool to study the rheology of spherical, rigid particle suspensions. It captures the many-body HI theoretically with excellent rheological agreement with experiments [40, 41, 42]. Although it intrinsically scale cubically with the number of particles, N, recent attempts have been made to enhance SD to O(NlnN) or O(N) scales through sophisticated computational algorithms [43, 44, 45, 46]. Nevertheless, the SD method remains to be extended to particulate suspensions involving complex geometries/solid boundaries.

Lagrangian-Eulerian direct-coupling approaches have shown good potential to handle complex particle geometry and capture suspension of submicron-sized particles including Brownian effect and HI with intrinsically linear scalability. The inception of this class of approach starts by adding the so-called Landau-Lifshitz stress [47] to the fluid phase and coupling the subsequent fluctuating hydrodynamics (FH) method with the Newtonian dynamics for colloidal particles. The FH method explicitly captures the thermal fluctuations in the fluid phase and implicitly gives rise to the Brownian motion of suspended fine particles. Theoretical proofs [48, 49] have shown that the fluctuating stresses exerted on the particle render the particle equation of motion into a Langevin equation, in which the hydrodynamically induced random force term directly satisfies the fluctuation-dissipation theorem (FDT). Following the idea of FH, Ladd [50] proposes a fluctuating lattice-Boltzmann (FLB) method to handle Brownian motion of colloidal particles. The method captures the many-body HI in both concentrated and dilute regime with O(N) scale [51]. In order to satisfy the FDT, the FH-rooted method needs to directly resolve the fluid-solid interface to satisfy the no-slip boundary condition. However, this requirement poses heavy computational expense when it comes to simulating a large number of particles or concurrently handling particles with disparate length scales. To overcome this limitation, Dunweg [52,

53] couples the FLB method with a MD-type approach for point particles through a simple Stokesian friction term. Similar approaches were later developed and applied to studying the DNA translocation through nano-pores [54, 55, 56]. In this approach, thermal noises are included in both the fluid phase and particle phase. As a consequence, this method can not capture the temperature scale (thus the Brownian motion) directly and advocates an empirical rescaling of the friction coefficient. More recently, Mynam $et\ al.$ [57] show that such empirical operation can be neglected by omitting the thermal fluctuation in the fluid phase while keeping the fluctuation in the particle phase.

Following the idea of coupling fluctuating particles dynamics with non-fluctuating hydrodynamics, we develop a coupled lattice Boltzmann/Langevin dyanmics (LB-LD) approach to simulate nanoscale particle and polymer suspensions in the presence of both thermal fluctuation and many-body HI. Different from the work in Mynam $et\ al.$ [57], we couple the two phases through a forcing source distribution term [58] that can recover the Navier-Stokes equation in the physical time scale [59]. Moreover, through multiple sample problems, we demonstrate that the two-way coupled LB-LD approach not only captures the Brownian motion directly (consistent with [57]) but also resolves the long-range HI favorably. Through careful numerical treatment, we also demonstrate the effective applicability of the LB-LD approach to both nanoscale particle and polymer suspension problems. On the computational performance side, an Eulerian host algorithm is proposed to conduct localized neighboring particle search and interaction. This algorithm takes advantage of the existing Eulerian LB nodes and the sub-grid nature of the Lagrangian particles. With this approach, the overhead of particle dynamics (through LD) is shown to scale linearly with respect to the number of particles while adding negligible overhead to the LD framework. Since the particle dynamics is essentially resolved in a sub-grid fashion, the LB-LD approach can be easily coupled with direct-numerical-simulation (DNS) suspension solvers to tackle multiscale, multicomponent particulate suspension flows. One example of such flows is blood flow suspended with numerous, interacting nanoscale biomolecules and mi-

croscale blood cells through microfluidic systems [13, 60, 61] or biological structures [24, 62].

2.2 Computational Methods

2.2.1 Lattice-Boltzmann method

The method for the fluid phase with suspended particle interaction is based on the three-dimensional LB method developed in Aidun $et\ al.$ [63, 64, 2]. The LB method solves the discretized Boltzmann equation in velocity space through the propagation of the particle distribution functions f_i along the discrete lattice velocities $\mathbf{e}_i$ and the collision operation of the local distributions to be relaxed to the equilibrium distribution $f_i^{(0)}$. The collision term is simplified to the single-relaxation-time (SRT) Bhatnagar-Gross-Krook (BGK) collision operator [65], while the more generalized multi-relaxation-time (MRT) [66] and entropic [67, 68, 69, 70] collision operators can be also adopted to gain higher numerical stability. The temporal evolution of the particle distribution function with a single relaxation time takes the form of

$$f_i(\mathbf{r} - \Delta t\mathbf{e}_i, t + \Delta t) = f_i(\mathbf{r}, t) - \frac{\Delta t}{\tau}[f_i(\mathbf{r}, t) - f_i^{(0)}(\mathbf{r}, t)] + f_i^S(\mathbf{r}, t), \qquad (2.1)$$

where τ is the single relaxation time scale associated with the rate of relaxation to the local equilibrium, and f_i^S is a forcing source term introduced to account for the discrete external force effect [58]. The specific formalism for f_i^S is presented in §3.2.2. This method has a pseudo-sound-speed of c_s=$\Delta r/(\sqrt{3}\Delta t)$ and a fluid kinematic viscosity of ν=$(\tau - \Delta t/2)c_s^2$, where Δt is the time step and Δr is the unit lattice distance. The positivity of ν requires τ>$\Delta t/2$. In the LB method, time and space in Equation (2.1) are normalized by Δt and Δr such that Δt_{LB}=Δr_{LB}=1 are applied to advance the system. Details of the mapping between dimensional units and LB units are discussed in §2.2.5. In the near incompressible

limit (

$$i.e.$$

, the Mach number, Ma=$u/c_s \ll 1$), the LB equation recovers the Navier-Stokes equation [71] with the equilibrium distribution function in terms of local macroscopic variables as

$$f_i^{(0)}(\mathbf{r},t) = \omega_i \rho[1 + \frac{1}{c_s^2}(\mathbf{e}_i \cdot \mathbf{u}) + \frac{1}{2c_s^4}(\mathbf{e}_i \cdot \mathbf{u})^2 - \frac{1}{2c_s^2}(\mathbf{u} \cdot \mathbf{u})], \tag{2.2}$$

where ω_i denotes the set of lattice weights defined by the LB stencil in use. The macroscopic properties such as the fluid density, ρ, velocity, $\mathbf{u}$ and pressure p can be obtained via moments of the equilibrium distribution functions:

$$\sum_{i=1}^{Q} f_i^{(0)}(\mathbf{r},t) = \rho, \tag{2.3a}$$

$$\sum_{i=1}^{Q} f_i^{(0)}(\mathbf{r},t)\mathbf{e}_i = \rho\mathbf{u}, \tag{2.3b}$$

$$\sum_{i=1}^{Q} f_i^{(0)}(\mathbf{r},t)\mathbf{e}_i\mathbf{e}_i = p\mathsf{I} + \rho\mathbf{u}\mathbf{u}, \tag{2.3c}$$

where I is the identity tensor. The current study adopts the D3Q19 velocity set; that is 3 dimensions and 19 discrete velocity vectors,

$$i.e.$$

, $Q = 19$. Along the rest, non-diagonal, and diagonal lattice directions, ω_i is equal to 1/3, 1/18, and 1/36, and $|\mathbf{e}_i|$ is equal to 0, $\Delta r/\Delta t$, and $\sqrt{2}(\Delta r/\Delta t)$, correspondingly. The LB method is extensively validated [63, 64, 72, 2] and proved to be suitable for the direct numerical simulation (DNS) of dense suspensions of both rigid particles and deformable capsules in complex flows with good efficiency and scalability [73, 74, 7, 4, 2].

2.2.2 Langevin-dynamics method

Governing equation

Particles suspended in a fluid system are subjected to the impacts of the randomly fast-moving liquid molecules. When particle size is below micron-scale, such instantaneously fluctuating momentum transferred from the solvent molecules spurs the particle to yield irregular movements, known as the Brownian motion. The dynamics of such Brownian particles can be described via the Langevin equation (LE),

$$m_p^i \frac{d\mathbf{u}_p^i}{dt} = \mathbf{C}_p^i + \mathbf{F}_p^i + \mathbf{S}_p^i, \tag{2.4}$$

where m_p is the mass of the particle of index i. Provided the particle's initial position, $r_{p,0}$, the displacement of the particle can be updated by integrating the particle velocity with respect to time through $\mathbf{r}_p^i$=$\mathbf{r}_{p,0}^i$+$\int \mathbf{u}_p^i dt$.

The right-hand-side (RHS) of Equation (2.4) can be decomposed into three systematic forces that drive the motion of the particle. The conservative force, $\mathbf{C}_p^i$, specifies the interparticle or particle-surface interaction force that exerted on particle i. It is often approximated as a linear superposition of the directional derivatives of the pairwise potentials as

$$\mathbf{C}_p^i = -\sum_{j=0;\ j\neq i}^{N-1} \frac{dU(R_{ij})}{dR_{ij}} \frac{\mathbf{R}_{ij}}{R_{ij}}, \tag{2.5}$$

where $U(R_{ij})$ is the pairwise inter-particle potential, and $\mathbf{R}_{ij}$ is a directional vector, $\mathbf{R}_{ij} = \mathbf{r}_p^i - \mathbf{r}_p^j$, connecting particles i and j. The ingredients of $U(R_{ij})$ carry different formalism depending on the physical origins of the potential forces, which is discussed in detail in §2.2.4. The frictional force $\mathbf{F}_p^i$ is assumed to be proportional to the relative velocity of the particle with respect to the local viscous fluid [18],

$$\mathbf{F}_p^i = -\zeta[\mathbf{u}_p^i(t) - \mathbf{u}(\mathbf{r}_p^i, t)], \tag{2.6}$$

where $\mathbf{u}_p$ denotes the particle velocity, and $\mathbf{u}(\mathbf{r}_p, t)$ is the interpolated fluid velocity at the position where the center of the particle resides. Equation (2.6) ensures the Galilean invariance of the particle-fluid system. The details on calculating $u(\mathbf{r}_p, t)$ through interpolation are illustrated in §3.2.2. The friction coefficient, ζ, is determined by the Stokes' drag law,

$$\zeta = 3\pi\mu d_p \psi, \tag{2.7}$$

where μ is the dynamic viscosity of the liquid, and ψ is the particle shape factor that is set to one in this study to account for spherical shape effect. The stochastic force term, $\mathbf{S}_p$, implicitly accounts for the thermal fluctuation of the solvent, and explicitly gives rise to the Brownian motion of the particle. Through the equipartition principle and the integration of the Langevin equation [75], the stochastic force can be related to the friction, reflecting a balance between the random thermal fluctuation and the frictional dissipation,

$$i.e.$$

, the FDT [76]. Specifically, the Cartesian component of the stochastic force exhibiting a zero mean with the covariance determined by the FDT, which reads

$$\langle S^i_{p,\alpha}(t) \rangle = 0, \tag{2.8a}$$

$$\langle S^i_{p,\alpha}(t) S^j_{p,\beta}(t) \rangle = 2k_B T \zeta \delta_{ij} \delta_{\alpha\beta} \delta(t - t'), \tag{2.8b}$$

where $\alpha, \beta \in \{x, y, z\}$, i and j run through all the particle indices, δ_{ij} and $\delta_{\alpha\beta}$ are Kronecker deltas, $\delta(t - t')$ is the Dirac-delta function, k_B is the Boltzmann constant, T is the absolute temperature of the fluid bath, and the angle brackets denote the average over the ensemble of realizations of the random variables. Equations (2.8b) statistically state that the Cartesian component of $\mathbf{S}_p$ exhibits a Gaussian distribution with a zero mean.

Time scales and numerical treatment

A colloidal system is physically enriched with multiple critical time scales, including (i) the short atomistic time scale, $\tau_a \sim 10^{-12}$ sec, that is related to the frequency of rapid collisions of solvent molecules on the suspending colloidal particle, (ii) the viscous diffusion time scale,

$$\tau_\nu = \frac{d_p^2}{4\nu}, \tag{2.9}$$

which accounts for the time for the hydrodynamic momentum to diffuse over a distance of the particle radius, (iii) the particle velocity relaxation time scale,

$$\tau_r = \frac{m_p}{\zeta}, \tag{2.10}$$

over which the particle velocity decays to the algebraic long-time tail regime, and (iv) the Brownian diffusion time scale,

$$\tau_B = \frac{d_p^2 \zeta}{4k_B T}, \tag{2.11}$$

which measures the time the particle has diffused its own radius. To fully resolve the HI among particles, τ_ν needs to be much shorter than τ_B, $i.e.$, the Schmidt number $Sc = \tau_B/\tau_\nu \gg 1$, allowing viscous momentum to diffuse much faster than the particle Brownian diffusion time scale [75]. In the current study, Sc lies in the range of 250$\sim$1500 for the particle size (50$\sim$300 nm) considered as follows. To avoid excessive computational expense when solving the LE, it is also ideal to advance the LD system with the same time step Δt as that of the LB system. However, this requires conditional treatment of the LE to maintain stability requirement. A Stokes number, defined as St=$\tau_r/\Delta t$, can be introduced to characterize the relative importance of the short-time particle inertial effect. When $St < 1$, $i.e.$, the LE is advanced based on a time step greater than the particle relaxation time scale, the over-damped LE can be solved to avoid introducing sub-time steps. Under such condition, the particle motion is expected to be inertia-free and tightly follow the local fluid stream-

line. When $St \geq 1$, $i.e.$, the LE is updated with a time interval comparable to or shorter than the particle relaxation time scale, the under-damped LE needs to be solved to retain the short-time particle inertia during each time step. Under such condition, the particle tends to deviate from the streamline due to inertial effect. Since the LB evolution equation is only first-order accurate in time, a forward-differencing Euler scheme with first-order accuracy is employed to solve the discretized LE. Therefore, the velocity and displacement of the Brownian particle can be advanced, according to the St number conditions, by

$$\mathbf{u}_p(t+\Delta t) = \mathbf{u}(\mathbf{r}_p, t) + \frac{1}{\zeta}[\mathbf{C}_p(t) + \mathbf{S}_p(t)], \quad (St < 1) \tag{2.12a}$$

$$\mathbf{u}_p(t+\Delta t) = \mathbf{u}_p(t) + \frac{\Delta t}{m_p}\{\mathbf{C}_p(t) + \mathbf{S}_p(t) - \zeta[\mathbf{u}_p(t) - \mathbf{u}(\mathbf{r}_p, t)]\}, \quad (St \geq 1) \tag{2.12b}$$

where the two discretized forms of the LE become equivalent when St=1. Through stability analysis, it can be shown that the condition, $|1 - \Delta t\zeta/m_p| \leq 1$, $i.e.$, $St \geq 0.5$, needs to be satisfied for the discretized under-damped LE to be numerically stable. The conditional treatment as shown in equations (2.12a-2.12b) directly satisfies this numerical stability criterion and avoids compromising to sub-time steps [52, 53, 77, 57]. The Gaussian distribution associated with the stochastic force $\mathbf{S}_p(t)$ is realized via a random number generator based on the Box-Muller transformation [78].

2.2.3 Particle-fluid coupling

To directly capture the many-body HI mediated by the fluid phase, the interaction between the Brownian particle and the fluid is resolved by coupling the LD method to the LB method in a two-way fashion. The hydrodynamic force exerted on the particle, $\mathbf{F}_p^H$, can be system-

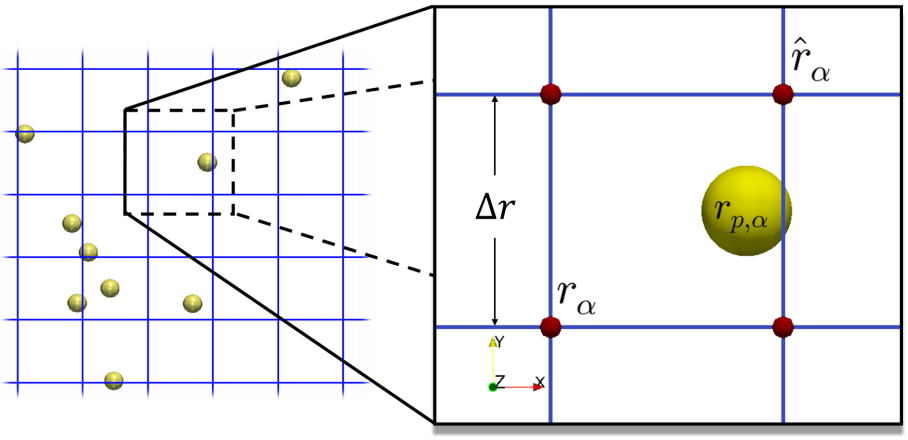

Figure 2.1: 2-D representation of a nanoscale particle (yellow) located at position $\mathbf{r}_p$ in a lattice cell. The lattice node $\hat{\mathbf{r}}$ is at the diagonal position of lattice node $\mathbf{r}$, and α denotes one of the Cartesian components.

atically decomposed into a frictional component and a stochastic component [52] as

$$\mathbf{F}_p^H = \mathbf{F}_p + \mathbf{S}_p = -\zeta[\mathbf{u}_p(t) - \mathbf{u}(\mathbf{r}_p, t)] + \mathbf{S}_p(t), \tag{2.13}$$

which is applied to partially drive the particle dynamics through the LE. Meanwhile, since $\mathbf{F}_p$ and $\mathbf{S}_p$ are both originated from the collision between the particle and liquid molecules, $\mathbf{F}_p^H$ (instead of $\mathbf{F}_p$) should be assigned back to the fluid phase to conserve momentum for the entire particle-fluid system. Provided each particle or monomer is treated as a point particle and moves continuously in the lattice domain, as shown in Fig. 2.1, both the construction of the fluid velocity at the center of the particle and the redistribution of the inter-phase momentum need to employ certain interpolation or extrapolation schemes.

Two options of distance-based spatial distribution stencils with different orders of accuracy have been implemented in the current approach. For the simple trilinear stencil [52, 53], a weight function, $w(\mathbf{r}, \mathbf{r}_p)$, can be introduced as

$$w(\mathbf{r}, \mathbf{r}_p) = \prod_{\alpha \in \{X,Y,Z\}} \frac{|\hat{r}_\alpha - r_{p,\alpha}|}{\Delta r}, \tag{2.14}$$

which is of first-order accuracy and only reads the coordinates of the first-layer, neighboring

lattice nodes owned by the particle-resided lattice cell. For the stencil via Peskin's method [79], the weight function can be introduced as

$$w(\mathbf{r}, \mathbf{r}_p) = \prod_{\alpha \in \{X,Y,Z\}} \frac{1 + cos[\frac{\pi(r_\alpha - r_{p,\alpha})}{4\Delta r}]}{4\Delta r}, \tag{2.15}$$

which yields second-order accuracy and involves two layers of lattice nodes surrounding the particle. Peskin's stencil has also been successfully applied to LB method with the external boundary force (EBF) [80] to resolve the curved fluid-solid boundary, which shows better accuracy and efficiency compared to the standard bounce-back (SBB) method. The following studies employ the trilinear stencil for simplicity. By employing the weight function, the background fluid velocity at the particle center can be interpolated as

$$\mathbf{u}(\mathbf{r}_p, t) = \sum_{\mathbf{r} \in N_c} w(\mathbf{r}, \mathbf{r}_p)\mathbf{u}(\mathbf{r}, t), \tag{2.16}$$

where N_c denotes the group of nodes on the lattice cell occupied by the particle. The same weight function can be applied to the construction and distribution of the reactionary impulse due to the particle-fluid interactions. Specifically, the reactionary impulse density [64], during each time step, can be assigned to the surrounding lattice nodes as

$$\mathbf{J}(\mathbf{r}, \mathbf{r}_p) = -w(\mathbf{r}, \mathbf{r}_p)\frac{\mathbf{F}_p^H \Delta t}{\Delta r^3}, \tag{2.17}$$

where $\mathbf{J}(\mathbf{r}, \mathbf{r}_p)$ is the impulse density to be assigned to the lattice node, $\mathbf{r}$, due to particle-fluid interaction at the particle position, $\mathbf{r}_p$, at each time step. A local forcing source distribution term, $f_i^S(\mathbf{r}, t)$, based on the method proposed in He $et\ al.$ [58] can then be calculated as

$$f_i^S(\mathbf{r}, t) = \frac{\omega_i \mathbf{J}(\mathbf{r}, \mathbf{r}_p) \cdot \mathbf{e}_i}{c_s^2}. \tag{2.18}$$

Instead of modifying the local equilibrium distribution functions as shown in previous studies [52, 57], the current approach, similar to the EBF method [80], modifies the general LB

evolution equation into Equation (2.1) by adding the forcing distribution function $f_i^S(\mathbf{r}, t)$, which is shown to approximate the Navier-Stokes equation in the physical time scale [59]. The same forcing term has been applied to the studies of DNA translocation through nanopores [54, 55, 56]. However, those studies use zeroth order spatial distribution schemes and introduce thermal fluctuation in both fluid and solid phases, which is not aligned with the LB-LD approach proposed in the current study.

2.2.4 Particle-particle interactions

Interparticle potential for suspended particles

The inter-particle interactions between unconnected particles are assumed to follow the classic Derjaguin-Landau-Verwey-Overbeek (DLVO) theory that includes both the standard van der Waals potential [81] and the electrostatic contribution to the overall DLVO potential, as advocated in Schunk $et\ al.$ [82]. For the attractive component of the van der Waals potential, the formulation of Hamaker $et\ al.$ [83] is employed as follows,

$$U_A(R_{ij}) = \frac{A_{cc}}{6}[\frac{d_p^2}{2(R_{ij}^2 - d_p^2)} + \frac{d_p^2}{2R_{ij}^2} + \ln(\frac{R_{ij}^2 - d_p^2}{R_{ij}^2})], \tag{2.19}$$

where A_{cc} is the Hamaker constant that is set to $A_{cc} = 4\pi^2 k_B T$ according to [82]. The repulsive component of the van der Waals potential adopts the integrated Lennard-Jones (LJ) potential derived in [81] as

$$U_R(R_{ij}) = \frac{A_{cc}\sigma^6}{37800 R_{ij}}[\frac{R_{ij}^2 - 7d_pR_{ij} + 13.5d_p^2}{(R_{ij} - d_p)^7} + \frac{R_{ij}^2 + 7d_pR_{ij} + 13.5d_p^2}{(R_{ij} + d_p)^7} - 2\frac{R_{ij}^2 - 7.5d_p^2}{R_{ij}^7}], \tag{2.20}$$

where σ is the repulsive scaling factor that can be set to $\sigma = d_p/10$ as suggested in previous studies [82, 84]. Together with the screened electrostatic potential, U_E [82], the total DLVO potential can be calculated as $U_{DLVO} = U_A + U_R + U_E$. In the following study (§2.3.3),

neutral electrostatic effects are considered, $i.e.$, $U_E = 0$. However, the charge effect can be incorporated through various electrostatic models [82, 60].

Interparticle potential for chain of particles

In the case of polymer chains, particles (beads) are connected by elastic springs to form bead-spring chains. To account for the inter-bead cohesive effect and the bead volume-exclusion effect, the standard Lennard-Jones (LJ) potential is employed according to

$$U_{LJ}(R_{ij}) = \tilde{\epsilon} k_B T[(\frac{d_p}{R_{ij}})^{12} - 2(\frac{d_p}{R_{ij}})^6], \tag{2.21}$$

where $\tilde{\epsilon}$ is the scaling factor of the LJ potential well depth, which can be tuned to adjust the cohesiveness of the polymer chain. In the following simulations, $\tilde{\epsilon}$ is set to 1.8 to obtain the best fit to the experimental data discussed in §2.3.5. Equation 2.21 is truncated at a cut-off distance R_{ij}^c=8d_p to limit the bound for neighboring bead search but still preserve the major cohesive effect between adjacent beads. The cohesive strength among beads plays a critical role in regulating the conformation of self-associable polymers, such as von Willbrand factors (vWF) [85]. The inter-bead connectivity is established through a finitely extensible nonlinear elastic (FENE) spring [86] as

$$U_S(R_{ii'}) = -\frac{2\tilde{k} k_B T \Delta R_{max}^2}{d_p^2} \ln[1 - (\frac{R_{ii'} - d_p}{\Delta R_{max}})^2], \tag{2.22}$$

where $R_{ii'}$ is the center-to-center distance between bead i and its neighbor $i' = i + 1$ (or $i - 1$), $\tilde{k}$ is the scaling factor of the spring tensile elasticity, and ΔR_{max} denotes the maximum bond extension. Here, ΔR_{max} is chosen to be $0.25 d_p$ to limit the extension of the polymer chain [53]. The spring scaling factor, $\tilde{k}$, is set to 200.0 as suggested in [85]. Unlike the linear Hookean connectivity model used in other studies [85, 87], the FENE spring captures the hyperelastic-like behavior when the polymer bond elongation reaches its maximum.

2.2.5 Mapping between physical units and LB units

All equations and variables thus far are introduced in physical units for consistency. To follow the convention of the LB method, the time, length, and density/mass units of the entire LB-LD system need to be mapped to LB units in the simulations [2]. The mapping is performed such that t, r, and ρ are normalized by Δt, Δr, and ρ, respectively. Therefore, the unit lattice distance, time step, and fluid density in LB units are obtained as Δr_{LB}=Δt_{LB}=ρ_{LB}=1. The normalized single relaxation time scale and the corresponding LB viscosity are τ_{LB}=$\tau/\Delta t$ and ν_{LB}=$(2\tau_{LB}-1)/6$, respectively. As mentioned in §2.2.1, the LB single relaxation time, τ_{LB}, needs to satisfy τ_{LB} >0.5 to produce positive viscosity.

The current study selects mapping ratios of $\frac{\Delta t}{\Delta t_{LB}}$=$\frac{\nu_{LB}}{\nu}(\frac{\Delta r}{\Delta r_{LB}})^2$ for time, $\frac{\Delta r}{\Delta r_{LB}}$=333 nm for length, and $\frac{\rho}{\rho_{LB}}$=1000 kg/m^3 for density. The time mapping ratio depends on the fluid kinematic viscosity and the LB single relaxation time in use. The fluid density is selected to be 1000 kg/m^3 and the viscosity 1.2 cP. The temperature is set to $T = 310\ K$. It should be noted that the current mapping strategy is based on the SRT LB method. However, more flexibility can be obtained to match a broader spectrum of fluid and thermal properties with the MRT and entropic LB method [66, 67, 68, 69]. For clarity, the LB counterparts of previously introduced quantities in physical units are denoted with the subscript 'LB' hereafter.

2.2.6 Eulerian-host algorithm

Previous hybrid approaches for simulating particle suspensions have been reported to scale linearly with respect to the number of particles, N, [52, 53, 57]. However, when simple search (SS) ($i.e.$, the exhaustive pairwise search) algorithm is applied to unconnected particle-particle interactions, the scaling of the particle dynamics could still degrade to $O(N^2)$, which consequently undermines the overall scalability of the method. To overcome this issue, two types of algorithms have been proposed in the MD community. The Verlet neighbor list (VNL) algorithm [88] limits the pair search to a list of N_{nl} adjacent

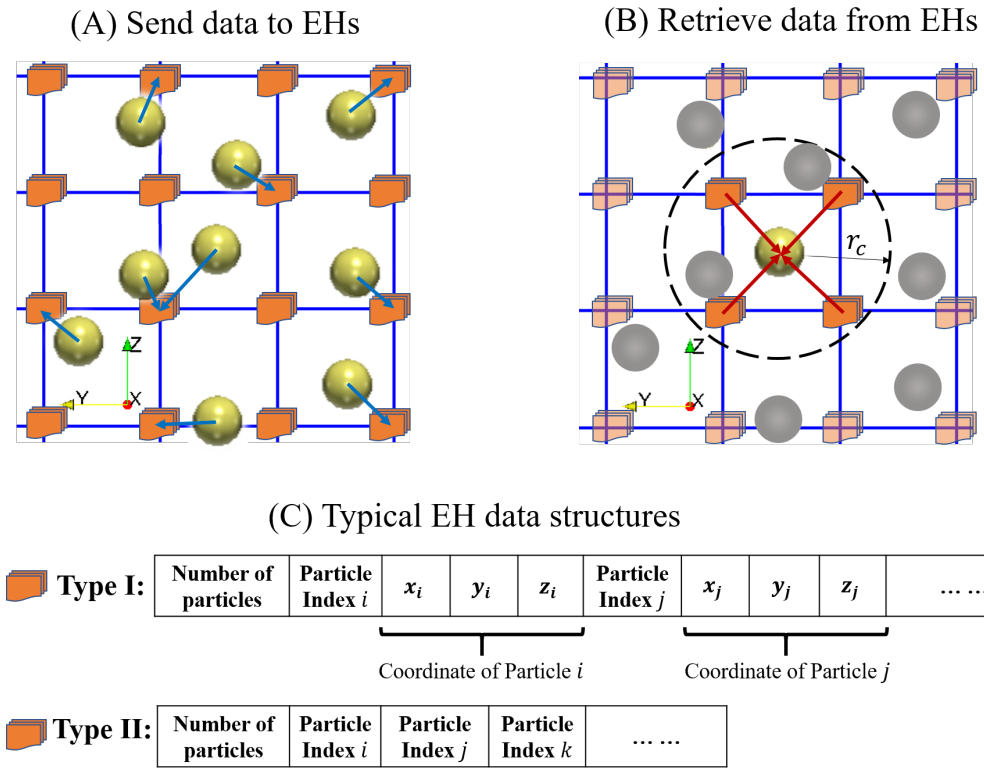

Figure 2.2: Schematics of the EH algorithm: (A) Once an updated particle position is obtained, the coordinates of the particle is sent to its nearest EH; (B) A single particle interacts with its neighboring EHs that contain the coordinates of the adjacent particles; (C) Typical date structures of the Eulerian host.

particles for a given particle, which reduces the search scaling to $O(NN_{nl})$; however, the construction of the neighbor list still scales as $O(N^2)$, which undermines the overall efficiency when N becomes reasonably large. The cell linked list (CLL) algorithm [89] partitions the simulation domain into cellular domains, and each particle only interacts with the particles within the same cell. The CLL algorithm truly scales as $O(N)$ but requires extra computational infrastructure to handle domain decomposition.

Inspired by the merit of both VNL and CLL algorithm and noticing the Eularian nature of the LB method, we propose a linear short-range particle-pair search algorithm that makes use of the Eulerian LB nodes as information hosts for the Lagrangian particles. As illustrated in Figure 2.2 (A), during each LB time step, the updated information of each sub-grid particle can be stored in a data structure on its nearest LB node, which is denoted as an Eulerian host (EH). When performing particle-particle short-distance interactions, each particle only interacts with its surrounding EHs that carry the information of the neighboring particles within a cut-off distance, as illustrated in Figure 2.2 (B). Each EH could contain information such as the number of particles, the index of each particle and even the coordinate of each particle, as indicated in Figure 2.2 (C). The complexity of the data structure for EHs varies depending on the concentration of the sub-grid particles. Specifically, when the particle volume fraction is low, $i.e.$, each EH only contains 1$\sim$2 particles, data structure of type I can be used with the information of particle coordinates included; when the particle volume fraction is high, $i.e.$, each EH could contain more than two particles, data structure of type II can be used to avoid excessive memory allocation for each LB node. The benefit of using EHs of type I is that the particle information can be directly communicated together with the LB fluid node information during MPI permutations. Therefore, no separate MPI communications are needed for the particle phase. However, when type II EH is applied, separate MPI communications for the particle phase are necessary since the particle coordinates are stored separately from the LB fluid nodes information. For the case with dilute particle concentrations, EHs of type I data structure

Table 2.1: Scaling performance comparison between the Eulerian-host algorithm and the simple search algorithm.

Number of Particles, N	**0**	**100**	**1 000**	**10 000**
TWCT (s), EH	464.3	470.3	522.2	1 050.7
TWCT (s), SS	300.7	307.2	565.8	21 857.7
LD overhead (s), EH	0	6.0	57.9	568.5
LD overhead (s), SS	0	6.4	265.1	8 442.4

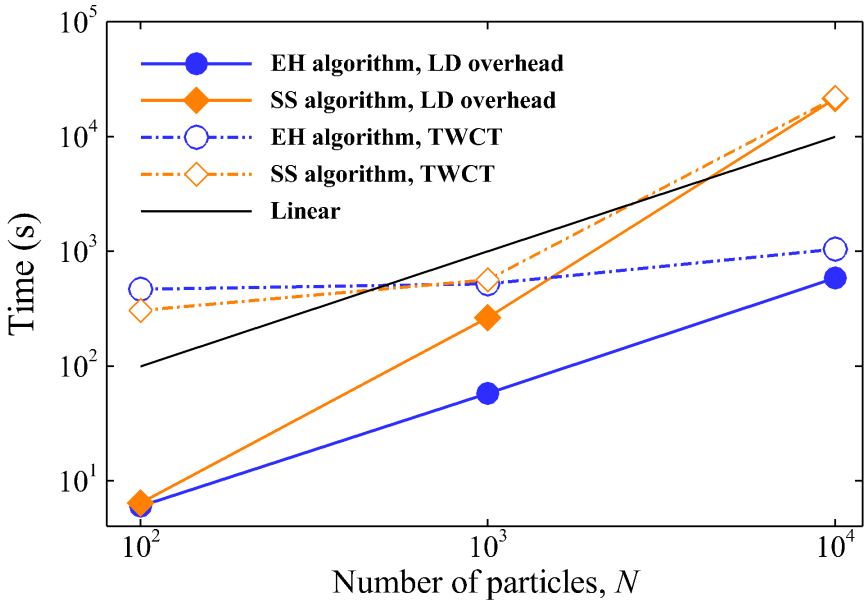

Figure 2.3: The Langevin-dynamics(LD) overhead and the total wall clock time (TWCT) using the Eulerian-host (EH) algorithm or simple-search (SS) algorithm plotted against the number of particles in log-log scale. The EH algorithm is shown to scale linearly with respect to the number of particles, N, in contrast to the quadratic scale of the SS algorithm.

are adopted.

The particle-number scalability of the LB-LD approach embedded with the EH algorithm is tested by simulating different number (N=0, 100, 1000, and 10000) of particles under a wall-bounded shear flow within a 50^3 LB domain. For each case, five runs are sampled to obtain an averaged total wall clock time. All the cases are tested for 10 000 LB steps in serial mode on the TACC Stampede-2 supercomputer. Each computing node is configured by one Intel Xeon Phi 7250 processor, which has a base frequency 1.4 GHz and contains 68 cores. The total wall clock time (TWCT) for each case and the corresponding overhead associated with LD operations are tabulated in Table 2.1. The LD overhead for

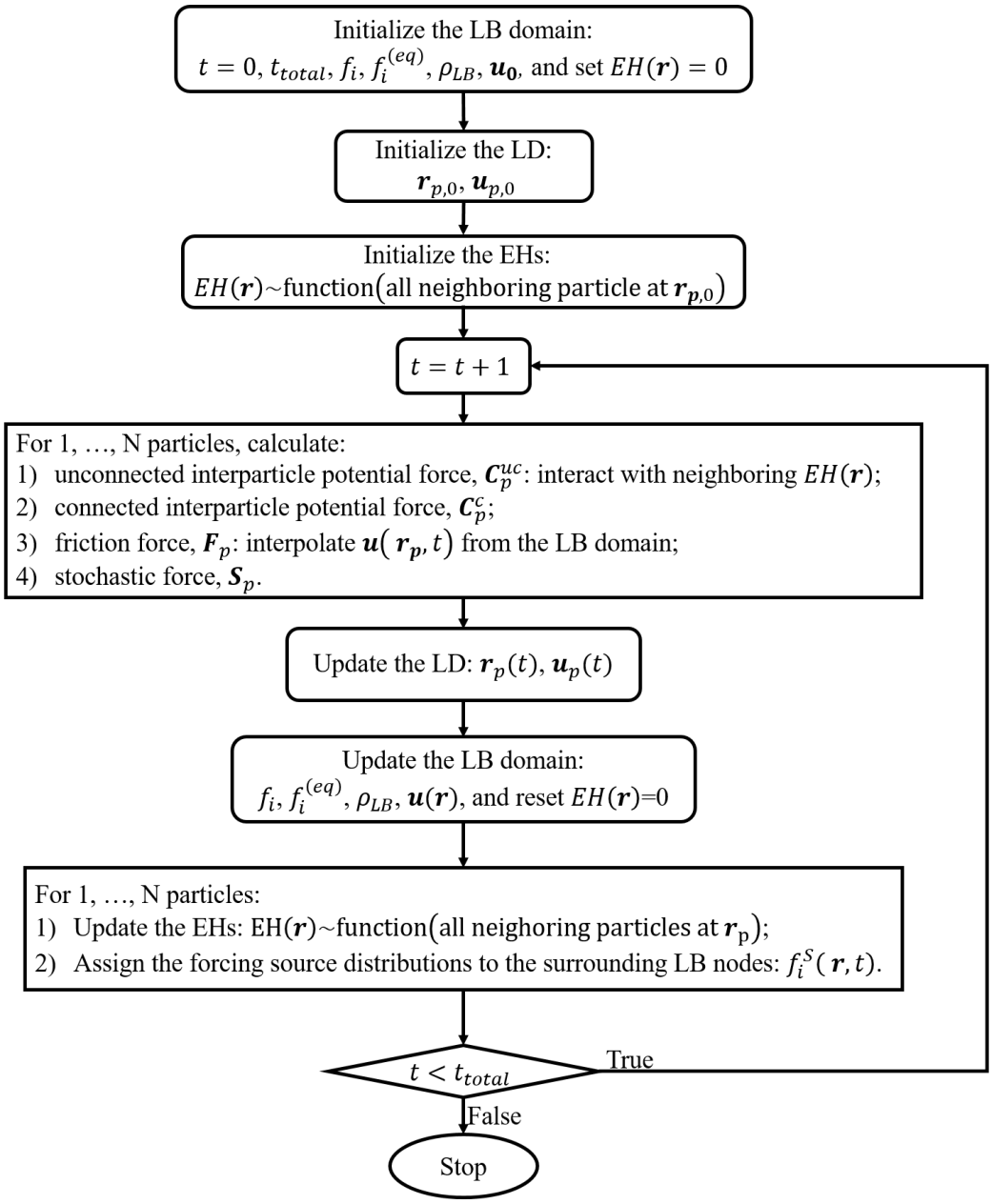

Figure 2.4: The flow chart of the current LB-LD method embedded with the EH algorithm to handle short-distance, unconnected particle-particle interaction.

cases with $N > 0$ is calculated by subtracting the corresponding TWCT with that of the N=0 case. As plotted in Figure 2.3, the EH algorithm compared to the SS algorithm shows slightly higher TWCT when $N \leq 100$. This is understandable since the introduction of EHs adds overhead to the update of the Eulerian LB domain. However, as the number of particles increase, the EH cases starts to show much lower TWCT compared to the SS cases. In fact, when N=10 000, the TWCT with EH algorithm becomes more than one magnitude lower than that with the SS algorithm. A linear scalability curve, generated by setting the overhead equal to the number of particles, is also plotted as a reference. The results clearly show that the LD overhead with EH algorithm scales almost linearly with the number of particles $\sim O(N)$, while the simple search algorithm exhibits $\sim O(N^2)$ scales.

Both the construction of EHs and the interaction with EHs are localized, therefore scaling as $O(N)$. For interactions among 100 nm NPs, a search of neighboring 8 EHs is shown to be enough to cover all the nearby particles within the cut-off distance. As the particle size increases, a slight expansion of the search range is needed, which however doesn't undermine the $O(N)$ merit. When the particle is encountered with a periodic boundary, a wrapping operation is needed to ensure the availability of EHs. By applying the EH algorithm, the particle-particle interaction can be conveniently handled together with the particle-fluid coupling procedures. The EH algorithm provides the localized data structure for the particle dynamics of Lagrangian nature, which is fundamentally more convenient for parallelization. Figure 2.4 depicts the flow chart of the current LB-LD method with the EH algorithm embedded with the LB-LD two-way coupling scheme. Both the rectangular blocks in Figure 2.4 denote the processes of force calculation and particle-fluid/particle interaction associated with each particle, which are purely localized operations and scale as $O(N)$.

2.3 Sample Problems

The validity and accuracy of the LB-LD approach to capturing the dynamics of nanoscale particle and polymer suspensions subject to both the thermal fluctuation and HI are demonstrated through several sample problems. First, the momentum relaxation of an isolated particle is presented to show the correctness of the particle-fluid coupling. Then, the self-diffusion of colloidal particles in infinite dilution is demonstrated to show the direct capture of Brownian motion. As follows, the hindrance of particle diffusion in concentrated colloidal suspension is discussed to shown the validity of the short-distance particle-particle interaction model. The self-globularization process of a cohesive polymer chain and the shear-induced unfolding of a collapsed polymer globule are further presented to show the applicability of the LB-LD model to nano-polymer suspension dynamics subject to HI effects. All cases adopt a LB relaxation time τ_{LB}=1 unless otherwise prescribed.

2.3.1 Momentum relaxation of an isolated particle

The fluid-particle coupling is first verified by analyzing the slowing-down process of an isolated particle with an initial momentum in a quiescent viscous fluid. A cubic LB domain with periodic boundary condition enforced in each direction is selected for all the simulations. Three computational domains with different dimensions (50^3, 70^3, and 100^3) are considered to study the domain size dependency. A particle of mass $m_{p,LB}$=29.3 with an initial velocity $u_{p,LB}$ (0)=0.01 along the X direction is released in the center of the domain. By setting τ_{LB}=0.51 and d_p=100 nm, a friction coefficient ζ_{LB}=0.48 is prescribed to dissipate the kinetic energy of the particle. Given $St > 1$, under-damped LE is solved for this problem.

The deterministic response of the particle momentum relaxation is first presented by omitting the Brownian effect. The inset of Figure 2.5 (a) shows a snapshot of the flow field induced by the decelerating particle right after its release. Such double vortex flow

structure has also been observed in previous numerical studies [90, 35]. The time evolution of the particle velocity normalized by the initial velocity for three domain sizes are depicted in Figure 2.5 (a), where the corresponding asymptotic behaviors are also presented for comparison. At short-time scales, $i.e.$, when $t/\tau_r < 10$, the particle velocity decays exponentially for all three domain sizes, which also agrees well with the asymptotic short-time exponential decay behavior, $exp(-t/\tau_r)$. At long-time scales, Alder $et\ al.$ [90] show the particle velocity should eventually decay according to a power law scale, $(t/\tau_r)^{-3/2}$, known as the long-time tail behavior, which reflects the fluid-particle coupling effect. As shown in Figure 2.5 (a), the long-time tail behavior is not significant for the 50^3 domain size, where instead a plateau is observed right subsequent to the exponential decay. However, as the domain size increases to 100^3, the long-time tail behavior appears to be more pronounced. The eventual flattening of all cases manifests the fluid and particle eventually translate at the same velocity as a result of the periodicity of the finite LB domain and the conservation of momentum for the particle-fluid system. The same problem with domain size of 100^3 is further simulated using the over-damped LE with zero particle inertia, as also depicted in Figure 2.5 (a). As expected, the particle velocity directly relaxes to the long-time tail regime without yielding the exponential decay behavior. The jittering of the relaxation curves for the zero-inertia case is due to the temporal discretization effect and can be eliminated by reducing the time step [52, 57].

According to the FDT, the stochastic relaxation behavior of a Brownian particle should be in accordance with the deterministic relaxation behavior of the particle under the same flow condition with no Brownian effect. This can be demonstrated by adding the Brownian noise to the previous deterministic case. For simplicity, the stochastic force is only applied to the particle along the +X direction, thus the motion of particle is constraint in a one-dimensional fashion. The particle velocity relaxation process can be quantified by the normalized velocity autocorrelation function (VAF), $\langle u_p(t)u_p(0)\rangle/u_p^2(0)$, which reduces to $u_p(t)/u_p(0)$ for the deterministic case. In Figure 2.5 (b), the particle VAF for cases with or

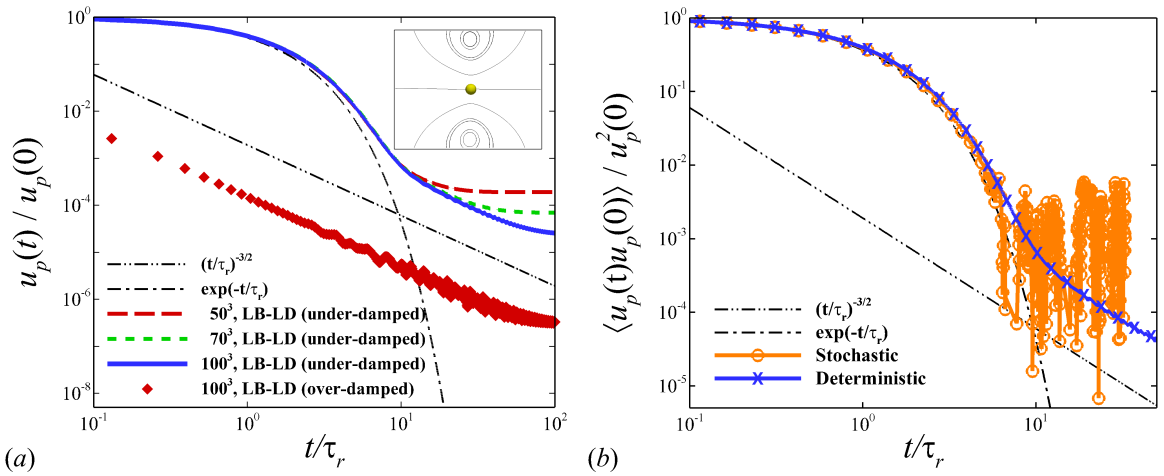

Figure 2.5: The momentum relaxation process of a point particle with an initial disturbance in periodic LB fluid domains of different sizes (a) under deterministic condition or (b) subject to stochastic noise effects.

without Brownian effect is plotted against the LB time. The VAF curve for the stochastic case is obtained by averaging over an ensemble of ten independent runs. Overall good agreements between the stochastic case and the deterministic case are obtained. These results show the particle-fluid coupling and the FDT are correctly captured using the current LB-LD method.

2.3.2 Brownian diffusion in dilute colloidal suspensions

Previous analysis [48, 49] show that once the fluid phase satisfies the FDT through FH, the particle dynamics is automatically rendered to yield the FDT through the particle-fluid coupling. However, when both the particle and fluid phase are introduced with fluctuation that satisfies the FDT individually [52, 53], the coupled system requires an empirical rescaling of the particle mobility to produce the correct temperature and hence the Brownian effect. Below, we study the self-diffusion of colloidal particles in the dilute regime to show that the current LB-LD approach, which introduces thermal fluctuation solely to the particle phase, directly captures the correct Brownian effect.

Colloidal suspensions in the dilute regime with five particle sizes, $d_p = 10, 30, 100, 300$

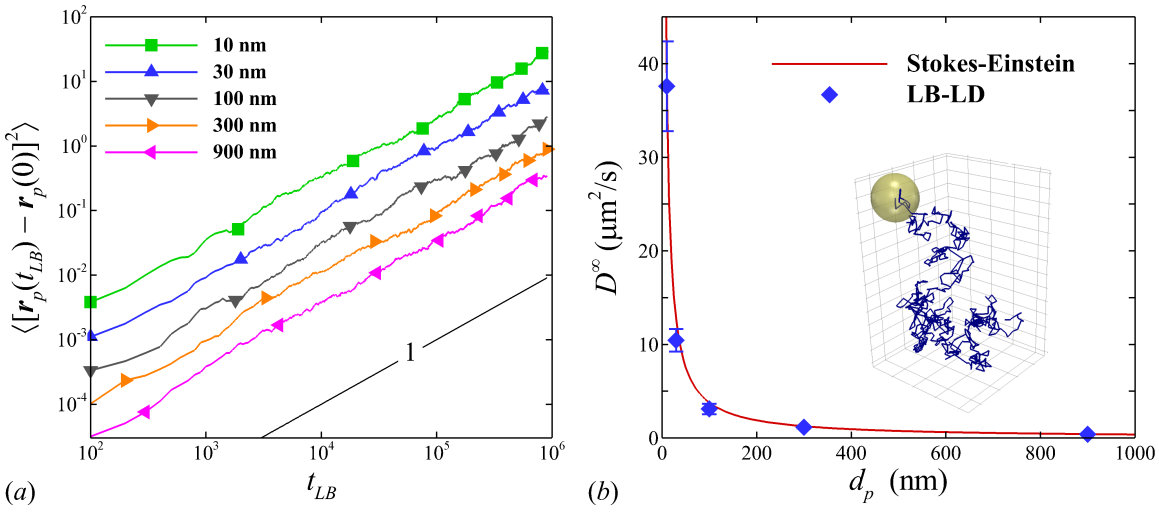

Figure 2.6: (a) The mean squared displacements for various particle sizes in dilute concentraions. (b) Normalized self-diffusivity of colloidal particles as a function of particle size at infinite dilution. The symbols are the simulation results. The line is the theoretical results based on the Stokes-Einstein relation.

and 900 nm, are simulated independently to evaluate the long-time particle diffusivity. Since only the long-time diffusion is of concern, the over-damped LE is employed in this study. By sampling the mean-squared displacement (MSD) of the Brownian particle, the particle long-time diffusivity, D^∞, can be calculated as

$$D^\infty = \frac{1}{6}\frac{d}{dt}\langle[\mathbf{r}_p(t) - \mathbf{r}_p(0)]^2\rangle|_{t\to\infty}, \tag{2.23}$$

at $t/\tau_r \gg 1$, where the angle brackets denote an ensemble of 1 000 particles in one simulation. All cases are simulated in a periodic cubic domain with dimensions of 100^3. This setup ensures the particle volume concentration being kept below 0.1%. The theoretical Brownian diffusion in dilute, unconfined suspension systems is determined by the Stokes-Einstein relation as,

$$D^B = \frac{k_B T}{\zeta}, \tag{2.24}$$

which is a nice, compact manifestation of the FDT by quantitatively relating the particle thermally induced diffusive behavior to the dissipative property of the particle-fluid system.

Figure 2.6 (a) shows the transient growth of the particle MSD for different particle size. All the cases exhibit linear temporal growth of the MSD due to the neglecting the of the particle inertia. Besides, as the particle size decreases, an increase of the MSD is observed at the same instance. Figure 2.6 (b) further plots the dimensional long-time particle diffusivity versus the particle size. The inset in Figure 2.6 (b) shows a typical example of the particle trajectory. The particle long-time diffusivity predicted by the LB-LD simulation shows excellent agreement with the Stokes-Einstein theory. This observation proves that the LB-LD approach, which only introduces thermal fluctuation in the particle phase, directly captures the Brownian motion without the any empirical adjustment.

2.3.3 Hindered particle diffusion in concentrated colloidal suspensions

In concentrated colloidal particle suspensions under quiescent flow condition, the particle self-diffusion is often hindered due to the frequent, short-distance particle-particle interactions. The hindered particle long-time diffusivity, D^{∞} is known to be sensitive to the number of particles, N, considered in the system [91]. To correct for such finite-size effects, Ladd $et\ al.$ [91] proposes a correction of the long-time diffusivity to link the N-particle system to an infinite-particle system through

$$\frac{D^{\infty}}{D^{B}} = \frac{D^{t}(N)}{D^{B}} + \frac{\mu}{\mu_{\phi}}[1.7601(\frac{\phi}{N})^{1/3} - \frac{\phi}{N}], \tag{2.25}$$

where $D^{t}(N)$ is the particle self-diffusivity measured with a N-particle system at time t, μ is the viscosity of the pure liquid and μ_{ϕ} is the viscosity of the particle suspension at various concentrations. To further validate the LB-LD model, we simulated concentrated colloidal suspension with particle size of $d_p = 600\ nm$ and particle packing fractions ranging from ϕ =0 to 42%. Three problem sizes are considered with particle number $N = 1073, 1637$ and 2096. The periodic compuational cube for each setup is adjusted according to the particle packing fraction. The long-time diffusivity is measured at $t/\tau_B = 1.0$, which

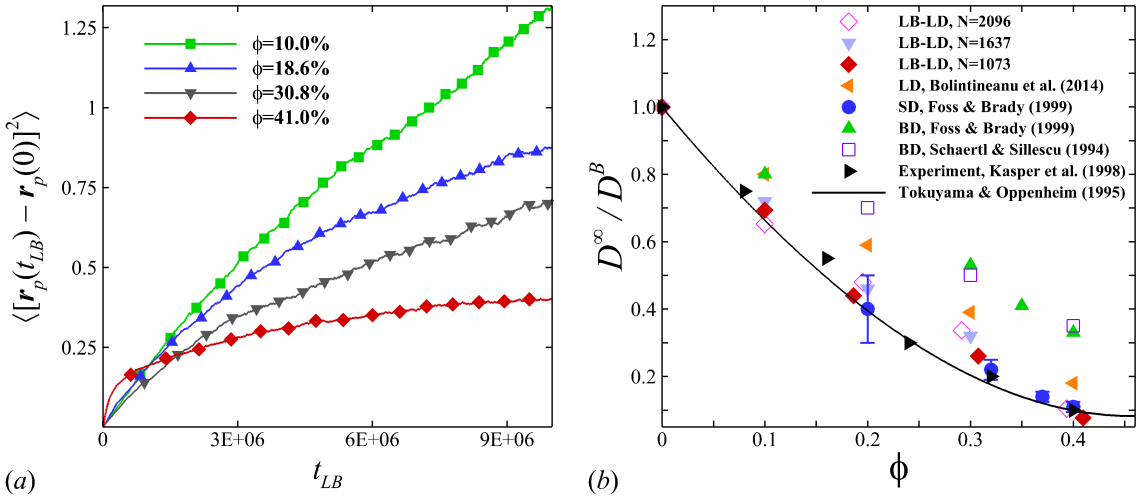

Figure 2.7: (a) The mean squared displacements at various particle packing fractions with $N = 1073$. (b) The normalized self-diffusivity of colloidal particles as a function of particle volume concentration. Experimental results, theory and particle-scale simulation results are also plotted for comparison purpose.

is shown to be the least time needed in order to reach the long-time diffusivity plateau [82]. It should be noted that the $t/\tau_B = 1.0$ criteria, somewhat empirical, might need future verification to ensure the full long-time regime arrived. The measured diffusion coefficients, $D^t(N)$, are further corrected based on Equation 2.25, where the suspension viscosity adopts the values reported in [84].

Figure 2.7 (a) shows the evolution of the particle MSD for various particle packing fractions with $N = 1073$. A clear decrease of the MSD slope with increasing particle concentration is observed. Figure 2.7 (b) further presents the normalized long-time diffusivity against the particle packing fraction. Results from existing simulation studies [40, 92, 93, 84], experimental measurements [94] and theory [95] are also plotted for comparison. At zero particle packing fraction, all results agree excellently with the theoretical Brownian diffusivity. At non-zero particle packing fraction, the BD method [92, 93], which completely neglects the effect of the fluid-solid coupling, shows the largest deviation from both experiment and theory. By improving the contact modeling, the LD model [84] exhibits improved accuracy. The SD method [40] shows excellent accuracy since it fully resolves

both the near-field and far-field HI. The LB-LD method, which empolys the DLVO contact modeling and includes the fluid-mediated effect through two-way coupling, show good agreement with both the experiment and theory at low ($\phi = 0.1$) and high ($\phi = 0.4$) particle packing fraction. The small deviation at moderate concentration ($\phi = 0.2 \sim 0.3$) might be related to the exclusion of the lubrication effect, which plays a vital role at semidilute particle suspensions [96]. Overall, the LB-LD method shows satisfactory accuracy given its simplicity in handling the many-body long-range and short-range interactions.

2.3.4 Self-globularization of a cohesive polymer chain

Polymer chains, such as deoxyribonucleic acid (DNA) [97] and von Willebrand factor (vWF) [85], tend to form a collapsed globule conformation in a quiescent solvent. The mechanistic drivers for this process primarily include the Brownian motion and the intra-cohesiveness between adjacent monomers. The polymer longest relaxation time (LRT), τ_p, can be used to characterize the rate of the self-globularization process. The LRT is known to increase with the polymer length defined as the number of monomers, N. Specifically, under free-draining (FD) condition wherein the many-body HI is neglected, the polymer LRT suggested by [98], $\tau_{p,R}$, scales as

$$\tau_{p,R} \sim O(N^{2.0}); \tag{2.26}$$

when including the effect of HI, the polymer LRT, $\tau_{p,Z}$, according to [99] should scale as

$$\tau_{p,Z} \sim O(N^{1.5}). \tag{2.27}$$

The self-globularization process of a single polymer chain in a quiescent flow under FD or HI conditions is interrogated using the current LB-LD approach. Four polymer lengths, N=20, 40, 60 and 80, are considered to obtain a scaling observation. The diameter of each monomer is set to d_p=60 nm. A periodic computational domain with dimensions of 100^3 is

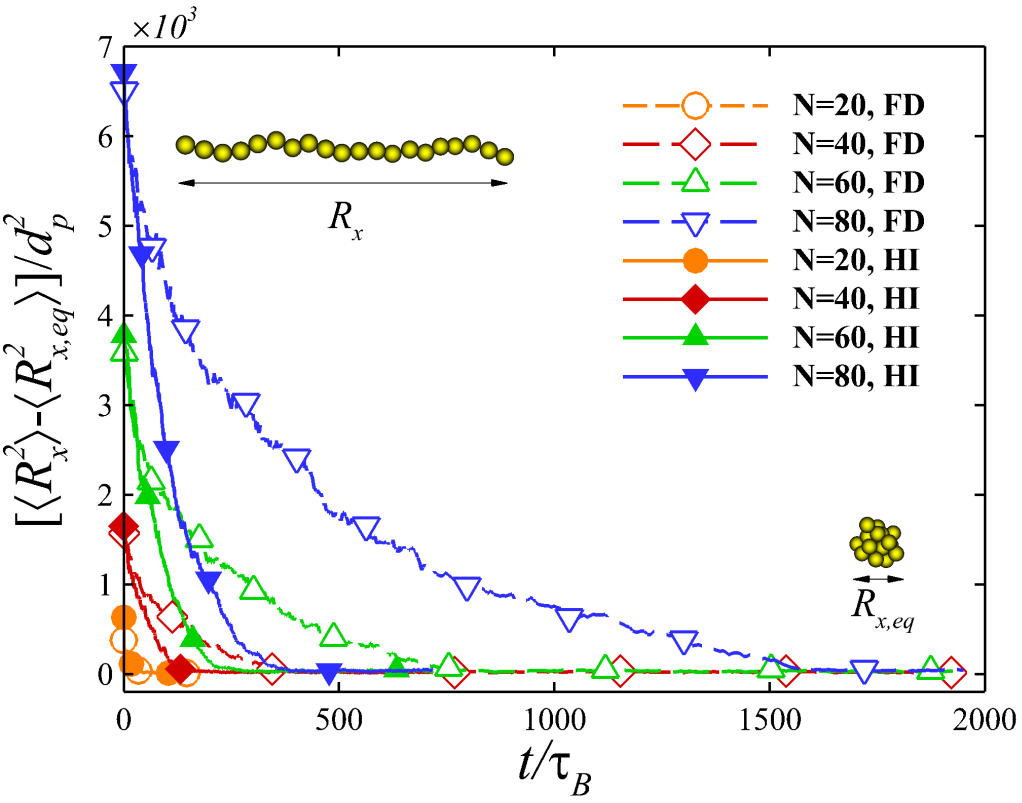

Figure 2.8: Temporal evolution of normalized MSE, $\langle R_x^2 \rangle / d_p^2$, for various polymer length ($N = 20 \sim 80$) under either HI or FD condition. The left inset shows the streched state of the polymer chain, while the right inset shows the globular state (after relaxation) of the polymer chain.

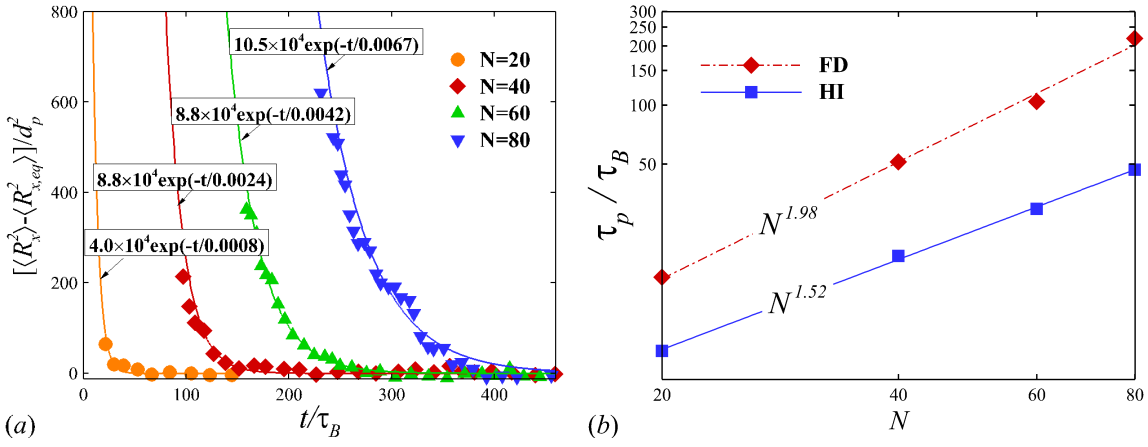

Figure 2.9: (a) The instantaneous shifted MSE data points and the corresponding exponential curve fittings for polymers of various length N=20, 40, 60, and 80, under hydrodynamic interaction conditions. Only the data points at $\langle R_x \rangle / (N d_p) \sim 0.3$ are considered for the curve fitting procedure. The curve fitting is performed for all points satisfying $\langle R_x \rangle / (N d_p) \leq 0.3$. (b) Polymer longest relaxation time τ_p as a function polymer length N.

selected to minimize the periodic boundary effect. The polymer extension, R_x, defined as the polymer projection length along the X direction (streamwise direction), is introduced to quantify the instantaneous conformation of the polymer. The over-damped LE is employed, given the time scale of the polymer conformational change is much larger than the particle relaxation time scale. Figure 2.8 plots the normalized mean-square polymer extension (MSE), $\langle R_x^2 \rangle / d_p^2$, versus normalized time, t/τ_B. Each curve is obtained through ensemble average over three independent runs with the same polymer length. The insets of Figure 2.8 demonstrate the initial and final conformation of a polymer chain with $N = 20$. For both the FD and HI cases, longer polymers (larger N) take longer time to reach equilibrium globular conformation. Additionally, polymers of the same length under HI conditions tend to tend to form a globule conformation more rapidly compared to under FD conditions. The underlying mechanism causing this time-scale discrepancy between HI and FD conditions is that the flow pattern induced by the polymer itself leads to smaller relative velocity and hence smaller drag force exerted on each monomer [100].

The polymer relaxation time τ_p can be quantitatively evaluated by fitting the instantaneous MSE, $[\langle R_x^2 \rangle - \langle R_{x,eq}^2 \rangle]/d_p^2$, with an exponential function form in the final relaxation regime when $\langle R_x \rangle / N d_p \leq 0.3$, as suggested in [101]. The obtained exponential curve satisfies the following expression

$$\frac{\langle R_x^2 \rangle - \langle R_{x,eq}^2 \rangle}{d_p^2} = \mathcal{A} e^{-t/\tau_p}, \tag{2.28}$$

where $\mathcal{A}$ is a fitting constant, and the denominator of the exponent readily gives τ_p. Figure 2.9 (a) presents the exponential curve fittings for the instantaneous $[\langle R_x^2 \rangle - \langle R_{x,eq}^2 \rangle]/d_p^2$ data points at $\langle R_x \rangle / N d_p \leq 0.3$ under HI condition. The corresponding exponential functions are denoted beside each curve as shown in Figure 2.9 (a). Same curve fitting procedure is also performed for the FD case to obtain the LRT of the polymer chain under FD condition, which is not shown here for clarity. The obtained τ_p for both FD and HI cases are further

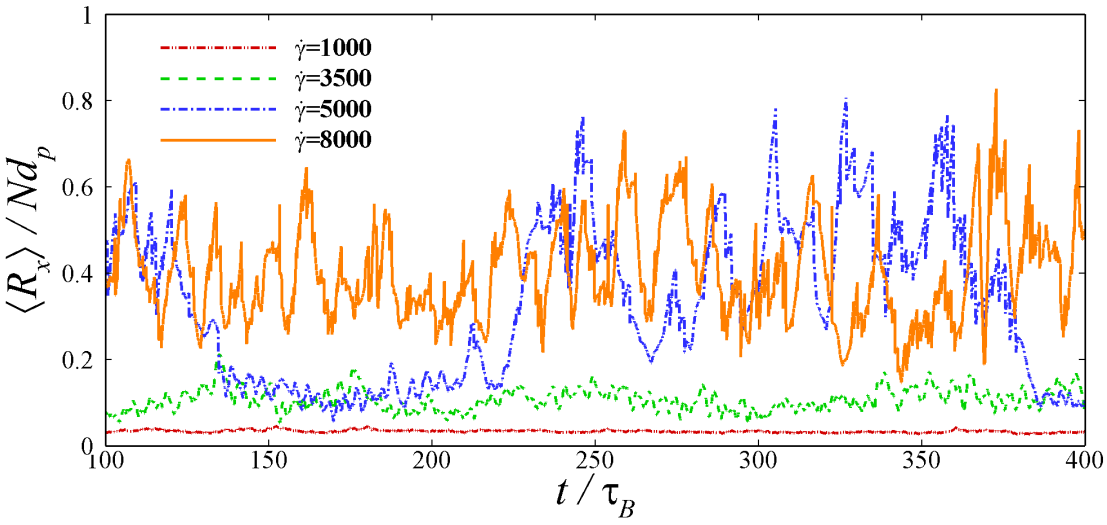

Figure 2.10: The temporal evolution of the normalized mean extension of a single polymer chain (model vWF) subject to various shear rates in an unbounded simple shear flow.

plotted against the polymer length N in Figure 2.9 (b), where the two straight lines are the best power-law fits for $\tau_{p,R}$ and $\tau_{p,Z}$ data points, respectively. The relaxation time τ_p of the single polymer chain captured based on the LB-LD approach show scaling exponents of 1.98 and 1.52 for the FD and the HI conditions, respectively. These scaling behaviors agree nicely with the theoretical scaling arguments [98, 99]. These results show the conformational dynamics of a single polymer chain subject to many-body HI is favorably captured through the current LB-LD approach. It also confirms the significance of including the effect of HI for simulating nanoscale particulate suspensions.

2.3.5 Shear-induced unfolding of a collapsed polymer chain

When subject to shear flow above certain critical shear rate, the collapsed biopolymer chains (e.g. vWF, DNA, etc.) tend to be unfolded and exhibit periodic stretch/coil conformation changes while tumbling [97, 85, 87]. Such shear-induced unfolding phenomenon of the collapsed polymer chain is a manifestation of the competition between the viscous, elongational flow effect and the intra-monomer cohesive effect [85]. In this section, we further validate the LB-LD approach by simulating a single vWF strand subject to different shear rates and comparing its conformational statistics with existing experimental data.

To exclude the confinement effect, the Lees-Edwards boundary condition [102, 74] is employed to impose the unbounded simple shear flow. Shear rates, ranging from 1 to 8 000 s^{-1}, are considered to replicate the flow conditions considered in the experiment [87]. The vWF strand is modeled as a 200-bead ($i.e.\ N = 200$) polymer chain. Each bead represents a dimer (repeating unit of a vWF polymer chain) with a diameter of $d_p = 160\ nm$ closely matching measured dimer size reported in [103]. The selected bead size and bead number yield a contour length of $32\ \mu m$ for the model vWF, which is also close to the actual size of the vWF considered in the experiment [87]. All computations adopt a periodic LB domain with dimensions of 60×30×30 μm^3 in the flow, the velocity-gradient and the vorticity directions, respectively.

The conformation state of a single polymer chain under shear flow can be quantified by the normalized mean polymer extension (ME) in the streamwise direction, $\langle R_x \rangle / N d_p$, where the ensemble average of the polymer extension is performed in time. As shown in Figure 3.3, the instantaneous polymer extension exhibits fluctuation over time. Moreover, the magnitude of the fluctuation and the ME increase with shear rate changing from 1 000 s^{-1} to 8 000 s^{-1}. Figure 2.11 plots the ME of the polymer chain versus shear rate in both dimensional and dimensionless units. A Weissenberg number, defined as $Wi = \dot{\gamma}\tau_B$, is employed as the nondimensional shear rate. It is shown that the ME measured in the LB-LD simulation compares favorably well with the experimental measurements reported in Schneider $et\ al.$ [87]. Particularly, a range of critical shear rates (5 000 ∼6 000 s^{-1}) around which the polymer chain exhibits an abrupt increase of the ME is well captured in the LB-LD simulation. The insets in Figure 2.11 presents the representative polymer conformations under simple shear flow. As expected, below critical shear rate, the vWF polymer remains in a compact globular conformation; while above critical shear rate, the vWF polymer undergoes periodically stretched/coiled conformational transitions. The simulation results reported in [85] using Brownian dynamics are also adopted for comparison, where the critical shear rate is shown to be well captured. However, their simulation de-

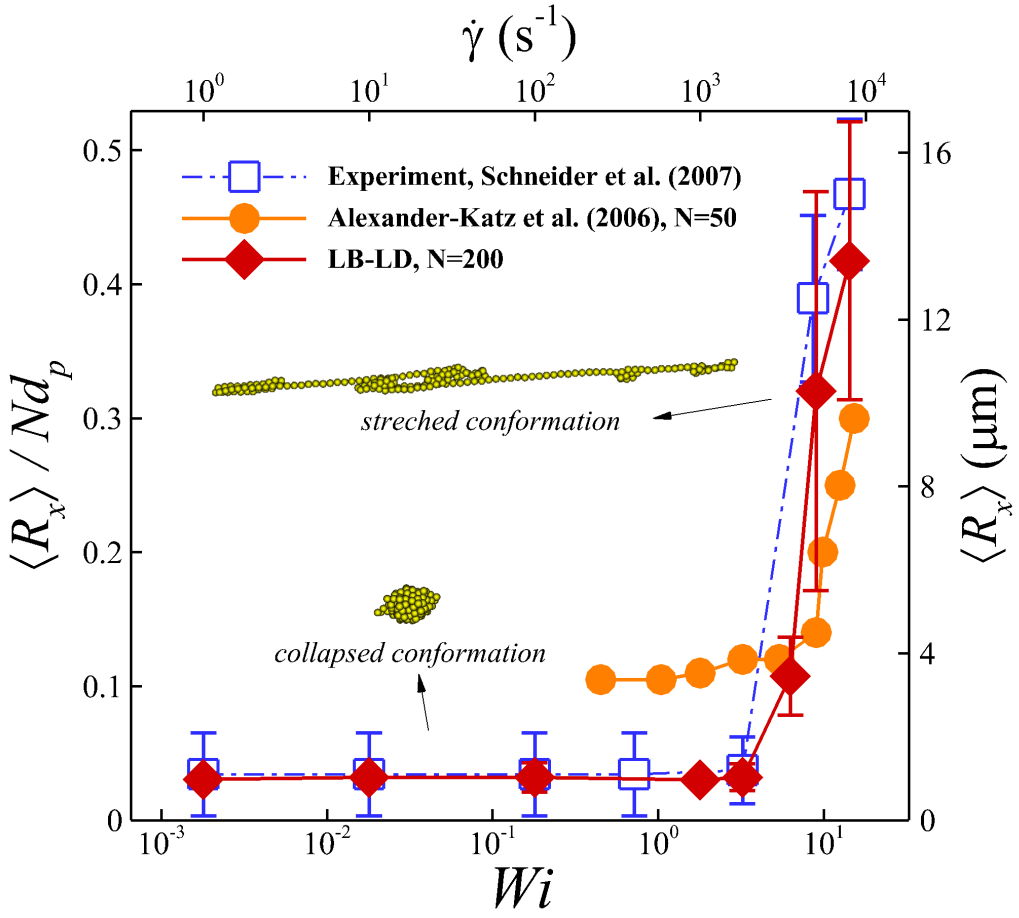

Figure 2.11: Unfolding of a single polymer chain under a critical shear rate. The measured polymer mean extension using a microfluidic device by [87] is adopted to validate the LB-LD model. The simulation results reported in [85] are also plotted for comparison. The right vertical axis (dimensional) applies to experimental results and the LB-LD results; the left vertical (dimensionless) axis applies to all three sets of results.

viates from the experimental results in terms of normalized mean extension particularly at low shear rates, which is due to the shorter contour length ($N = 50$) considered in their model vWF. Since the vWF model parameters (except N) considered in the LB-LD polymer model is close to the ones employed in [85], the results also qualitatively confirm the weak polymer length dependence of the critical shear rate as concluded in [85]. The good agreement between the LB-LD simulation and experiment results for the shear-induced unfolding process of vWF strand again show the validity of the current LB-LD approach in capturing the conformational dynamics of long-chain polymers under shear flow.

2.4 Summary

A hybrid Eulerian-Lagrangian approach coupling the non-fluctuating LB method and a LD method is developed to simulate suspensions of nanoscale particles and long-chain polymers including the effects of thermal fluctuation, many-body HI, and particle-particle short-distance interactions with linear particle-number scalability. The LB-LD approach is verified and validated with both thoery and experiment. An EH algorithm is also developed to handle the short-range pairwise particle search and interaction, which ensures localization and hence linear scalability of the method while performing particle neighbour search. The LB-LD approach embedded with the EH algorithm is purely local and can be readily extended for parallelization. Liu2018JFM The LB-LD approach confirms the idea of coupling non-fluctuating LB method with LD method to directly capture the correct Brownian diffusion without empirical rescaling of the particle mobility [57]. Furthermore, the current method demonstrates that the long-distance many-body HI can be directly included via the LB-LD two-way coupling scheme, which was not shown in [57]. Compared to using mobility matrix approach to capture HI [85], the direct two-way coupling approach, in addition to being more efficient, also has the flexibility of including the modified HI effects subject to complex geometries/boundaries [24, 118]. Besides, the two-way coupled LB-LD approach embedded with the DLVO potentials allows simulating nanoscale particulate

suspension across dilute-to-dense concentrations with good accuracy.

Liu2018JFM Since the entire nanoscale particulate suspension dynamics are resolved through sub-lattice techniques, the LB-LD method is particularly suitable for multimodal particulate suspension applications that involve particles, polymer chains and capsules with disparate length scales [24, 118], where DNS of such systems is computationally prohibitivoute. One example is the simulation of multiscale, multicomponent complex blood flow by coupling the LB-LD method with cellular blood solvers, where the dynamics and deformation of both microscale blood cells (e.g. red blood cell, platelet, etc.) and nanoscale molecules and bioproteins (e.g., vWF, albumen, etc) can be simulated concurrently with neither refining the grids nor introducing sub-timesteps. In Figure 2.12, we present a simulation snapshot demonstrating a simulation of multiscale and multicomponent whole blood through a 40 μm microvessel. This simulation captures a concentrated poly-dispersed suspension tubular flow of 40% volume fraction of deformable red blood cells (red), $\sim$1% volume fraction of rigid platelets, $3\times10^{10}/ml$ vWF and $1\times10^{9}/ml$ nanoscale particles under a wall shear rate of 2000 s^{-1}. The development of the LB-LD method forms a multiscale computational framework to tackle biophysical suspension flow problems across nano-to-microscale, such as high-shear induced thrombus formation in blood [11], which will be discussed in following chapters.

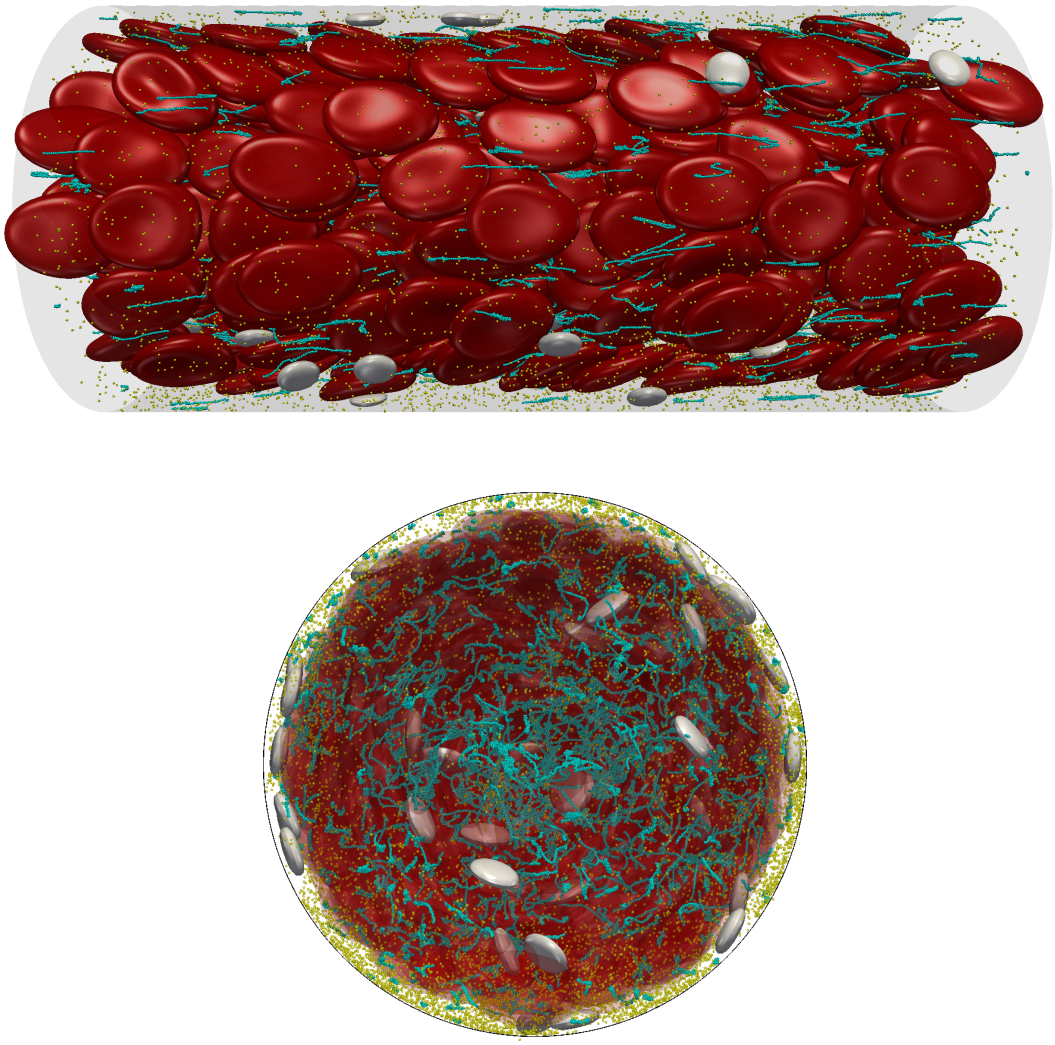

Figure 2.12: The side view (top) and frontal view (bottom) of complex whole blood flow through a microvessel with a 40 μm diameter, simulated using the LB-LD method coupled with the spectrin-link method [3]. A total of 427 deformable red blood cells (RBCs) (red capsules) are resolved in the simulation, resulting in a 40% heamatocrit. The platelet (white oblate capsules)-RBC number ratio is $\sim 1/20$. The vWF (light blue strands) molecule number concentration is $\sim 3 \times 10^{10}/ml$. The wall shear stress is $2000\ s^{-1}$. All above parameters match the blood physiological condition. The nanoparticle (yellow particles) number concentration is $\sim 1 \times 10^{9}/ml$ consistent with the typical dosage used $in\ vivo$.

CHAPTER 3

DISPERSION OF NANO-TO-MICROSCALE PARTICLES IN CELLULAR BLOOD FLOW THROUGH MICRO-VESSELS.

Transport of solid particles in blood flow exhibits qualitative differences in the transport mechanism when the particle varies from nanoscale to microscale size comparable to the red blood cell (RBC). The effect of microscale particle margination has been investigated by several groups. Also, the transport of nanoscale particles (NPs) in blood has received considerable attention in the past. This study attempts to bridge the gap by quantitatively showing how the transport mechanism varies with particle size from nano- to microscale. Using a three-dimensional (3D) multiscale method, the dispersion of particles in microscale tubular flows is investigated for various hematocrits, vessel diameters and particle sizes. NPs exhibit a nonuniform, smoothly-dispersed distribution across the tube radius due to severe Brownian motion. The near-wall concentration of NPs can be moderately enhanced by increasing hematocrit and confinement. Moreover, there exists a critical particle size ($\sim$1 μm) that leads to excessive retention of particles in the cell-free region near the wall, $i.e.$, margination. Above this threshold, the margination propensity increases with the particle size. The dominance of RBC-enhanced shear-induced diffusivity (RESID) over Brownian diffusivity (BD) results in 10 times higher radial diffusion rates in the RBC-laden region compared to that in the cell-free layer, correlated with the high margination propensity of microscale particles. This work captures the particle size-dependent transition from Brownian-motion dominant dispersion to margination using a unified 3D multiscale computational approach, and highlights the linkage between the radial distribution of RESID and the margination of particles in confined blood flows.

3.1 Introduction

Blood is a complex fluid suspended with multiple species, primarily including red blood cells (RBCs), platelets, white blood cells and various biomolecules (such as von Willebrand factors, albumin, fibrinogen, etc.). In microvessels under physiological flow conditions, RBCs migrate towards the center of the tube and leave a cell-free layer (CFL) near the wall [105, 106]. Such phenomenon, well known as the Fahraeus-Lindquist effect [107], contributes to the hemorheological heterogeneity of the blood flow. Unraveling the dispersion properties of solutes and cells of various sizes ranging from nanometer to micrometer in such heterogeneous blood flows under vascular confinement can potentially lead to optimal design of drug carriers and better understanding, intervention and control of vascular diseases.

As a relevant example of microscale particle transport in blood, platelets margination has shown to play an important role in affecting the rate of clot formation in hemostasis and thrombosis [11]. Motivated by that, a plethora of studies over the past decades have dedicated to unravel the mechanistic mechanisms of margination or segregation of microscale particles/cells in blood(-like) flows through perfusion experiements [12, 108, 109, 13], continuum-level modeling [14, 15] and direct numerical simulations [16, 17, 18, 110, 19, 111, 13, 20, 112, 113]. The platelet margination is found to be primarily driven by the cross-stream hydrodynamic fluctuation [17, 18, 114] or equivalently the RBC-enhanced shear-induced diffusion [15, 111] in the RBC-laden region synergistically accompanied by the sink-like effect of the CFL [111].

Nanoscale particle (NP) dispersion in blood flow, on the other end of the spectrum, has recently received considerable attention due to the fast development of nano-drug delivery techniques that have the potential to revolutionize the traditional therapeutics [115]. Although the effective diffusivity of nanoscale solutes in blood flow were measured decades ago [116], it is not until the past several years multiscale particle-level simulation tech-

niques [117, 23, 22, 24] become feasible. Tan $et\ al.$ [117] apply a coupled Brownian dynamics and immersed finite-element (FE) method to study the influence of RBCs on the NP dispersion in blood flows, showing substantial margination behavior for 100 nm particles. Through both in vivo and in silico techniques, Lee $et\ al.$ [23] show that submicron particles (>500 nm) can marginate while NPs ($\sim$100 nm) are mostly trapped in the RBC-laden region. Muller $et\ al.$ [22] performed two-dimensional (2D) simulations and suggest that microscale particles compared to submicroscale particles show better margination propensity. Liu $et\ al.$ [24] developed a multiscale complex blood solver and evaluate the role of BD versus RESID in affecting the biodistribution of NPs. Recently, Liu $et\ al.$ [118] characterize the complete 3-D diffusivity tensor of NP in blood under various shear rates and hematocrits, which can be employed to modeling large-scale NP biotransport applications.

Although the transport of both nanoscale and microscale particles in blood have been understood to a large extent, there is still a lack of a systematic interrogation of the particle dispersion behavior across nano-to-microscale sizes using a unified computational approach. Consequently, questions such as whether nanoscale particles exhibit margination qualitatively the same as microscale particle still remains controversial. A recent effort by Cooley $et\ al.$ [119] using in vitro experiment and 2D in silico simulation to understand the cross-length-scale particle margination and adhesion propensity has set an example for a unified understanding of the nano-to-microscale particle dispersion in blood flows. However, the general physical mechanisms behind the multiscale particle dispersion/margination phenomenon in blood are still not presented; besides, the 2D simulation could still overlook the 3D nature of the tubular blood flow phenomena.

In this work, we employ a recently developed 3D multiscale and multicomponent blood flow solver [3, 24, 120, 118] to tackle the dispersive characteristics of spherical, rigid particles with sizes spanning nano-to-microscale in a tubular blood flow. Particle suspension dynamics in the presence of thermal fluctuation, RBC-particle direct and hydrodynamic interactions and wall-bounded confinement effect are captured under a unified 3D compu-

tational framework. The strong correlation between the non-uniform distribution of particle radial diffusivity and the equilibrium distribution of particle radial concentration is highlighted to gain mechanistic understanding of the occurrence of particle-size-induced dispersion-to-margination transition.

3.2 Methodology

The numerical method used to simulate the bi-disperse particle-RBC suspensions confined in a tubular flow is through a multiscale and multicomponent complex blood flow method [24, 118] that couples the lattice-Boltzmann/Spectrin-link (LB-SL) method [3] with the lattice-Boltzmann/Langevin-dynamics (LB-LD) method [120]. This method leverages the off-lattice nature of the LB-LD approach and the efficiency of the course-grained SL RBC membrane method to concurrently simulate the dynamics of across nano-to-microscale particles and microscale deformable capsules with a fixed LB lattice resolution [24, 120]. The hybrid LB-LD-SL method has previously been verified with theory [24, 120] and validated against experiments [3, 7, 118]. Fig 4.1 demonstrates a nanoscale particle-RBC bidisperse suspension flow through a 40 μm vessel, where the computational methods for each module are denoted accordingly and presented in detail as follows.

3.2.1 Spectrin-link method

The modeling of RBC dynamics and deformation is through the coarse-grained spectrin-link (SL) membrane method [**Pivkin2008**, 121] coupled to the LB method [3]. The hybrid LB-SL method has been extensively validated against experimental measurements and is capable of capturing both the deformation and dynamics of single RBC [3] and the rheology of RBC suspensions at physiological hematocrit [7] with good accuracy and efficiency.

In the LB-SL model, the RBC membrane is modeled as a triangulated network with a collection of vertices mimicking actin vertex coordinates. The Helmholtz free energy of the network system, E, including in-plane, bending, volume and surface area energy

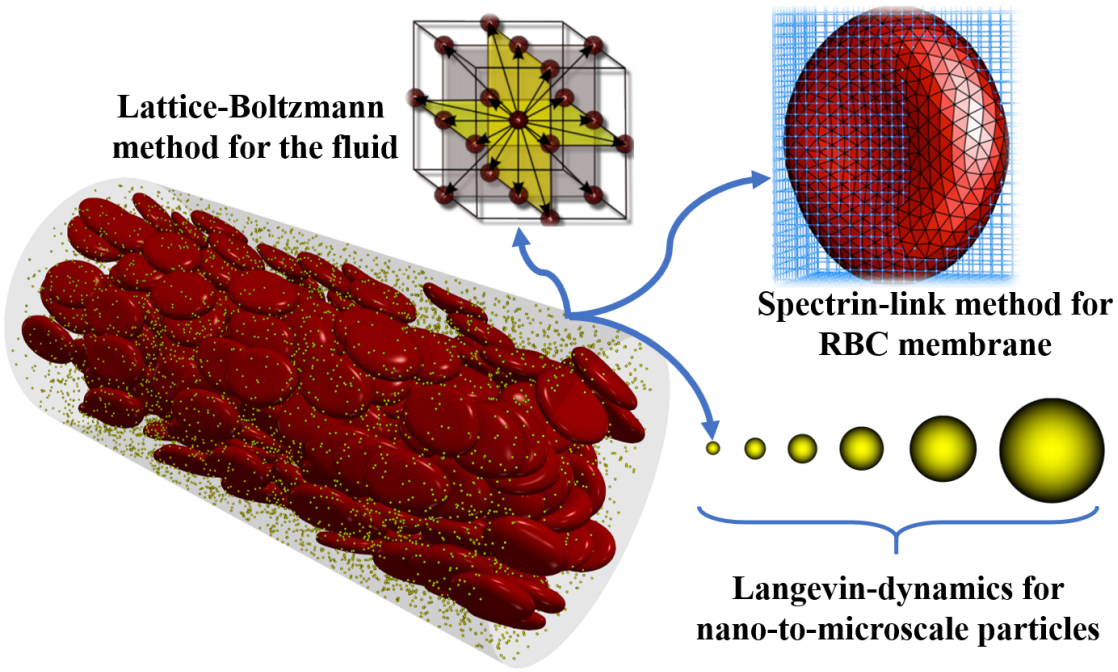

Figure 3.1: Nano-to-microscale particle transport in cellular blood flow through microvessels. The fluid phase is simulated using the lattice-Boltzmann (LB) method [2]. The deformation and dynamics of red blood cells (RBCs) are simulated by coupling a course-grained spectrin-link (SL) method with LB method [3]. The multiscale (nanoscale to microscale) particles (yellow) are simulated via a coupled LB-Langevin dynamics (LD) method [24, 120]. The particle-RBC interaction and inter-cell interactions are resolved through various contact modeling techniques [8, 74, 24, 118].

components [122], is given by

$$E = E_{IP} + E_B + E_\Omega + E_A, \tag{3.1}$$

where the in-plane energy, E_{IP}, characterizes the membrane shear modulus through a worm-like chain (WLC) potential [123] coupled with a hydrostatic component [121]; the bending energy, E_B, specifies the membrane bending stiffness, which is essential in characterizing the equilibrium RBC biconcave morphology [122, 121]; the volumetric contraint energy, E_Ω, and the area constraint energy, E_A, preserve the RBC volume and area conservation, respectively, when subject to external forces.

The dynamics of each vertice are updated according to the Newton's equations of motion,

$$\frac{d\boldsymbol{x}_n}{dt} = \boldsymbol{v}_n, \;\; M\frac{d\boldsymbol{v}_n}{dt} = \mathbf{f}_n^{SL} + \mathbf{f}_n^{LB} + \mathbf{f}_n^{CC} \tag{3.2}$$

where $\boldsymbol{v}_n$ is the velocity of the vertice at the position x_n and M is taken as the fictitious mass of the RBC that is evaluated as the total mass of the cell divided by the number of vertices, N_v [19, 118]. The number of vertices used to discretize the RBC membrane is N_v=613, which has shown to yield adequate resolution to resolve the hydrodynamic forces [8] and capture single RBC dynamics [3] and concentrated RBC suspension rheology [7] when coupled with the LB method. $\mathbf{f}_n^{LB}$ specifies the forces on the vertex due to the fluid-solid coupling. $\mathbf{f}_n^{CC}$ are the forces due to cell-cell interactions. The forces due to the Helmholtz free energy based on the SL model is determined by

$$\mathbf{f}_n^{SL} = -\frac{\partial E(\boldsymbol{x}_n)}{\partial \boldsymbol{x}_n}. \tag{3.3}$$

The SL method is solved by integrating equations 3.2 at each LB time step using a first-order-accurate forward Euler scheme in consistency with the LB evolution equation to avoid excessive computational expense [3, 24].

3.2.2 Fluid-RBC coupling

The coupling between fluid and RBC is accomplished through the ALD fluid-solid interaction scheme [64]. In this method, the momentum transfer at the fluid-solid interface is accounted for by applying the bounce-back operation along lattice links that cross solid surfaces. As a result, the no-slip condition is enforced by adjusting the PDFs of the fluid nodes at the end point of a link along the i direction through

$$f_{i'}(\boldsymbol{r}, t+1) = f_i(\boldsymbol{r}, t^+) - 6\rho\omega_i \boldsymbol{u}_b \cdot \boldsymbol{e}_i, \tag{3.4}$$

where i' is the direction opposite to i, $f_i(\boldsymbol{r}, t^+)$ is the post-collision distribution, and $\boldsymbol{u}_b$ is the solid velocity at the intersection point with the link. The fluid force exerted on the vertex on the RBC membrane mesh can be determined by

$$\mathbf{f}_n^{LB}(\boldsymbol{r} + \frac{1}{2}\boldsymbol{e}_i, t) = 2\boldsymbol{e}_i[f_i(\boldsymbol{r}, t^+) + 3\rho\omega_i \boldsymbol{u}_b \cdot \boldsymbol{e}_{i'}], \tag{3.5}$$

which is applied to the advancement of the RBC dynamic equation through equation 3.2.

3.2.3 Contact modeling

The short-distance interactions between particle and RBC or between particle and the vessel wall is through Morse potential that forbids particles from penetrating the RBC membrane or the vascular wall. This contact model has previously been used in the characterization of the NP long-time diffusion tensor in an unbounded sheared blood, where the calculated NP diffusivity compares favorably with experimental measurements [118]. The Morse potential function is given as

$$U_M(r) = D_e[e^{-2\beta(r-r_0)} - 2e^{-\beta(r-r_0)}], \;\; (r \leq r_0) \tag{3.6}$$

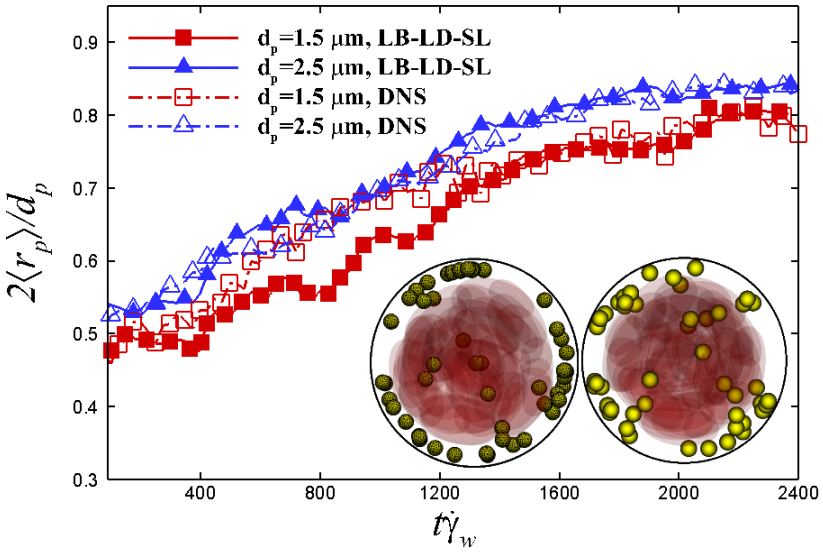

Figure 3.2: Time change of the average radial location of the microscale particles simulated using the multiscale LB-LD-SL method [24, 118] and the DNS approach [19]. The tube diameter is 20 μm; the wall shear rate is 1000 s^{-1}; the hematocrit is 20%. Particles with diameters of d_p=1.5 or 2.5 μm have been selected for comparisons. The inset shows snapshots (frontal views) of 1.5 μm particle distribution in tubular blood flows at $t\dot{\gamma}_w$=2000 simulated using the DNS method [19] (left) or the LB-LD-SL multiscale approach [24, 118] (right).

where r is the normal distance between the particle center to the RBC surface, r_0 is a cut-off distance in which no interaction forces are present, D_e is the potential well depth and β is a scaling factor. The Morse potential is imposed when $r \leq r_0$ to preserve the repulsive effect. Model parameters are adjusted to match the measured inter-cell potential energy, as discussed in [24, 118]. Specifically, the scaling factor is set to $\beta = 2\ \mu m^{-1}$, the surface energy has a value of $D_e = 10^7 k_B T$ and the equilibrium distance is set to $r_0 = d_p/2 + 10\ nm$. This simple contact model, bridging the LB-LD approach [24, 120] and the LB-SL method [3, 7], can capture the margination phenomenon of microscale particles comparably well as the DNS approach does [3, 111]. Fig 3.2 presents the temporal evolution of the ensemble average of the radial displacement of microscale particles, $2\langle r_p \rangle / d_p$, where the particle margination process through the LB-LD-SL approach and that via DNS compares favorably well especially when approaching the equilibrium stage ($t\dot{\gamma}_w \geq$2000).

3.2.4 Evaluation of the particle radial concentration

The particle number concentration at specific radial location, $C_n(r,t)$, can be evaluated as

$$C_n(r,t) = \frac{\sum_{\alpha \in N}\{\delta[r_p^\alpha(t) - r]\}}{2\pi r \Delta r L_v}, \tag{3.7}$$

where N denotes all LD particles in the simulation and L_v is the length of the tube. The radial bin width, Δr, is set to one tenth of the tube radius to accurately resolve the radial profiles of the particle concentration distribution [19]. The bulk ensemble-averaged particle number concentration can be calculated as $\langle C_n \rangle = 4N/\pi d_v^2 L_v$, which is later used to normalize the pariticle local concentration.

3.2.5 Evaluation of the particle radial diffusivity

The particle radial diffusivity is evaluated through a moving time-origin measurement [84] of the particle mean squared displacement (MSD) based on a fixed sampling time interval (STI). The STI is properly chosen to exclude the short-time ballistic regime [24, 120]. By measuring the radial MSD of particles at a radial location r, the local instantaneous particle radial diffusivity can be evaluated according to

$$D_{rr}(r,t) = \frac{\sum_{\alpha \in N}\{\delta[r_p^\alpha(t) - r][r_p^\alpha(t+\Delta t) - r_p^\alpha(t)]^2\}}{2\Delta t \sum_{\alpha \in N}\{\delta[r_p^\alpha(t) - r]\}}, \tag{3.8}$$

where N denotes all LD particles in the simulation and Δt is chosen to be 1000 in lattice units [118]. Same technique can be applied to measure the radial distribution of RESID, $D_{rr}^{RBC}(r,t)$, where the BD is excluded by setting $\boldsymbol{S}_p = 0$. The bulk ensemble-averaged particle radial diffusivity is calculated as $\langle D_{rr}(t) \rangle = \frac{\sum_{\alpha \in N}\{[r_p^\alpha(t+\Delta t) - r_p^\alpha(t)]^2\}}{2\Delta t}$; similarly, the bulk ensemble-averaged RESID can be obtained as $\langle D_{rr}^{RBC}(t) \rangle = \frac{\sum_{\alpha \in N}\{[r_p^\alpha(t+\Delta t) - r_p^\alpha(t)]^2\}}{2\Delta t}|_{\boldsymbol{S}_p=0}$. The equilibrium counterparts of the particle radial diffusivity are denoted as $\langle D_{rr} \rangle$ and $\langle D_{rr}^{RBC} \rangle$ without time dependence.

3.3 Results and Discussion

3.3.1 Problem Setup

The physical problem of particle-RBC suspension flow through a straight tube can be defined by the vessel diameter, d_v, the systemic hematocrit, ϕ, the particle diameter, d_p, the wall shear rate, $\dot{\gamma}_w$, and temperature, T, given fixed RBC properties (hydrodynamic radius, a_{RBC}, and membrane shear modulus, G). Apart from the hematocrit, the corresponding non-dimensional parameters are the confinement ratio, $d_v^* = \frac{a_{RBC}}{d_v}$, which determines the severity of the RBC finite size effect; the particle-cell size ratio, $d_p^* = \frac{d_p}{a_{RBC}}$, that quantifies the length-scale discrepancy between the two species suspended; the Peclet number, $Pe = \frac{3\mu\pi\dot{\gamma}_w d_p a_{RBC}^2}{k_B T}$, which describes the competition between the shear-induced diffusion and the Brownian diffusion; and the capillary number, $Ca = \frac{\mu\dot{\gamma}_w a_{RBC}}{G}$, which defines the deformability of the RBC capsule.

In this work, we consider d_v^* ranging from 0.07$\sim$0.29, corresponding to typical diameters of arterioles [124]. The particle-cell size ratio considered ranges from d_p^*=0.003$\sim$0.86, covering typical size of biomolecules and cells (such as von Willebrand factor, vWF, and platelet) in blood flows. Given the low sensitivity of platelet margination to shear rate [111], a physiologically relevant wall shear rate, $\dot{\gamma}_w$=1000 s^{-1}, typical in arterioles or capillaries is considered for all cases. The fluid viscosity is set to the same as blood plasma, μ= 1.2 cp. The temperature is set to the body temperature, T= 310 K. The RBC membrane has a shear modulus of G=0.0063 $dynes/cm$. The effective hydrodynamic radius of RBC is a_{RBC}= 2.9 μm. As a result, the dependence on Pe is determined by d_p^*. The deformability of RBC is fixed with Ca_G=0.55.

All simulations are initialized with the particles and RBCs uniformly and randomly mixed in the tube, except the particles are only seeded at $2r/d_v \leq 0.6$. Periodic boundary conditions are imposed on the two ends of the tube. The tube has a length of $L_v/a_{RBC} \geq 10$ to ensure the periodic boundary treatment exerting negligible effect on the particle/cell

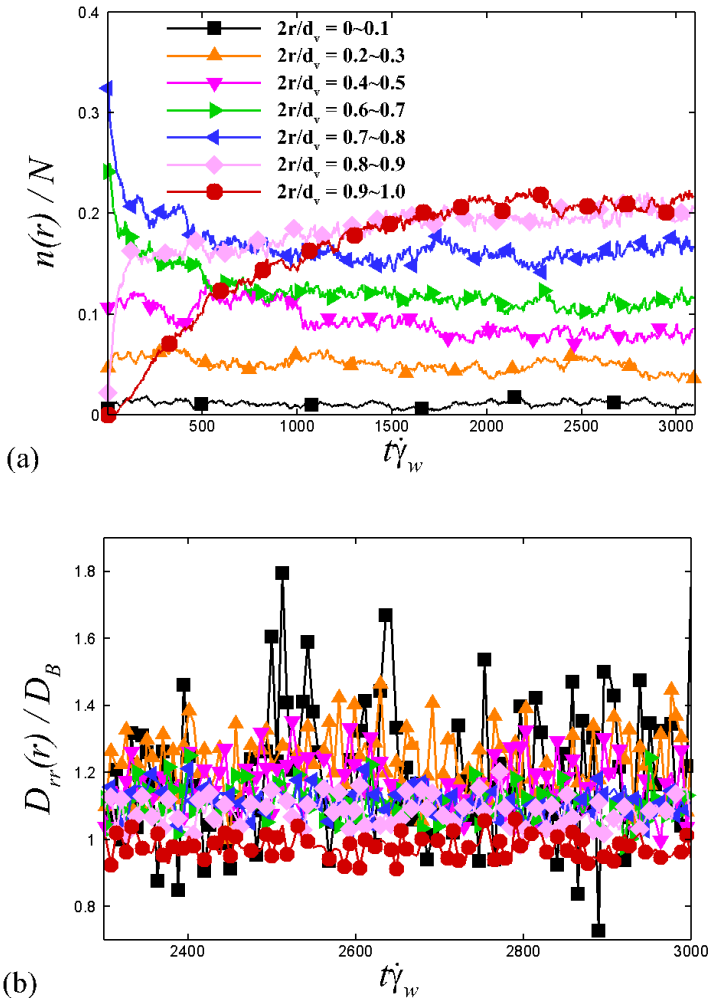

Figure 3.3: Temporal change of (a) particle number percentage and (b) particle radial diffusivity at different radial locations. Here, the particle number percentage, $n(r)/N$, is defined as the number of particles within certain peripheral layer, $n(r)$, normalized by the total particle number, N. Simulation is performed with d_p=100 nm, d_v=20 μm and $\dot{\gamma}_w$=1000 s^{-1}. Simulation reaches equilibrium after $t\dot{\gamma}_w \sim 2000$.

transport. This is paper focuses on the dispersive characteristics at equilibrium, albeit the transient effects may play a significant role in the particle distribution in microvascular bifurcating structures[124, 125, 126, 127, 128]. The equilibrium conditions are determined by tracking the particle accumulation at each radial location until it plateaus. As an example in Fig 3.3, we present the temporal change of particle number percentage and radial diffusivity at different radial locations; where the particle number percentage, $n(r)/N$, is defined as the number of particles within certain radial layer, $n(r) = \sum_{\alpha \in N}\{\delta[r_p^{\alpha}(t) - r]\}$,

normalized by the total particle number, N, within the simulation domain. The simulation is performed with d_p=100 nm, d_v=20 μm and ϕ=0.2. The equilibrium state is arrived at $t\dot{\gamma}_w \sim 2000$, when the mean values of both $n(r)/N$ and $D_{rr}(r)/D_B$ remain unchanged with respect to time.

3.3.2 Dependence on confinement

We first interrogate the dispersion characteristics of NPs under different confinement ratios controlled by adjusting vessel diameters in the range of d_v=10$\sim$40 μm (corresponding to d_v^*=0.29$\sim$0.073), which corresponds to typical size of arterioles or capillaries in human [124]. The particle size is fixed to d_p=100 nm. The wall shear rate is set to $\dot{\gamma}_w$=1000 s^{-1} and the systemic hematocrit is set to ϕ=0.2, which are within the range of physiological hemorheological ranges in human arterioles or capillaries [124]. The number of particles simulated in the microvessels are N=4000, 1000 and 250 from large to small vessels, respectively, to conserve the particle volume concentration.

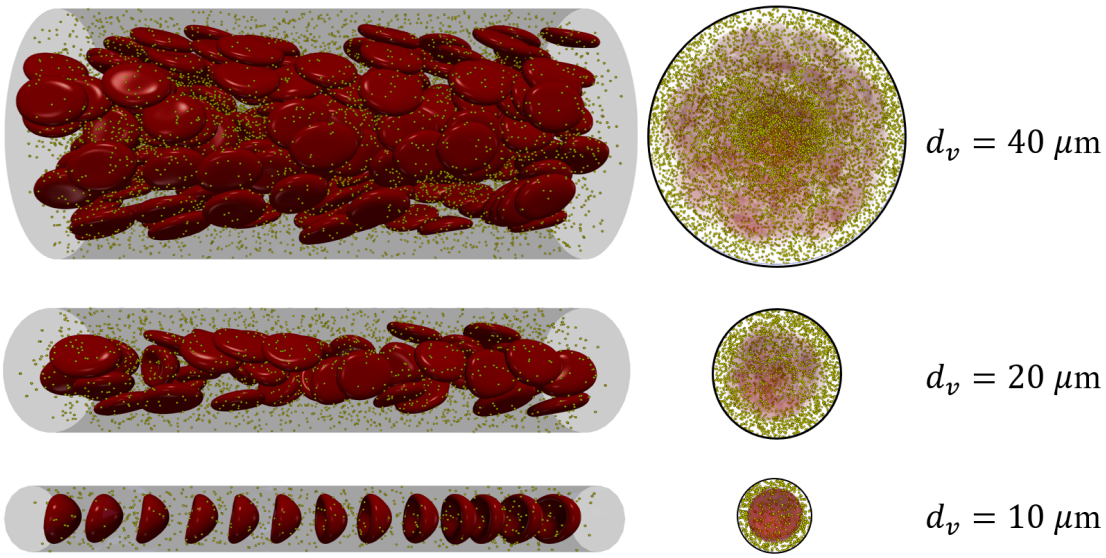

Figure 3.4: NP and RBC distribution at equilibrium within microvessels of different diameters $d_v = 40$ (top), 20 (middle) or 10 (bottom) μm at $\phi = 0.2$ and $\dot{\gamma}_w = 1000\ s^{-1}$. Left columns show the side views of the microvessels; right columns show the end views of the microvessels.

Fig 3.4 presents the simulation snapshots of NP and RBC equilibrium distribution in microvessels under various confinement conditions. Qualitatively, the RBC dynamic mode

changes from tank-treading/tumbling dominant to parachuting dominant [3], as the vessel diameter decreases from 40 to 10 μm. Such an increase of confinement does not alter the radial distribution of shear rate significantly but does change the radial distribution of local hematocrit to a large extent, as shown in Fig 3.5a and 3.5b. Specifically, for the case with d_v=40 μm, the RBC-laden region shows a relatively uniform distribution except near the center of the tube where the shear rate is close to zero. Consequently, the NP concentration, $C_n(r)$, at $0<2r/d_v<0.2$ appears twice the bulk average NP concentration, $\langle C_n \rangle$, while $C_n(r)$ near the wall exbhit slightly lower values than $\langle C_n \rangle$. As the vessel diameter decreases to 20 μm, the dimensionless CFL thickness δ_{CFL}/d_v increases from $\sim$0.2 to $\sim$0.4, $i.e.$, the RBC-laden region becomes relatively more focused. Moreover, the local hematocrits get intensified especially at the inner boundary of the CFL and near the tube axis. These hemorheological changes substantially affect the equilibrium radial distribution of $C_n(r)/\langle C_n \rangle$. As a result, the location of peak NP concentration shifts towards the CFL region, as shown in Fig 3.5c. Further confining the system to d_v=10 μm, allowing only one train of RBCs parachuting through the vessel, appears to slightly enhance the peak concentration of NP at the CFL region while decreasing the NP concentration at the RBC-laden region. Previous microfluidic experiments by [129] also show the enhancement of the number percentage of particles adhered to the wall when the width of a $\sim$40 μm channel is reduced by half.

The distributions of the NP radial concentration can be better understood by evaluating the NP radial diffusivity, as depicted in Fig 3.5d. The NP diffusivity in the velocity-gradient direction based on the theoretical NP diffusion rate evaluated in an unconfined shear-flow setting [118] is also plotted for comparison using the local shear rate and hematocrit at specific radial location for the d_v=40 μm case. In general, increasing the confinement reduces the magnitude of NP radial diffusivity, where the unconfined case shows up to two folds the radial diffusivity, $D_{rr}(r)/D_B$, of the d_v=40 μm case. Besides changing the magnitude of $D_{rr}(r)/D_B$, adjusting confinement ratio also alters the radial distribution

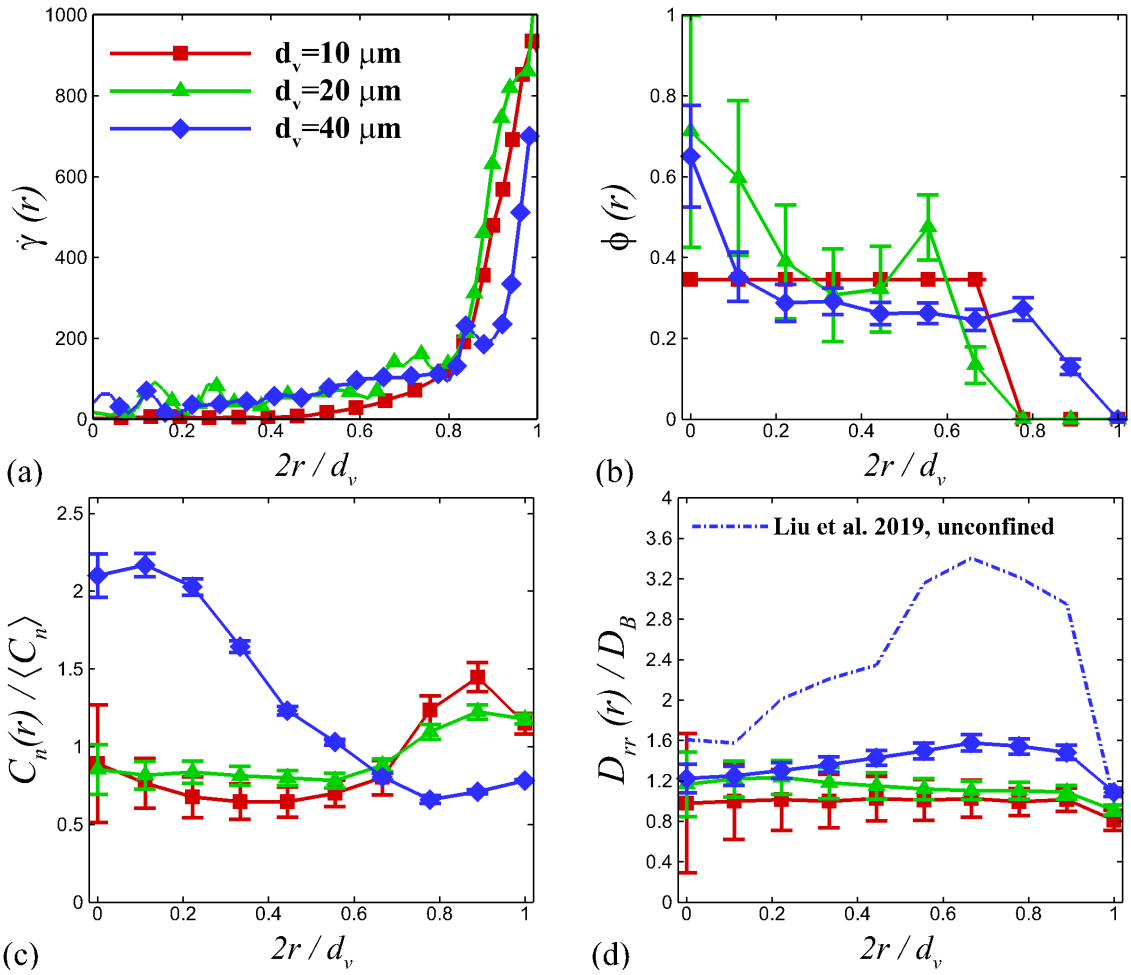

Figure 3.5: Radial distribution of (a) shear rate, (b) hematocrit, (c) NP equilibrium distribution and (d) NP dispersion rate for various confinement ratios at $\dot{\gamma}_w = 1000\ s^{-1}$, $\phi = 0.2$ and $d_p = 100\ nm$. The radial diffusivity based on the empirical correlation of NP diffusion tensor [118] in a unconfined simple shear flow is plotted in (d) for comparison, where the calculation adopts the local hemorheological parameters specific to the radial locations for the d_v=40 μm case. Error bars denote the standard deviation.

of $D_{rr}(r)/D_B$. For the d_v=40 μm case, the NP radial diffusivity shows high values near the CFL inner boundary and low value in the RBC-laden region, which is similar to the $D_{rr}(r)/D_B$ distribution in the unconfined case. This distribution of $D_{rr}(r)/D_B$ seems to be the cause of the low concentration of NPs near the CFL region and the high concentration at the RBC-core region. The increase of confinement (decrease of vessel diameter to 20 or 10 μm) renders the radial location of high $D_{rr}(r)/D_B$ to move towards the RBC-laden region, which appears to be responsible for the shift of the high NP concentration region towards the CFL, as observed in the high confinement cases (d_v=10 and 20 μm).

Overall, the increase of confinement ratio enhances the NP near-wall concentration by inhibiting the NP diffusion near the wall. This however does not warrant the margination of NPs, given no excessive NP concentration ($C_n(r) < 1.5\langle C_n \rangle$) is observed near the wall as the vessel confinement increases to capillary scale. It is noted that when vessel size decreases to capillary scale, retention of microscale particles in the RBC-induced recirculation is reported [130], which however is not observed in the current study with NPs under the studied hemorheological conditions.

3.3.3 Dependence on hematocrit

Changing hematocrit significantly modifies the apparent viscosity of blood [131, 7] and could drastically influence the RBC-enhanced shear-induced diffusivity of NPs in sheared blood flow [118]. To understand how the variation of systemic hematocrit in microvessels changes the local hemorheology and hence the NP radial distribution, we investigate the hematocrit dependence of the NP radial dispersion behavior under various systemic hematocrits in the range of ϕ=0$\sim$0.3. For the cases considered here, we select a fixed vessel diameter of d_v=20 μm and a NP size of d_p=100 nm. The wall shear rate is set to $\dot{\gamma}_w$= 1000 s^{-1}. The number of NPs are set to N=1000.

Fig 3.6 plots two snapshots of NP-RBC distribution in a 20 μm vessel, where the high hematocrit case (ϕ=0.3) exhbits a thinner CFL compared to the low hematocrit case (ϕ=0.15) as expected. Fig 3.7a and 3.7b present quantitative analysis of the hemorheological response to the change of systemic hematocrit, where the increase of systemic hematocrit affects the radial distribution of both the local shear rate, $\dot{\gamma}(r)$, and the local hematocrit, $\phi(r)$, which are two competing drivers for the particle cross-stream migration. On one hand, it alters the flow structure from a Poissuelle-type flow towards a plug-type flow; as a result, the local shear rate in the RBC-laden region decreases, which drives the Brownian particles to the tube center. One the other hand, it increases the local hematocrit in the RBC-laden region, which drives the particles to migrate to the wall.

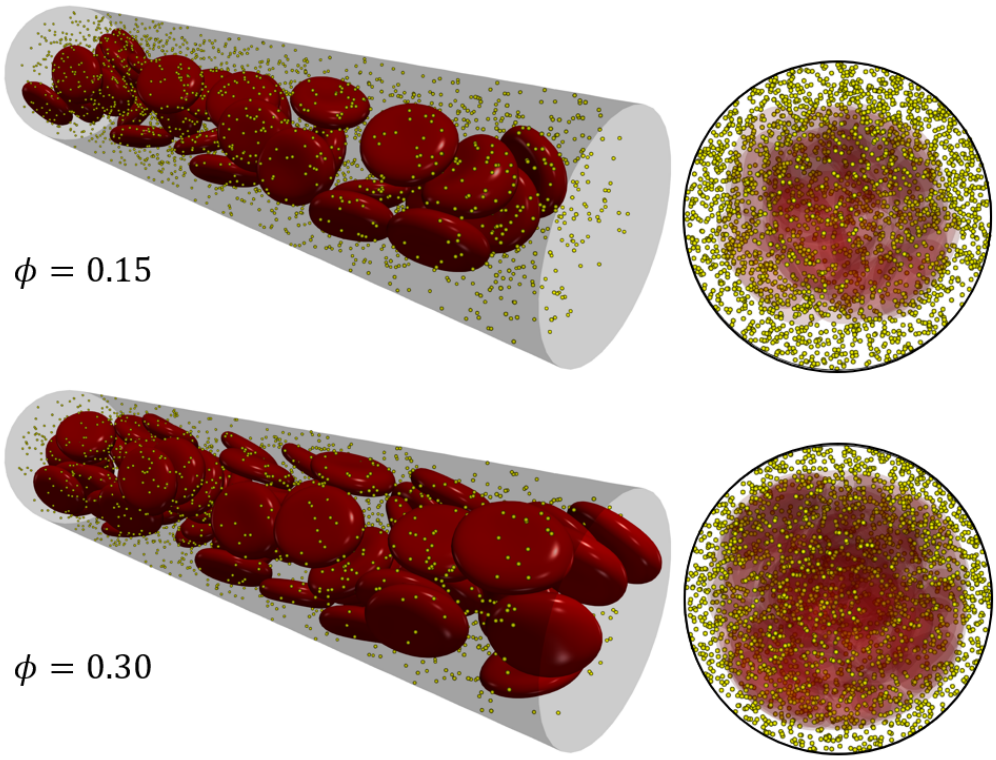

Figure 3.6: NP and RBC distribution at equilibrium in a 20 μm microvessel with $\phi = 0.15$ (top) or $\phi = 0.30$ (bottom) at $\dot{\gamma}_w = 1000\ s^{-1}$ and $d_p = 100\ nm$. Left column shows the isometric view of the tubular blood flow; right column shows the end view of the microvessels.

The adjustment of the two competing effects lead to certain variation of the NP radial distribution, as presented in Fig 3.7c. At ϕ=0, the NP dispersion is purely driven by the Brownian diffusivity and the shear-gradient driven dispersion. The former is isotropic, while the latter tends to drive the particle towards low shear region [129]. As a result, the NP distribution shows a high NP concentration in the core and a low concentration near the wall. Increasing the systemic hematocrit generally alters the NP distribution such that the high NP concentration region shifts to the CFL. Interestingly, a slight increase of ϕ from 0 to 0.05 appears to be enough to shift this paradigm of NP distribution, leading to about 3-fold decrease of NP concentration at the core and $\sim$1.5 folds increase of NP near wall concentration. Further increasing ϕ slightly increases the near wall NP concentration but also increases the NP concentration at the RBC-laden region. Correspondingly, in Fig 3.7d, the $D_{rr}(r)$ value (especially in the RBC-laden region) shows a non-monotonic change with

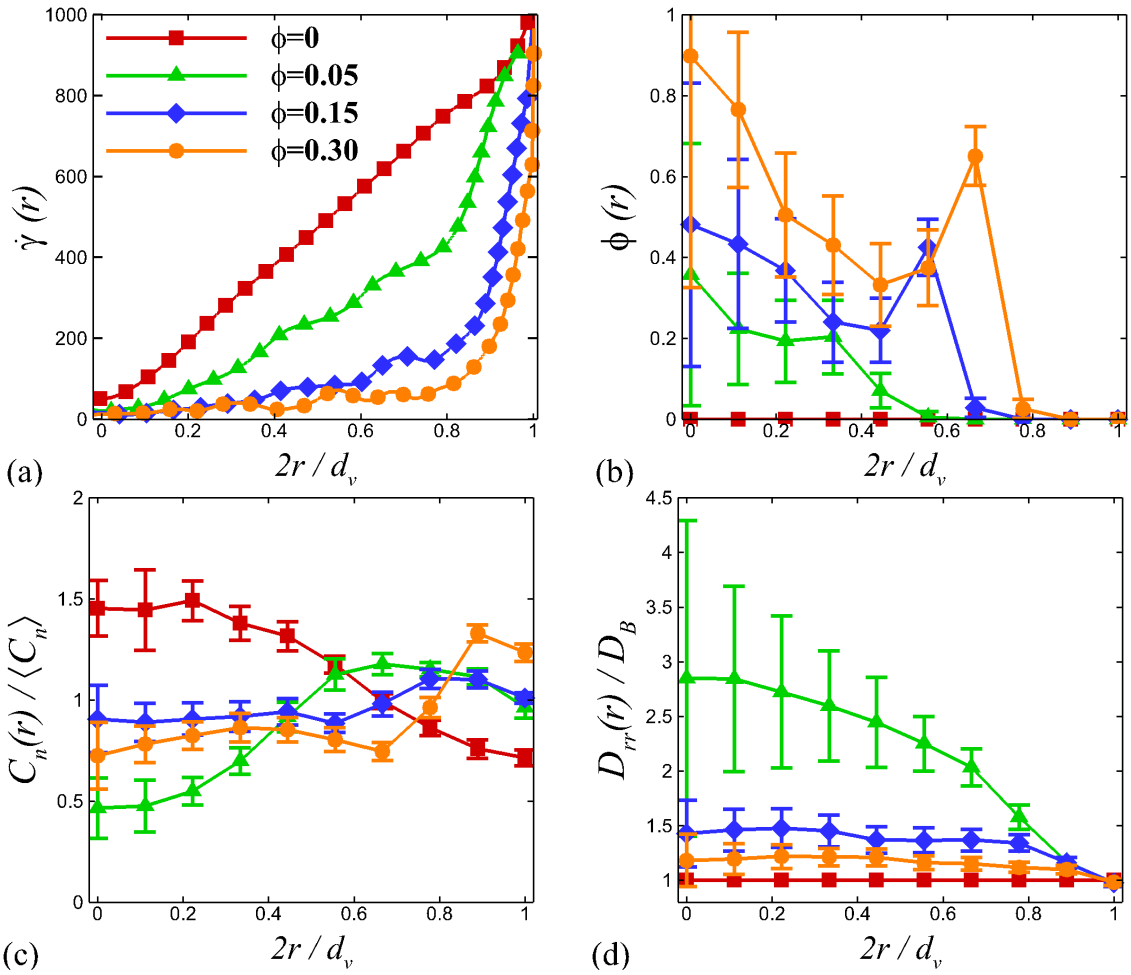

Figure 3.7: Radial distribution of (a) shear rate, (b) hematocrit, (c) NP equilibrium distribution and (d) NP dispersion rate for various hematocrits at $\dot{\gamma}_w = 1000\ s^{-1}$, $d_v = 20\ \mu m$ and $d_p = 100\ nm$. Error bars denote the standard deviation.

respect to ϕ, which first increases by up to 3 folds as ϕ rises to 0.05 and gradually gets inhibited to be close to the theoretical Brownian diffusivity as ϕ further increases to 0.3. The inhibition of NP radial diffusiviy at high hematocrit can be explained by the excessive local $\phi(r)$ and low $\dot{\gamma}(r)$, as shown in Fig 3.7a and 3.7b.

Therefore, low systemic hematocrits appear to be optimal to enhance the NP near-wall concentration in microvessels, owing to the relatively high local shear rates and moderate local hematocrits that does not inhibits the NP dispersion in the tubular core. Nevertheless, changing hematocrit does not lead to the margination of NP.

3.3.4 Dependence on particle size

So far we have focused on the long-time dispersion behavior of NPs in microvessels under various confinement ratios and hematocrit conditions. In these cases, particles do not show margination behavior. Instead, a non-uniform radial distribution of particles is observed with the particle concentration near the wall being less than 1.5 times the bulk average concentration. Besides, the near-wall concentration of NP is dynamically conserved at equilibrium, accompanied by the cross-migration of NPs between the CFL and the RBC-laden region due to severe Brownian effect[24].

In this section, we consider the size-dependent dispersion behavior of nano-to-microscale particles in microvessels. Particles with sizes ranging from d_p=10$\sim$2500 nm are considered, covering particles ranging from nanoscale biomolecules such as vWFs in globular conformation to microscale cells such as platelets. The vessel diameter is fixed to d_v= 20 μm. The wall shear rate is set to 1000 s^{-1}. The systemic hematocrit is kept at ϕ=0.2. To maintain the volumetric concentration of the particle phase in the dilution limit ($i.e.$, $\ll 1\%$), the number of large particles considered in the system is reduced accordingly but kept above 50 to ensure statistical significance as suggested in previous margination study [19].

Fig 3.8 presents the equilibrium distributions of RBCs and particles. Qualitatively, NPs show non-uniformly dispersed distribution across the vessel, where NPs at any radial position can disperse to a random radial location given enough time owing to severe Brownian effect. These features are qualitatively different from the margination behavior of microscale particles, where ecessive concentration and retention of particles in the CFL can be observed [19, 111]. Fig 3.9a further depicts the radial distribution of $C_n(r)/\langle C_n\rangle$ for various particle sizes. As the particle size increases above 1 μm, the CFL region exhibits a prominently high particle concentration. Specifically, for particles with a diameter d_v=2.5 μm, a five times bulk average particle concentration, $C_n(r) \approx 5\langle C_n\rangle$, can be observed at the CFL region. These observations are consistent with the microfluidic perfusion experi-

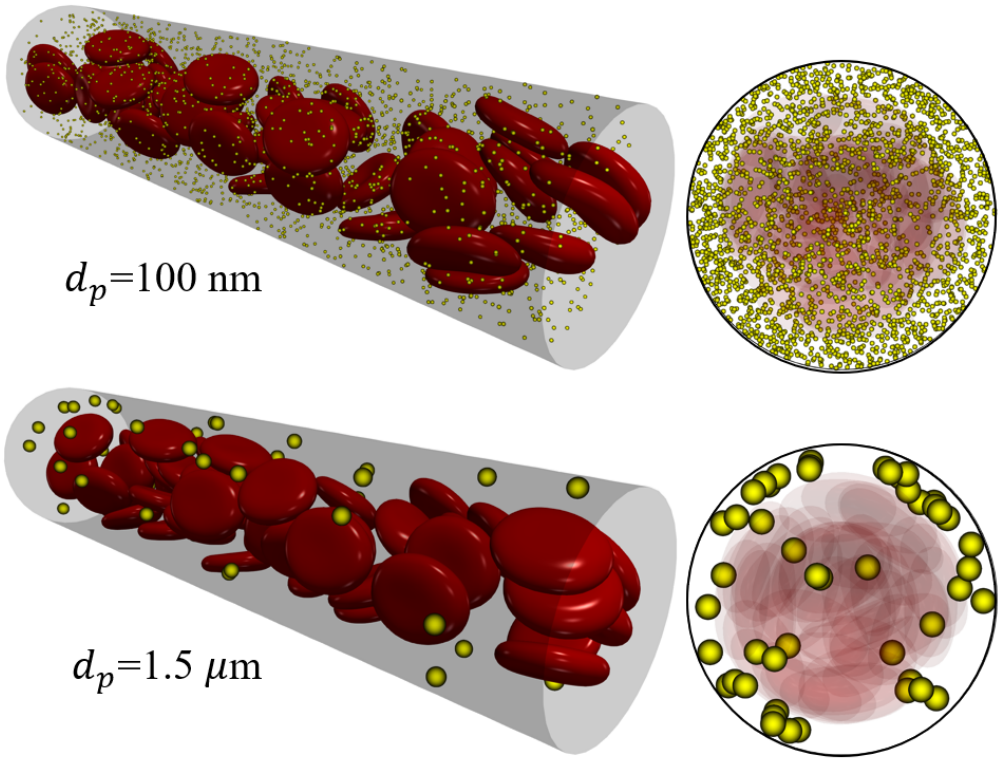

Figure 3.8: Particle and RBC distribution at equilibrium with particles size being nanoscale (top) or microscale (bottom) at $\phi = 0.2$, $d_v = 20\ \mu m$ and $\dot{\gamma}_w = 1000\ s^{-1}$. Left column shows the isometric view of the tubular blood flow; right column shows the end view of the microvessels.

ment by [132], where the number percentage of particles adhered to the wall gets increased by 5$\sim$7 times as the particle size changes from nanoscale to microscale. The change of the particle number concentration at the CFL, C_n^{CFL}, versus that at the RBC-laden region, $\langle C_n \rangle^{non-CFL}$, as a function of particle size is further plotted in Fig 3.9b. When the particle size is below 1 μm, the $C_n^{CFL}/\langle C_n \rangle^{non-CFL}$ value shows weak dependence on the particle size; which only shows a slight increase from 1.0 to about 1.5 as d_p changing from 10 nm to 1000 nm. As particle size exceeds 1 μm, the $C_n^{CFL}/\langle C_n \rangle^{non-CFL}$ value increases abruptly and margination occurs. Particle size d_p=1 μm seems to be a critical watershed that divides the $dispersion$ state and the $margination$ state, as denoted in Fig 3.9b.

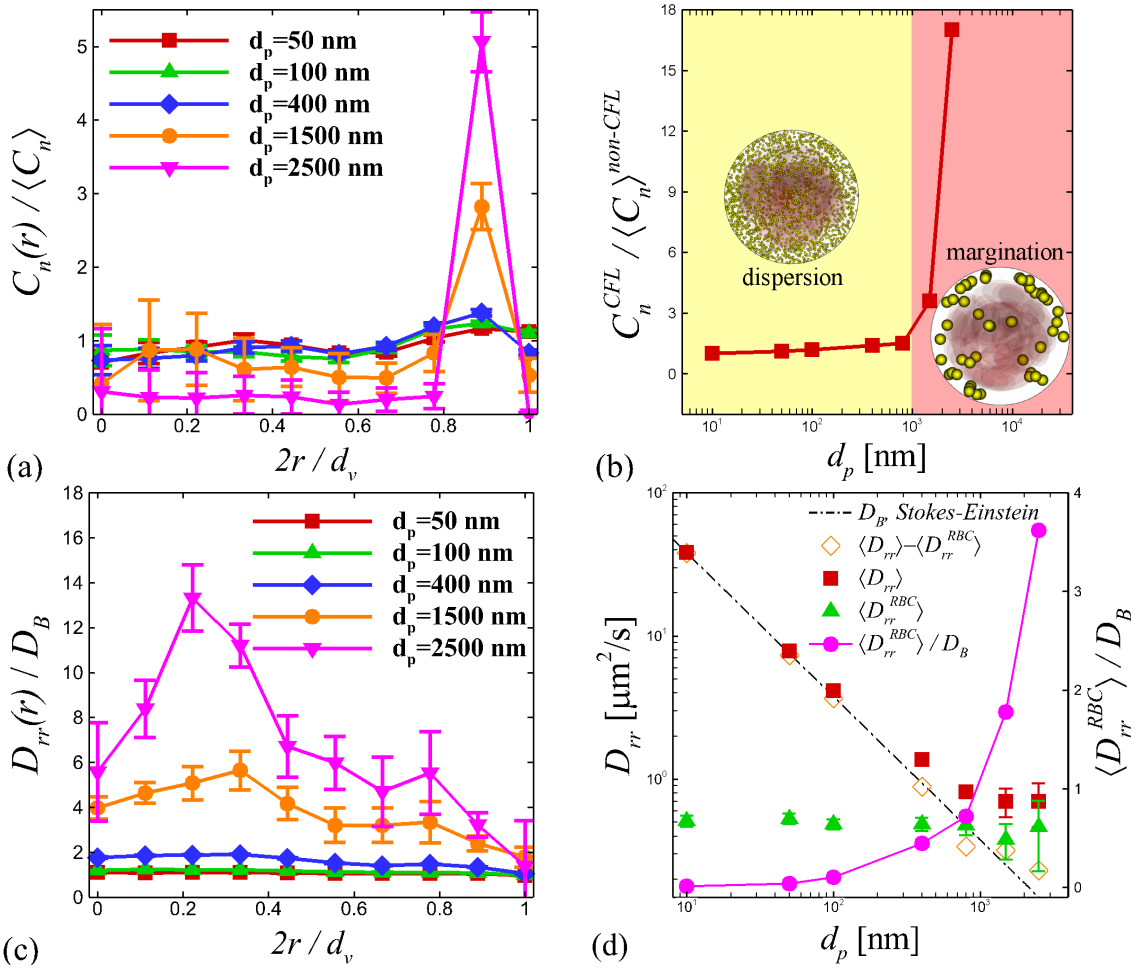

Figure 3.9: (a) The radial distribution of particle number concentration normalized by the bulk average number concentration of the particles for different particle sizes at $\phi = 0.2$, $d_v = 20\ \mu m$ and $\dot{\gamma}_w = 1000\ s^{-1}$. (b) The particle number concentration in the CFL normalized by that in the RBC-laden region, $C_n^{CFL}/\langle C_n \rangle^{non-CFL}$, plotted against particle size. The yellow area shows the dispersion (no margination) regime; the pink area show the margination regime. (c) The radial distribution of particle radial diffusivity normalized by the Brownian diffusivity for various particle sizes. (d) The ensemble-averaged particle radial diffusivity plotted against particle sizes; the diffusivity ratio, $\langle D_{rr}^{RBC} \rangle$, is also plotted with the vertical axis on the right. Error bars denote the standard deviation.

To shed light on the size-dependent dispersion behavior of particles in tubular blood flows, the distribution of particle radial diffusivity, $D_{rr}(r)/D_B$, is plotted in Fig 3.9c. For NPs, the $D_{rr}(r)/D_B$ distribution tends to be uniform due to the dominance of isotropic Brownian diffusivity. As the particle size increases above one micronmetre, the RBC-laden

region shows prominent enhancement of $D_{rr}(r)/D_B$ compared to the CFL. Moreover, both at the CFL edge ($2r/d_v \sim 0.8$) and close to the tube center ($2r/d_v \sim 0.2$), the magnitude of $D_{rr}(r)/D_B$ peaks and the inner peak is more pronounced than the peak close to the CFL. For the 2500 nm particles, the inner peak shows more than $\sim$10 times $D_{rr}(r)/D_B$ values of that at the CFL. The radial distribution of $D_{rr}(r)/D_B$ seems to be inversely correlated to the radial distribution of $C_n(r)/\langle C_n \rangle$ in terms of the radial location, suggesting that the margination of microscale particles is probably due to the large magnitude difference in $D_{rr}(r)/D_B$ between the RBC-laden region and the CFL region.

In Fig 3.9d, we plot the ensemble-averaged radial diffusivity, $\langle D_{rr} \rangle$, as a function of the particle size. The ensemble average is performed among all particles located at various radial locations at equilibrium state. For small d_p, the $\langle D_{rr} \rangle$ value asymptotically matches the Stokes-Einstein relation due to the dominance of Brownian diffusion. Increasing the particle size decreases the effect of thermal fluctuation and leads to the deviation of $\langle D_{rr} \rangle$ from D_B. The value of $\langle D_{rr} \rangle$ eventually plateaus at the microscale size regime, where the RESID is dominant over BD. The bulk ensemble-averaged RESID, $\langle D_{rr}^{RBC} \rangle$, seems to be weakly dependent on the particle size, similar to the particle diffusivity observed in a unbounded sheared blood flow [118]. Subtracting the $\langle D_{rr} \rangle$ with $\langle D_{rr}^{RBC} \rangle$ shows an overlap of the dataset $\langle D_{rr} \rangle$-$\langle D_{rr}^{RBC} \rangle$ with the theoretical Brownian diffusivty, confirming the RESID is linearly superimposed with the Browanian diffusivity [24]. More interestingly, the increase of $\langle D_{rr}^{RBC} \rangle / D_B$ shows a strong positive correlation with the increase of $C_n^{CFL}/\langle C_n \rangle^{non-CFL}$, as shown in Fig 3.9b and 3.9d. This strong linkage between the dispersion-to-margination transition and the particle-size relevant change of RESID-to-Brownian diffusivity ratio is consistent with the margination characterization based on a kinetic theory-based analysis [133], where the margination of microscale particles is shown to be weakened as strong Brownian effect comes into play.

3.4 Conclusions

Using a three-dimensional multiscale complex blood flow solver [3, 24, 120], we have interrogated the long-time dispersive characteristics of rigid spherical particles with sizes across nano-to-micrometers in blood flow through microvessels. The role of the confinement ratio and the systemic hematocrit in altering the nanoparticle radial dispersion is quantitatively analyzed in terms of the radial distribution of particle concentration and particle radial diffusion rate. The effect of changing particle size on the alteration of the particle dispersive characteristics is highlighted.

It is found that nanoscale particles do not marginate under various confinement effects or hematocrit levels, but rather show a non-uniform radial distribution across the vessel. Increasing the confinement effect by decreasing the vessel diameter hinders the particle radial diffusivity but also enhances the equilibrium concentration of nanoscale particles in the cell free layer. Low hematocrit level ($\phi \sim 5\%$) in the microvessel appears to be optimal to the radial dispersion of nanoscale particles, leading to high radial diffusion rate and near-wall concentrations being higher than the average concentration. High hematocrits (ϕ=30$\%$) slightly increases the near-wall concentration but meantime inhibits the dispersion of nanoscale particles in the RBC-laden region at the tube center.

Microscale particles exhibit pronounced margination behavior, where at equilibrium the particles get concentrated in the cell-free layer at 4 to 17 times the average particle concentration in the RBC-laden region. The margination propensity seems to be enhanced with the particle size. For microscale particles, the RBC-enhanced shear-induced diffusivity is dominant over the Brownian diffusivity, where the RBC-laden area shows more than 10 times higher diffusivity compared to that in the RBC-free layer. These particle-size induced changes of particle radial diffusivity in both distribution and magnitude collectively give rise to margination of microscale particles in confined tubular blood flows.

CHAPTER 4

PARTITIONING OF CELLULAR BLOOD-BORNE NANOPARTICLES THROUGH MICROVASCULAR BIFURCATIONS

Blood flowing through microvascular bifurcations has been an active research topic for many decades, while the partitioning pattern of nanoscale solutes in the blood remains relatively unexplored. Here, we demonstrate a multiscale computational framework for direct numerical simulation of the nanoparticle (NP) partitioning through physiologically-relevant vascular bifurcations in the presence of red blood cells (RBCs). The computational framework is established by embedding a newly-developed particulate suspension inflow/outflow boundary condition into a multiscale blood flow solver. The computational framework is verified by recovering a tubular blood flow without a bifurcation and validated against the experimental measurement of an intravital bifurcation flow. The classic Zweifach-Fung (ZF) effect is shown to be well captured by the method. Moreover, we observe that NPs exhibit a ZF-like heterogeneous partition in response to the heterogeneous partition of the RBC phase. The NP partitioning prioritizes the high-flow-rate daughter branch except for extreme (large or small) suspension flow partition ratios under which the complete phase separation tends to occur. By analyzing the flow field and the particle trajectories, we show that the ZF-like heterogeneity in NP partition can be explained by the RBC-entrainment effect caused by the deviation of the flow separatrix preceded by the tank-treading of RBCs near the bifurcation junction. The recovery of homogeneity in the NP partition under extreme flow partition ratios is due to the plasma skimming of NPs in the cell free layer. These findings, based on the multiscale computational framework, provide biophysical insights to the heterogeneous distribution of NPs in microvascular beds that are observed pathophysiologically.

4.1 Introduction

Blood is a biological fluid that conveys nutrients and wastes throughout the body. The primary constituents of blood are red blood cells (RBCs) that make up $\sim$45% of the systemic blood volume and plasma that contains a variety of biomolecules including clotting factors and nutrients, etc. The exchange of materials between the blood and tissues primarily occurs in the microvasculatures where blood vessels feature complex tree-like bifurcating structures. Such microvascular bifurcations allow the blood flow to be partitioned and disseminated to the bulk of tissues for efficient mass exchanges [134].

Given its significance in physiology and fluid mechanics, blood flowing through microvascular bifurcations has been a topic of research for many decades [135, 136, 137]. Among all the studies, substantial efforts have been dedicated to the understanding of the pattern and biomechanistic mechanisms of RBC partitioning through single or multi-generation bifurcations using in vivo [138, 139], in vitro [140, 141] and theoretical [142, 135, 126] approaches. It has been well accepted that the RBC volume concentration ($i.e.$, hematocrit) in the two daughter branches are oftentimes not equally partitioned due to the particulate nature of the blood cells. Rather, the hematocrit in the high-flow-rate daughter branch often gets elevated while the other daughter branch receives a diluted or even depleted hematocrit level. This heterogeneous partition of RBCs, often referred to as the Zweifach–Fung (ZF) effect [138, 141], is physiologically essential since it biomechanistically explains the reduction and heterogeneous distribution of the hematocrit in microvasculatures that has been observed physiologically [143, 144]. Utilizing the ZF effect, novel microfluidic devices have also been developed for cell or bioprotein seperation and other relevant biomedical applications [145, 146].

Besides the large body of research focusing on the RBC partition through microvascular bifurcations, a few studies investigate the distribution and adhesion of other blood species through bifurcating structures. The effect of size and shape of microscale particles,

mimicking white blood cells, on their adhesion propensity at bifurcations has been studied in vitro using synthetic microvascular networks [147, 148]. The model platelet distribution in blood flow through idealized, vascular bifurcations or confluences has been simulated directly, where the platelets shows anti-margination behaviors at the downstream of a confluence [149]. The distribution and adhesion of nanoparticles (NPs) in vascular bifurcations has been interrogated in silico without explicit consideration of RBCs [21, 150].

Notwithstanding current understanding of the RBC partitioning characteristics through microvascular bifurcations, there is clearly a lack of knowledge regarding the partitioning behaviors of nanoscale solutes through capillary beds subject to the influence of RBCs, partly because of the difficulty imposed by the multiscale nature of the problem [24]. Nonetheless, studying the partition of nanoscale solutes through microvascular bifurcations holds considerable significance biophysically and clinically. For example, the undesired heterogeneous distribution of nanomedicine in tumor microvasculature remains to be a major hurdle that limits the overall therapeutic efficiency [151]. Understanding the partitioning of solutes through microvascular bifurcations may provide possible mechanisms that could be applied to regulate the heterogeneity of solute distribution in microcirculation. Accordingly, novel design of NP-based drugs with improved drug delivery efficacy could be inspired [152].

The goal of this paper is to develop a multiscale computational framework for direct numerical simulation of NP partition through microvascular bifurcations, while quantitatively elucidating the NP partitioning in the presence of RBCs. Towards that end, an general index-based manipulation strategy for the particle inflow/outflow boundary conditions embedded in a verified and validated multiscale blood flow solver [24, 120, 118] has been developed and validated. Using the multiscale computational framework, the partition of the blood-borne NPs through microvascular bifurcations in response to the ZF effect is found to be heterogeneous as well. The heterogeneity in the NP partition is conditional depending on the ratio of the flow rates between the daughter branches. The physical mech-

anisms responsible for the heterogeneity in the NP partition is found to be associated with the flow separatrix deviation at the bifurcation junction caused by the RBC motion.

4.2 Materials and Methods

The computational framework proposed for this study is a 3D lattice-Boltzmann (LB) based multiscale complex blood flow solver [64, 2, 3, 24, 120], augmented with a particulate inflow and outflow boundary condition. The LB method is a well-established numerical model for hydrodynamics and proves to be a highly scalable method for direct numerical simulation (DNS) of dense particle suspensions [4, 2]. Modeling of the RBC dynamics and deformation is via a coupled spectrin-link (SL)/LB method [3, 3, 7]. The NP suspension dynamics are resolved via a two-way coupled lattice-Boltzmann Langevin-dynamics (LB-LD) method with both particle Brownian motion and long-range hydrodynamic interactions (HI) directly resolved and validated [24, 120]. The solver has been applied to a variety of problems pertaining to particle and biomolecule transport in blood flow [7, 19, 111, 13, 24, 118, 153]. The newly developed open boundary conditions (BCs) are especially suitable for complex geometries such as microvasculatures. All modules are two-way coupled and embedded in a massively parallelized framework, as shown in Fig 4.1. To validate the numerical methods, the blood flow through a microvascular bifurcation within the chicken chorioallantoic membrane (CAM) in vivo model has been characterized through microscale particle image velocimetry (μPIV).

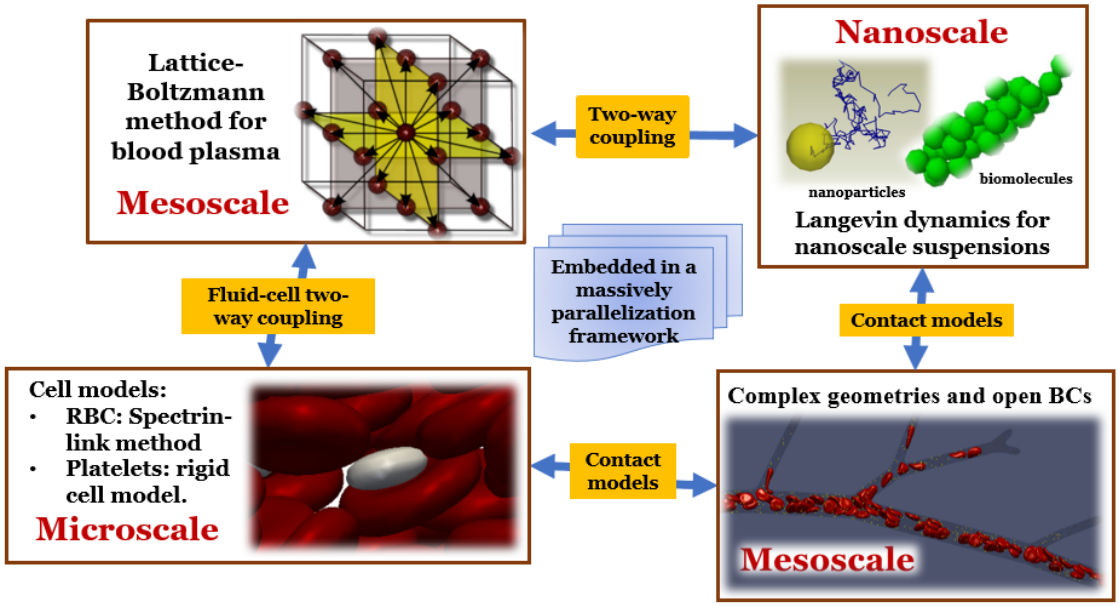

Figure 4.1: The multiscale computational framework for simulating blood-borne nanoparticle partitioning through microvasculatures. The method directly and concurrently resolves the dynamics of microscale cells and nanoscale particles and molecules suspended in blood plasma through complex microvascular networks, where open boundary conditions (BCs) are prescribed.

4.2.1 Open boundary strategies for particulate suspension inflow and outflow

Periodic boundary condition (P-BC), due to its computational efficiency, has been widely used for simulations of blood flows through straight tubes/channels [17, 111, 24, 153] or artificial bifurcation structures [154, 126]. Physiologically, microvascular bifurcations often involve one inlet but multiple outlets where flow conditions are non-periodic. To overcome the methodological limitation, several open boundary strategies have been developed for inflow and outflow of particle or cell suspensions in the context of dissipative particle dynamics (DPD) [155, 156] or immersed-boundary (IB)/LB method [157]. Here we propose a general particulate suspension inflow and outflow boundary condition (PSIO-BC),

which in principle is applicable to any index-based particle suspension methods. Applying the PSIO-BC to both the LB-SL method [3] and the LB-LD method [120], we simulate the RBC-NP suspension through a model microvascular bifurcation (Fig 4.2a) where the number of particles initially increases and eventually plateaus when the system reaches equilibrium (Fig 4.2b).

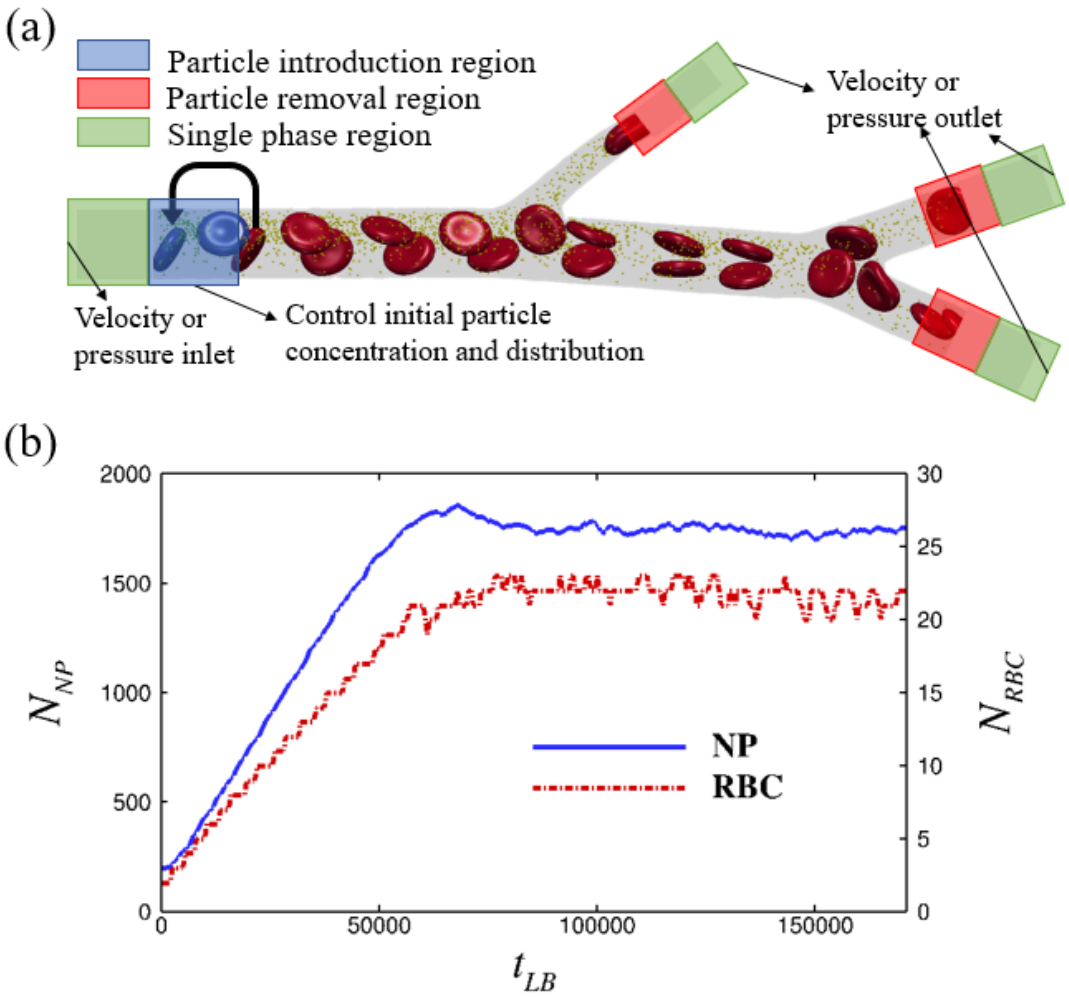

Figure 4.2: Demonstration of the particulate suspension inflow and outflow boundary condition (PSIO-BC). The schematic illustration of the PSIO-BC applied to a NP-RBC bidisperse suspension flowing through a two-generation microvascular bifurcation (a). The time course of the particle number simulated in the bifurcation (b), where at equilibrium the particle number becomes quasi-conserved.

Fluid phase

The Dirichlet BCs are applied to prescribe the velocity or pressure of the flow field at the inlet and outlet. In the context of LB method, we employ the regularization BC procedure [158, 159] to construct the incoming unknown PDFs based on prescribed macroscopic properties at the inlet and outlet as

$$f_i^R = f_i^{(eq)} + f_i^{(neq)} = f_i^{(eq)}(\rho, \boldsymbol{u}) + \frac{\omega_i}{2c_s^4}\boldsymbol{Q}_i : \boldsymbol{\Pi}^{(1)}, \tag{4.1}$$

where the tensor $\boldsymbol{Q}_i$ is defined as $\boldsymbol{Q}_i = \boldsymbol{e}_i\boldsymbol{e}_i - c_s\boldsymbol{I}$ and the stress tensor $\boldsymbol{\Pi}^{(1)}$ is evaluated based on the non-equilibrium components of the outward-pointing PDFs (in the opposite directions of the unknown PDFs) [159]. Single phase regions are arranged to the upstream of the particle introduction region as well as to the downstream of the particle removal regions, as shown in Fig 4.2a. This way, the velocity or pressure can be prescribed within the single phase region such that simple analytical solutions can be used. The aspect ratio of the single phase regions is chosen to be roughly one to allow smooth transitions of the properties from the single-phase to multi-phase regions or vice versa.

Particle phase

The introduction of particles at inlet is realized by inserting a particle introduction section downstream proximal to the single phase region, as depicted in Fig 4.2a. Inside the seeding section, the number of particles is conserved to control the particle concentration and number flow rate introduced to the downstream. Similar to other approaches [157, 155, 156], particles in this section periodically leave and re-enter the domain, while at the exit new particles are introduced to the downstream by duplicating the particle (and its properties such as mesh coordinates, velocity and mechanical properties, etc) that are wrapped to the entrance (upstream end) of the particle introduction region. Besides, random motions can be introduced to the particles within the introduction region to reduce the periodic pat-

terning of the particle distribution. Through these operations, new particles at controlled concentration and flow rate are introduced to the downstream with the surrounding flow field being well-perturbed.

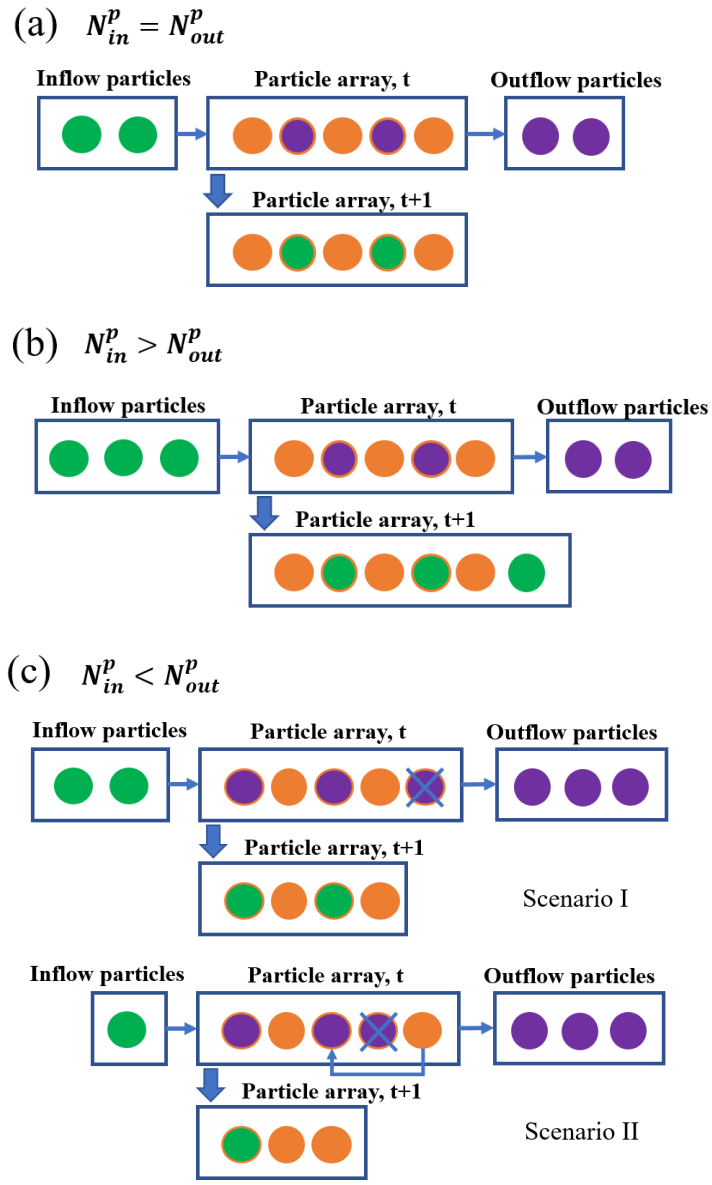

Figure 4.3: Schematics for the general particulate inflow and outflow boundary condition (PSIO-BC). The particle array represents the array storing the particle information according to the particle index, which increases from 1 to N_{max} from left to right. Here for example $N_{max} = 5$ at time t

Similarly, the particle removals are realized by embedding a particle removal region upstream proximal to a single phase region where the outlet fluid BCs are imposed. At the particle removal region, the particle information will be deleted at the local processor (assuming multi-processor parallelization is employed). Meanwhile, the particle index and the total number of removed particles at each time step will be recorded and communicated to the processors in charge of the particle introduction. To minimize the memory allocation for the particle array and perform minimal particle index manipulation, the indices of newly introduced particles are assigned conditionally according to the number of inflow and outflow particles (N_{in}^{p} and N_{out}^{p}). The schematics for the PSIO-BC operations are shown in Fig 4.3.

Algorithm 1 The Particulate Suspension Inflow and Outflow (PSIO) Algorithm

Require: $i, j, i_p, j_p, k_p \in \mathbb{Z}^+ \cup \{0\}$,

Count the number of inflow particles N_{in}^p
Store properties (location, velocity, etc) of inflow particles $\mathcal{P}_{in}^p(i)|_{i\in\{0,...,N_{in}^p-1\}}$
Count the number of outflow particles, N_{out}^p
Store indices of outflow particles, $\boldsymbol{I}_{out}^p(i)|_{i\in\{0,...,N_{out}^p-1\}}$
Update total particle number: $N_t^p \leftarrow N_{t-1}^p + N_{in}^p - N_{out}^p$
if $N_{in}^p = N_{out}^p$
  for $i \leftarrow 0$ to $N_{out}^p - 1$
    Assign $\mathcal{P}_{in}^p(i)$ to particle $\boldsymbol{I}_{out}^p(i)$
  end for
else if $N_{in}^p > N_{out}^p$
  for $i \leftarrow 0$ to $N_{out}^p - 1$
    Assign $\mathcal{P}_{in}^p(i)$ to particle $\boldsymbol{I}_{out}^p(i)$
  end for
  Allocate memory for particles N_{t-1}^p, ..., $N_t^p - 1$
  for $i \leftarrow N_{t-1}^p$ to $N_t^p - 1$
    $i_p \leftarrow i - N_{t-1}^p + N_{out}^p$
    Assign $\mathcal{P}_{in}^p(i_p)$ to particle i
  end for
else if $N_{in}^p < N_{out}^p$
  $j_p \leftarrow 0$
  for $i \leftarrow 0$ to $N_{in}^p - 1$
    $i_p \leftarrow \boldsymbol{I}_{out}^p(i)$
    while $i_p \geq N_t^p$
      $j_p \leftarrow j_p + 1$
      $i_p \leftarrow \boldsymbol{I}_{out}^p(j_p)$
    end while
    $j_p \leftarrow j_p + 1$
    Assign $\mathcal{P}_{in}^p(i)$ to particle i_p
  end for
  $k_p \leftarrow 0$
  for $i \leftarrow N_t^p$ to $N_{t-1}^p - 1$
    for $j \leftarrow 0$ to $N_{out}^p - 1$
      if $i \neq \boldsymbol{I}_{out}^p(j)$
        $\boldsymbol{I}_s^p(k_p) \leftarrow i$
        $k_p \leftarrow k_p + 1$
      end if
    end for
  end for
  for $i \leftarrow j_p$ to $N_{out}^p - 1$
    $k_p \leftarrow i - j_p$
    Assign $\mathcal{P}_{in}^p(\boldsymbol{I}_s^p(k_p))$ to particle $\boldsymbol{I}_{out}^p(i)$
    Free the memory of particle $\boldsymbol{I}_s^p(k_p)$
  end for
end if

Specifically, if $N_{in}^p = N_{out}^p$, the inflow particle properties are assigned to the indices

corresponding to the outflow particles, as indicated in Fig 4.3a. If $N_{in}^{p} > N_{out}^{p}$, in addition to the same procedure as above, the data structure for storing all the particle information in the computational domain (referred to as particle array) will be extended to accomodate for the incremental particles, shown in Fig 4.3b. If $N_{in}^{p} < N_{out}^{p}$, the particle array will be truncated to reflect the reduction of the total particle number. When the truncated particle indices are all associated with outflow particles (denoted as Scenario I in Fig 4.3c), the outflow particles and their memory allocation will be simply eliminated, and the inflow particles will take the indices of the outflow particles starting from the lowest index. When the truncated particle indices contain particles remaining in the computational domain (denoted as Scenario II in Fig 4.3c), in addition to the operations in Scenario I, the remained particle information will be assigned to the unoccupied outflow particle indices that are within the range of the updated particle array. The detailed procedure for the PSIO-BC algorithm is listed in the pseudo-code shown in Algorithm 1.

4.2.2 Reconstruction of physiologic microvascular bifurcations

Microvascular networks are comprised of many generations of single bifurcations connecting all the way from arterioles or venules to capillaries [105]. Each single bifurcation follows certain physiologic laws that constrain the geometric relation between parent and daughter branches. The radii of parent and daughter branches have been found to obey the Murray's law [160] stated as,

$$R_0^3 = R_1^3 + R_2^3, \tag{4.2}$$

where R_0 is the radius of the parent branch; R_1 and R_2 are the radii of the daughter branches. Complying to this simple geometric relationship leads to a more uniform distribution of vessel wall shear stress and consequently minimizes the power consumption [161]. The bifurcating angles of two daughter branches also satisfy certain physiologic optimality

relating to the vessel radius based on Zamir's law [162],

$$\cos\alpha_1 = \frac{R_0^4 + R_1^4 - R_2^4}{2R_0^2R_1^2};\ \ \cos\alpha_2 = \frac{R_0^4 + R_2^4 - R_1^4}{2R_0^2R_2^2}, \tag{4.3}$$

where α_1 and α_2 are the bifurcating angles of the two daughter branches with respect to the axial direction of the parent branch. Obeying Zamir's law minimizes the lumen volume of a single bifurcation [162]. In addition, we also assume the axes of three branches of a single bifurcation are in-plane as suggested previously [163]. The vessel length is assumed to be proportional to the vessel diameter with certain randomness [164]. The cross-section shape of the branches are assumed to be circular.

Based on the above physiologic constraints, microvascular bifurcations of multiple generations of branches can be reconstructed as shown in Fig 4.4, provided the radius of the parental branch, r_0, and the size ratio of two daughter branches, $\eta_D = \frac{R_1}{R_2}$, being prescribed randomly within the physiological range [163].

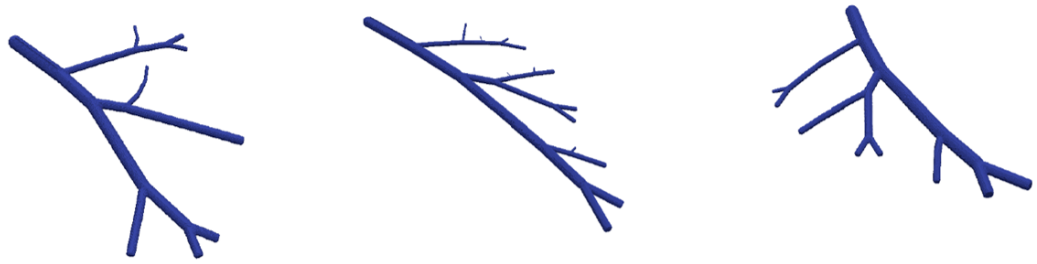

Figure 4.4: Demonstration of three reconstructed microvascular bifurcations of physiologic relevance.

4.2.3 In vivo experiment

To validate the numerical methods, the blood flow through a microvascular bifurcation within the chicken chorioallantoic membrane (CAM) in vivo model has been characterized through microscale particle image velocimetry (μPIV). The CAM model is a highly vascularized extraembryonic membrane that is readily accessible for intravital imaging. In-house

synthesized mesoporous silica nanoparticles (MS-NP) were used as tracking particles.

The μPIV system is shown in Fig 4.5 (left), which mainly consists an upright microscope (Zeiss Axio Examiner Z.1) modified with a heated stage operated at 63 magnification to image the CAM model (10 days post fertilization). The microscope is fitted with a water immersion lens (LDC-APO Chromat 63 1.15W) to facilitate imaging of deep vessels. Imaging was performed using a high-speed camera (Hamamatsu Orca Flash 4.0) operated at 142 frames/sec, enabling a resolution of 0.1 microns/pixel. A broadband light source was used along with careful image and PIV processing methods through the LaVision PIV software package DaVis v8.4 to mitigate image blur effects especially at peak velocities.

The CAM model is depicted in Fig 4.5 (middle). The ex-ovo avian embryos were handled according to published methods [165] with all experiments conducted following an institutional approval protocol (11-100652-T-HSC). Embryos were utilized for experimentation 7 days post removal from shells (day 10 post fertilization). A dosage of 50 μg MS-NPs with size $\sim$130 nm were injected into tertiary veins of the CAM. After injection, embryos were placed in a customized avian embryo chamber for imaging.

Applying the preceding methodology, a greyscale image of a vascular bifurcation is shown in Fig 4.5 (right). The image location was chosen such that the vessel branches remain relatively flat over the entire field-of-view. To obtain the dynamic velocity field, 5000 images were acquired in total. A sliding sum-of-correlation method was used to calculate vector fields [166]. In § 4.3.2, the mean velocity field obtained based on the NP flow is compared with the computed counterparts through the current multiscale computational framework.

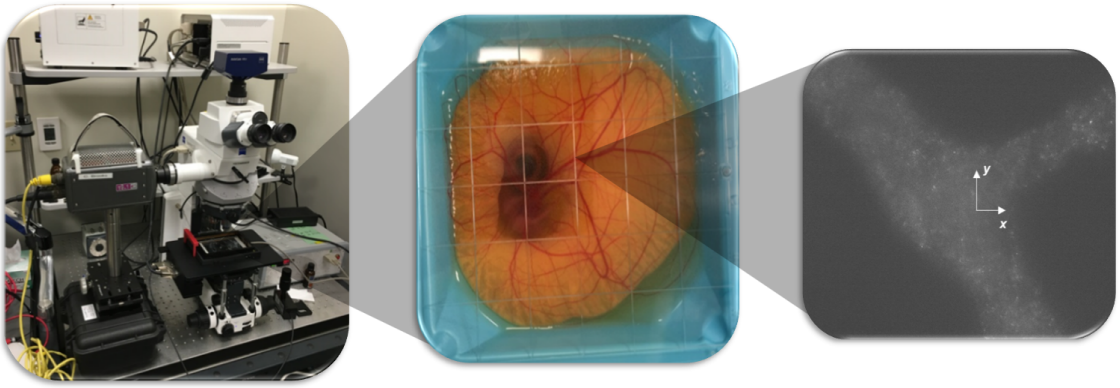

Figure 4.5: The benchtop microscale particle image velocimetry (μPIV) system (left), the chick chorioallantoic membrane microvasculature model (middle) and the grey-scale visualization of the flow field of a selected region of interest (right).

4.3 Results and Discussion

In this section, we first verify the PSIO-BC by recovering a tubular blood flow and comparing the results with that obtained from the typical periodic boundary condition. Furthermore, the multiscale computational framework is further validated by reconstructing the CAM bifurcation flow in silico and comparing simulation against the experimental measurement. As follows, the NP partitioning pattern in the presence of RBCs is interrogated quantitatively by simulating a bidisperse RBC-NP suspension through single physiologically-relevant microvascular bifurcation under different flow partition ratios with or without geometric asymmetry. Physical mechanisms leading to specific NP partitioning characteristics are discussed in detail.

4.3.1 Recovering tubular flows

Flow through a straight tube with or without RBCs is simulated with both PSIO-BC and P-BC. The tube has a diameter of $2R$=20 μm and a length of L=80 μm. The fluid viscosity is selected as μ=1.2 cP. A hematocrit of ϕ=30% is selected for the multiphase simulations. The RBC has a shear modulus of G=0.0063 $dynes/cm$. For the P-BC simulations,

a constant pressure gradient, $-\frac{dp}{dz}$=240 Pa/mm, is applied to drive the flow (from left to right according to Fig 4.6a) such that the wall shear rate is $\dot{\gamma}_w$=1000 s^{-1}. For the single phase simulation using the PSIO-BC, parabolic velocity profiles, $u(r)$=$|\frac{dp}{dz}|\frac{(R^2-r^2)}{4\mu}$, are prescribed at both the inlet and outlet. For RBC case through PSIO-BC, inlet and outlet pressures are prescribed at the outmost ends of the single phase regions. The inlet pressure is p_i=p_0+$|\frac{dp}{dz}|(L+L_{BC})$ and the outlet pressure is p_o=p_0, where p_0 is chosen as the atmospheric pressure and L_{BC}=60 μm that accounts for the extra tube sections for PSIO-BC.

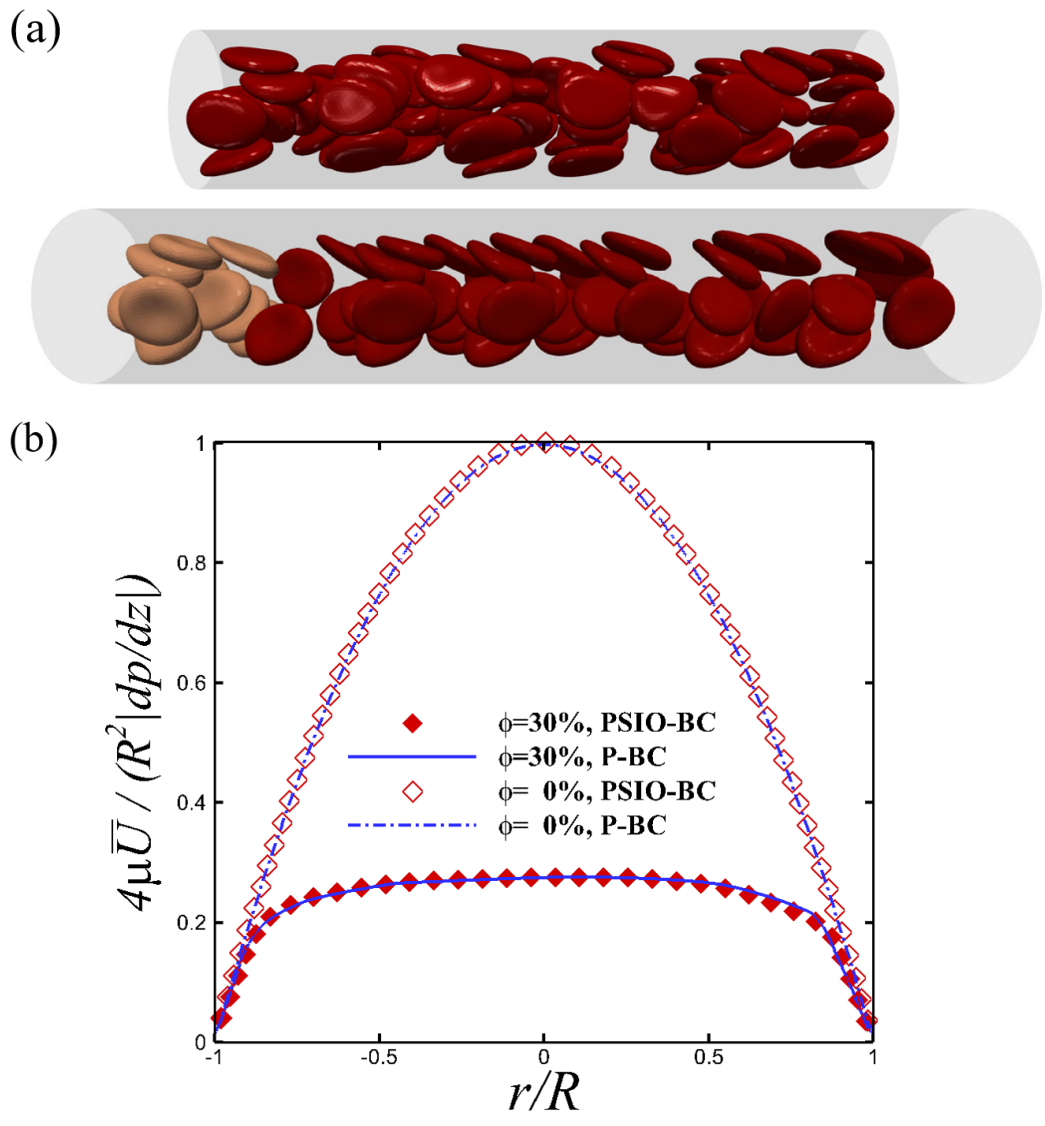

Figure 4.6: Normalized axial flow velocity plotted against vessel radial locations for a tubular flow with or without red blood cells, computed with the P-BC or the PSIO-BC.

The velocity profiles for the tubular flow simulations using both PSIO-BC and P-BC are plotted in Fig 4.6b. The velocity profiles for the cases with ϕ=30% are averaged over 10 different axial locations at one time point during equilibrium. It is shown that the results via PSIO-BC agrees well with that via P-BC, showing the validity of the PSIO-BC algorithm.

4.3.2 Comparing with in vivo measurements

To further validate the current multiscale computational framework, we simulate a NP-RBC suspension flow through a CAM microvascular bifurcation (see supplemental video 1) and compared the results against experimental measurements through μPIV. An arterial branch in the CAM model is selected for the study due to its relatively big size and flat orientation, which are suitable for measurement. The parent branch has a radius of R_0=20 μm and the two daughter branches have radii of R_1=7.5 μm and R_2=17.5 μm respectively, shown in Fig 4.7a. Slight pulsatility of the flow is observed with a frequency of $f = 3\ Hz$. The Womersley number for this problem can be estimated as α=$\sqrt{\rho f R_0^2/\mu} \approx 0.03 \ll 1$, which suggests the pulsation effect is insignificant. Therefore, the study below concentrates on comparing the mean velocity as a reasonable simplification.

Contour maps of the mean velocity field from the μPIV measurement are demonstrated in Fig 4.7a on the left. The mean streamlines are overlaid, indicating the flow direction. We simulate the NP-RBC suspension flow through the same reconstructed geometry using the multiscale computational method, where Dirichlet velocity BCs based on the in vivo measurements are applied at the inlet and outlet using the PSIO-BC. The hematocrit is assumed to be 20% which is an average physiological value for CAM blood flows [167]. The NP number concentration is set to $10^7/ml$ for statistic purposes. The RBC size is selected to be the same as human RBC size, while the rigidity (shear modulus) of the RBC membrane is elevated by three folds to be consistence with low deformability observed in avian RBCs [168]. As shown in Fig 4.7, the fluid velocity distribution reproduced by simulation qualitatively matches well with the PIV results.

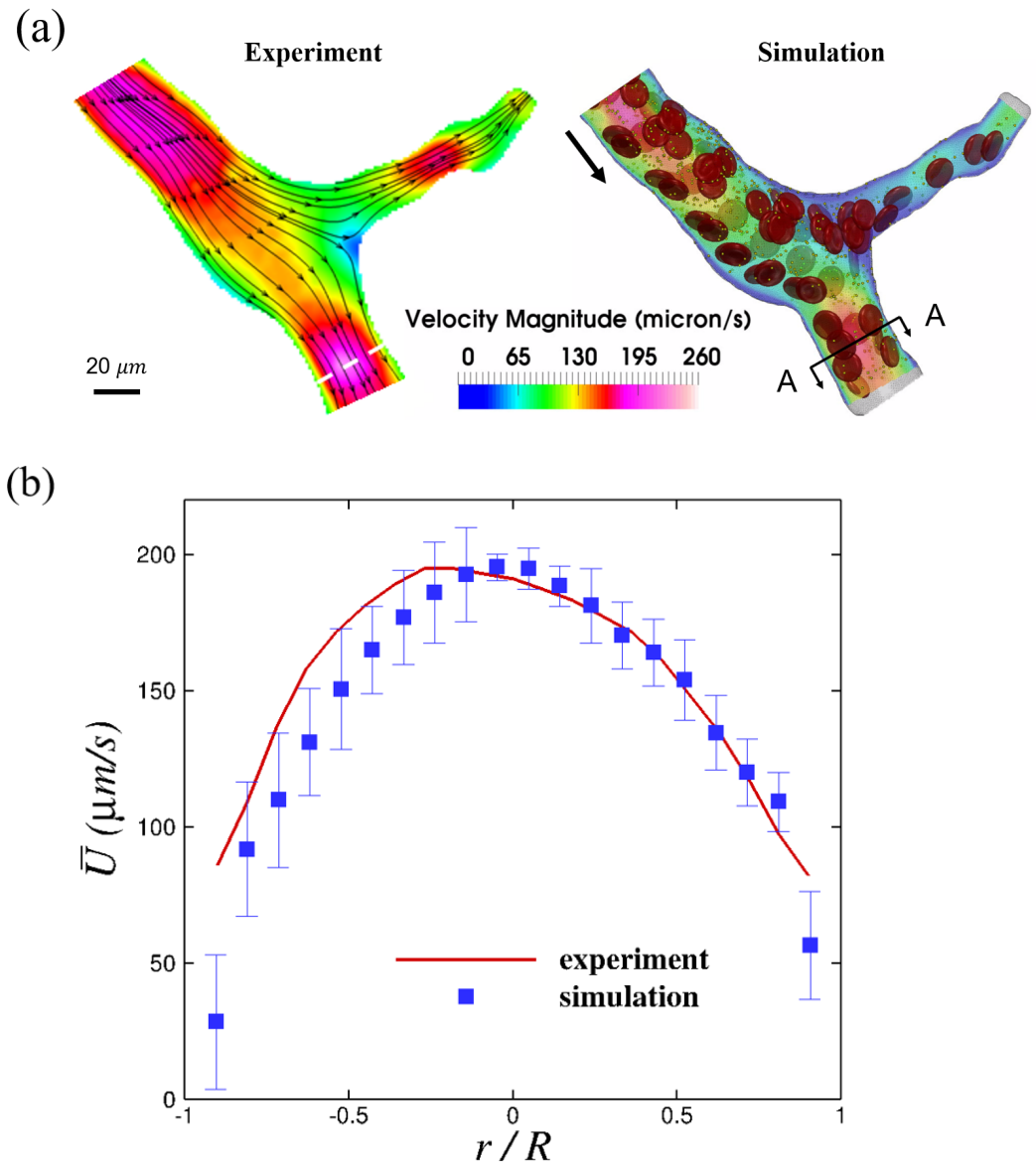

Figure 4.7: (a) Comparisons of the mean velocity distribution between the experiment and simulation through a CAM vascular bifurcation. The velocity contour for the simulation is an snapshot after the system reaches equilibrium (*i.e.*, the number of particles reach plateau). (b) The radial distribution of the mean axial velocity at the A-A cross-section annotated in (a). The asymmetry of the experimental curve may be related to the non-circular shape of the actual cross-section area.

The velocity profiles across the diameter of the larger daughter branch at the A-A lo-

cation (denoted) are further plotted in Fig 4.7b. The velocity profile in the simulation is obtained by tracking the streamwise velocity of the NP flowing through the A-A cross-section at equilibrium to mimic the μPIV process. The mean velocity near the wall has a finite number for both the simulation and experiment as a result of the sliding nature of the NP adjacent to the wall. The velocity profile in the RBC-laden region shows overall good agreements between experiment and simulation.

4.3.3 NP partition through microvascular bifurcations

To understand how NPs partition at the junction of a microvascular bifurcation, a trade study of NP-RBC suspension flow through single microvascular bifurcations is performed, taking into account the asymmetry in both the flow partitioning and vascular geometry. To control the partitioning of the bulk fluid, a flow partition ratio (FPR) is defined as $\eta^F_{Q,i} = Q_i/Q_0$ where Q_i (i=1 or 2) denotes the suspension flow rate at one daughter branch and Q_0 is the suspension flow rate at the parental branch. Similarly, a particle partition ratio (PPR) is defined as $\eta^p_{Q,i} = N_i/N_0$, where N denotes the number of particles entering the corresponding branch. The PPR is used to quantitatively describe the partition pattern of the particle phase (RBC and NP) under different FPR. For the following studies, the parental branch has a size of $2R_0$=20 μm, a wall shear rate of $\dot{\gamma}$=2000 s^{-1} and a hematocrit of ϕ=20%, reflecting physiologic conditions of arterioles [136, 105]. The Dirichlet velocity boundaries are applied to both the inlet and outlet, where the Poiseuille flow velocity profiles are imposed at the single phase region pertaining to specific $\eta^F_{Q,i}$. The vascular geometric effect is controlled by the daughter branch size ratio, η_D. Provided R_0 and η_D, the exact size and bifurcating angle of the two daugher branches are uniquely constrained by the physiologic laws discussed in 4.2.2.

Symmetric bifurcations

We first study the NP-RBC suspension flow partitioning through a geometrically symmetric bifurcation by setting $\eta_D = 1$, as shown in Fig 4.8a. As a control, when there is no RBC in the bifurcation, the η_Q^p of NP changes linearly as the η_Q^F changing from 0.1 to 0.9, as shown in the inset of Fig 4.8b. This partitioning pattern is termed homogeneous partition, as the flow of the particle phase follows the fluid phase while branching towards the downstream.

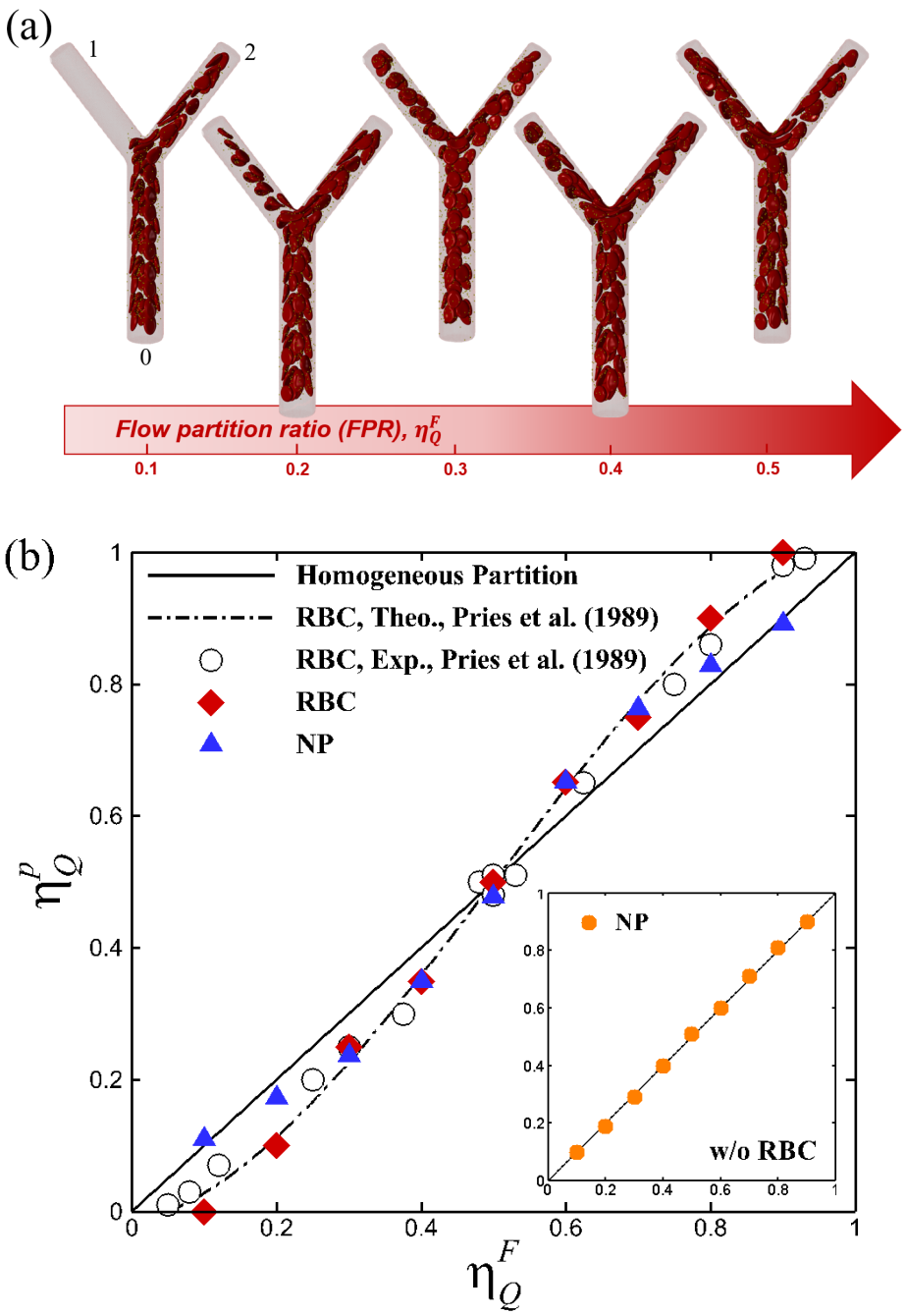

Figure 4.8: (a) Snapshots of RBC-NP suspension flow through symmetric bifurcations under various suspension flow flux partition ratio, η_Q^F. (b) Particle flow partition ratios, η_Q^p, plotted against suspension flow partition ratio, η_Q^F, for symmetric microvascular bifurcations. The inset shows the results without the presence of RBCs.

When RBCs are introduced from the parental branch, the simulated η_Q^p of the RBC

phase exhibits a sigmodal trend with respect to η_Q^F, as shown in Fig 4.8b. This trend agrees well with both the experimental measurement and theoretical correlation by [139], indicating the classic ZF effect is well captured by the current computational methods. Such heterogeneous partition of RBC is most prominent at $\eta_Q^F = 0.1$ or 0.9, where complete phase separation of RBC occurs in one of the daughter branches, as shown in Fig 4.8a. Similar to the ZF effect in the RBC phase, the η_Q^p for NP also deviates from the linear line, suggesting the NP partitioning also becomes heterogeneous. However, such heterogeneity in the NP partitioning seems to be conditional as the η_Q^p falls back on the linear line at about η_Q^F=0.1 or 0.9 while complete phase separation of RBC occurs.

Asymmetric bifurcations

To introduce the effect of geometric asymmetry, we set $\eta_D = 0.8$ as a physiological ratio of asymmetry reported in [163]. The resulting geometry of the asymmetric bifurcation is shown in Fig 4.9a. Similar to the symmetric bifurcation case, NP shows mainly homogeneous partition when RBCs are not present, as shown in the inset of Fig 4.9b. However, due to geometric asymmetry, the η_Q^p of NP is deviated from the linear curve at $\eta_Q^F = 0.5$. This can be explained by the slight deviation of the bifurcation junction towards the smaller daughter branch which causes the uniformly dispersed NPs [153] prioritizing entering the larger daughter branch (branch 1).

As further shown in Fig 4.9b, the asymmetric bifurcation exhibits a more pronounced heterogeneity in the RBC partition, as predicted by both our simulations and the theory in [139]. Different from the symmetric bifurcation, the heterogeneity of RBC partition even occurs during equal flow partitioning ($\eta_Q^F = 0.5$) as another manifestation of the effect of the geometric asymmetry. The enhanced heterogeneity of the RBC partitioning further elevates the heterogeneity in the NP partitioning compared to the symmetric bifurcation case. Again, the partitioning of NP recovers homogeneity at extreme flow partition ratios when severe phase separate occurs.

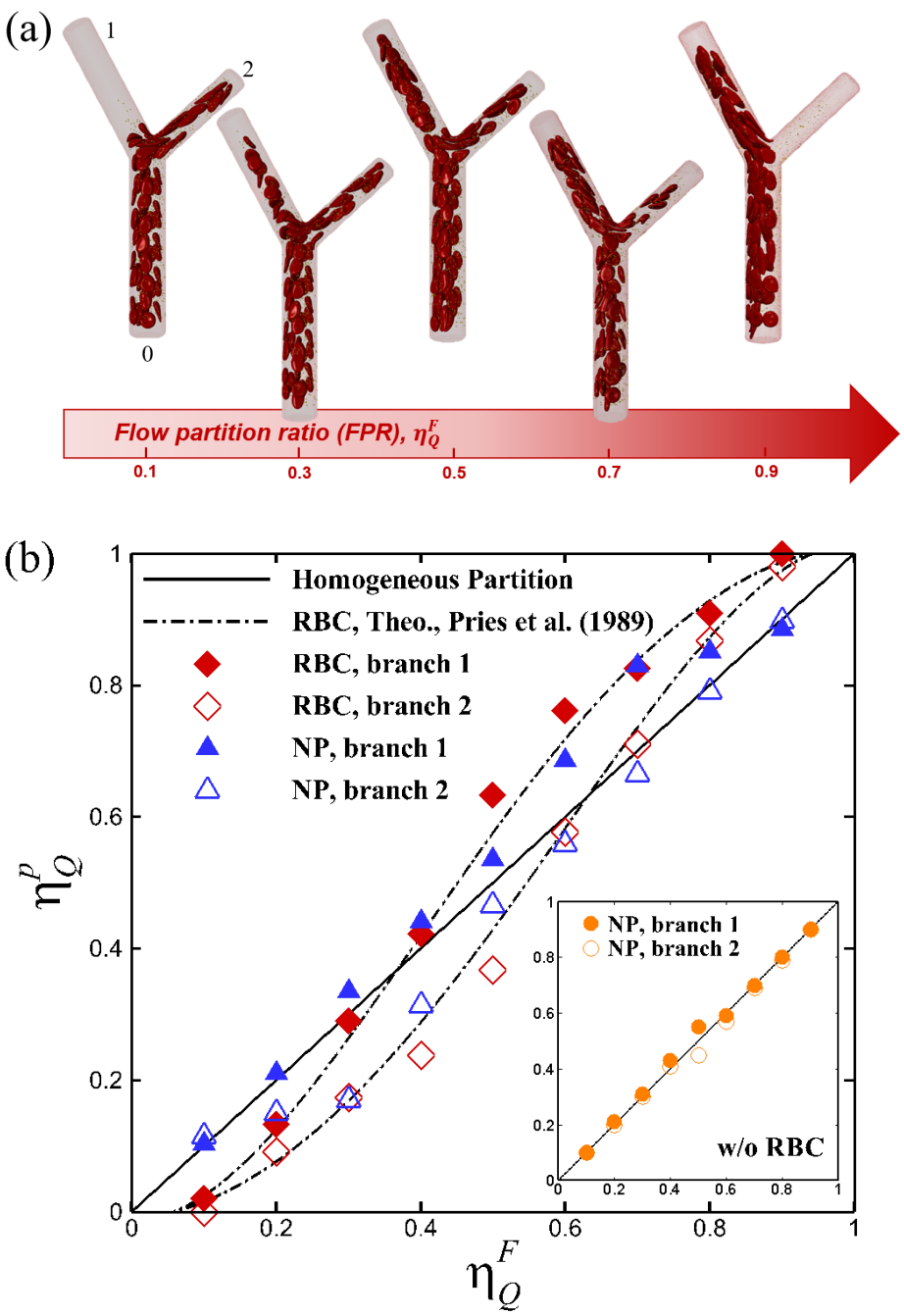

Figure 4.9: (a) Snapshots of RBC-NP suspension flow through asymmetric bifurcations under various suspension flow flux partition ratio, η_Q^F. (b) Particle partition ratio, η_Q^p, plotted against suspension flow partition ratio, η_Q^F, for asymmetric microvascular bifurcations. The inset shows the results without the presence of RBCs.

4.3.4 Mechanisms for conditional heterogeneity in NP partition

Next, we take a detailed look at the particle trajectory and flow structure of the asymmetric bifurcation case to understand the underlying mechanisms governing the conditional heterogeneity in the NP partition through microvascular bifurcations. Specifically, we look at two flow partition ratios, $\eta_Q^F = 0.7$ and 0.9, that gives rise to the high heterogeneity in NP partition and the recovery of homogeneous partition, respectively.

At $\eta_Q^F = 0.7$, RBCs periodically collide onto the junction, linger for a while and exhibit a higher frequency of entering the higher-velocity branch in consistence with the ZF effect [141]. As an example shown in Fig 4.10a, the RBC (denoted in blue) is lingering while performing a tank-treading motion and sliding into the upper branch where the flow rate is higher. The upper sliding motion occurs more frequently than the lower sliding motion, which consequently leads to $\eta_Q^p = 0.83$ being higher than η_Q^F. The RBC tank-treading motion at the bifurcation junction will further alter the local flow field. As shown in Fig 4.10c, at the condition of $\eta_Q^F = 0.7$, without RBCs the flow separatrix is well aligned with the geometric dividing line at the junction; with RBCs lingering and tank-treading towards the upper branch, the flow separatrix tends to locally shift towards the lower branch, which locally leads to the recruitment of more NPs towards the upper branch. This RBC-induced entrainment effect seems to be the mechanism that causes the heterogeneity in the NP partition when RBCs are present.

When the recovery of homogeneous partitioning occurs at $\eta_Q^F = 0.9$, a certain amount of NPs can still flow into the RBC-free branch, as shown in Fig 4.10b. As indicated by the trajectories of NP throughout the bifurcation, the majority of the NPs that enter the lower branch come from the cell-free layer (CFL) of the parental branch. Unlike the deformable RBCs that tend to concentrate to the center of the tube as a result of the lift force exerted by the vessel wall [169], NPs tend to disperse throughout all the radial locations due to the severe Brownian effect [24, 153]. In other words, the NP phase can always enter the cell-free branch so long as the plasma skimming occurs, which will reasonably contribute to

the homogeneity in the NP partitioning. As further shown in Fig 4.10b, the flow separatrix at $\eta_Q^F = 0.9$ does not seem to be drastically distorted when the RBC is present. Therefore, given the incoming NPs are uniformed distributed in the parental tube [153], the ratio of NP partitioning with RBCs is expected to be similar to the case without RBCs.

Taken together, the heterogeneity in the NP partition in the presence of RBCs seems to be associated with an RBC-induced entrainment effect, that distorts the flow separatrix to the low flow rate branch and thus entrains more NPs to the high flow rate branch. The presence of NPs in the CFL accompanied by the normalization of flow separatrix at the extreme flow partition ratios (when blood plasma skimming occurs) leads to the return of NP partitioning from heterogeneity to homogeneity in the presence of RBCs. The competition between th RBC-induced entrainment effect and the presence of NP in the CFL contributes to the conditional heterogeneity of the NP partitioning as observed in 4.3.3.

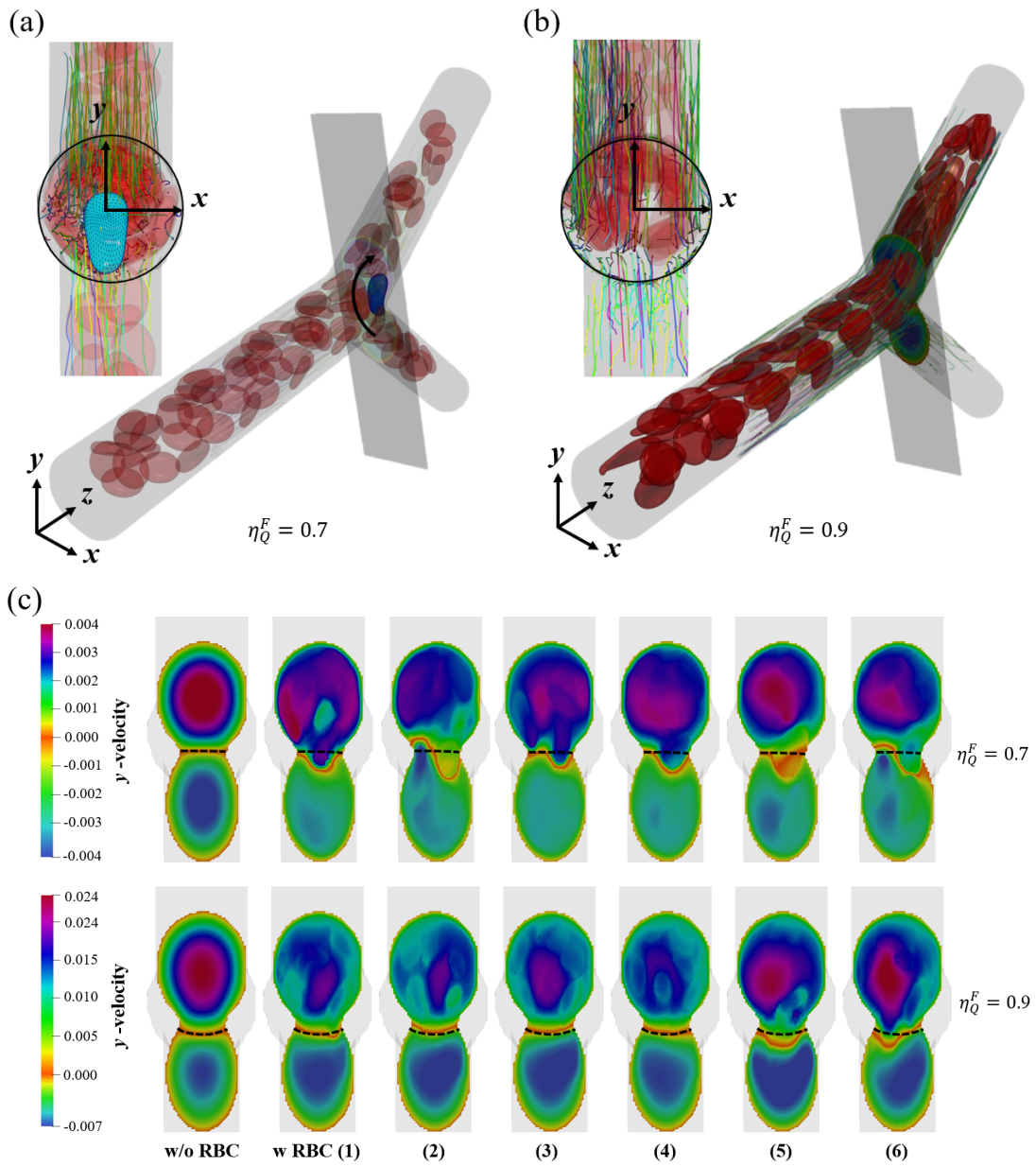

Figure 4.10: (a-b) The cell distribution, NP trajectories and a cross-section of interest within an asymmetric microvascular bifurcation. (c) The contours of the Y velocity component at the cross-section adjacent to the bifurcation junction. The left column shows the case without the presence of RBCs. The other six columns corresponds to six time points when a RBC sliding towards the upper branch. The black dashed line denotes the zero velocity line for the cases without particles (RBCs and NPs), which shows the flow separatrix that divides the flow entering two daughter branches.

4.4 Summary

In this work, we have developed a multiscale computational framework to directly simulate the NP distribution and partition through the microvascular bifurcations in the presence of RBCs. A general particulate suspension inflow and outflow boundary condition has been developed and embedded in the computational framework, and later applied to both the RBC and NP suspension dynamics. To validate the model, in vivo measurements of the NP flow through a CAM microvascular bifurcation have been performed. The current computational framework is able to quantitatively reconstruct the detailed physiological bifurcation flow by directly simulating both the RBC and NP suspensions. The velocity distribution for the NP phase through simulation matches well with the experimental measurement, showing the accuracy and validity of the present multiscale computational framework.

Applying the multiscale computational framework, we further interrogate the RBC-NP suspension flow through idealized single bifurcations under physiologically relevant geometry and flow conditions. The classic Zweifach-Fung effect is found to be well captured by the method. Moreover, we find the partition of the blood-borne NP through microvascular bifurcations in response to the ZF effect also shows a substantial heterogeneity. The heterogeneity in the NP partition is however conditional depending on the level of disproportionality in the flow partitioning between the daughter branches. The physical mechanisms responsible for the heterogeneity in the NP partition has been analyzed in terms of the flow structure and the particle trajectories. It is found that the heterogeneity in the NP partition in the presence of RBCs seems to be associated with the flow separatrix deviation at the bifurcation junction caused by the RBC tank-treading motion. The recovery of homogeneity in the NP partitioning however has to do with the plasma skimming of the NPs in the CFL accompanied with the normalization of flow separatrix at the extreme flow partition.

This study presents a numerical tool that can be used to directly analyze the blood-borne NP distribution within microcirculation that often comprises complex branching structures

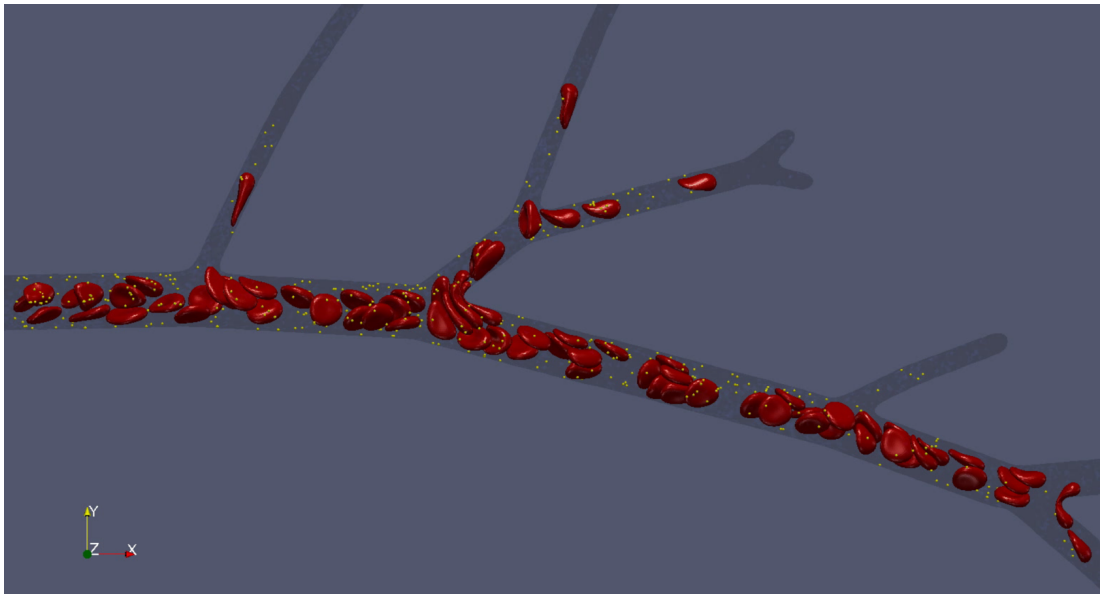

Figure 4.11: In silico reconstruction of cellular-blood-borne nanoparticles through a multi-generation microvascular bifurcation using the developed PSIO-BC.

(see Fig 4.11). The results imply the importance of the presence of the RBC phase in directing the blood solute distributions and provides possible physical mechanisms that contribute to the heterogeneous distribution of blood solute in microvasculatures observed clinically [151]. Such insights can provide valuable information for a upscaling to a network model of the full vasculature [164] and may help the design of nanocarriers with improved drug delivery efficacy [152]. It is also noteworthy that the proposed particulate suspension inflow and outflow boundary condition is general and can be applied to other applications such as modeling arterial thrombosis [170] or other reacting flows that often involve consumption of particles or species.

CHAPTER 5

SHEAR-INDUCED DIFFUSION OF NANOPARTICLES IN CELLULAR BLOOD FLOW UNDERGOING UNBOUNDED SIMPLE SHEAR

Using a multiscale blood flow solver, the complete diffusion tensor of nanoparticle (NP) in sheared cellular blood flow is calculated over a wide range of shear rate and hematocrit. In the short-time regime, NPs exhibit anomalous dispersive behaviors under high shear and high hematocrit due to the transient elongation and alignment of the red blood cells (RBCs). In the long-time regime, the NP diffusion tensor features high anisotropy. Particularly, there exists a critical shear rate ($\sim$100 s^{-1}) around which the shear-rate dependence of the diffusivity tensor changes from linear to nonlinear scale. Above the critical shear rate, the cross-stream diffusivity terms vary sublinearly with shear rate, while the longitudinal term varies superlinearly. The dependence on hematocrit is linear in general except at high shear rates, where a sublinear scale is found for the vorticity term and a quadratic scale for the longitudinal term. Through analysis of the suspension microstructure and numerical experiments, the nonlinear hemorheological dependence of the NP diffusion tensor is attributed to the streamwise elongation and cross-stream contraction of RBCs under high shear, quantified by a Capillary number. The RBC size is shown to be the characteristic length scale affecting the RBC-enhanced shear-induced diffusion (RESID), while the NP size at submicron exhibits negligible influence on the RESID. Based on the observed scaling behaviors, empirical correlations are proposed to bridge the NP diffusion tensor to specific shear rate and hematocrit. The characterized NP diffusion tensor provides a constitutive relation that can lead to more effective continuum models to tackle large-scale NP biotransport applications.

5.1 Introduction

The rapid advancement of nanotechnology and nanomaterial manufacturing has led to emerging exposure of human biological systems, such as cardiovascular systems, to nano-sized particulate matters [115, 171], ranging from engineered nanocarriers functioning as medicine/imaging agents [172, 173, 60] to aerosol pollutant particulates potentially causing fatal cardiovascular disease [174, 175, 176]. Both the design of optimal nanocarrier systems and the prevention and control of nanoparticle (NP) toxicity rely heavily on the knowledge of NP distribution in vascular systems [115]. Nevertheless, the biodistribution of NP remains elusive to date and limits the bio-availability of NP systems to the human bio-environment. One of the primary bottlenecks is the lack of understanding on the NP dispersive mechanisms in blood flow with respect to specific hemorheological conditions.

Multi-scale computational models [23, 22, 24] have been developed and applied to predict the NP distribution in micro-vessels by directly simulating NPs and red blood cells (RBCs) suspended in blood plasma. Although these models, as particle-based approaches, provide a straightforward means to predict the NP distribution in realistic, micro-scale vessels, they are still computationally intractable when it comes to organ- and circulation-level applications. Alternatively, continuum models [14, 25, 177, 15] have the ability to predict NP distribution in large-scale vascular systems by solving the three-dimensional (3D) convection-diffusion equation

$$\frac{\partial c}{\partial t} + \boldsymbol{u} \cdot \boldsymbol{\nabla} c + \boldsymbol{\nabla} \cdot \boldsymbol{J} = 0, \tag{5.1}$$

where t is time, c is the NP concentration, $\boldsymbol{u}$ is the local fluid velocity and $\boldsymbol{J}$ is the flux of NP concentration. Here, $\boldsymbol{J}$ is often estimated by the Fick's law as $\boldsymbol{J} = -\boldsymbol{D}^{\infty} \cdot \boldsymbol{\nabla}\, c$, where the NP diffusion tensor, $\boldsymbol{D}^{\infty}$, is so far treated as isotropic, Brownian diffusivity [177] or solute diffusivity measured in a single principal direction [178]. Since the particle diffusion tensor is anisotropic in nature even for monodisperse rigid sphere suspensions [40, 41], an

improved constitutive relation capturing the anisotropy of $\boldsymbol{D}^{\infty}$ subject to local hemorheological properties is therefore necessary to form a better closure of this convection-diffusion problem.

Using Couette-type flow devices, experiments have been conducted to characterize the particle self-diffusivity [179, 180] and effective solute diffusivity [181, 178, 180] in non-colloidal particle suspensions under linear shear flow for various shear rates and particle volume fractions. However, due to the difficulties in particle tracking in the presence of the affine flow effect, only the particle diffusivity in the cross-stream directions are reported. Apart from the experimental efforts, particle-scale simulations have become an important tool for characterizing the anisotropic particle diffusivity tensor in both colloidal [40, 41, 93] and noncolloidal [42, 182, 74] suspensions under shear flow. Owing to the success of those particle-scale simulation techniques, substantial progress have been made in understanding the rheological and hydrodynamic response of the particle diffusion tensor in sheared monodisperse suspensions. Nonetheless, the bidisperse RBC-NP suspension system remains largely unexplored and entails unique transport phenomenology that is unavailable to the conventional monodisperse particle suspensions.

First, there is a large length-scale discrepancy between NPs $\sim O(10\ nm)$ and RBCs $\sim O(10\ \mu m)$. Consequently, NPs are subject to both molecular level thermal fluctuations (Brownian motion) and cellular level interactions with RBCs. On macroscopic scales, the two effects synergistically give rise to an apparent diffusivity contributed by both Brownian diffusivity (BD) and the so-called RBC-enhanced shear-induced diffusivity (RESID) [15, 111, 24]. Second, the NP phase shows infinite dilution while the RBC phase exhibits a range of physiological concentrations from $\sim 10\%$ to $\sim 40\%$. Consequently, the BD shows insignificant dependence on shear rate and hematocrit, while the RESID is highly dependent on the hemorheological conditions [111]. Third, RBCs deform considerably under shear, from biconcave shape in equilibrium to large elongation and tank treading of the membrane under high shear [183]. Such geometric asymmetry and morphological changes

of RBCs could alter RESID substantially.

Therefore, the objective of the present work is to characterize the bulk diffusivity tensor of NP in sheared blood flow and interrogate the NP dispersive mechanism specific to a broad range of hematocrit and shear rate. Given the large length-scale discrepancy ($3\sim4$ orders of magnitude) between NP and RBC, resolving both particle phases using direct numerical simulation (DNS) is computationally prohibitive. Therefore, a multiscale complex blood flow solver [2, 3, 7, 24, 120] is employed to treat NP as effective Brownian particles while directly resolving the RBC phase. Such multiscale treatment can substantially reduce the computational expense but still preserve the critical suspension physics at distinct scales. As will be shown in the following section ($\S5.3.3$), good comparison between the simulation and experimental results can be obtained using this multiscale approach. Since confinement (wall) effects in general lead to spatial heterogeneity of the blood flow [184] that forbids the calculation of NP diffusivity related to specific hematocrit and shear rate, the Lees-Edwards boundary condition (LEbc) [102] is implemented [8] to impose unconfined simple shear flow to obtain the NP bulk diffusive properties.

Note that blood flow typically occurs under confinement (e.g., blood flow in arteries) involving heterogeneous flow structures that could induce cell segregation [184, 13] and margination [17, 18, 19, 15, 111]. Such phenomena are found to be a synergistic outcome of the RBC-induced diffusion in the RBC-laden region and the formation of cell free layer (CFL) near the wall [15, 111]. For NPs with negligible inertia and much smaller length scale compared to the CFL thickness [18, 111], it is expected that the presence of wall has insignificant direct influence on the NP diffusion in the RBC-laden region. Besides, large-scale problems suitable for continuum modeling (such as blood flow through coronary arteries) typically feature much larger length and time scales compared to those considered in the current cellular-scale studies. It is therefore plausible to hypothesize the long-time NP diffusion tensor evaluated in an unbounded simple shear flow should closely capture the NP diffusive behavior subject to the same local hemorheological condition in a macroscale

heterogeneous blood flow environment.

One unique contribution of this work is the development of a multiscale-simulation-informed empirical expression that links the anisotropic NP diffusion tensor to the local hemorheological conditions. Such 3D NP diffusive information in sheared blood is intractable to measure through either experiment or DNS simulation. On the application side, the developed NP diffusion tensor provides a constitutive relation that can lead to more effective continuum-level models to tackle large-scale NP biotransport problems. On the suspension rheology side, the diffusive phenomenology observed in such a biophysical, bidisperse RBC-NP suspension system could entail novel suspension physics that is unavailable to conventional suspension flows.

The remainder of this chapter is organized as follows. In §5.2.1, the details of the computational methodology are presented. In §5.3, we present results and perform numerical experiments. In §5.3.1, the numerical problem is formulated with careful consideration of numerical resolution as well as physiological significance. In §5.3.2, the transient dispersive behaviors of NP are presented. As follows in §5.3.3, the long-time diffusive behaviors of NP subject to a wide range of shear rate and hematocrit are validated with available experimental data and interrogated with various hemorheological scaling behaviors. In §5.3.4, the NP-RBC suspension microstructure is analyzed to give mechanistic insights to the hemorheological scaling observations. In §5.3.5 and §5.3.6, numerical experiments are conducted to shed light on the physical mechanisms governing the nonlinear shear-rate dependence of the NP diffusion tensor. In §5.3.7, empirical correlations are proposed based on the hemorheological scalings observed in previous sections. In §5.4, we conclude this work with some remarks.

5.2 Methodology

5.2.1 Multiscale whole blood flow solver

The numerical method for this study is through a 3D lattice-Boltzmann based multiscale complex blood flow solver that efficiently resolves both the dynamics and interactions of nanoscale particles and microscale capsules [185, 3, 24, 120], as demonstrated in figure 5.1. The LB method is a well-established numerical model for hydrodynamics and proves to be a highly scalable method for direct numerical simulation (DNS) of dense particulate suspensions [4]. Modeling of the RBC dynamics and deformation is via a coarse-grained spectrin-link membrane method [6, 121] coupled to the LB method[3], which has been validated against experimental results[3, 7]. The NP suspension dynamics are resolved via a two-way coupled lattice-Boltzmann Langevin-dynamics (LB-LD) method with both particle Brownian motion and long-range hydrodynamic interactions (HI) directly resolved and validated [24, 120]. The solver has been successfully applied to several studies of particle and biopolymer transport in cellular blood flow [7, 19, 111, 13, 24, 60].

5.2.2 Lees-Edwards boundary condition

Since the primary focus of this study is on the particle bulk diffusive behavior subject to no wall effect, simulations are performed in an unbounded, triply periodic cubic domain where a constant shear rate is imposed through the Lees-Edwards boundary condition (LEbc) [102]. This method, originally developed for molecular dynamics simulations, was extended to the LB method by [186] and later applied to deformable suspensions on parallel computing architectures by [74, 7]. In addition to the operations associated with regular periodic boundary conditions, both the particle (NP and RBC) phase and the fluid phase undergo a shift in position and velocity according to the LEbc scheme as they cross the top ($+y$) or bottom ($-y$) boundary.

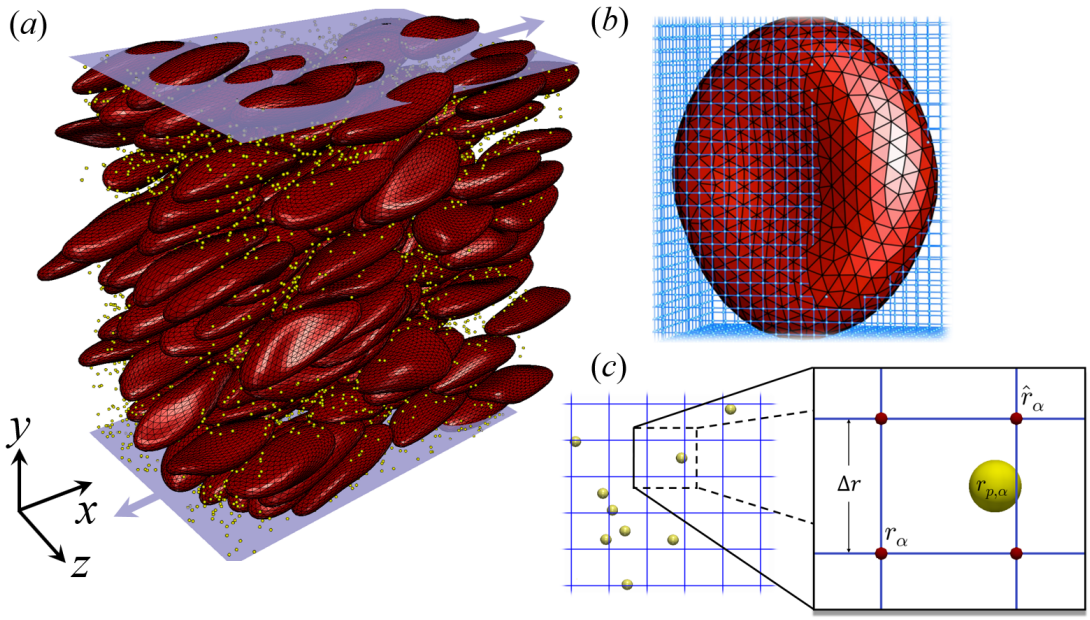

Figure 5.1: (a) The RBC-NP bidisperse suspension in a triply periodic domain at shear rate $\dot{\gamma} = 1\ 000\ s^{-1}$ and hematocrit, $\phi = 40\%$. (b) The RBC membrane immersed in the LB lattice domain. The RBC membrane dynamics and deformation is captured by the course-grained spectrin-link method [6, 121, 3]. (c) The NP suspension dynamics is captured by the LB-LD method [24, 120], which captures the NP Brownian motion and long-ranged HI in an off-lattice fashion.

5.2.3 Characterization of the particle diffusion tensor

The presence of shearing flow imposes a convective effect on the particle suspension and complicates the characterization of particle diffusion tensor. The major difficulty lies in determination of the longitudinal diffusivity (D_{xx}^{∞}) and off-diagonal diffusivity (D_{xy}^{∞}), which require careful subtraction of the affine particle displacement. The diffusion tensor in sheared monodisperse colloidal suspensions have been successfully quantified by sampling the non-affine particle mean square displacements (MSDs) [187, 40, 41, 188]. Therefore, this study calculates the long-time NP diffusion tensor, $\boldsymbol{D}^{\infty}$, in the form of

$$\boldsymbol{D}^{\infty} = \begin{pmatrix} D_{xx}^{\infty} & D_{xy}^{\infty} & 0 \\ D_{yx}^{\infty} & D_{yy}^{\infty} & 0 \\ 0 & 0 & D_{zz}^{\infty} \end{pmatrix} \tag{5.2}$$

where each non-zero diffusion component is calculated by

$$D_{xx}^{\infty} = \frac{1}{2}\frac{d}{dt}[\langle x^{na}(t)x^{na}(t)\rangle - \langle x^{na}(t)\rangle\langle x^{na}(t)\rangle], \tag{5.3a}$$

$$D_{xy}^{\infty} = \frac{1}{2}\frac{d}{dt}[\langle x^{na}(t)y(t)\rangle - \langle x^{na}(t)\rangle\langle y(t)\rangle], \tag{5.3b}$$

$$D_{yy}^{\infty} = \frac{1}{2}\frac{d}{dt}[\langle y(t)y(t)\rangle - \langle y(t)\rangle\langle y(t)\rangle], \tag{5.3c}$$

$$D_{zz}^{\infty} = \frac{1}{2}\frac{d}{dt}[\langle z(t)z(t)\rangle - \langle z(t)\rangle\langle z(t)\rangle], \tag{5.3d}$$

as $t \to \infty$. Here, and hereinafter, the angle brackets denote an ensemble average over all NPs in the system; x, y and z denote the absolute displacement of NP in three principal flow directions, $i.e.$, longitudinal, velocity-gradient, and vorticity direction, respectively.

The diffusivity tensor is symmetric, thus D_{xy}^{∞} and D_{yx}^{∞} are equal; D_{xz}^{∞} and D_{yz}^{∞} (and the transpose) are insignificant [189], which is also confirmed in our simulation. The non-affine displacement, x^{na}, is calculated by subtracting the absolute displacement with its affine component, x^a, *i.e.* $x^{na}(t) = x(t) - x^a(t)$, where $x^a(t) = \int_0^t \dot{\gamma} y(\tau) d\tau$ and $\dot{\gamma}$ is the imposed shear rate through LEbc. When calculating the absolute displacement of NPs that undergo a shift of position due to the LEbc, the particle reference position is shifted accordingly to subtract the shift effect. Particle displacements are followed every $\sim 0.06\ \dot{\gamma} t$ to ensure the growth of MSDs captured with adequate accuracy. For clarity, the superscript of the affine displacement and the expectation terms are both dropped in the MSD notations as follows.

5.2.4 Sensitivity to NP-RBC contact model

The NP-RBC short-distance interaction is through Morse potential that forbids NP from penetrating the RBC membrane. The potential parameters are adjusted to match the measured inter-cell potential energy, as discussed in [10]. The Morse potential function is given as

$$U_M(r) = D_e[e^{-2\beta(r-r_0)} - 2e^{-\beta(r-r_0)}], \ \ (r \leq r_0) \tag{5.4}$$

where r is the normal distance between the particle center to the RBC surface, r_0 is a cut-off distance in which no interaction forces are present, D_e is the potential well depth and β is a scaling factor. The surface energy is set to $D_e = 1 \times 10^7 k_B T$ and the equilibrium distance is set to $r_0 = a_1 + 10\ nm$. In figure 5.2, we explore the sensitivity of the NP diffusivity calculation to the adjustment of the Morse model parameters. Figure 5.2 (a) and (b) show the D_{yy}^{∞} and D_{zz}^{∞} calculation exhibits less than 5% variation when changing the magnitude of the energy and equilibrium distance, respectively, by up to $\pm 60\%$. This indicates the NP diffusion is largely driven by the hydrodynamic interaction rather than the direct contact between NP and RBC membrane.

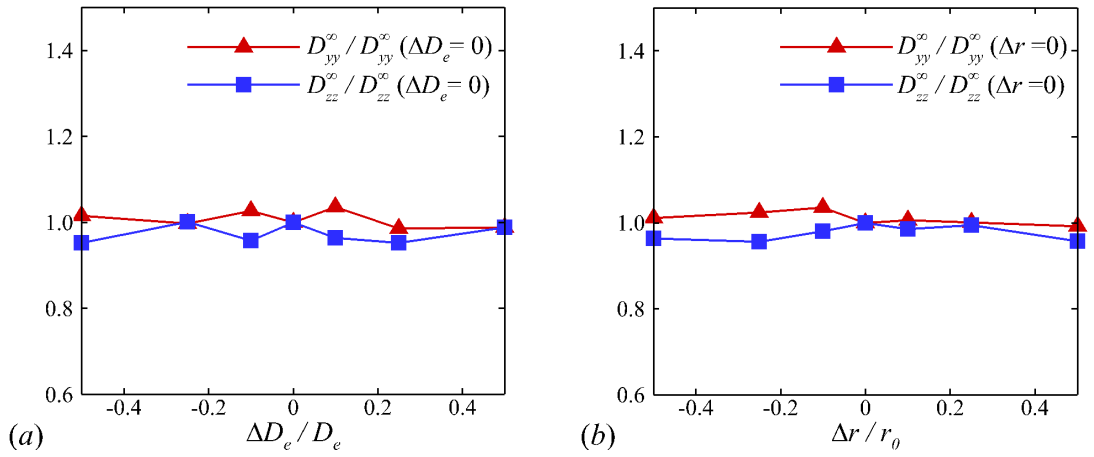

Figure 5.2: (a) NP long-time diffusivities in the cross-stream directions plotted against the relative variation of the Morse potential (a) well depth and (b) equilibrium distance.

5.2.5 Calculation of the partial pair distribution function

In the bidisperse RBC-NP suspension system, the NP-RBC partial pair distribution function (PPDF), $g_{21}(\boldsymbol{r})$, quantifies the conditional probability of finding a NP (species 1) at a position of $\boldsymbol{r}$ with respect to the geometric center of a single RBC (species 2). This quantity can be calculated as

$$g_{21}(\boldsymbol{r}) = \frac{1}{n_2}\left\langle \sum_{i\in LB}\sum_{j\in b} \frac{\delta(\boldsymbol{r}-\boldsymbol{r}_2^i+\boldsymbol{r}_1^j)}{n_1^i L_b^3}\right\rangle, \tag{5.5}$$

where L_b defines the cubic box size for PPDF sampling around one RBC, index j goes through all NPs within the local sampling box, and i goes through all RBCs in the computational LB domain. r_2^i and r_1^j denotes the position of RBC and NP, respectively. n_1^i shows the number concentration of NP within the sampling box, while n_2 denotes the number concentration of RBC in the entire domain. The angle bracket represents the ensemble average among independent realizations, which in the current case is through time averaging given the ergodic hypothesis. Similar techniques have recently been used in calculating PPDFs in bidisperse and polydisperse rigid particle suspensions [190, 191]. Projection of $g_{21}(\boldsymbol{r})$

to principal planes follows the integration procedure discussed in [192] but with a smaller integration interval, $[-a_2/4, a_2/4]$, to better capture the RBC morphological change.

The PPDF sampling box size for all cases is selected to be three times of the RBC maximum diameter at equalibrium in biconcave shape, $i.e.$, L_b=24 μm. To capture the PPDF in the long-time regime ($t\dot{\gamma}$>100) with detailed suspension microstructure, a total number of 300 strain units are employed for time averaging. In the short-regime ($t\dot{\gamma}\sim$1), owing to limited time steps associated with specific suspension configuration (e.g. the string ordered configuration), about 3 strain units are adopted for averaging.

5.3 Results and Discussion

In this section, we first formulate the simulations based on both physiological and numerical rationales. As follows, the transient growth of the NP mobility is discussed to understand the short-time response of the NP dispersive behavior at various hematocrit and shear rate. Then, focus will be shifted to understanding the NP long-time diffusive behavior under different hemorheological conditions with appropriate scaling, where the simulation results are also compared with available experimental data. To gain insight into the mechanisms governing the nonlinear hematocrit and shear-rate dependence of the NP diffusion tensor, we visualize the NP-RBC microstructure and carry out numerical experiments. Eventually, we construct empirical correlations for the complete NP diffusion tensor.

5.3.1 Problem formulation

The apparent diffusivity of NPs in unbounded blood flow under simple shear is determined by NP radius, a_1, shear rate, $\dot{\gamma}$, and hematocrit, ϕ, with NP concentration in the dilute regime. The relevant dimensionless parameters (besides ϕ) primarily include the NP Péclet number,

$$Pe = \frac{\dot{\gamma} a_1^2}{D^B}, \tag{5.6}$$

Table 5.1: Simulation data. Each case is simulated independently in a LB domain of size 128×128×80 at specified *Pe*, Ca_G and ϕ. NP long-time diffusivities, D^{∞}_{xx}, D^{∞}_{yy}, D^{∞}_{zz} and D^{∞}_{xy}, normalized by the theoretical Brownian diffusivity, D^B, are listed for all cases. The unlisted off-diagonal diffusivities, D^{∞}_{xz} and D^{∞}_{yz}, are found to be negligible. RBC has an effective radius of $a_2 = 2.9\ \mu m$, yielding a particle size ratio of $a_1/a_2 = 0.017$. Brownian diffusivity is calculated by $D^B = k_B T/6\mu\pi a_1$ at temperature $T = 310\ K$.

$\dot{\gamma}\ [s^{-1}]$	ϕ	N^{RBC}	N^{NP}	*Pe*	Ca_G	D^{∞}_{xx}/D^B	D^{∞}_{yy}/D^B	D^{∞}_{zz}/D^B	D^{∞}_{xy}/D^B
10	0.0	0	5 000	0.0066	0.0055	1.0	1.0	1.0	0.0
10	0.1	52	5 000	0.0066	0.0055	1.4	1.1	1.1	0.05
10	0.2	104	5 000	0.0066	0.0055	2.5	1.1	1.2	0.03
10	0.3	156	5 000	0.0066	0.0055	2.6	1.1	1.3	0.05
10	0.4	208	5 000	0.0066	0.0055	3.2	1.2	1.4	0.03
30	0.0	0	5 000	0.020	0.017	1.0	1.0	1.0	0.0
30	0.1	52	5 000	0.020	0.017	2.6	1.3	1.2	-0.1
30	0.2	104	5 000	0.020	0.017	4.8	1.6	1.3	-0.2
30	0.3	156	5 000	0.020	0.017	6.7	1.9	1.5	-0.2
30	0.4	208	5 000	0.020	0.017	7.2	2.0	1.8	-0.4
100	0.0	0	5 000	0.066	0.055	1.1	1.0	1.1	0.0
100	0.1	52	5 000	0.066	0.055	7.3	1.9	1.6	-0.6
100	0.2	104	5 000	0.066	0.055	14.5	2.9	2.0	-1.0
100	0.3	156	5 000	0.066	0.055	18.9	3.7	3.1	-1.3
100	0.4	208	5 000	0.066	0.055	29.2	4.1	3.8	-2.0
300	0.0	0	5 000	0.198	0.165	1.0	1.0	1.0	0.0
300	0.1	52	5 000	0.198	0.165	28.0	3.3	2.9	-2.2
300	0.2	104	5 000	0.198	0.165	67.9	5.7	3.7	-4.3
300	0.3	156	5 000	0.198	0.165	133.0	8.8	6.3	-7.6
300	0.4	208	5 000	0.198	0.165	216.4	10.8	8.0	-9.1
1 000	0.0	0	5 000	0.66	0.55	1.0	1.0	1.0	0.0
1 000	0.1	52	5 000	0.66	0.55	73.8	7.0	8.1	-10.1
1 000	0.2	104	5 000	0.66	0.55	211.1	12.5	10.5	-14.9
1 000	0.3	156	5 000	0.66	0.55	674.2	19.1	16.1	-26.9
1 000	0.4	208	5 000	0.66	0.55	2095.9	23.2	18.8	-38.1
2 000	0.0	0	5 000	1.32	1.10	0.9	1.0	1.0	0.0
2 000	0.1	52	5 000	1.32	1.10	122.8	12.5	15.6	-19.9
2 000	0.2	104	5 000	1.32	1.10	350.0	20.7	21.5	-25.7
2 000	0.3	156	5 000	1.32	1.10	1379.3	29.6	26.3	-50.0
2 000	0.4	208	5 000	1.32	1.10	4150.3	36.6	29.4	-82.8
10 000	0.0	0	5 000	6.60	5.52	1.1	1.0	1.0	0.0
10 000	0.1	52	5 000	6.60	5.52	606.7	40.9	77.3	-73.1
10 000	0.2	104	5 000	6.60	5.52	1363.7	44.9	86.4	-81.8
10 000	0.3	156	5 000	6.60	5.52	2788.5	64.0	110.8	-138.0
10 000	0.4	208	5 000	6.60	5.52	7575.6	80.4	120.3	-220.9

expressing the ratio of shear-induced diffusion to Brownian diffusion, and the RBC capillary number,

$$Ca_G = \frac{\mu\dot{\gamma}a_2}{G}, \tag{5.7}$$

quantifying the competition between the fluid viscous stress and the membrane elastic stress. Here, μ is the dynamic viscosity of suspending plasma, a_2 is the effective radius of RBC and G is the elastic shear modulus of the RBC membrane; D^B is the Brownian diffusivity, which is determined by the Stokes-Einstein relation, D^B=$k_BT/6\pi\mu a_1$, where k_B is Boltzmann's constant and T is the absolute temperature. The NP Péclet number quantifies the severity of the NP Brownian effect, while the RBC capillary number determines the deformability of the RBC capsule.

To obtain appropriate scaling relations, we performed a large number of independent 3D simulations. Table 5.1 lists all the simulation parameters and the measured NP diffusivities. A wide range of shear rate ($10 \leq \dot{\gamma} \leq 10\,000\ s^{-1}$) and hematocrit ($0 \leq \phi \leq 0.4$) with physiological relevance [124, 193] is covered. Cases with $\dot{\gamma}$=$10\,000\ s^{-1}$ are to match certain vascular pathological conditions, e.g., the high shear induced thrombosis [11]. For discussions in this section, NP size is set to $2a_1$=$100\ nm$. RBCs are assumed to be in healthy state with an effective radius a_2=$2.9\ \mu m$ and a membrane shear modulus G=$0.0063\ dynes/cm$. The absolute temperature is set to T=37 °C, at which the plasma has a viscosity μ=$1.2\ cP$ and a density ρ=$1.0\ g/cm^3$. The viscosity ratio of RBC cytoplasm to plasma is set to the physiological value λ=5.0. The density of cytoplasm is set to that of the plasma. The corresponding *Pe* and Ca_G lie in the range of $0.0066 \leq$*Pe*≤ 6.60 and $0.0055 \leq Ca_G \leq 5.52$, respectively. All simulations are formulated by matching the dimensionless group, $i.e.$, ϕ, *Pe* and Ca_G.

Simulations are initiated by imposing steady shear flow on the uniformly, randomly mixed NPs and RBCs at specific shear rate in a LEbc computational domain, as shown in figure 5.3 (a). The domain has a dimension of $128 \times 128 \times 80$ ($42.7 \times 42.7 \times 26.7\ \mu m^3$) in longitudinal ($x$), velocity-gradient ($y$) and vorticity ($z$) directions, respectively. This LB

domain size matches the highest resolution applied for the rheological characterization of cellular blood flow under shear by [7]. The selected LB grid resolution ($300\ nm$ per lattice unit) and the equilibrium RBC mesh size (1.5 lattice units per link length), has previously proven to be fine enough to capture both the single RBC dynamics [8, 3] and the rheological properties of concentrated cellular blood flow [8, 7].

To obtain converged long-time diffusivity, sufficient strains ($t\dot{\gamma}\sim 1\ 000$) and a large number of particles (5 000 NPs and up to 208 RBCs) are employed for each simulation. The resolution of these simulations in terms of strain units and number of particles is on the higher end compared to other numerical studies on particle diffusion in colloidal/non-colloidal suspensions [40, 41, 42, 182, 74, 183, 194]. As will be discussed in §5.3.3, the selected resolution produces good agreement between the simulation results and the available experimental data.

Simulations are performed on the Intel Xeon Skylake nodes of the TACC (Texas Advanced Computing Center) Stampede-2 system where each node features 48 cores and a 2.1 GHz clock rate. For the case at $\phi = 0.4$ with 208 RBCs and 5 000 NPs, each run takes $\sim$168 hours on 32 cores ($\sim$5 376 core hours) to accomplish 1 000 strains ($t\dot{\gamma}$). The total computational cost for the 35 independent cases listed in table 5.1 is approximately 140 000 core hours.

5.3.2 Temporal growth of NP transient mobility

To understand the short-time dispersive characteristics of the NP phase, we examine the transient behavior of NP mobility by tracking the temporal growth of NP MSDs. Cross-stream MSDs, $\langle y(t)y(t)\rangle/a_1^2$ and $\langle z(t)z(t)\rangle/a_1^2$, are sampled from the initial configuration ($t\dot{\gamma}$=0) where NPs and RBCs are randomly and uniformly mixed, as shown in figure 5.3 (a). Longitudinal and off-diagonal MSDs, $\langle x(t)x(t)\rangle/a_1^2$ and $\langle x(t)y(t)\rangle/a_1^2$, are sampled starting from a long-time configuration ($t\dot{\gamma}$=400) to avoid extra convective effect caused by the transient elongation and reorientation of RBCs. Such transient effects are found to

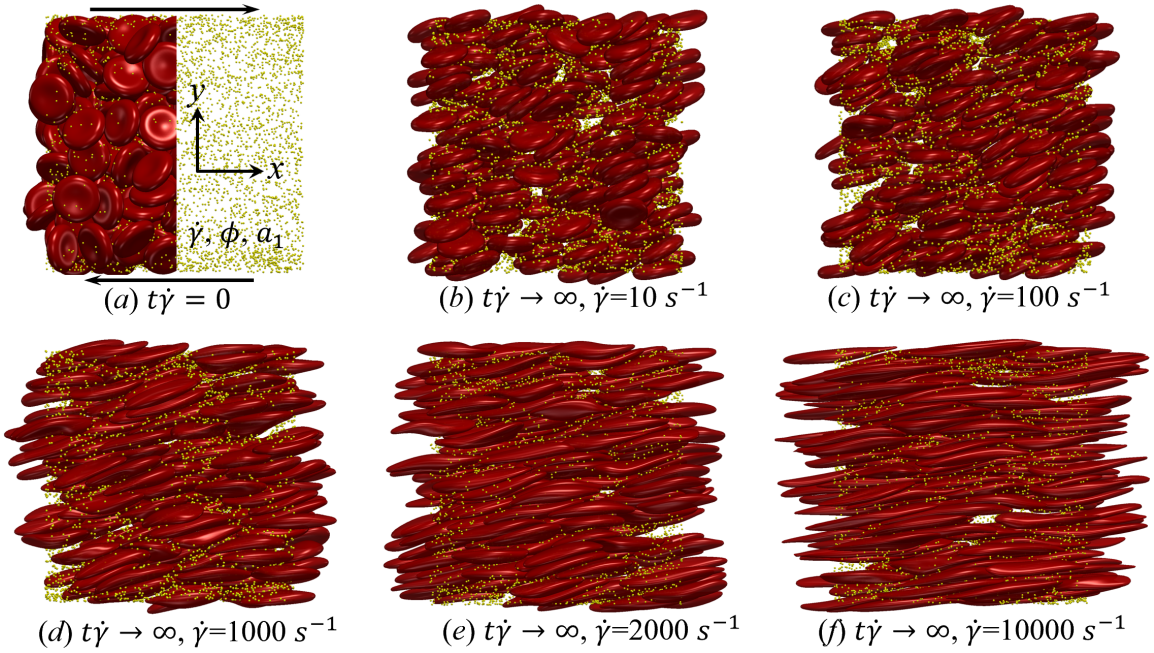

Figure 5.3: (a) The RBC-NP complex configuration at $t\dot{\gamma}$=0. NPs and RBCs are randomly and uniformly mixed in an unbounded shear flow. RBCs are shown partially in the domain to visualize the NP phase. The athermal system is determined by shear rate, $\dot{\gamma}$, hematocrit, ϕ and NP radius, a_1. (b-f) The RBC-NP complex configuration in the long-time scale regime under a shear rate of $\dot{\gamma}$ = (b) 10, (c) 100, (d) 1 000, (e) 2 000 and (f) 10 000 s^{-1} with $\phi = 0.4$.

introduce extra affine displacement leading to $\sim t^3$ growth of MSDs and hence jeopardize the measurement of the long-time diffusivity in the x-relevant directions. The necessity of eliminating affine effect for calculating streamwise diffusivities is elaborated by [41] in the context of sheared colloidal suspensions.

Figure 5.4 plots the particle normalized MSDs growth with respect to the relative strains sampled. At ϕ=0, all diagonal MSDs grow according to the Stokes-Einstein (SE) prediction with no dependence on shear rate, while off-diagonal MSD produces zero value (not shown). This is consistent with the isotropic nature of NP Brownian motion in a dilute and unbounded solution, and also serves as a verification of the MSD calculations. At $\phi>0$, a deviation from SE relation occurs in all diagonal MSDs as a result of NP-RBC interactions. At the $\dot{\gamma}$=10 s^{-1}, only slight deviation from SE relation is observed given the dominance of Brownian diffusion; see figure 5.4 (a).

The transient deviation of NP mobility from the SE relation can be further interrogated through the evolution of cross-stream MSDs, as depicted in figure 5.4 (a-d, g-h). In the short-time regime ($t\dot{\gamma}\ll 1$), a linear growth of MSD ($\sim t$) is observed particularly under low shear rate (e.g. $\dot{\gamma}\leq$100 s^{-1}) or high shear rate and high hematocrit (e.g. $\dot{\gamma}\geq$2000 s^{-1} and ϕ=0.4) condition, as shown in figure 5.4 (b) and (c), respectively. The short-time linear growth of MSD suggests a short-time diffusive mechanism. Since the short-time linear growth of MSD always occurs before the ballistic regime ($\sim t^2$) where RBC-NP collisions start to occur, such short-time diffusive driver should logically be the Brownian effect. Therefore, the initial linear MSD growth at low shear rates (with ϕ=0$\sim$0.4) or high shear rates (with ϕ=0.4) can be explained by the Brownian diffusive time scale being much shorter than the RBC-NP collision time scale under such hemorheological conditions. However, under high shear rate (e.g. $\dot{\gamma}\geq$2000 s^{-1}), the diffusive behavior ($\sim t$) turns to ballistic ($\sim t^2$) as ϕ increase to 0.4; see figure 5.4 (c,d,g,h). This is likely due to the high convective (high shear rate) and low inertial (low hematocrit) effects that reduce the RBC-NP collision time scale to be comparable to the Brownian diffusion time scale. As

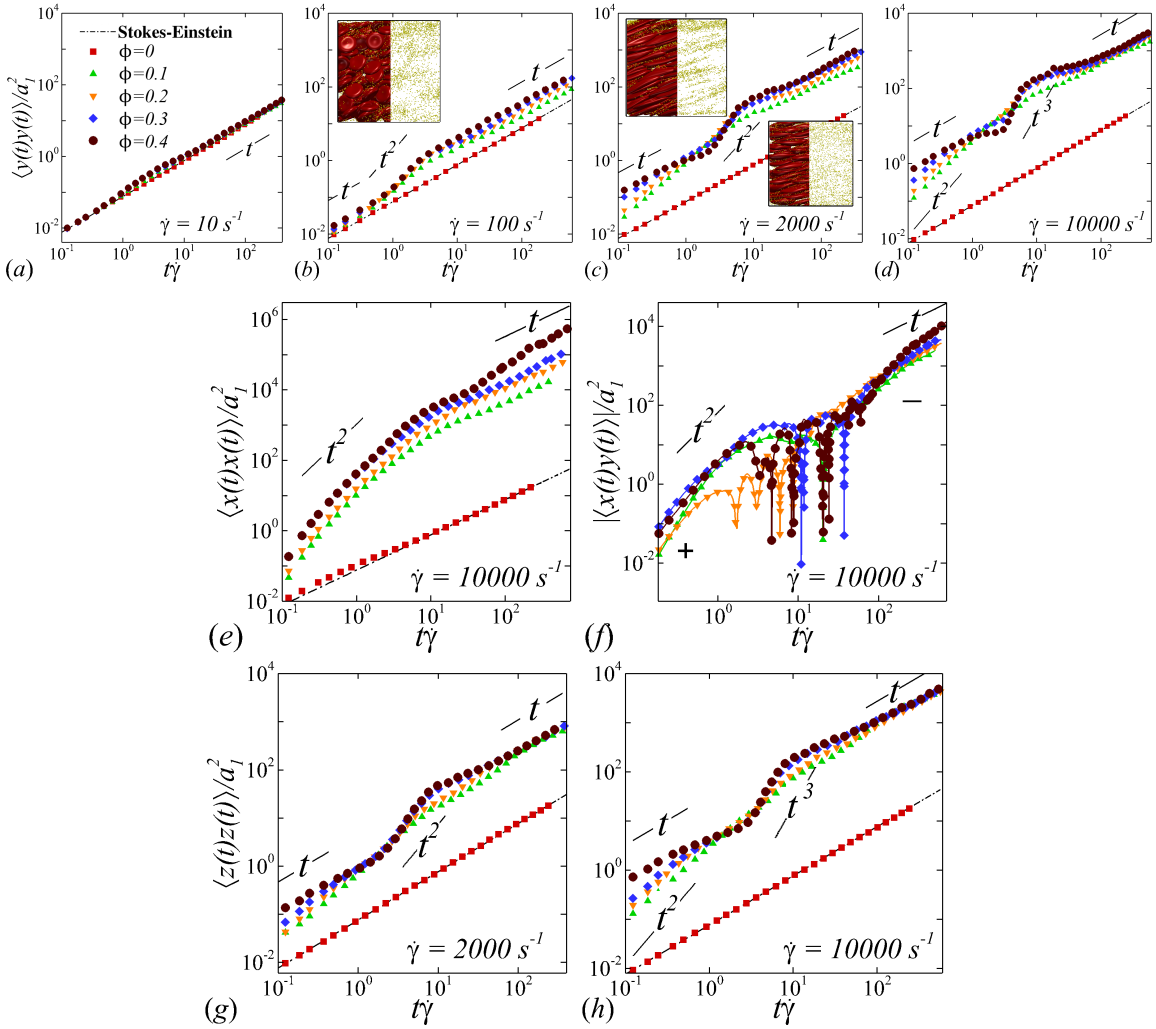

Figure 5.4: Normalized MSDs plotted against relative shear strains in logarithm scale at various hematocrits for different shear rate. (a), (b), (c) and (d) are concerned with evolutions of $\langle y(t)y(t)\rangle/a_1^2$; (e) and (f) depict evolutions of $\langle x(t)x(t)\rangle/a_1^2$ and $|\langle x(t)y(t)\rangle|/a_1^2$, respectively; (g) and (h) depict evolutions of $\langle z(t)z(t)\rangle/a_1^2$. The imposed shear rate is denoted on each plot. Inset of (b) shows the RBC-NP distribution at $t\dot{\gamma}\sim1$ under $\dot{\gamma} = 100s^{-1}$. Insets of (c) shows the RBC-NP distribution at $t\dot{\gamma}\sim1$ (upper) and $t\dot{\gamma}\sim100$ (lower) under $\dot{\gamma} = 2000s^{-1}$ and $\phi = 0.4$. A NP radius of a_1=50 nm is used for normalization. Cross-stream MSDs (a-d) and (g,h) are sampled starting from $t\dot{\gamma}$=0 to capture the transient NP dispersive behavior; stream-wise and off-diagonal MSDs are sampled starting from $t\dot{\gamma}$=400 to avoid the initial extra affine displacement induced by RBC elongation and orientation.

a result, the Brownian diffusion of NP is overwhelmed by the ballistic behavior caused by insufficient RBC-NP collisions.

In the intermediate-time regime, $t\dot{\gamma}$=$O(1)\sim O(10)$, anomalous dispersive behavior is observed as RBCs start to elongate and rotate to be aligned with the streamwise direction due to shear. For cases at high shear rates ($\dot{\gamma}\geq$2 000 s^{-1}) and high hematocrit ($\phi = 0.4$), we observe a sublinear growth of MSD, representing a temporary hindrance of the NP mobility. This hindrance effect is caused by a string-ordered microstructure of NP in the shearing plane accompanied by the elongation and alignment of RBCs; see the contrast between upper inset of figure 5.4 (c) and inset of figure 5.4 (b). Such string-ordered NP distribution can be better visualized by plotting the RBC-NP partial pair distribution function (PPDF), $g_{21}(\boldsymbol{r})$, projected on the xy plane (the computing procedure of PPDF in the short-time regime is discussed in §5.2.5). As shown in figure 5.5, $g_{21}(\boldsymbol{r})$ in xy plane exhibits streaks showing intensified distribution particularly near the RBC surface under high shear rate and high hematocrit, while in contrast no significant string structure is found in low shear rate ($\dot{\gamma}\leq$100 s^{-1}) or/and low hematocrit ($\phi = 0.1$) cases, as shown in figure 5.5 (a-c). Note that suspension string-like structure often occurs in sheared monodisperse colloidal suspensions at equilibrium as a consequence of the absence of interparticle lubrication interactions at high concentration [195, 41] or the presence of long-range repulsive forces at low concentration [196]. However, in the current case, ordering of NP occurs at a non-equilibrium state that involves the change of the RBC suspension structure from a uniformly distributed and randomly oriented configuration to a streamwise-aligned and elongated configuration under high shear and high hematocrit. The sublinear growth of MSD is followed by a super-ballistic behavior ($\sim t^3$) at high shear rate ($\dot{\gamma}$=10 000 s^{-1}), which might be associated with the large jump of NP between strings when the NP phase gradually evolves from the string-like structure towards the more uniform structure featuring in the long-time diffusive regime.

In the long-time regime ($t\dot{\gamma}>100$), MSD reaches the second linear-growth stage ($\sim t$),

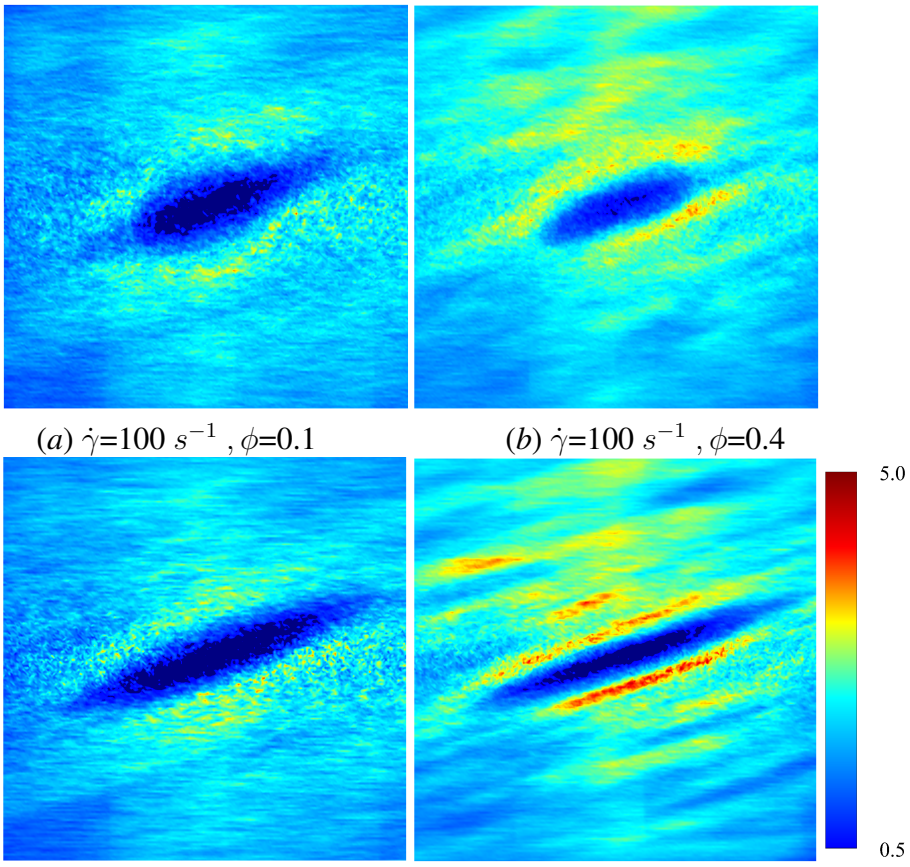

(*a*) $\dot{\gamma}$=100 s^{-1} , ϕ=0.1 (*b*) $\dot{\gamma}$=100 s^{-1} , ϕ=0.4

(*c*) $\dot{\gamma}$=2000 s^{-1} , ϕ=0.1 (*d*) $\dot{\gamma}$=2000 s^{-1} , ϕ=0.4

Figure 5.5: RBC-NP partial pair distribution function, $g_{21}(\boldsymbol{r})$, projected on the xy plane under various hemorheological conditions. The results are sampled through temporal averaging in the strain range of $t\dot{\gamma}$=1$\sim$3.

where RESID becomes the dominate diffusive mechanism leading to an uniform distribution of NP (see lower inset of figure 5.4 (c)). Such three-stage (diffusive/super-ballistic/diffusive) anomalous dispersion behavior has previously been reported in the dispersion of Brownian particles subjected to external forces [197]. Here, we show that such dispersive anomalies also occur in a sheared NP-RBC bidisperse suspension, where the anomalous NP dispersion is, however, driven by an internal shear-induced mechanism, $i.e.$, the elongation and the alignment of the concentrated RBCs along streamwise direction under high shear. Such transient shear-induced morphological adaptation of RBCs contributes to extra mobility of the NP phase, seemingly playing a role of external forces exerted on the NP phase.

Figures 5.4 (e, f) depict the longitudinal and off-diagonal MSD evolution at $\dot{\gamma}$=10 000 s^{-1}.

Results for lower shear rate show similar MSD behaviors and are not presented for discussion. Because the initial transient regime is neglected, the longitudinal and off-diagonal MSDs yield classical ballistic-diffusive transitions similar to the dispersive behavior of rigid particle suspensions under shear [40, 74]. The off-diagonal MSD under high shear starts with positive values during the ballistic regime, exhibits a crossover transition involving a change of sign, and eventually maintains negative values in the diffusive regime. Absolute values are shown for the off-diagonal MSDs with the sign at certain temporal stage denoted in figure 5.4 (f). The change of sign from positive (+) to negative (-) is a hallmark of the dominant NP migration direction shifted from along the extensional axes (1st and 3rd quadrants) to along the compressive axes (2nd and 4th quadrants) of the flow, as also observed in sheared colloidal suspensions [40].

5.3.3 Hemorheological dependence of NP long-time diffusivity

In this section, we focus on examining the NP long-time diffusive behavior. The NP long-time diffusivities are evaluated in the long time regime (after 100 strain units) and listed in table 5.1. Experimental statistics from various sources [12, 198, 116, 181] are selected for comparison to gain credibility of the simulation results. Given the distinct time scales associated with the Brownian ($\tau_B \sim 10^{-4}\ s$) and the long-time RBC-enhanced diffusion ($\tau_R \sim 100/\dot{\gamma}$) phenomenon, the coupling of BD and RESID follows simple superposition, $D_{ij}^{\infty} = D_{ij}^{R} + D^{B}\delta_{ij}$, as confirmed in previous studies, e.g., [24], where D_{ij}^{R} denotes the RESID. Since D^B at infinite dilution follows SE relation with negligible dependence on flow conditions, the hemorheological response of D_{ij}^{∞} is essentially determined by D_{ij}^{R}.

Shear-rate dependence

Figure 5.6 plots the normalized RESID, $\hat{D}_{ij}^{R} = D_{ij}^{\infty}/D^{B} - \delta_{ij}$ against normalized shear rate, *Pe* (or Ca_G). To first validate the simulation results, experimental results of solute or cell velocity-gradient (yy) diffusivity in sheared human or animal blood are selected for

comparison; see figure 5.6 (b). [181] measured the augmentation of ferricyanide solute diffusivity in both bovine and human RBC suspensions using a rotating Couette flow device. [116] measured the enhanced radial diffusivity of oxygen solute in human blood using a tube oxygenator device. [12] calculated the platelet velocity-gradient diffusivity in cavine blood flowing through a channel by measuring the platelet rate of adhesion/deposition to a foreign surface attached to the flow chamber. Similar experiment was later conducted by [198] to measure the platelet radial diffusivity in human blood. These measured diffusivity in 40% hematocrit normalized based on our notation compares favorably with the calculated $\hat{D}^R_{yy}$ at ϕ=0.4 based on the simulation, as shown in figure 5.6 (b).

Depending on the level of shear rate imposed at various hematocrit, the diffusion tensor of NP in sheared blood shows different shear-rate dependence. At low shear rates ($\dot{\gamma}\leq$100), all RESID terms exhibit linear dependence on shear rate ($\sim\dot{\gamma}$), matching the linear $\dot{\gamma}$ scaling of shear-induced diffusivity in rigid particle suspensions [40, 42]. This is also consistent with the insignificant RBC morphological changes at $\dot{\gamma}\leq 100\ s^{-1}$, as shown in figures 5.3 (a-c).

At intermediate shear rates ($100\leq\dot{\gamma}\leq 2\,000$), significant streamwise elongation of RBCs occurs with increasing shear rate; see figure 5.3 (c-e). As a result, nonlinear $\dot{\gamma}$ scaling is observed in all diagonal RESID terms. Specifically, cross-stream diffusivities, $\hat{D}^R_{yy}$ and $\hat{D}^R_{zz}$, show sublinear scales ($\sim\dot{\gamma}^m$, m=$0.7\sim0.8$), while streamwise diffusivity, $\hat{D}^R_{xx}$, exhibits superlinear scales ($\sim\dot{\gamma}^n$, n=$1\sim1.8$). In contrast to the nonlinear scaling in diagonal diffusivities, $\hat{D}^R_{xy}$ maintains largely a linear scale at the intermediate shear-rate regime, as shown in figure 5.6 (d). It is also noted that such nonlinear shear-rate scaling in diagonal RESID terms is most prominent at intermediate to high hematocrit ($\phi>0.1$), which implies the RBC deformability plays less important role in altering the RESID shear-dependence at low hematocrits. This observation is consistent with the results of shear-augmented solute diffusivity in model-RBC suspensions at various RBC deformability reported by [181], where they found changing RBC deformability barely affects the augmentation at particle volume

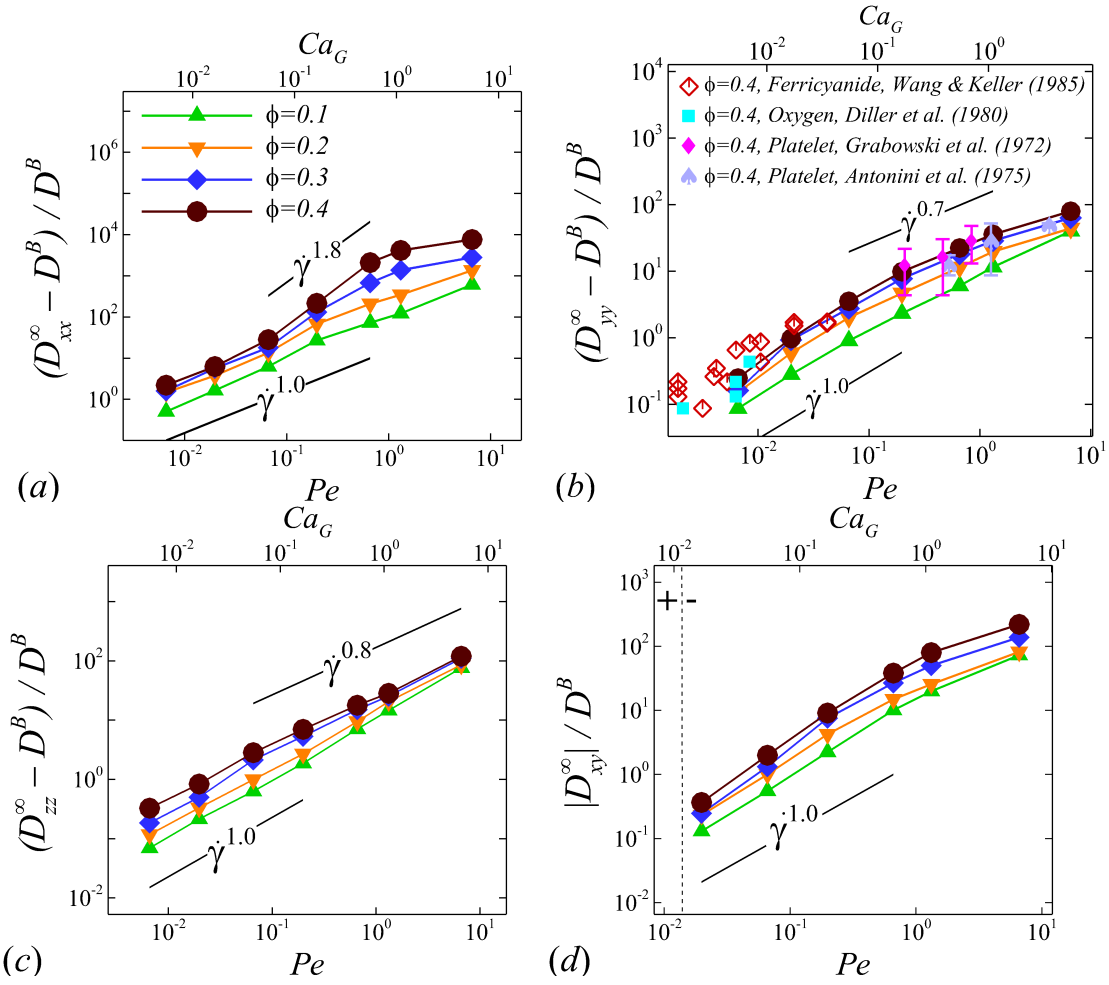

Figure 5.6: Normalized particle long-time RESID in (a) xx, (b) yy, (c) zz and (d) xy directions against normalized shear rate (*Pe* or Ca_G) in a log-log scale. Each curve at specific ϕ forms by connecting $\hat{D}^R_{ij}$ data at shear rate, $\dot{\gamma}$ =10, 30, 100, 300, 1000, 2000 and 10 000 s^{-1}, from left to right; $\hat{D}^R_{xy}$ at $\dot{\gamma}$=10 s^{-1} is not shown for scaling purpose due to its small magnitude. Experimental results for RBC enhanced solute [116, 181] and platelet [12, 198] diffusivity in the velocity gradient (yy) direction are plotted for comparison. NPs of size $2a_1$=100 nm yield D^B=3.78 $\mu m^2/s$.

concentration of 0.1 or less. [181] also find a sublinear scaling of $\sim\dot{\gamma}^{\beta}$ ($0.67\leq\beta\leq0.89$) for the solute diffusivity in velocity-gradient directions, while our simulations observe a exponent of β=0.7.

At high shear rates ($\dot{\gamma}\geq2\ 000$) and intermediate to high hematocrit ($\phi>0.1$), all RESID terms except $\hat{D}^R_{zz}$ exhibit reduced shear-rate dependence compared to the intermediate shear-rate regime. In the velocity-gradient (y) direction, the hindrance of diffusion is due to the fact that the concentrated RBCs become more aligned and elongated with flow such that RBCs act as obstacles against the NP cross-stream diffusion in y-direction; see figure 5.3 (f). Such effect however shows less hindrance on $\hat{D}^R_{zz}$, as it does not forbid the NP migration in the vorticity (z) direction. In the streamwise (x) direction, the reduction of the shear dependence of $\hat{D}^R_{xx}$ is likely to be associated with the saturation of the RBC elongation. Owing to the compound effects in both x and y directions, the off-diagonal diffusivty, $\hat{D}^R_{xy}$, also exhibit certain reduction of the shear-rate dependence.

hematocrit dependence

Figure 5.7 display the same data as figure 5.6 but plotted against ϕ to show the hematocrit dependence of RESID at different shear rate. At low shear rates ($\dot{\gamma}\leq100$), all diffusion terms manifest a linear ϕ scaling. Note that linear concentration dependence of particle self-diffusivity has been observed in sheared monodisperse suspensions in the presence of surface roughness [199] or residual Brownian motion [189], which causes the two-body interaction being irreversible and hence giving rise to a diffusive behavior. Since the shear-induced diffusion of NP is driven by NP-RBC interaction, it is likely that the ϕ scaling of NP diffusion tensor results from the irreversible two-body interaction between NP and RBC induced by the RBC membrane roughness/flexibility and the NP Brownian effect. The off-diagonal diffusivity $\hat{D}^R_{xy}$ is found to be positive (+) at very low shear rate ($\dot{\gamma}\leq10\ s^{-1}$) and otherwise negative (-). The change-of-sign behavior of the off-diagonal diffusivity designate the dominant displacement direction of NP changing from along the extensional

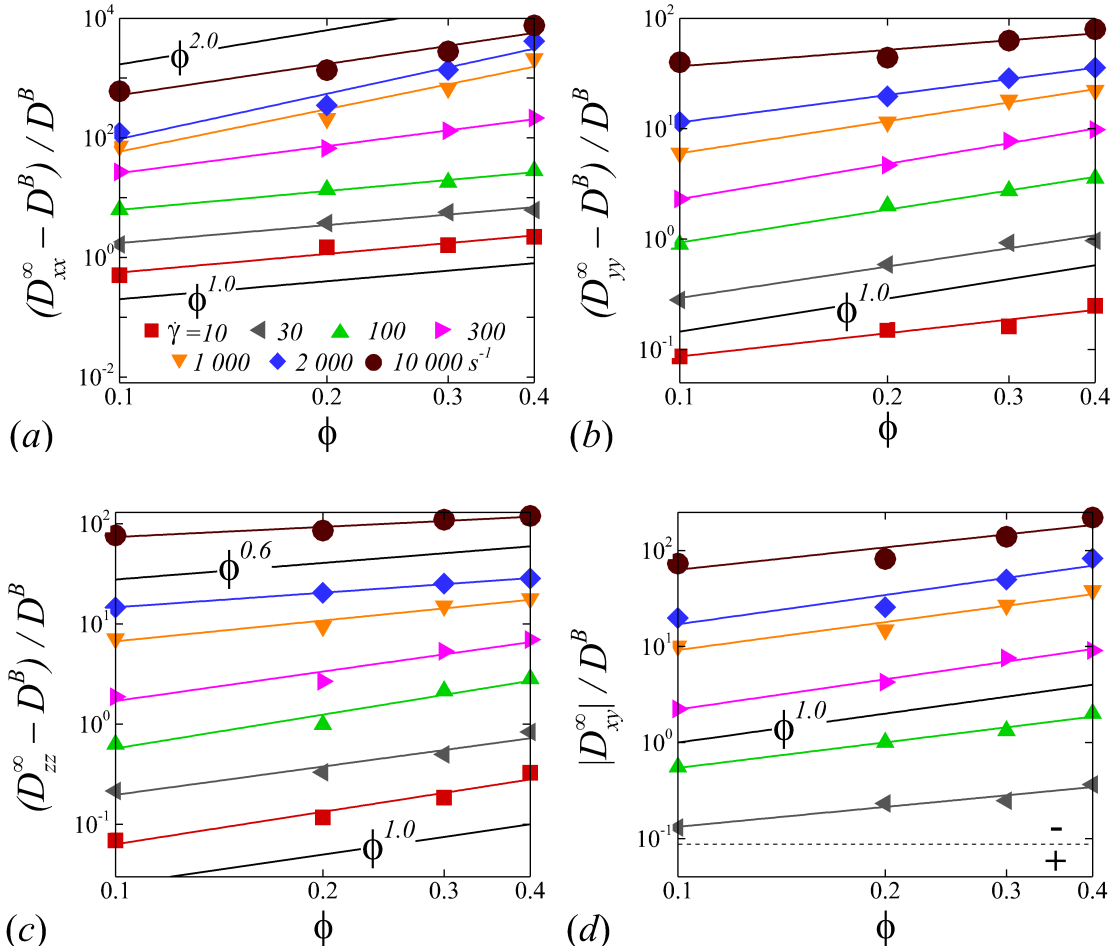

Figure 5.7: Normalized particle long-time RESID in (a) xx, (b) yy, (c) zz and (d) xy directions against hematocrit under different shear rate in logarithm scale. Lines are the best power-law fits to the data points at specific $\dot{\gamma}$. $\hat{D}^R_{xy}$ at $\dot{\gamma}$=10 s^{-1} (not shown) is positive with negligible magnitude compared to other diffusion terms. NPs of size $2a_1$=100 nm yield D^B=3.78 $\mu m^2/s$.

axes to along the compressive axes of the flow as shear rate increases. Similar observation has been reported in sheared monodisperse colloidal suspensions [40].

As shear rate grows above 100 s^{-1}, various ϕ scaling arises in different RESID components. $\hat{D}^R_{xx}$ exhibits a quadratic ϕ scaling ($\sim\phi^2$), which suggests that in the x-direction additional effects exist to drive the NP diffusive motion besides the irreversible pairwise interactions. $\hat{D}^R_{yy}$ and $\hat{D}^R_{xy}$ scale linearly with ϕ, suggesting the irreversible pairwise interaction remains to be the dominant diffusive mechanism. $\hat{D}^R_{zz}$ exhibits a transition from linear to sublinear ϕ scale ($\sim\phi^{0.6}$). The mostly linear ϕ scale in $\hat{D}^R_{yy}$ observed in the current numerical study is consistent with the experimental observation in [181], where they show that the solute diffusivity in the velocity-gradient (y) direction is augmented by about three folds when the particle concentration increases from 0.1 to 0.31. Since suspension viscosity typically increases with the particle concentration [41], the enhancement of solute (e.g. NP) diffusivity at increased ϕ indicates the RESID is due to the RBC-NP interaction rather than the secondary flow effect [181].

5.3.4 Microstructure

The rheological properties of particle suspensions are often determined by the mechanistic phenomenon occurred on the particle length scales. To elucidate the physical mechanisms that govern the hemorheological scaling behaviors of the NP diffusion tensor observed in §5.3.3, the RBC-NP PPDF, $g_{21}(\boldsymbol{r})$, in the long-time regime are plotted to visualize the configurational microstructure of the RBC-NP bidisperse suspension under various hematocrit and shear rate. The techniques used to compute and project $g_{21}(\boldsymbol{r})$ are discussed in detail in §5.2.5.

Figure 5.8 presents a matrix of $g_{21}(\boldsymbol{r})$ projections onto the velocity-velocity gradient (xy) plane, the velocity-vorticity (xz) plane and the velocity gradient-vorticity (yz) plane under two shear rates ($\dot{\gamma}$=100 or 2000 s^{-1}) and two hematocrits (ϕ=0.1 or 0.4). In general, all PPDFs feature a large-scale rhombus shape as opposed to typical circular shape com-

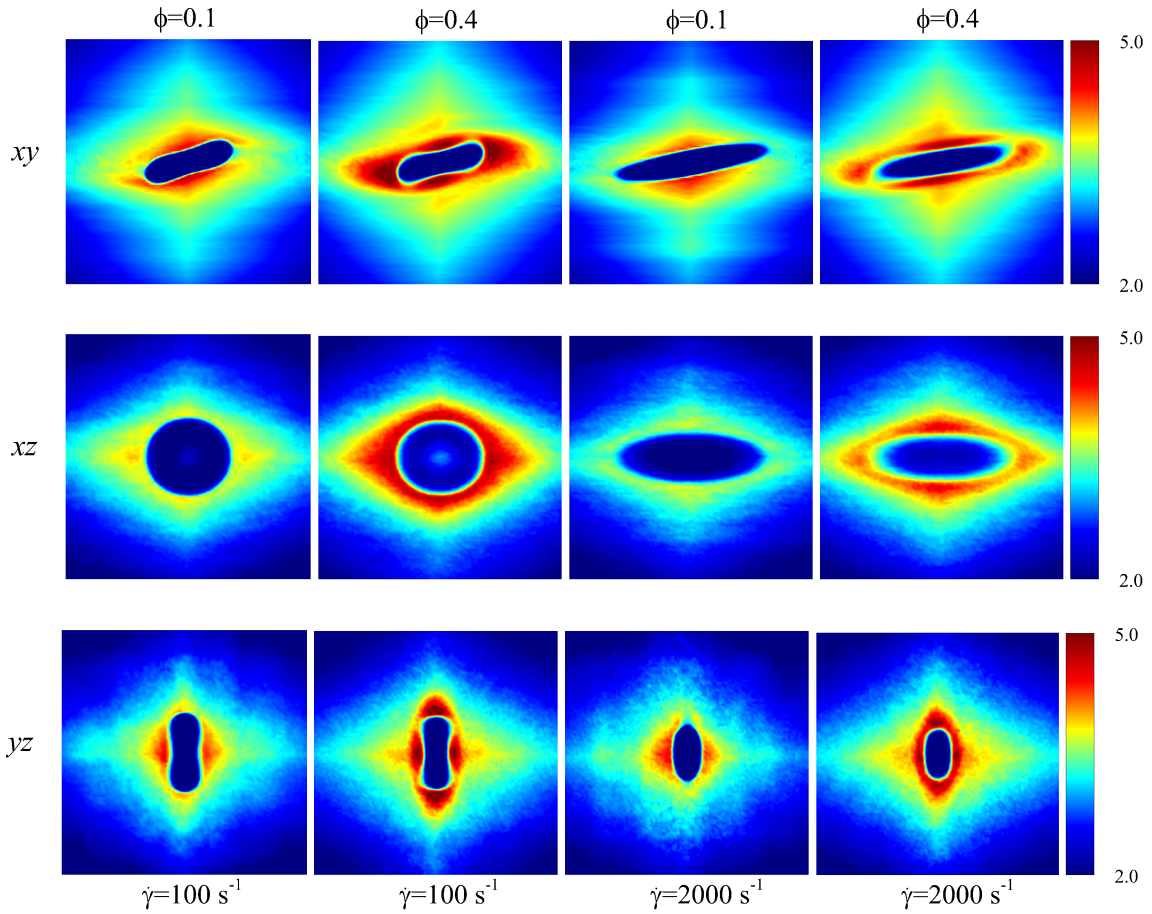

Figure 5.8: RBC-NP partial pair distribution function, $g_{21}(\boldsymbol{r})$, projected onto the xy, xz and yz planes in the long-time regime under various hemorheological conditions, where the PPDF contour has the horizontal edge aligned with the first axis (e.g., xy PPDF contour has the horizontal edge aligned with x axis.). The edge length of the sampling box for computing $g_{21}(\boldsymbol{r})$ is three times of the maximum diameter of the undeformed RBC.

monly observed in rigid-sphere-particle suspensions [93, 190, 191]. This can be attributed to the disk-shape of RBC that causes geometry-specific anisotropy of the microstructure. The average RBC shapes under various hemorheological conditions, as shown in the central low-intensity region of the PPDF contours, are nicely captured through the PPDF sampling procedure. All PPDFs considered in the xy plane show more intensified distribution ($i.e.$, higher probability of RBC-NP interaction) near the RBC disk surfaces, of which the surface normal directions are more aligned with the compressive axes (in 2nd and 4th quadrants) in accordance with the negative values of $\hat{D}^R_{xy}$. In the xz and yz plane, the PPDF distribution tends to be symmetric about the principal axes (x, y or z), which explains the zero values of the xz and yz diffusivities.

As the hemorheological condition changes, the detailed configuration of the PPDF within the rhombus structure also varies. At low hematocrit (ϕ=0.1), the xy PPDF shows fore-aft low intensity similar to rigid particle suspensions [192]. However, the break of the fore-aft symmetry, being different from the rigid particle suspensions, seems to be related to the RBC orientation algned with the extensional flow axes that is further caused by the tank-treading motion of the RBC membrane [7]. As the hematocrit increases to ϕ=0.4, the overall PPDF around the RBC becomes more intensified, meaning the local NP concentration near RBC surface increases. More interestingly, the fore-aft low PPDF region observed under low hematocrit gets intensified substantially. The change of the NP microstructure with increased hematocrit can be explained by smaller inter-cell separation and hence NP getting squeezed in a smaller inter-cell region. At low shear rate ($\dot{\gamma}$=100 s^{-1}), RBC shows a close-to-equilibrium biconcave shape. Increasing shear rate to $\dot{\gamma}$=2 000 s^{-1} results in a significant elongation of the average RBC shape in the flow (x) direction accompanied by certain contraction in the velocity-gradient (y) and vorticity (z) directions.

The above configurational changes of $g_{21}(\boldsymbol{r})$ under various shear rates and hematocrits provide possible mechanistic explanations for the nonlinear ϕ dependence observed at high shear rates, as discussed in §5.3.3. The quadradic dependence of $\hat{D}^R_{xx}$ ($\sim\phi^2$), shown in

figure 5.7 (a), is likely due to the occurrance of three-body RBC-NP interactions in the longitudinal (x) direction caused by the compound effect of the elevated NP concentration at the RBC fore-aft surface and the elongation of the RBC in the x direction. The reduced ϕ dependence in $\hat{D}^R_{zz}$ at high shear rate, as shown in figure 5.7 (c), can be attributed to the relatively large contraction of the RBC in the vorticity direction, which reduces the effective ϕ in the z direction. The less reduction of the ϕ dependence in the y direction, as shown in figure 5.7 (c), is owing to the y direction contraction of RBC under shear being less significant than that in the z direction, as clearly indicated in the PPDF contours.

5.3.5 Role of RBC deformability

The above PPDF analysis shows prominent RBC morphological change with elevated shear rate, which suggests the RBC deformability may play an important role in causing the nonlinear $\dot{\gamma}$ dependence of the NP diffusion tensor. In this section, we perform numerical experiments to further quantitatively explain the nonlinear $\dot{\gamma}$ scaling of RESID in the intermediate shear-rate regime ($100 \leq \dot{\gamma} \leq 2\,000\ s^{-1}$), as observed in §5.3.3. Changing shear rate alters both the fluid inertia and RBC deformability, quantified by *Pe* and Ca_G, respectively. To interrogate the isolated effect of RBC deformability (Ca_G), we fix Ca_G by scaling up G while increasing *Pe* (through increasing $\dot{\gamma}$). Two Capillary numbers, Ca_G=0.055 and 0.55, are considered corresponding to the Ca_G regime where the nonlinear shear-rate dependence of RESID occurs. For these simulations, we select a fixed hematocrit of ϕ=0.4 and a NP size of $2a_1$=$100\ nm$. Table 5.2 lists all parameters and the NP diffusivity values for the cases tested.

As presented in figure 5.9 (a, b), instead of exhibiting nonlinear *Pe* scaling as observed in 5.3.3, all RESID components show linear dependence on *Pe* at fixed RBC capilary number of Ca_G=0.55 or 0.055 across the wide range of shear rates. This recovers the linear *Pe* dependence of solute/self-diffusivity in sheared rigid particle suspensions [178, 40, 42] since we intentionally fix the RBC deformation (Ca_G) while adjusting *Pe*.

Table 5.2: Simulation data for numerical experiments concerning the isolated RBC deformation effect in NP-RBC suspensions. The RBC membrane shear modulus, G, is re-scaled to numerically match specific Ca_G while changing shear rate. Here, the NP size is fixed to $2a_1$=100 nm RBC has an effective radius of a_2=2.9 μm. Brownian diffusivity is calculated by D^B=$k_BT/6\mu\pi a_1$ at a temperature of T=310 K.

$\dot{\gamma}$ $[s^{-1}]$	ϕ	N^{RBC}	N^{NP}	Pe	Ca_G	D^{∞}_{xx}/D^B	D^{∞}_{yy}/D^B	D^{∞}_{zz}/D^B	D^{∞}_{xy}/D^B
10	0.4	208	5 000	0.0066	0.055	3.4	1.2	1.2	0.06
100	0.4	208	5 000	0.066	0.055	29.2	4.1	3.8	-2.0
1 000	0.4	208	5 000	0.66	0.055	317.6	31.6	23.8	-36.1
10 000	0.4	208	5 000	6.60	0.055	2999.8	286.9	248.6	-416.0
10	0.4	208	5 000	0.0066	0.55	14.6	1.1	1.1	0.35
100	0.4	208	5 000	0.066	0.55	247.6	3.3	2.6	-1.66
1 000	0.4	208	5 000	0.66	0.55	2095.9	23.2	18.8	-38.1
10 000	0.4	208	5 000	6.60	0.55	31698.3	209.0	158.3	-499.3

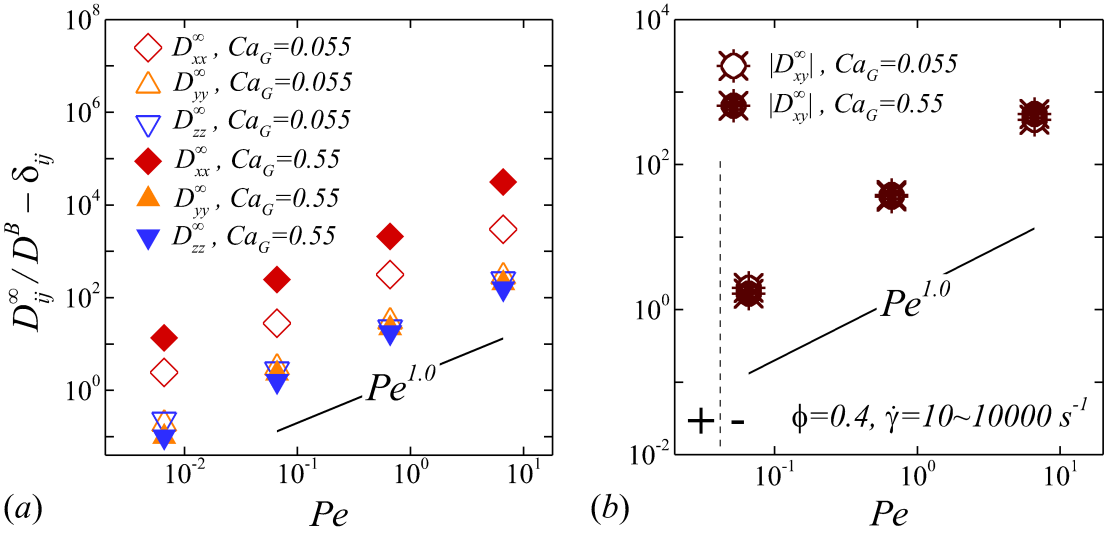

Figure 5.9: The *Pe* dependence of the (a) diagonal and (b) off-diagonal RESID terms at fixed capillary number (by rescaling G) with ϕ=0.4. Two RBC capillary numbers, Ca_G=0.55 and 0.055, are considered to see the isolated effect of changing RBC deformability (Ca_G) or adjusting the inertial effect (*Pe*).

Table 5.3: Simulation data for numerical experiments concerning the relevant length scale in NP-RBC suspensions. NP size is varied in the range of $2a_1$=50$\sim$800 nm. RBC has an effective radius of a_2=2.9 μm. Brownian diffusivity is calculated by D^B=$k_BT/6\mu\pi a_1$ at temperature T=310 K. For the 800 nm case, the number of NP is set to 500 to satisfy the dilute condition for the NP volume fraction. The last three cases are performed with adjusted G to fix Ca_G. The hematocrit of $\phi = 0.2$ corresponds to 104 RBCs in the LB domain.

$\dot{\gamma}$ $[s^{-1}]$	ϕ	a_1/a_2	N^{NP}	Pe	Ca_G	D^{∞}_{xx}/D^B	D^{∞}_{yy}/D^B	D^{∞}_{zz}/D^B	D^{∞}_{xy}/D^B
1 000	0.2	0.017	5 000	0.66	0.55	211.1	12.5	10.5	-14.9
1 000	0.2	0.034	5 000	5.28	0.55	801.1	26.3	21.9	-34.1
1 000	0.2	0.069	5 000	42.28	0.55	1491.9	53.3	38.1	-64.7
1 000	0.2	0.14	500	338.23	0.55	3309.1	106.9	84.9	-186.8
10	0.2	0.017	5 000	0.0066	0.55	3.1	1.0	1.1	0.2
100	0.2	0.017	5 000	0.066	0.55	40.9	2.3	1.8	-1.3
10 000	0.2	0.017	5 000	6.60	0.55	6109.4	113.0	102.2	-270.5

Moreover, an increase of Ca_G (from 0.055 to 0.55) leads to an increase of $\hat{D}^R_{xx}$ but a decrease of $\hat{D}^R_{yy}$ and $\hat{D}^R_{zz}$, as shown in figure 5.9 (a). These results are direct evidence indicating that the nonlinear shear-rate scaling of the diagonal RESID terms observed in §5.3.3 is due to the variation of RBC deformability (Ca_G) induced by changing shear rate at fixed G. More specifically, the increase of Ca_G with increasing shear rate at 100<$\dot{\gamma}$<2 000 s^{-1} under fixed G leads to the superlinear shear-rate dependence of longitudinal diffusivity and meanwhile the sublinear dependence of cross-stream diffusivities. In figure 5.9 (b), the off-diagonal diffusivity shows insignificant change at different Ca_G, in consistency with its mostly linear shear-rate dependence shown in figure 5.6 (d).

5.3.6 Relevant length scales

Although the shear-adaption of the RBC deformability is shown to be responsible for the nonlinear shear-rate dependence of the RESID, it is still unclear in what way it alters the RESID. In this section, we further identify the characteristic length scale relevant to the RESID to gain more in-depth understanding of this nonlinear phenomenon.

In a series of experiments measuring the particle diffusivity in a concentrated non-

colloidal suspension, [180] show that the ratio of the diffusivity of fluid tracers to the self-diffusivity of non-colloidal particles is close to unity. Through DNS of the cellular blood flow in a micro-channel, [18] show that the cross-stream diffusivity of platelets ($\sim$2 μm) in blood exhibits similar magnitude to that of passive tracers. These findings imply that the shear-induced diffusivity is insensitive to the size of the scarce (in terms of volume fraction), small particles. Following these results, we hypothesize that RESID is insensitive to the size of NP. Moreover, the characteristic length scale associated with the RESID should be the size of RBC. To confirm this hypothesis, we evaluate the RESID at fixed hemorheological condition with various NP size. The NP size is kept in submicron-scale such that the NP-RBC size ratio satisfies $a_1/a_2 \ll 1$. The volume fraction of the NP phase are kept below 0.32% to satify the dilute condition. The set up and measured diffusivities are listed in table 5.3.

In Figure 5.10 (a), we plot the RESID versus *Pe* at $\dot{\gamma}$=1 000 s^{-1} and ϕ=0.2. Here, *Pe* is adjusted by NP size in the range of $50 \leq 2a_1 \leq 800$ nm. A sublinear $\hat{D}_{ij}^R$-*Pe* relationship is observed for all diffusion coefficients. Figure 5.10 (b) further plots the same data as figure 5.10 (a), but with *Pe* rescaled by the NP-RBC size ratio as

$$\widetilde{Pe} = Pe(\frac{a_2}{a_1})^2 = \frac{\dot{\gamma} a_2^2}{D^B}. \tag{5.8}$$

This simple rescaling leads to a strong linear relationship between all RESID terms and the rescaled Péclet number, $\widetilde{Pe}$. Moreover, the observed linear relationship, $(D_{ij}^{\infty}/D^B - \delta_{ij}) \sim O(\widetilde{Pe})$, can be deduced to show that $D_{ij}^R \sim O(\dot{\gamma} a_2^2)$, which indicates that the dimensional RESID is indeed insensitive to the NP size within the range of NP sizes considered in the current study. This also suggests NP size at submicron plays a secondary role in affecting the NP apparent diffusivity primarily through altering BD.

To further justify the universality of the rescaled Péclet number, $\widetilde{Pe}$, $i.e.$, whether the RBC size is the reasonable length scale associated with RBC-enhanced diffusion or not,

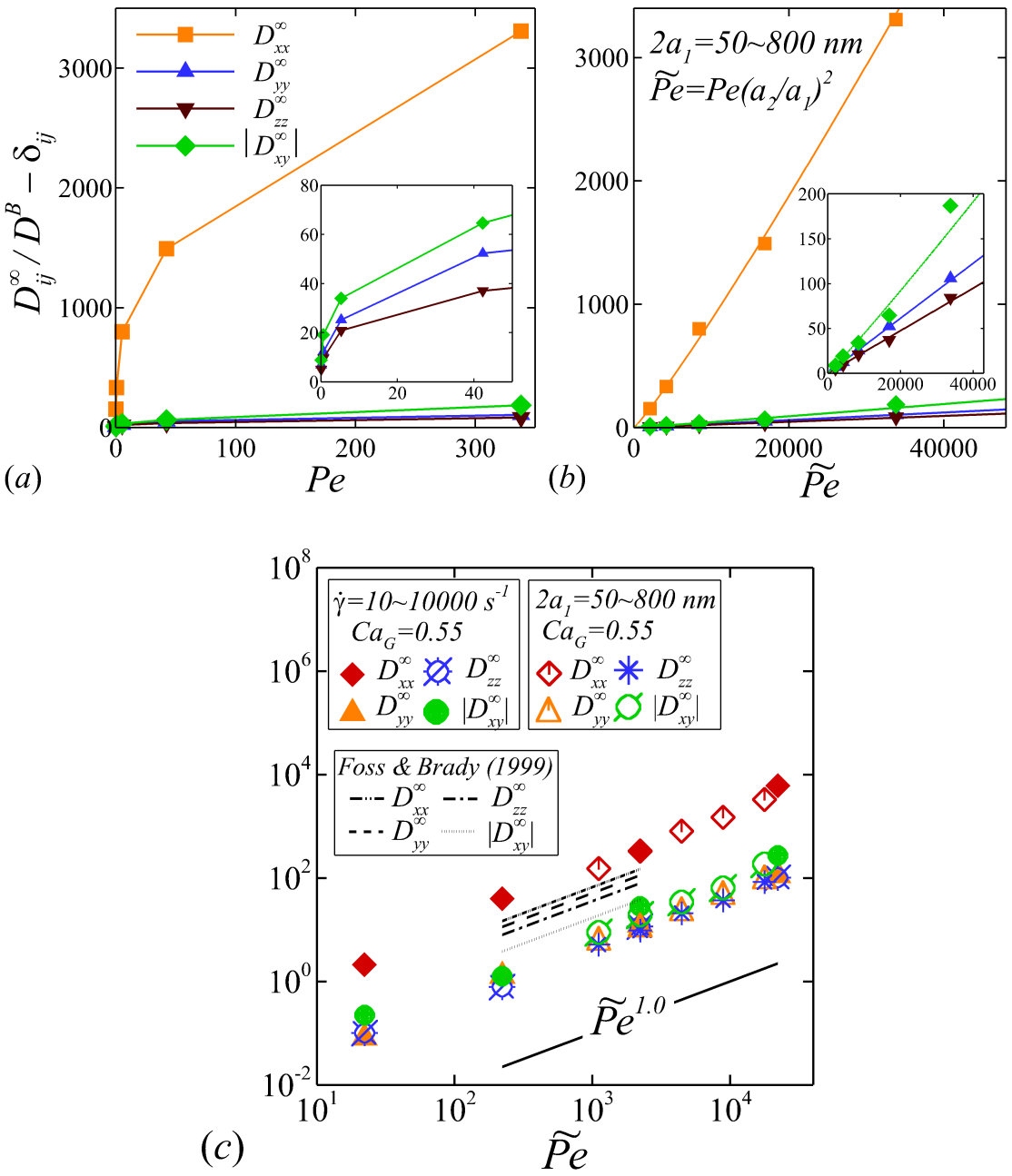

Figure 5.10: RESID plotted against (a) Péclet number *Pe* and (b) the rescaled Péclet number, $\widetilde{Pe}$, at $\dot{\gamma}$=1 000 s^{-1} and ϕ=0.2 in logarithm scales. Both *Pe* and $\widetilde{Pe}$ are adjusted with NP size in the ranges of $2a_1$=50$\sim$800 nm. (c) Linear dependence of RESID on $\widetilde{Pe}$ at fixed $Ca_G = 0.55$ and ϕ=0.2; $\widetilde{Pe}$ is adjusted by shear rate (with $2a_1$=100 nm) or NP size (with $\dot{\gamma}$=1 000 s^{-1}). The diffusion tensor in monodisperse colloidal suspensions [40] are also plotted for comparison, where $\widetilde{Pe}$ degrades to *Pe*.

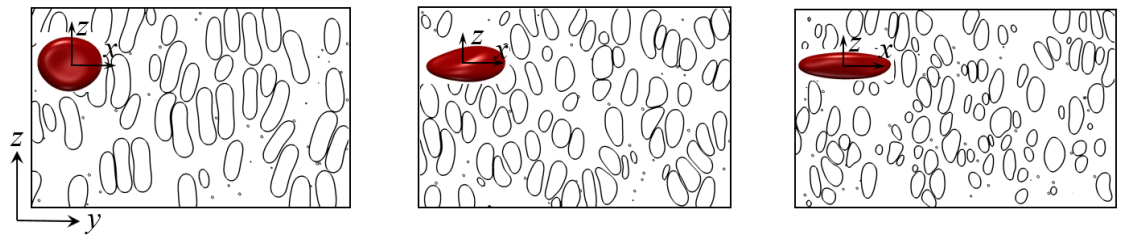

(*a*) Ca_G=0.055, $\bar{a}_{2,yz}$ ≈2.33 μm (*b*) Ca_G=0.55, $\bar{a}_{2,yz}$ ≈1.34 μm (*c*) Ca_G=1.1, $\bar{a}_{2,yz}$ ≈0.85 μm

Figure 5.11: RBC and NP distributions and morphology in the cross-stream plane (y-z) with (a) Ca_G=0.055, (b) Ca_G=0.55 and (c) Ca_G=1.1 at *Pe*=0.066 and ϕ=0.4. Large non-circular disks are RBC cross-sectional contours. Small circles are NP cross-sectional contours. $\bar{a}_{2,yz}$ can be estimated from the PPDF analysis.

we plot RESID against $\widetilde{Pe}$ at Ca_G=0.55 and ϕ=0.2, with $\widetilde{Pe}$ adjusted by either shear rate or NP size. As shown in figure 5.10 (c), the data points for particular RESID coefficient are found to be well aligned on the same linear $\widetilde{Pe}$ scaling line. This directly confirms that the RBC size is the characteristic length scale governing the RBC-enhanced diffusion, and $\widetilde{Pe}$ is a more general nondimensional term quantifying the RESID.

Identifying RBC size being the RESID length scale helps further understanding the nonlinear shear-rate dependence of the RESID. In figure 5.11, we present snapshots of RBC and NP distribution and morphology in the mid cross-stream cross-sectional plane. As shown in figure 5.11, the x-direction elongation of RBCs under high shear causes a contraction of RBCs in the yz plane, which causes a reduction of the average effective RBC size ($i.e.$, the length scale $\bar{a}_{2,yz}$) and hence a decrease of the effective $\widetilde{Pe}$ in cross-stream directions. This explains the sublinear shear-rate scaling of the cross-stream RESID when increasing Ca_G. Likewise, the super-linear shear-rate scaling of the longitudinal RESID can be attributed to the elongation of RBC in the streamwise direction, $i.e.$ the increase of the RESID length scale in the longitudinal direction. The change of the RESID length scales in different principal directions due to shear is the root cause of the nonlinear shear-rate dependence of the NP diffusion tensor.

5.3.7 Theory for RESID

In this section, we construct empirical correlations for the long-time NP diffusion tensor in sheared blood based on the scaling observations in the previous sections. Since all RESID coefficients scales linearly with $\widetilde{Pe}$ at fixed Ca_G, and the nonlinear shear-rate dependence of RESID is primarily due to the variation of Ca_G, as demonstrated in §5.3.5 and §5.3.6; there hence exists a scaling relation, $\hat{D}^R_{ij} \sim O(\phi^{p_1}\ \widetilde{Pe}\ Ca_G^{p_2})$, such that the exponents p_1 and p_2 can be estimated through matching the nonlinear ϕ and $\dot{\gamma}$ scalings, respectively, as observed in §5.3.3. Therefore, empirical correlations of NP long-time diffusivities can be constructed as functions of ϕ, $\widetilde{Pe}$ and Ca_G in the hemorheological range of $10 \leq \dot{\gamma} \leq 2\,000$ s^{-1} and $0.1 \leq \phi \leq 0.4$ as following

$$\frac{D^\infty_{xx}}{D^B} = \begin{cases} 1 + \mathcal{C}^l_{xx}\phi\ \widetilde{Pe}, & 0.0055 \leq Ca_G \leq 0.055 \\ 1 + \mathcal{C}^h_{xx}\phi^{Ca_G+0.945}\ \widetilde{Pe}\ Ca_G^{0.8}, & 0.055 < Ca_G \leq 1.10 \end{cases} \tag{5.9a}$$

$$\frac{D^\infty_{yy}}{D^B} = \begin{cases} 1 + \mathcal{C}^l_{yy}\phi\ \widetilde{Pe}, & 0.0055 \leq Ca_G \leq 0.055 \\ 1 + \mathcal{C}^h_{yy}\phi\ \widetilde{Pe}\ Ca_G^{-0.3}, & 0.055 < Ca_G \leq 1.10 \end{cases} \tag{5.9b}$$

$$\frac{D^\infty_{zz}}{D^B} = \begin{cases} 1 + \mathcal{C}^l_{zz}\phi\ \widetilde{Pe}, & 0.0055 \leq Ca_G \leq 0.055 \\ 1 + \mathcal{C}^h_{zz}\phi^{1.022-0.4Ca_G}\ \widetilde{Pe}\ Ca_G^{-0.2}, & 0.055 < Ca_G \leq 1.10 \end{cases} \tag{5.9c}$$

$$\frac{D^\infty_{xy}}{D^B} = \frac{D^\infty_{yx}}{D^B} = \begin{cases} \mathcal{C}^l_{xy}, & 0.0055 \leq Ca_G \leq 0.055 \\ \mathcal{C}^h_{xy}\phi\ \widetilde{Pe}, & 0.055 < Ca_G \leq 1.10 \end{cases} \tag{5.9d}$$

where $\mathcal{C}^q_{ij}$ with $q \in \{l, h\}$ are constants fitting the correlation values with the simulation measurements at low or high shear rates. The dimensional NP diffusion tensor can then be

written in terms of the conventional shear-induced diffusion scaling, $O(\dot{\gamma}a_2^2)$, as

$$\boldsymbol{D}^{\infty} = D^B \boldsymbol{I} + \phi\dot{\gamma}a_2^2 \boldsymbol{M}^q, \tag{5.10}$$

where the anisotropic tensor, $\boldsymbol{M}^q$, according to the severity of the RBC deformability (Ca_G=$\mu\dot{\gamma}a_2/G$) at different level of shear rates, yields piecewise expressions:

$$\boldsymbol{M}^l = \begin{pmatrix} \mathcal{C}_{xx}^l & \mathcal{C}_{xy}^l & 0 \\ \mathcal{C}_{yx}^l & \mathcal{C}_{yy}^l & 0 \\ 0 & 0 & \mathcal{C}_{zz}^l \end{pmatrix}, \qquad 10 \leq \dot{\gamma} \leq 100\ s^{-1} \tag{5.11a}$$

$$\boldsymbol{M}^h = \begin{pmatrix} \mathcal{C}_{xx}^h \phi^{Ca_G - 0.055} Ca_G^{0.8} & \mathcal{C}_{xy}^h & 0 \\ \mathcal{C}_{yx}^h & \mathcal{C}_{yy}^h / Ca_G^{0.3} & 0 \\ 0 & 0 & \mathcal{C}_{zz}^h / (\phi^{2Ca_G + 0.11} Ca_G)^{0.2} \end{pmatrix}, \qquad 100 < \dot{\gamma} \leq 2\,000\ s^{-1} \tag{5.11b}$$

where $\boldsymbol{M}^q$ quantifies the anisotropic behavior of the NP diffusion tensor and characterizes its departure from the conventional shear-induced diffusion scaling, $O(\dot{\gamma}a_2^2)$, due to the presence of the deformable RBC phase. Table 5.4 lists all the constants, $\mathcal{C}_{ij}^q$. Each constant is obtained by calculating the slope of the best linear fit to the data set, ($D_{ij}^{(R,m)}$,$D_{ij}^{(R,th)}/\mathcal{C}_{ij}^q$), for specific i, j and q at various $\dot{\gamma}$ and ϕ. Here, $D_{ij}^{(R,m)}$=$D_{ij}^{\infty} - D^B\delta_{ij}$ denotes the measured RESID evaluated by the calculated D_{ij}^{∞} subtracted by the theoretical BD; $D_{ij}^{(R,th)}$=$\phi\dot{\gamma}a_2^2 M_{ij}^q$ denotes the theoretical diffusivity based on the proposed empirical correlations. $\mathcal{C}_{xy}^l$ is set to zero given its small magnitude. $\mathcal{C}_{xy}^h$ is negative, suggesting the predominant direction of NP migration in the long-time regime is along the contractile flow direction under high shear flow [40]. For cases at $\dot{\gamma}$<10 s^{-1} and ϕ<0.1, $\boldsymbol{D}^{\infty}$ can be approximated by the isotropic Brownian diffusivity provided the small magnitude of the RESID.

Table 5.4: Correlation constants for the empirical correlations of NP diffusion tensor in sheared cellular blood flow.

$\mathcal{C}_{xx}^{l}$	$\mathcal{C}_{xx}^{h}$	$\mathcal{C}_{yy}^{l}$	$\mathcal{C}_{yy}^{h}$	$\mathcal{C}_{zz}^{l}$	$\mathcal{C}_{zz}^{h}$	$\mathcal{C}_{xy}^{l}$	$\mathcal{C}_{xy}^{h}$
0.281	2.86	0.0432	0.0181	0.0241	0.0135	0	-0.0332

Figure 5.12 plots the measured NP diffusivities (subtracted by BD) versus the theoretical estimation based on the empirical correlations. The good collapse of the diffusivity measurements on the $D_{ij}^{(R,m)}$=$D_{ij}^{(R,th)}$ line demonstrates the empirical correlations can well reproduce the numerically measured diffusivity tensor of NP in sheared blood.

5.4 Conclusions

The dispersion of NP in cellular blood flow under unbounded, homogeneous shear has been investigated over a wide range of shear rate and hematocrit using a LB-LD-SL multiscale complex blood flow solver. In the short-time regimes, NP dispersive anomalies are observed and attributed to the transient morphology and orientation change of RBCs under high shear and high hematocrit. In the long-time regimes, results for the long-time diffusivity in the velocity gradient direction agree well with existing experimental data. The long-time NP diffusion tensor has been described as a function of shear-rate and hematocrit with various power-law scalings.

By plotting the RBC-NP PPDF, the NP microstructure in sheared blood has been visualized for the first time that features a rhombus configuration with the detailed inner structure changes according to specific hemorheological conditions. The RBC-NP PPDF analysis also suggests a novel approach to visualizing the average RBC morphology in concentrated RBC suspensions subject to different hemorheological conditions. Under high shear rate, the ϕ^2 dependence in $\hat{D}_{xx}^{R}$ is proposed to be related to the x-elongation of RBC and elevated RBC-NP PPDF near the fore-aft region, which together suggests possible more-than-two-body interaction occurred particularly in the streamwise direction. The sublinear ϕ dependence is suggested to be related to the reduced effective ϕ owing to the substantial

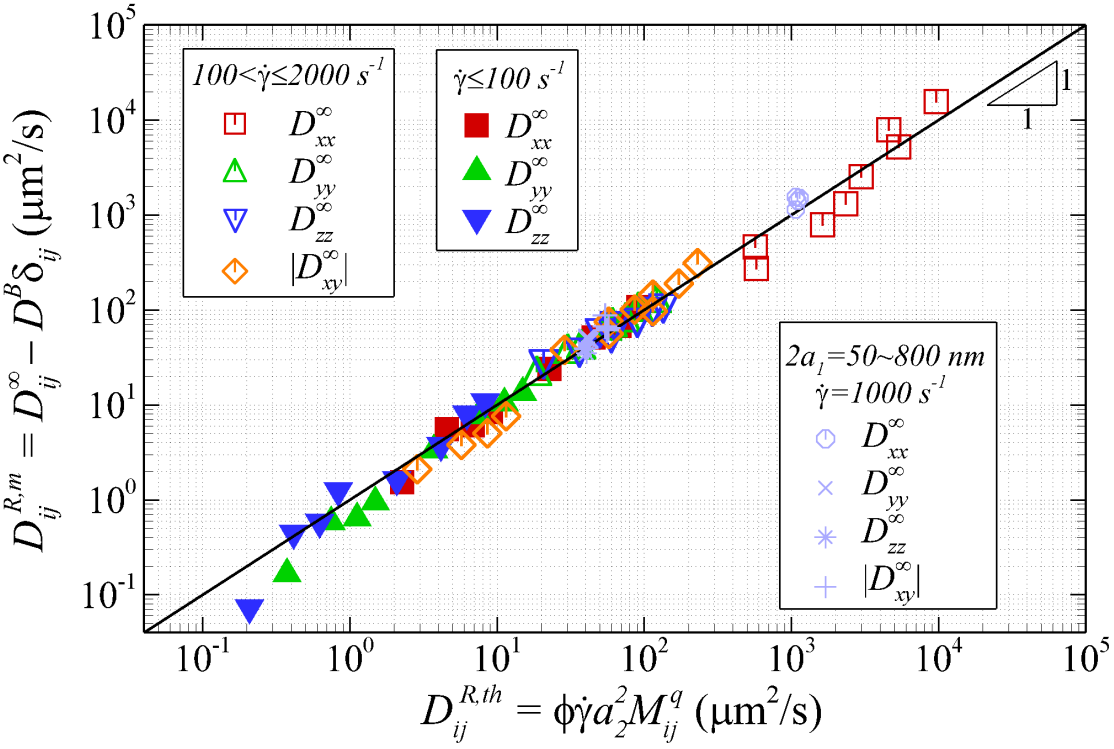

Figure 5.12: Measured NP RESID, $D_{ij}^{(R,m)} = D_{ij}^{\infty} - D^B\delta_{ij}$, as a function of the theoretical RESID, $D_{ij}^{(R,th)} = \phi\dot{\gamma}a_2^2M_{ij}^q$, based on the empirical correlations presented in equations 5.11a and 5.11b. For cases with $\dot{\gamma}\leq 100\ s^{-1}$ (filled symbols), M_{ij}^l is applied to calculate $D_{ij}^{(R,th)}$. For cases with $\dot{\gamma}>100\ s^{-1}$ (open symbols), M_{ij}^h is applied to calculate $D_{ij}^{(R,th)}$.

contraction of RBC in the vorticity direction subject to high shear. The RBC-NP bidisperse suspension presents an example of highly anisotropic microstructure of particle suspensions caused by the compound effect of particle-shape/orientation anisotropy and shear-flow anisotropy.

It is also found that there exists a critical shear rate ($\sim$100 s^{-1}) around which the RESID shear-rate dependence changes from linear to nonlinear scale. Through numerical experiments, the transition to nonlinear shear-rate scaling of RESID has been related to the prominent change of average RBC morphological state between different shear rate. Specifically, the superlinear scalings ($\dot{\gamma}^{1\sim1.8}$) of $\hat{D}^R_{xx}$ are due to the streamwise elongation of RBC, while the sublinar scalings ($\dot{\gamma}^{0.7\sim0.8}$) of $\hat{D}^R_{yy}$ and $\hat{D}^R_{zz}$ are associated with the cross-stream contraction of RBC (in response to the streamwise elongation). The morphological changes under shear alter the RESID length scale in different principal directions, which has been demonstrated to be the fundamental cause of the nonlinear shear-rate dependence of the RESID. This mechanism is also worth to be distinguished from the causes of the nonlinear shear-rate scaling of the self-diffusivity of RBCs [183, 194] or deformable capsules [74], where latter has been attributed to the heterogeneous interparticle 'collision' due to the cell deformability [184]. However, the nonlinear shear-rate dependence of NP diffusion in sheared blood, based on our interrogation, is more associated with a 'one-way' mechanism, $i.e.$, the RBC morphological adaptation to shear flow changes the RESID length scale which further alters the NP diffusion rate.

The determination of the rescaled Pélect number being a more general nondimensional term to describe the severity of RESID enables the comparison between the bidisperse NP-RBC suspension and the monodisperse colloidal suspensions. In the latter scenario where the particle size ratio is one, $\widetilde{Pe}$ drops to *Pe* and 'RESID' drops to the particle self-diffusivity. The self-diffusion tensor reported by [40] in a sheared monodisperse colloidal suspensions are plotted in figure 5.10 (c) for comparison. In both monodisperse and bidisperse scenario, $\hat{D}^R_{xx}$ shows the greatest magnitude among all diffusivity terms; $\hat{D}^R_{yy}$ is

slightly greater than $\hat{D}^R_{zz}$. In general, $\hat{D}^R_{ij}$ in RBC-NP suspension shows higher anisotropy than the monodisperse case owing to the geometric asymmetry of RBCs (x being greater than y and z dimensions). Such geometric asymmetry effect can be further increased with Ca_G, leading to higher anisotropy of the diffusivity tensor. In the monodisperse scenario, $\hat{D}^R_{xy}$ is the smallest; while in the NP-RBC bidisperse scenario, $\hat{D}^R_{xy}$ is greater than $\hat{D}^R_{yy}$ and $\hat{D}^R_{zz}$ due to the severe diffusive effect in x direction.

This work, to the authors' knowledge, offers the first detailed study of the complete 3D NP diffusion tensor in cellular blood flow over a wide range of shear rate and hematocrit. The proposed empirical correlations for the NP diffusion tensor offers a constitutive relation that can be adopted by effective continuum models to pursue large-scale NP biotransport applications (e.g. $in\ vivo$ NP drug delivery) with better accuracy.

CHAPTER 6

SHEAR-INDUCED PLATELET AGGREGATION THROUGH VON WILLEBRAND FACTOR ENTANGLEMENT UNDER ELEVATED HIGH SHEAR

Occlusive arterial thrombosis can lead to acute life-threatening events such as heart attacks and strokes. The rapid growth of thrombi against elevated high shear relies on shear-induced platelet aggregation (SIPA) through the entanglement of von Willebrand factor (VWF) multimers. The biophysical mechanism for SIPA remains unclear and hinders the better understanding of the pathology for occlusive arterial thrombosis. In this work, we develop a multiscale and multiphysics computational method informed by the $status\ quo$ single-molecule-level measurements to directly simulate the SIPA process. It is found that SIPA is a two-stage process involving agglomeration of platelets in the flow and capture of agglomerates to the thrombotic surface. Under elevated high shear ($\sim$10,000 s^{-1}), SIPA occurs in milliseconds as fast as the platelet transit time through the stenosis apex. In particular, the transition from the lag time (LT) regime to rapid platelet accumulation (RPA) is found to be attributable to the enhancement of agglomerate capture rate through elevating the local VWF concentration and/or the VWF size (length). Excessively shortening VWF size and/or lowering VWF concentration prevents SIPA, consistent with von Willebrand disease (VWD) conditions. Ultra-long VWF can form loose aggregate at normal or subnormal VWF concentration, consistent with pathological conditions such as thrombotic thrombocytopenic purpura (TTP). Besides, our work also reconciles some contradictory experimental observations in the field of high-shear thrombosis.

This work, for the first time, bridges the single-molecule bond force measurements to the microthrombi formation, and provides possible bio-physico-chemical explanations to thrombotic or bleeding complications. The multiscale $in\ silico$ approach provides a cross-scale tool for exploring novel biophysical mechanisms for SIPA that are typically

inaccessible to only single-molecule measurements and micro-/marcro-fluidic assays. Such new perspectives may lead to the discovery of novel anti-thrombotic therapies.

6.1 Introduction

Occlusive arterial thrombosis is an acute pathological condition under which a blood clot rapidly forms and occludes an artery, which are the direct cause of ischemic stroke or myocardial infarction as two of the leading causes of death globally [200]. The onset of arterial thrombosis typically stems from a chronic atherosclerotic plaque (over many decades) that narrows the artery and creates high, oscillating shear stresses (OSS) on the plaque surface [201]. Overtime the plaque cap becomes ruptured (owing to the OSS) and the sub-endothelial collagen gets exposed, which subsequently triggers the acute occlusive thrombosis process [11].

The arterial thrombosis specific to high shear is different from the low shear venous thrombosis governed by the Virchow's Triad [202]. Rather, it can be explained by a high-shear thrombosis triad, which includes (1) a pro-thrombotic surface, (2) pathologically high shear rates, and (3) necessary blood constituents mainly including platelets and von Willebrand factor (VWF) [29, 11, 170]. Based on this alternative triad, occlusive arterial thrombosis has been successfully modeled $in\ vitro$ [203] and $ex\ vivo$ [204] using blood flow-through systems. The time to occluding the vessel is found to be $\sim$20 minutes, which is consistent with the time related to sudden cardiac ischemic death [205]. Moreover, the high-shear occlusive thrombosis is characterized by three growing phases [204, 203, 11]. Phase I is the lag time (LT) phase which typically lasts for 1$\sim$5 minutes and shows mostly platelet adhesion with a limited thrombi accumulation. Phase II is the rapid platelet accumulation (RPA) phase, which features prominent shear-induced platelet aggregation (SIPA) with the thrombi accumulation rate being $4-6$ times that of Phase I [30, 33]. Following RPA, the vessel becomes occluded at Phase III. Despite RPA being the direct cause of thrombotic occlusion in arteries, the mechanism for the explosive thrombi growth during

RPA has remained unexplained.

VWF has now been recognized as a primary determinant for high-shear thrombosis. Under pathological high shear ($>3000\ s^{-1}$), platelet mural adhesion exclusively depends on VWF as opposed to other ligands such as fibrinogen that normally play a role under low shear ($\sim 100\ s^{-1}$) [206]. This is supported by the ultra-fast platelet-VWF binding via GP1b-A1 bonds [207, 208]. The GP1b-A1 kinetic on rate has been estimated theoretically [207] and recently measured $in\ vitro$ [208] with a rate from 10^6 to $10^9\ M^{-1}s^{-1}$, which is $2-5$ orders of magnitude faster than the platelet GPIIbIIIa-fibrinogen formation rate ($\sim 10^4\ M^{-1}s^{-1}$) [209]. In addition, under high shear VWF molecule changes its tertiary structure from a globular state to elongated state, which enhances its bind affinity (per molecule) by both exposing more A1 domains for multi-valency [87, 85] and elevating the A1 activity through local conformation unfolding [208]. These factors allow for platelet capture through VWF under ultra-high drag forces independent of platelet activation [207]. Moreover, SIPA specific to elevated high shear ($>10000\ s^{-1}$) has been demonstrated $in\ vitro$ and $in\ vivo$ to be platelet activation-independent while exclusively dependent on VWF [210, 26].

Furthermore, the VWF size and concentration varies under various pathophysiological conditions. For example, patients with von Willebrand disease (VWD) type 2A/2B or acquired von Willebrand syndrome (aVWS) systematically have a below-average size of VWF multimer [211, 212] and are accompanied with bleeding complications. Patients with thrombotic microangiopathies (TMA) or thrombotic thrombocytopenic purpura (TTP) are found to have an excessive amount of ultra-long VWF (ULVWF) in the microvasculatures which tend to form micro-aggregates and block small vessels [213]. VWF multimers formed in endothelial cells and platelet α-granules are rich in ULVWF at high concentrations [214]. Such pool of ULVWF can be released during the thrombotic events and enhance the local thrombogenicity [11]. Therefore, elucidating how the change of VWF conditions (size and concentration) affect the high-shear thrombosis through SIPA may

shed light on the RPA mechanism and meanwhile give physics-based interpretations to the pathology of various VWF-related diseases.

There are several research questions and controversies remaining to be addressed in the field of high-shear thrombosis. First, what is the timescale for SIPA to occur? Previous theoretical study by Wellings and Ku [207], based on force balance analysis, suggest a single platelet can be captured in microseconds, faster than the platelet transit time (millisecond-scale). It is however unclear how fast SIPA could occur, provided the millesecond-scale transit time. Second, where does the thrombi stem from, at the stenotic apex where the shear peaks or distal to the stenosis where the shear-gradient is highest? Using $in\ vivo$ and $in\ vitro$ stenoses that feature an apex narrower than 100 μm, Netsbitt $et\ al.$ [215, 216] observed the thrombi accumulates primarily downstream to the stenosis apex. In contrast, our group has consistently obserse the growth of thrombi primarily at the stenosis apex/throat using different scales of $in\ vitro$ [203, 30, 217, 29, 60] and $ex/in\ vivo$ [204, 218] stenosis models. Third, the GP1b-A1 bond lifetime measured by various researchers using single-molecule measurements [219, 220, 221] shows different degradation behavior with respect to bond force. How the molecular-level difference relates to or affects the high-shear thrombosis has not been interrogated.

$In\ silico$ biophysical models are powerful tools that can be efficiently and economically used to study the sensitivity of a particular parameter across a large parametric space. Previous $in\ silico$ methods [222, 223, 170] for high-shear thrombosis either completely neglect the presence of VWF or implicitly incorporate effect of VWF based on empirical data, lacking the ability to study the effect of VWF on high-shear thrombosis. Multiscale computational methods [224, 225] that directly model the suspension dynamics and interactions of molecule and cell/colloid can be further developed to model high-shear thrombosis based on first principles. A systematic study that bridges endpoints across molecular and cellular scales may shed light on the mechanism of RPA and help addressing the controversies primarily caused by limiting to single-scale perspectives.

The goal of this study is twofold. First, we will develop a multiscale and multiphysics computational method that incorporates the VWF polymer hydrodynamics, platelet particle suspension dynamics and the stochastic binding kinetics between VWFs and platelets for direct numerical simulation of the SIPA process. A experiment-informed GP1b-A1 binding model will be developed by combining the $status\ quo$ single-molecule-level measurements with the classical equilibrium kinetic theory to obtain cross-scale consistent results. The platelet and VWF polymer hydrodynamics are based on the multiscale particulate suspension dynamics developed and validated in previous chapters [24, 225, 104, 153]. Second, we will apply this bottom-up $in\ silico$ approach to explore a large parameter space to understand SIPA dependence on various VWF size, concentrations and kinetics rates so as to elucidate the mechanism for RPA and address some existing controversies in the field of high-shear thrombosis. This work appears to be the first attempt to bridge information across molecule-level, cellular-level and microthrombi-level based on first principles.

The remaining sections of the chapter are organized as follows. In § 6.2, we present the multiscale computational method for high-shear microthrombi formation. Particularly, a single-molecule-measurement informed kinetic model for platelet-VWF GP1b-A1 bond formation and rupture will be developed. In § 6.3, the dynamics of SIPA delineated in terms of the effect of VWF size, concentration and bond characteristics. In § 6.4, we will address several controversies in the field of high-shear thrombosis based on our computational results. The clinical relevance of the study is presented. In § 6.5, we summarize the new findings related to SIPA and occlusive arterial thrombosis.

6.2 Methodology

The computational method is developed to simulate mural thrombi formation at a growing arterial thrombus surface where the local shear rate is ultra-high ($> 10\ 000\ s^{-1}$), as shown in Fig. 6.1a. The three necessary ingredients for arterial thrombosis, including high shear, pro-thrombotic surface and necessary blood components (VWF and platelets), are included in the model system, as shown in Fig. 6.1b. The red blood cells (RBCs) are neglected for simplification, provided they are not necessary for the onset of SIPA [226] and the region of interest mainly locate within the RBC-free layer [111, 153]. The thrombus-blood interface region is simplified as a three-dimensional Couette flow domain, where the interaction and motion of each individual platelet and VWF strand at physiologically-relevant concentrations are computed over time. The thrombus surface is simplified as flat surface as the relatively low curvature compared to the size of the selected region. The surface is assumed to be coated with immobilized VWFs to be pro-thrombotic. The schematics of the entire model system are shown in Fig. 6.1c, where the suspension dynamics of platelets and VWF polymers, the GP1b-A1 binding and volume exclusion between VWF and platelets, the inter-/intra-association of VWF, and the fluid-structure interactions are all computed over time.

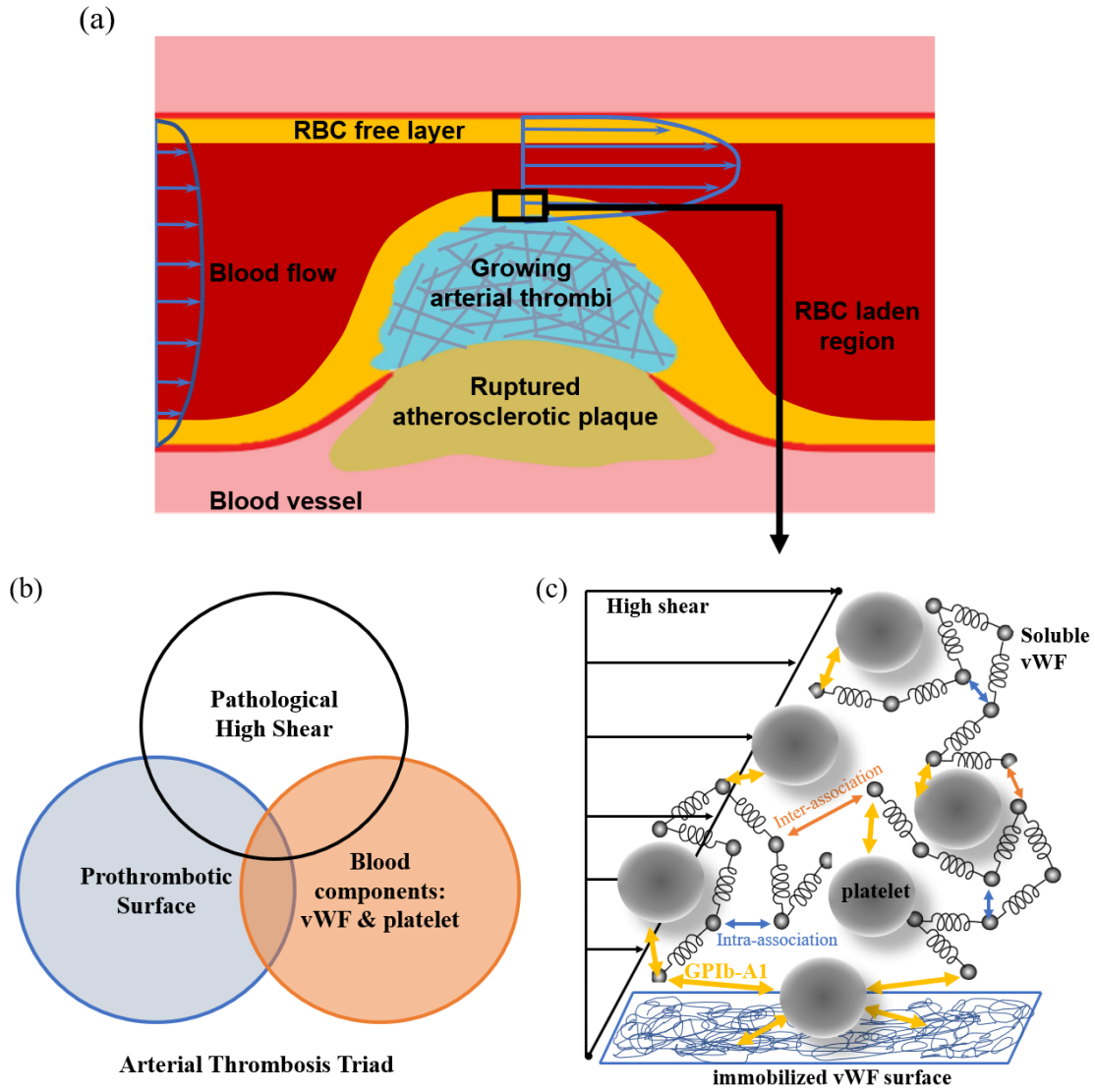

Figure 6.1: Schematics for the model system. (a) Blood flow through an arterial stenosis where an occlusive thrombi is forming and locally creating an elevated-high-shear environment. Further growth requires platelet aggregation under ultra-high shear stress. (b) The triad illustrates the necessary conditions for arterial thrombosis [11]. (c) The *in silico* model system represents a zoom-in view of the thrombi-blood interface subjected to elevated high shear. Shear-induced platelet aggregation (SIPA) occurs onto a VWF-rich prothrombotic surface. The SIPA process is supported by forming platelet-VWF GP1b-A1 bonds and the VWF inter-/intra-association bonds.

6.2.1 Langevin-dynamics for the VWF polymer dynamics

The VWF suspended in the blood plasma is modeled as a chain of beads connected with hyperelastic springs using the LB-LD method developed by Liu $et\ al.$ [225], as previously presented in §2. Each bead represents a VWF dimer that has a hydrodynamic radius of 80 nm. The VWF intra-association is realized through the LJ potential with a well-depth of $\epsilon_{intra} = 2k_BT$ [85] to match the critical shear rate for VWF unfolding.

The VWF inter-association has been reported to be controlled by complex multi-domain interactions [227]. The type of bond supporting the VWF inter-association possibly ranges from weak hydrogen bond to strong covalent bond, where former supports the observation that reversible VWF self-association can form under high shear [228] and latter has been reported in the context of forming disulfide bonds [229, 230]. The energy well-depth for hydrogen bonds typically ranges from $O(k_BT)$ to $O(10k_BT)$, while the covalent bond ranges from $O(10k_BT)$ to $O(10^2k_BT)$ [231]. To reflect the hybrid mode of the VWF inter-association, we model the VWF inter-association through LJ potential with an energy well-depth $\epsilon_{inter} = 20k_BT$.

6.2.2 Rigid-body dynamics for platelets

The translational and rotational dynamics of suspended platelets are modeled through Newtonian rigid-body dynamics coupled with the LB fluid [64]. Different from previous studies [19, 111] assuming disc shape platelets (Figure 6.2a), the current study focused on elevated shear conditions assumes the platelets adopting a spherical shape. This is to be consistent with the experimental observation by Maxwell $et\ al.$ [232], where the authors show nonactivated platelets under elevated shear rates (10000 to 20000 s^{-1}) tend to develop a smooth ball-like morphology as shown in Figure 6.2b.

(a) Low shear, Disc (b) High shear, Sphere

Figure 6.2: The differential interference contrast (DIC) image of nonactivated platelets under different shear rate conditions. Low shear rates ($<1000s^{-1}$) show disc shape platelets (a), while elevated high shear rates ($>10000s^{-1}$) give rise to spherical shape platelets (b). The scale bar is 1 μm. Images are adopted from Maxwell $et\ al.$ [232].

6.2.3 Single-molecule-measurement-informed stochastic GP1b-A1 binding model

To model the VWF-platelet adhesion through GP1b-A1 bond, We have developed a binding model particularly suitable for direct numerical simulation of ligand-receptor binding activity under hydrodynamic influence. Our theoretical approach combines the classic equilibrium binding kinetic theory [233, 234] with the recent single-molecule level kinetics measurements [208, 219, 220], enabling us to obtain the intrinsic GP1b-A1 kinetic rates that is decoupled from the transport effect.Such theoretical approach can be extended to model other ligand-receptor bindings subjected to hydrodynamic perturbation, given the apparent kinetic rates can be measured using fluidics approaches such as that in Fu $et\ al.$ [208].

GP1b-A1 on rate

Fu $et\ al.$ [208] applied a single-molecule microfluidic system to quantify the temporal binding percentage of the GP1b molecules onto a tethered VWF under various shear stresses. The apparent GP1b-A1 on rate, K_{on}, was found to be VWF tension force dependent, which

can be estimated as

$$K_{on} = \frac{K_{on}^{m}}{1 + \exp[(\Delta G - F_t \Delta x)/k_B T]}, \tag{6.1}$$

where F_t is the VWF internal tension force, K_{on}^{m} is the maximum on rate under sufficiently high VWF tension ($F_t \sim 100\ pN$), ΔG is the energy barrier between the no-tension state and the maximum-tension state, and Δx is the displacement between the two states along the tension axis. The model constants are given as $K_{on}^{m} = (50.8 \pm 4.2) \times 10^6\ M^{-1}s^{-1}$, $\Delta G \approx 6.2 k_B T$ and $\Delta x = 1$ nm by fitting the experimental data.

It should be noted that the apparent kinetic on rate is controlled by both transport (convection and diffusion) and intrinsic association (on) rate [233]. As a result, the apparent on rate is not generic and depends on the experimental setup. To obtain the GP1b-A1 intrinsic on rate that is transport-independent, the encounter and escape rates through convection/diffusion need to be estimated and decoupled from the apparent on rate.

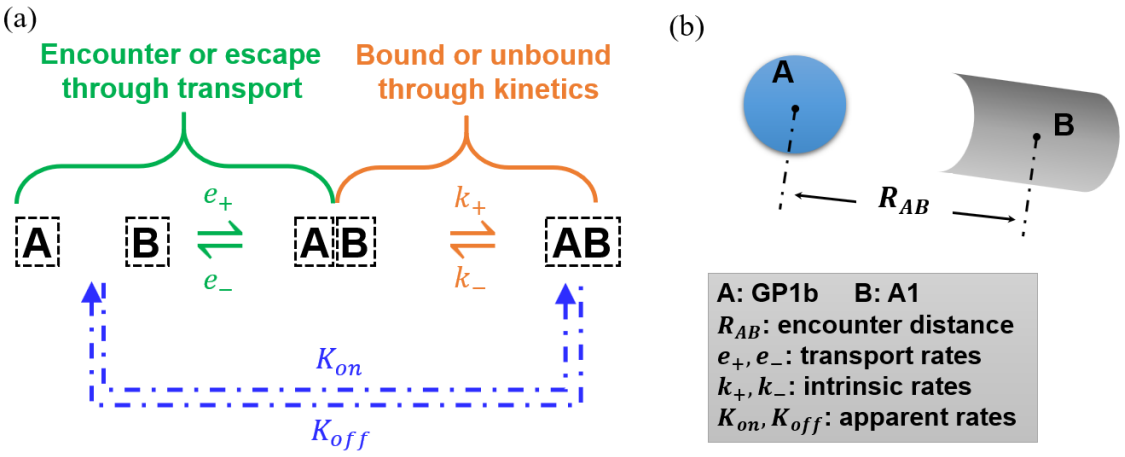

Figure 6.3: Schematic illustration of the ligand-receptor binding kinetics. (a) The apparent kinetic process can be decomposed into the transport portion and the intrinsic kinetics portion. The macroscopic association (dissociation) involves first the encounter (unbound) of the ligand and receptor, and then the bound (escape) of the two molecules. (b) The two reactive molecules (e.g., GP1b and A1) need to locate adjacent to each other within certain encounter distance, R_{Ab}, in order to proceed with the subsequent intrinsic kinetic process.

Noting that the molecule encounter and escape through transport (convection/diffusion induced translation and rotation) in the experimental system by Fu $et\ al.$ [208] is diffusion-limited, the transport-induced GP1b-A1 encounter rate, e_+, and escape rate, e_-, can therefore be estimated according to the statistical mechanics [235] as

$$e_+ = 4\pi(D_{GP1b} + D_{A1})R_{AB}, \tag{6.2}$$

$$e_- = 3(D_{GP1b} + D_{A1})R_{AB}^{-2}, \tag{6.3}$$

where D_{GP1b} and D_{A1} are the Brownian diffusion rate of GP1b molecules and A1 molecules, respectively, R_{AB} is the encounter distance, which can be estimated as twice the hydrodynamic radius of GP1b molecule, $R_{AB} \approx 2R_{GP1b}$. In the microfluidic system of Fu $et\ al.$ [208], the VWF strings (contains A1) were tethered onto the wall whereas the GP1b molecules were suspended in the liquid. Thus, the two diffusivities should satisfy $D_{GP1b} \gg D_{A1}$. The diffusion rate of GP1b can be quantified by its Brownian diffusivity, $i.e.$, $D_{GP1b} = k_BT/6\pi\mu R_{GP1b}$. Therefore, the encounter and escape rates between GP1b and A1 can be approximated as

$$e_+ \approx 8\pi D_{GP1b}R_{GP1b} = \frac{4k_BT}{3\mu}, \tag{6.4}$$

$$e_- \approx 3D_{GP1b}/4R_{GP1b}^2 = \frac{k_BT}{8\pi\mu R_{GP1b}^3}. \tag{6.5}$$

Quantitatively, the above expressions yield an encounter rate of $e_+ = 3.5 \times 10^9\ M^{-1}s^{-1}$ and an escape rate of $e_- = 7 \times 10^6\ s^{-1}$.

Based on the measured apparent on rate K_{on} and the encounter and escape rates esti-

mated above, the GPIb-A1 intrinsic on rate ,k_+, can be calculated according to

$$k_+ = \frac{K_{on} e_-}{e_+ - K_{on}} \approx \frac{k_+^m}{1 + \exp[(\Delta G - F_t \Delta x)/k_B T]}, \tag{6.6}$$

where the maximum intrinsic on rate is $k_+^m = K_{on}^m e_-/e_+ \approx 1 \times 10^5\ s^{-1}$. Our derived k_+^m quantitatively describes the minimal time required for the GP1bA1 bond formation is $1/k_+^m \sim 10\ \mu s$, which has not been directly measured before due to its ultra-short timescale. The k_+ value depends on the VWF tension force, F_t, which is explicitly tracked by the LB-LD method [225]. Note that the GP1b-A1 formation takes much shorter time ($\sim$10 μs) compared to the bond lifetime (0.01$\sim$1 s), which supports rapid accumulation of GP1b-A1 bonds needed for capturing platelets under elevated high shear ($>$10000 s^{-1}) [207].

GP1b-A1 off rate

The GP1b-A1 intrinsic off rate quantifies the rupture dynamics of the GP1b-A1 bond, which is also equivalent to the reciprocal of the bond lifetime. The general functional form for the intrinsic GP1b-A1 off rate follows the Bell's equation for the first-order dissociation kinetics,

$$k_- = k_-^0 \exp[F_b \sigma / k_B T], \tag{6.7}$$

where k_-^0 is the zero-force intrinsic off rate,and σ is the reactive compliance that determines the degradation rate of the bond stability subjected to the GP1b-A1 bond force, F_b.

The intrinsic GP1b-A1 off rate, k_-, has been measured by several groups using single-molecule force-measurement assays [219, 220, 221]. Fitting the measurements of wild-type GP1b-A1 bond lifetime by Kim $et\ al.$ [219], the rate constants can be obtained as $k_-^0 \approx 0.001 - 0.01\ s^{-1}$ and $\sigma = 2.0\ nm$. Fitting the measurements by Zhang $et\ al.$ [220] and Chen $et\ al.$ [221] yields the rate constants $k_-^0 \approx 0.1 - 1.0\ s^{-1}$ and $\sigma = 0.2\ nm$.

Fig. 6.4 depicts the measured GP1b-A1 bond lifetime and the corresponding Bell equations of GP1b-A1 bond lifetime and off rate with specific rate constants. Noticeably, the

major distinction among the different measurements lies in the difference in the bond degradation rate determined by the reactive compliance, σ, while k_-^0 only leads to minor difference. To address the discrepancy in the measured k_- primarily caused by the difference in the reactive compliance of GP1b-A1 bond, following studies in § 6.3.3 will access the effectiveness of various k_- data in causing platelet aggregation and capture.

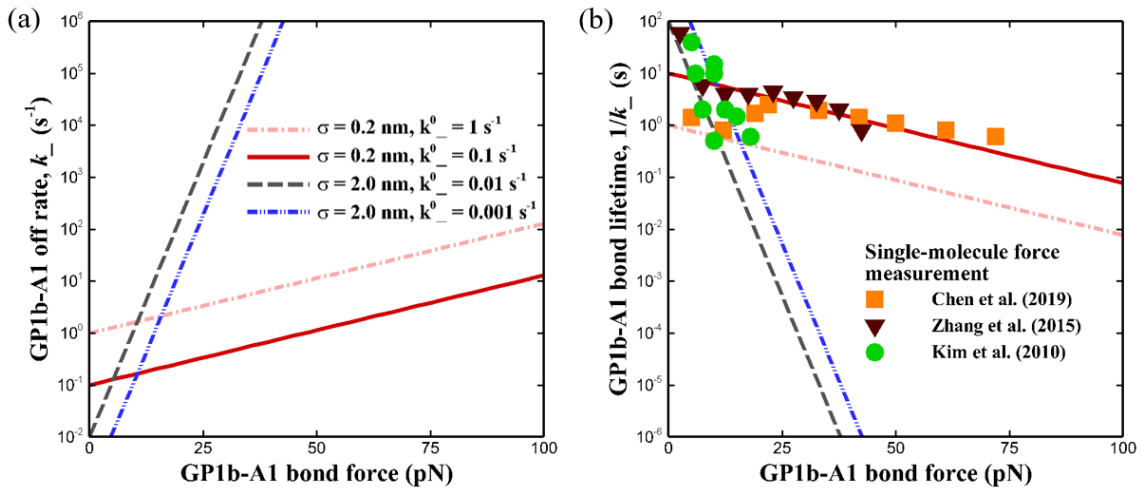

Figure 6.4: GP1b-A1 bond off rate (a) and bond life time (b) as functions of GP1b-A1 bond force. The curves are the best fit to the existing measurement based on the Bell-type functional form. The symbols are experimental single-molecule measurements of the bond lifetime from various groups. The off rate is obtained as the reciprocal of the bond lifetime.

Calculation of the bound/unbound probability

With the obtained GPIb-A1 intrinsic rates, k_+ and k_-, the probabilities for GP1b-A1 bond formation and rupture can then be determined. By solving the master equation, $\frac{P_i}{dt} = k_i(1 - P_i); i \in +, -$ [234], the bound probability for two reactants (GPIb and A1) upon encounter (through transport), P_+, and the unbound probability of the existing GP1b-A1 bond, P_-, can be calculated by

$$P_+ = 1 - \exp[-k_+ \Delta t], \tag{6.8}$$

$$P_{-} = 1 - \exp[-k_{-}\Delta t], \tag{6.9}$$

respectively, where Δt is the time interval used to update the binding state. Because of the high temporal resolution in our computational method, Δt is set to 100 LB timesteps, meaning the bound or rupture attempts between each VWF-A1 and platelet-GP1b are performed every 100 timesteps. The P_{+} and P_{-} are used to quantitatively regulate the likelihood of forming a new GP1b-A1 bond or rupturing an existing GP1b-A1 bond, respectively.

6.2.4 WLC model for the GP1b-A1 bond force

The GP1b-A1 bond is modeled as a worm-like chain (WLC) spring to capture its hyperelastic behavior observed experimentally [219, 220]. The WLC model can be expressed as follows,

$$F_b = \frac{k_B T}{L_p}[\frac{1}{4(1 - l/L_0)} - 0.25 + \frac{l}{L_0}], \tag{6.10}$$

where L_p is the bond persistence length, L_0 is the bond contour length and l is the bond extension. To account for the effective bond extension caused by the unfolding of the juxtamembrane mechanosensitive domain (jMSD) within the GP1b complex [220], the bond contour length is assumed to be $L_0 = 100\ nm$, longer than the actual GP1b-A1 bond; while the bond persistence length is set to $L_p = 0.08\ nm$. The bond force is cut off at $F_b = 100\ pN$, which is the typical maximum bond force under which the GP1b-A1 bond ruptures [221].

6.2.5 Parameter space

VWF length

VWF length varies under different pathphysiological conditions. As demonstrated by the western blot data in Fig. 6.5(c,d) [236, 237], VWF multimers formed in endothelial cells and platelet α-granules are typically rich in high-molecular-weight multimers (HMWMs)

that are up to 40 000 kDa, which corresponds to 80 dimers or 12.8 μm in VWF length [214]. After release to blood and subject to the cleavage of protease ADAMTS13, VWF multimers are regulated to containing about 1 to 40 dimers, featuring a VWF contour length of $0.16-6.4$ μm [238, 239]. Moreover, the size distribution of the plasma VWF exhibits an exponential distribution with the high-molar fraction highly polarizing the short-VWF side [240]. As a result, the average size (defined as the molar-fraction-weighted mean) of VWF in normal plasma is about 4 dimers or 0.64 μm in length.

von Willebrand disease (VWD) type 2A/2B shows a lack of intermediate ($4-10$ dimers or $0.64-1.6$ μm in length) and/or large ($10-40$ dimers or $1.6-6.4$ μm in length) size VWF [211, 212], as shown in Fig. 6.5(b). Clinically, VWD type 2A/2B is oftentimes associated with prolonged bleeding times [241, 213]. Besides, patients regularly undergoing extracorporeal membrane oxygenation (ECMO) or ventricular assist device (VAD) treatment often develop acquired von Willebrand syndrome (aVWS), which also features a shortening of VWF length and consequently bleeding disorders [242, 243]. These scenarios shift the average size of the plasma VWF towards $1-2$ dimers, $i.e.$, $0.16-0.32$ μm in length [239].

Under pathological conditions such as thrombotic microangiopathies (TMA) or thrombotic thrombocytopenic purpura (TTP), excessive presence of ultra-long VWF (ULVWF) (>60 dimers or >10 μm in length) would occur in the plasma or/and on the surface of endothelial cells (shown in Fig. 6.5e), as a result of the deficiency or abnormality in ADAMTS13 [213]. Such elevated level of ULVWF often leads to excessive microthrombi formation in microvasculatures, causing extravagant recruitment of platelets and consequently also leading to bleeding disorders.

To understand how the difference in VWF length alters the SIPA process and causes VWF-length dependent thrombotic/hemostatic complications, we simulate SIPA with a wide range of VWF multimer sizes ranging from $2-100$ dimers or $0.32-16.0$ μm in VWF length, as indicated by the VWF length spectrum in Fig. 6.5a. This spectrum covers the

short VWF (0.32 μm) observed in both inherited VWD as well as aVWS, intermediate-size VWF ($0.64-1.6$ μm) in normal plasma, long VWF ($1.6-6.4$ μm) as a minority in normal plasma, and ULVWFs (16 μm) secreted from endothelial cells or platelet α-granules that excessively exist in TMA or TTP.

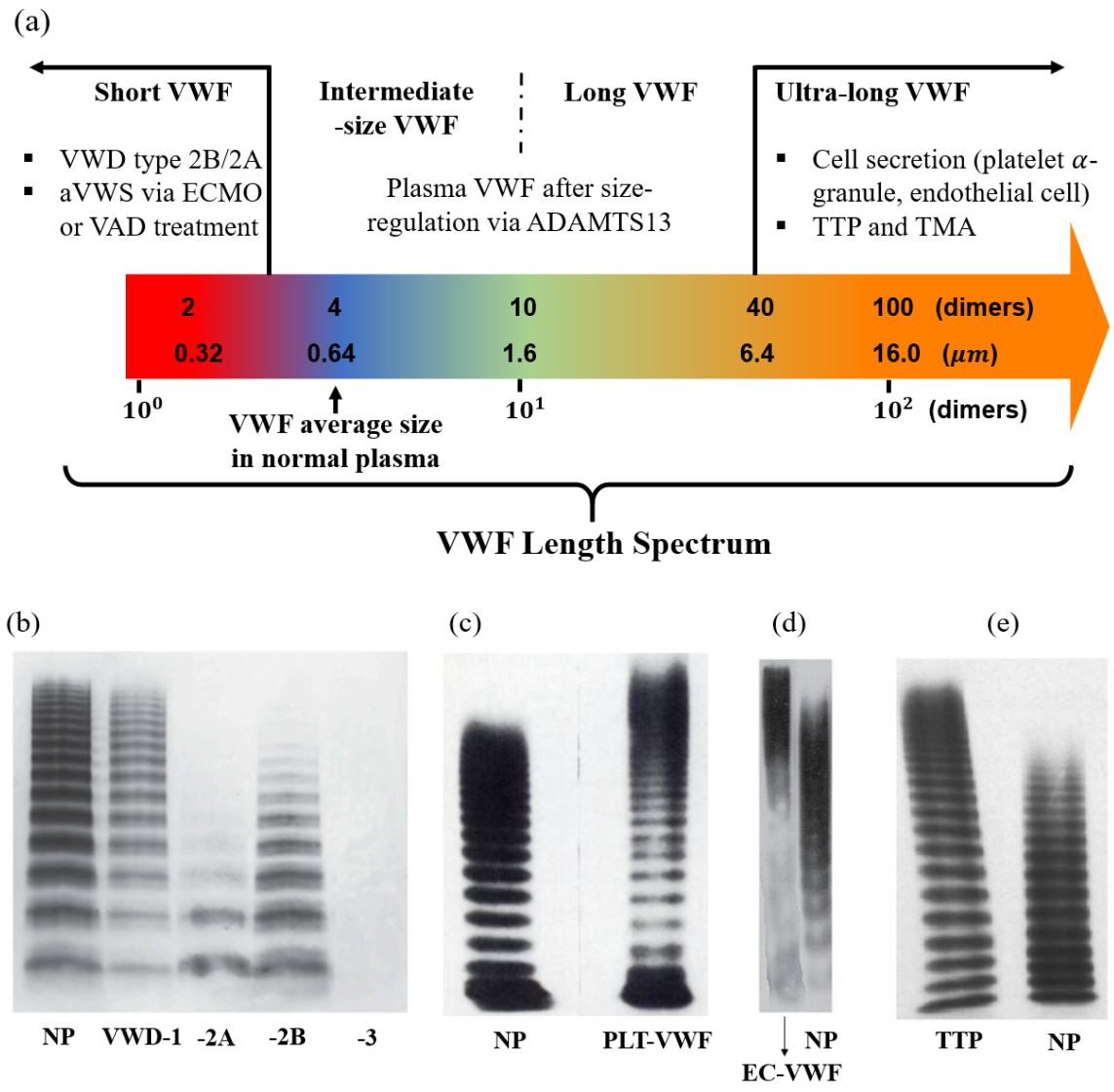

Figure 6.5: VWF length and concentration associated with pathophysiological events. (a) The VWF length spectrum (plotted in log scale) interrogated in the current study. Different VWF length corresponds to different pathophysiologic conditions as denoted. (b-e) The western blot data showing the difference in VWF size (length) distribution between normal plasma (NP) and VWD blood (b) [244], between NP and platelet-derived VWF (PLT-VWF) (c) [236], between NP and endothelial cell-derived VWF (EC-VWF) (d) [245], and between NP and TTP condition (e) [237].

VWF concentration

VWF concentration could also be altered through pathophysiological processes. The α-granule release upon platelet activation locally supplies VWFs that are not only long and ultra-long in length (Fig. 6.5c) but also up to 50$\times$ elevated in concentration [246]. Recent experiments using genetically modified mice that lack of α-granule showed α-granule release is necessary for occlusive thrombosis, suggesting the local elevation in VWF level may play an essential role in driving the rapid platelet accumulation and subsequently the thrombotic occlusion. In a separate pathological scenario, VWD type 1 is often associated with a partial quantitative deficiency of plasma VWF (Fig. 6.5b), while the structure and size distribution of VWF remains indistinguishable from normal [213]. In an more extreme scenario, VWD type 3 shows a complete deficiency of VWF [239] (Fig. 6.5b) and consequently results in excessive bleeding disorders in patients.

To reflect the role of VWF concentration in SIPA, a wide range of soluble VWF (sVWF) concentrations from $0.1\times$ to $18\times$ normal concentration are considered for each VWF length, where the normal VWF concentration is defined as 0.5% in terms of volume fraction as suggested in Chen $et\ al.$ [224]. Understanding the SIPA dependence on VWF concentration can provide biophysical insights to the pathology of VWD type 1 and 3 and help identifying the role of platelet-derived VWF in driving the occlusive thrombosis.

Other parameters

The shear rates selected for the following studies are $\dot{\gamma}$ $\geq$10 000 s^{-1}, which represent typical shear levels for occlusive arterial thrombosis [247, 248, 27] and was also reported to be critical shear levels that give rise to activation-independent platelet aggregation [210, 249]. The platelet concentration is set to $3\times$ normal platelet concentration to reflect the margination effect [19], which corresponds to a volume fraction of $\phi_{PLT} = 3.0\%$ [224]. The mural surface density of immobilized VWF (iVWF) is set to S_{VWF}=0.1 ng/mm^2, consistent with the existing $in\ vitro$ measurements of VWF surface absorption level [250,

251].

Three computational domains (10×20×10, 20×20×10 and 40×20×10 μm^3) are considered to ensure the results being independent of the periodic boundary condition in the streamwise direction, along which the VWF elongates. ULVWF is selected for the analysis, corresponding to a ratio of the streamwise domain size to the VWF length varying from L_x/L_{VWF}=0.6 to 2.5. The results suggest that the L_x/L_{VWF}=1.5 is the most cost-effective resolution (results are shown in the Appendix). Therefore, the intermediate-size domain 20×20×10 μm^3 is used for the subsequent studies.

All simulations are initiated by seeding the platelets and VWF uniformly distributed in the lower half of the domain to mitigate the confinement effect of the upper moving boundary. The VWF conformation is set to be a globular state initially to reflect the stress-free initial condition. The prescribed shear rate is imposed from time zero.

For the specifications of the GP1b-A1 intrinsic off-rate, the zero-bond-force off rate is fixed at $k_-^0 = 1\ s^{-1}$ and the reactive compliance is set to $\sigma = 0.2$ nm hereafter, except in § 6.3.3 where the influence of different σ from single-molecule measurements on SIPA will be discussed. Table 6.1 summarizes all 40 simulation cases, spanning the entire parameter space of interest to the current study.

6.2.6 SIPA metrics

To quantitatively describe the SIPA process in terms platelet agglomeration and capture, two dimensionless metrics are introduced. Following the concept of average coordination number that is typically used in chemistry or geology to describe the average number of neighbors surrounding a central atom/granule [252, 253], we define a platelet agglomeration index (PAI) as

$$\mathbf{PAI} = \frac{2N_{cnt}}{N_{plt}}, \tag{6.11}$$

where N_{cnt} denotes the number of pairs of platelets that are in close contact and N_{plt} is the total number of platelets existed in the system. The criterion for platelet contact is defined

such that the platelet-platelet separation is smaller than 10 nm.

To describe the level and rate of platelets being captured onto the thrombotic surface, a platelet mobility index (PMI) is defined as

$$\mathbf{PMI} = \frac{\langle V_{plt} \rangle}{\langle V_{fld} \rangle}, \tag{6.12}$$

where $\langle V_{plt} \rangle$ is the ensemble average of the platelet velocity in the system and $\langle V_{fld} \rangle$ denotes the volume-averaged fluid velocity within the control volume that initially suspended with platelets and VWFs.

Agglomeration is the ability of the platelets to come together to form a larger mass then may travel in the flow or stick to the wall. As the density of the mass increases, the PAI will increase. We use agglomerate to refer to the several platelets that may or may not be adherent to the wall. The PMI is 1 when the mass travels downstream in the flow, but goes to zero when the mass is captured by the wall and no longer moves. When an agglomerate is firmly captured to the wall and no longer moves (PAI$>$0 and PMI=0), then it is called an "aggregate" similar to common usage in platelet adhesion and aggregation studies.

6.3 Results

6.3.1 Dynamics of SIPA: platelet agglomeration and capture

Previous experiments [210, 249] observed platelet aggregates forming and adhering onto the wall under elevated shear. Such process is found to be independent of platelet activation and exclusively supported by VWF through GP1b-A1 bond formation.

More quantitative understanding of the SIPA process could be achieved by comparing the relevant timescales specific to the elevated high-shear environment, as shown in Fig. 6.6a. Considering a typical stenotic section that is 1000 μm long in the flow direction [254], the platelet transit time (defined as the time for the near-wall platelet to flow through the stenotic section) can be estimated as 100 to 1 ms as the wall shear rate chang-

ing from 10^4 to 10^6 s^{-1}. Hellums $et\ al.$ [255] experimentally quantified the minimal time required for the shear-induced platelet activation under various shear rates. The reported shear-induced platelet activation time, as plotted in Fig. 6.6a, is found to be much greater than the platelet transit time, when shear rate is $\ll 10^6$ s^{-1}. Although platelet activation may be possible within the platelet transit time when shear rate exceeds 10^6 s^{-1}, this high shear rate tends to be less relevant to the occlusive thrombosis since the net thrombotic growth approaches zero under that shear level [11]. As previously mentioned in Eqn 6.6, the formation of GP1b-A1 bond limited by its maximum intrinsic on-rate requires at least 10 μs, which acts as a lower bound for the time required for the capture of platelets and platelet aggregates.

Consistent with the experimental observations [210], our analysis suggests the SIPA under elevated shear should occur independent of the shear-induced platelet activation given the relatively short transit time. Moreover, in order for the mural capture of platelet aggregates as needed for thrombi growth, the timescale for SIPA under the shear rates of $10^4 - 10^6$ s^{-1} can be estimated to be within the range of $0.01-10$ ms, as denoted in the dark blue area of Fig. 6.6.

To verify the estimated timescales as well as the validity of the $in\ silico$ computational method, we conduct simulations (cases NO. 33-35 in Table 6.1) with parameters matching the $in\ vitro$ experiment by Ruggeri $et\ al.$ [210]. The VWF is $2\times$ the normal concentration to be consistent with the experiments. Three cases are conducted with different VWF length changing from $1.6\sim6.4$ μm to introduce possible variability. The shear rate is set to $20\ 000\ ^{-1}$, which also matches with the elevated shear imposed in Ruggeri $et\ al.$ [210].

Fig. 6.6b plots the time course of the SIPA in terms of platelet agglomeration and capture, quantified by PAI and PMI as defined in § 6.2.6. The two concepts of agglomeration and mobility in general feature different characteristics. Platelet agglomeration (PAI) forms quickly between 0-6 ms, and then plateaus when all the platelets in the domain are connected by sVWF. Platelet mobility (PMI), however, has a different time course. PMI

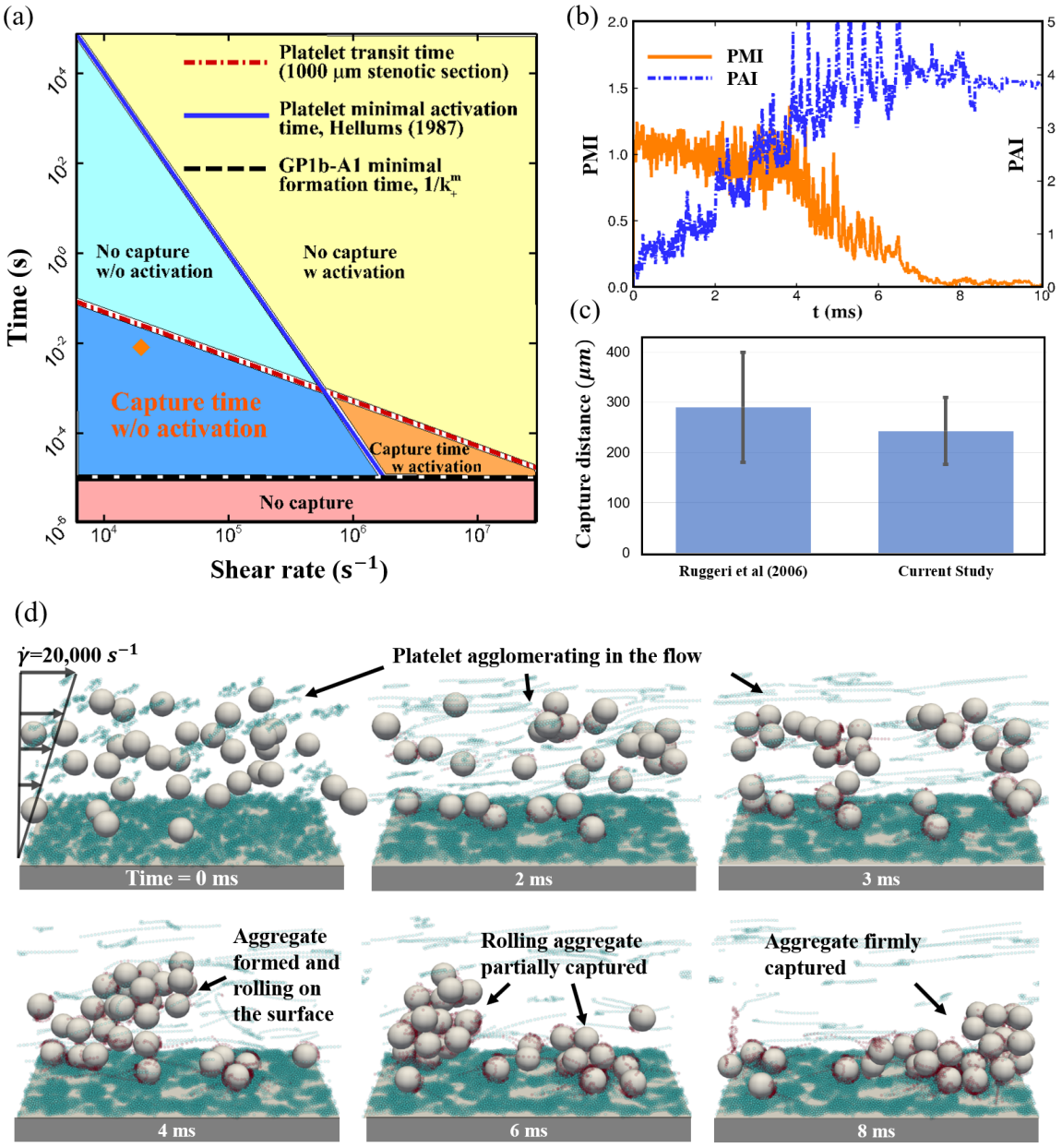

Figure 6.6: The dynamic process of SIPA specific to occlusive arterial thrombosis. (a) SIPA under elevated shear needs to be activation-independent and rapid ($< 10^{-2}$ s), given the relatively short platelet transit time and long platelet activation time. (b) SIPA under elevated shear involves platelet agglomeration and capture processes. (c) The platelet capture distance for SIPA under a shear rate of 20000 s^{-1}: a comparison between existing *in vitro* results and current *in silico* results. (d) The time sequence of the SIPA process under shear rate of 20000 s^{-1}. Green beads are regular VWF dimers; red beads are adhered VWF dimers (by forming GP1b-A1 bonds).

remains relatively constant between 0-4 ms, decreases after 4 ms, and then falls to zero at 8 ms as the agglomerate is firmly captured as an aggregate stuck on the wall. The different times for agglomeration and mobility processes suggests that platelets agglomerate in the flow before being captured at the wall. In other words, platelet agglomeration can gather platelets away from the wall before being captured at the wall.

Our model predicts that platelet aggregates would not form at the entrance of a high shear zone until the agglomerates are captured. By integrating the average velocity of platelets over time, the platelet capture distance can be calculated as $L_{cap} = \int_0^{t=8ms} \langle V_{plt} \rangle dt \approx 240 \pm 50 \mu m$. This streamwise travel length of $240\ \mu m$ compares favorably with the observation of no aggregates at the beginning of the high shear zone for $280 \pm 100 \mu m$ observed in vitro by Ruggeri $et\ al.$ [222], as demonstrated in Fig. 6.6c. Another way to interpret the lack of mural aggregates is to calculate a capture time, or the time to observe aggregates at the wall. The model estimates the capture time at about 8 ms ($t_{cap} \approx 8\ ms$) under the specific shear rate ($\dot{\gamma} = 20\ 000$). We mark this point on the Hellums-type plot that falls in the region of capture without activation as previously defined (Fig. 6.6a, diamond symbol). The analysis and simulation results collectively match the experimental observations that SIPA under elevated shear occurs in millisecond-scales, thus add credibility to the $in\ silico$ model developed in the current study.

6.3.2 Roles of soluble VWF and immobilized VWF

To further identify the specific roles of soluble VWF (sVWF) and immoblized VWF (iVWF) in SIPA, we selectively remove sVWF and/or iVWF in the system to study its effect on platelet agglomeration, aggregate capture and bond formation. For the cases simulated in this section, the shear rate is set to 10 000 s^{-1} and VWF length is 1.6 μm (normal whole blood). The sVWF concentration is set to 6$\times$physiologic concentration (3%) to shortening the computational time needed for observing phenomenological endpoint differences (such as whether capturing aggregates or not) between cases.

Fig. 6.7a and 6.7b shows the dynamics of platelet agglomeration and capture, respectively. In the presence of both sVWF and iVWF, the platelet agglomerates rapidly with PAI increasing from 0 to 5 in the first $\sim$3 ms. At about t=3 ms, the formed agglomerate in the system gets firmly captured and becomes an aggregate, as the PMI drops to $\sim$0. The small, finite fluctuation in PMI near zero is a result of the unsteadiness in flow caused by the fluid-structure interaction.

Removing all VWF (no VWF) serves as a control: the platelets do not agglomerate (PAI$\sim$0.9) and mobility stays at 1. Attached iVWF only has a small effect: PAI$\sim$0.9 and mobility is slightly less than 1 from a few individual platelets being captured at the wall; No platelet aggregation is observed. Plasma sVWF with no iVWF (sVWF only) causes the platelets to agglomerate with PAI increasing in a similar manner to the normal case. However, mobility in the sVWF only case actually increases dramatically. This rise in the platelet mobility is caused by the agglomerate migrating away from the wall and traveling in the higher velocity fluid away from the wall. The larger, deformable agglomerates are subject to cross-stream migration by the lift force caused by the hydrodynamic interactions with the wall, which has been experimentally observed previously [169].

The bond formation for the SIPA process is shown in Fig. 6.7c and 6.7d. For the normal case, more than 6000 GPIb-A1 bonds form to agglomerate and capture the aggregates. When sVWF only is present in the system, the formation of 6000 GP1b-A1 bonds is about the same as the normal case in the first 3 ms as agglomeration occurs. When iVWF only is present, only about 500 GP1b-A1 bonds can form as opposed to more than 6000 bonds formed when sVWF is present, as a result of lacking in-flow GP1b-A1 formation ($i.e.$, platelet agglomeration). When iVWF is present, the VWF-association bonds generally starts at a level of around $\sim$2000 bonds from the fast formation of mural VWF nets upon VWF elongation in less than 2 ms upon exposure to elevated shear rates (e.g., see Fig. 6.6d). In the presence of both sVWF and iVWF, further increase of the VWF-association bonds (from $\sim$2000 to $\sim$4000 bonds after 2 ms) predominantly comes from the inter-association

among sVWF. The number of VWF-association bonds in general shows a high-frequeny fluctuation over time when sVWF is present. Through power spectrum analysis, a peak frequency of $f_p = 15\ 000\ s^{-1}$ for the fluctuating VWF-association curves is obtained, which is close to the imposed shear rate ($\dot{\gamma}$=10 000 s^{-1}). This indicates that the rotational and elongational effect of the shear periodically rupture the VWF-association bonds.

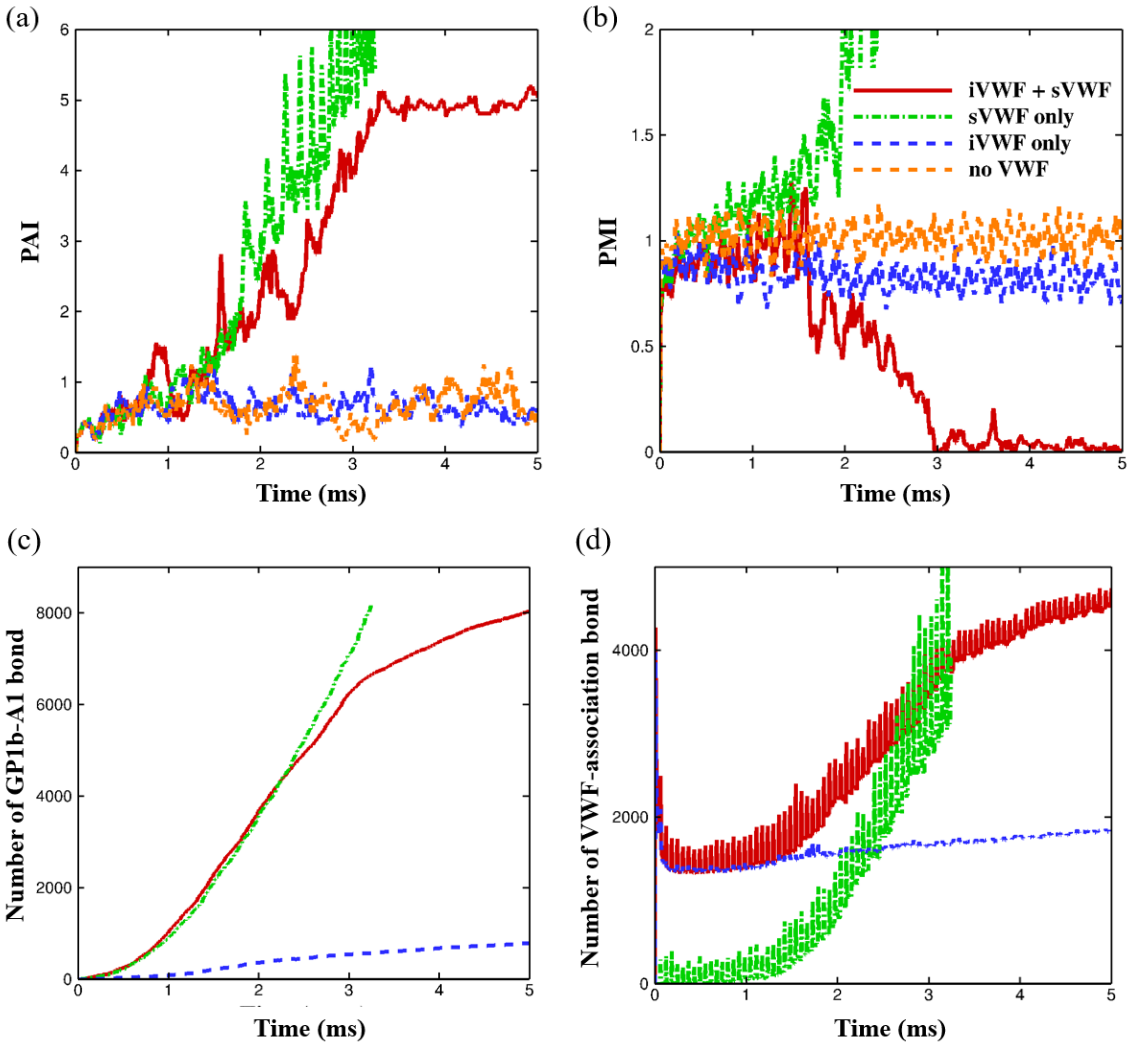

Figure 6.7: The time course of platelet agglomeration index (a), mobility index (b), number of GP1b-A1 bonds (c) and number of VWF-association bonds for selective VWF conditions. For the set of simulations, the shear rate is 10000 s^{-1} and the VWF length is set to 1.6 μm.

It should be noted that previous experiments by Ruggeri $et\ al.$ [210] demonstrated that sVWF is necessary for activation-independent platelet aggregation under elevated high shear. Here we describe the sub-second events that cause the platelet agglomerate to form in the flow and be captured as an aggregate onto the wall. Our computational work based on first principles explicitly show that the platelet micro-agglomerates can be assembled in the flow through the shear-induced entanglement of sVWF without the presence of iVWF. iVWF is then necessary for the mural capture of the flowing platelet agglomerate.

Our results directly demonstrate that SIPA is driven by in-flow platelet agglomeration that precedes the mural capture of the platelet agglomerate (if that occurs), as a two-step process. Note that this is different from the existing understanding of platelet aggregation under high shear, which generally presents a picture of single platelet capture on a surface with subsequent platelet aggregates forming on top of this captured platelet through various mechanisms [256, 215]. Our finding describes a new paradigm for high shear induced platelet aggregation forms from platelet agglomerates formed in the flow that are then captured as opposed to single platelet accumulation. This mechanism would allow the aggregate to grow much faster and could account for the rapid platelet accumulation (RPA) phase II as distinct from the an initial iVWF formation phase I (lag time) [204].

6.3.3 Effect of the GP1b-A1 bond reactive compliance

In this section, we aim to understanding how the difference in GP1b-A1 bond reactive compliance would impact the SIPA process so as to evaluate the actual prothrombotic effect of various existing GP1b-A1 bond lifetime measurements [220, 221, 219]. Two levels of GP1b-A1 bond reactive compliance, σ=0.2 versus 2.0 nm, are selected for the analysis, representing the reports of single-molecule assays by the Li group [220] and the Zhu group [221] versus that by the Springer group [219], respectively. The GP1b-A1 bond off-rate (lifetime) is much more sensitive to the change of σ compared to k_-^0, as previously shown in Fig. 6.4. Therefore, a fixed zero-bond-force off rate k_-^0=1 s^{-1} is selected

for this example. An intermediate-size (L_{VWF}=1.6 μm) VWF at normal and $6\times$normal concentrations are selected to bring in variation of the available A1 ligands.

As shown in Fig. 6.8, For a low reactive compliance ($\sigma = 0.2\ nm$) of the GP1b-A1 bond, platelet agglomeration occurs between 0 and 6 ms (blue trace on Fig. 6.8(a)) and the agglomerate is captured as a platelet aggregate around 7ms, as shown in Fig. 6.9(b). Adding more VWF to the system further elevates the agglomeration level and shortens the capture time to 3 ms. The rapid SIPA process occurred with $\sigma = 0.2\ nm$ is accompanied and driven by the rapid formation of $4000-9000$ GP1b-A1 bonds and $3000-7000$ VWF-association bonds in milliseconds. Moreover, elevating VWF concentration by $6\times$ increases the rate of GP1b-A1 and VWF-association bond formation by more than 2 folds. The platelet aggregates formed with the low reactive compliance GP1b-A1 bonds can be visualized in Fig. 6.9(a,c).

In contrast, a large reactive compliance ($\sigma = 2.0\ nm$) prevents SIPA even with $6\times$ elevated VWV concentration. Specifically, platelets located away from the wall largely remain translating with the flow, while the platelets adjacent to the wall show a capture-and-release pattern, as manifested by the large fluctuations in the PMI values((pink and light blue traces in Fig. 6.8(b)). Neither platelet agglomeration nor firm platelet adhesion are observed with $\sigma = 2.0\ nm$, as shown by the simulation snapshots in Fig. 6.9(b,d). This can be explained by the fast degradation of the GP1b-A1 bond stability at elevated shear stresses, such that the bond lifetime becomes comparable to or shorter than the minimal bond formation time ($t_b \leq 1/k_+^m \approx 10^{-5}\ s$). As a result, the net accumulation of GP1b-A1 bonds remains very low and insufficient to give rise to SIPA. Intriguingly, the number of VWF-association bond at $\sigma = 2.0\ nm$ is much smaller than that at $\sigma = 0.2\ nm$, despite the characteristics of the VWF-association bond remaining identical. This implies that the VWF-association bond formation depends on the GP1b-A1 bond formation; in other words, the VWF association seems to be an outcome of the platelet agglomeration primarily supported by GP1b-A1 bond formation.

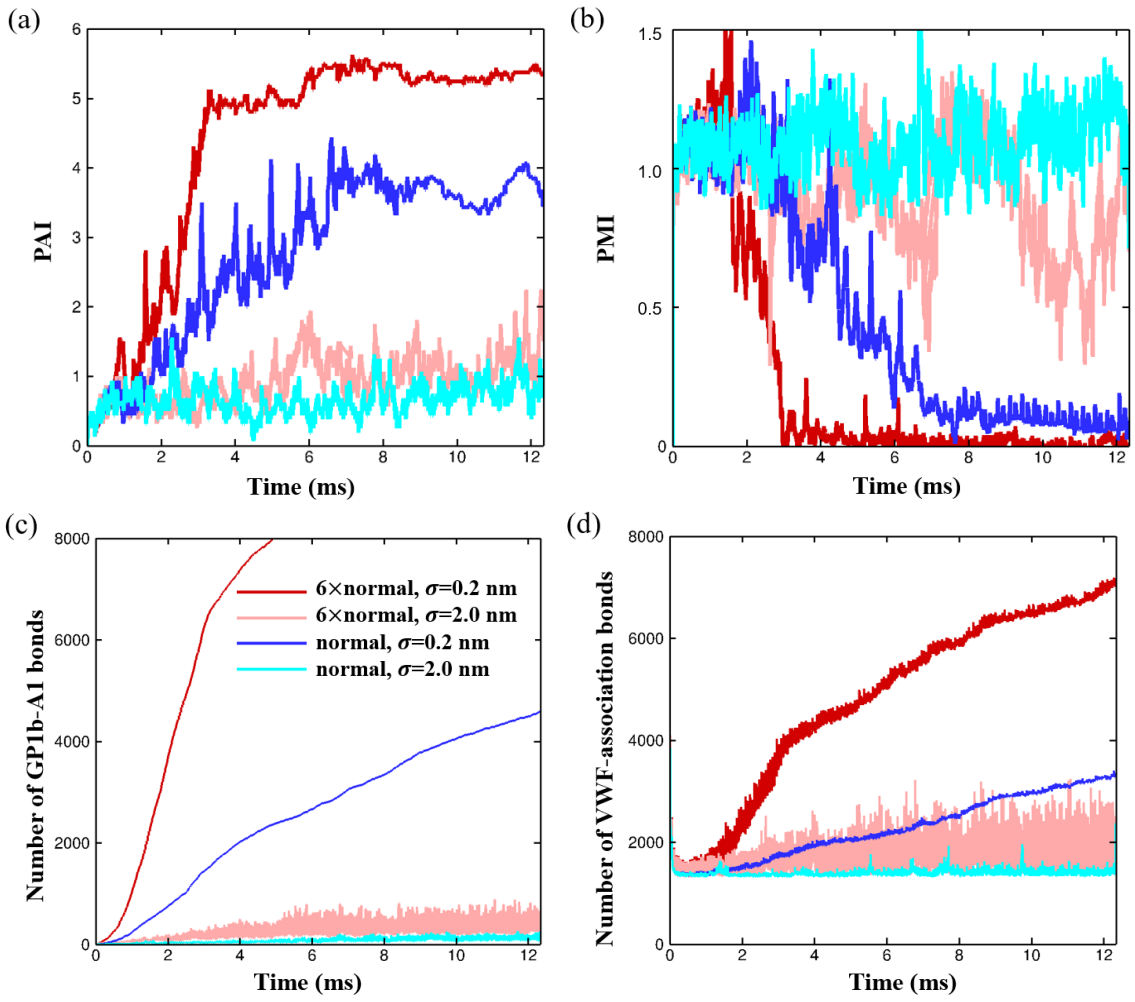

Figure 6.8: The time course of (a) platelet agglomeration index (PAI), (b) platelet mobility index (PMI), (c) number of GP1b-A1 bonds and (d) number of VWF-association bonds based on different GP1b-A1 bond reactive compliance, σ, for normal VWF concentration and elevated (6$\times$normal) VWF concentration. For this set of simulations, the shear rate is 10,000 s^{-1} and the VWF length is set to 1.6 μm.

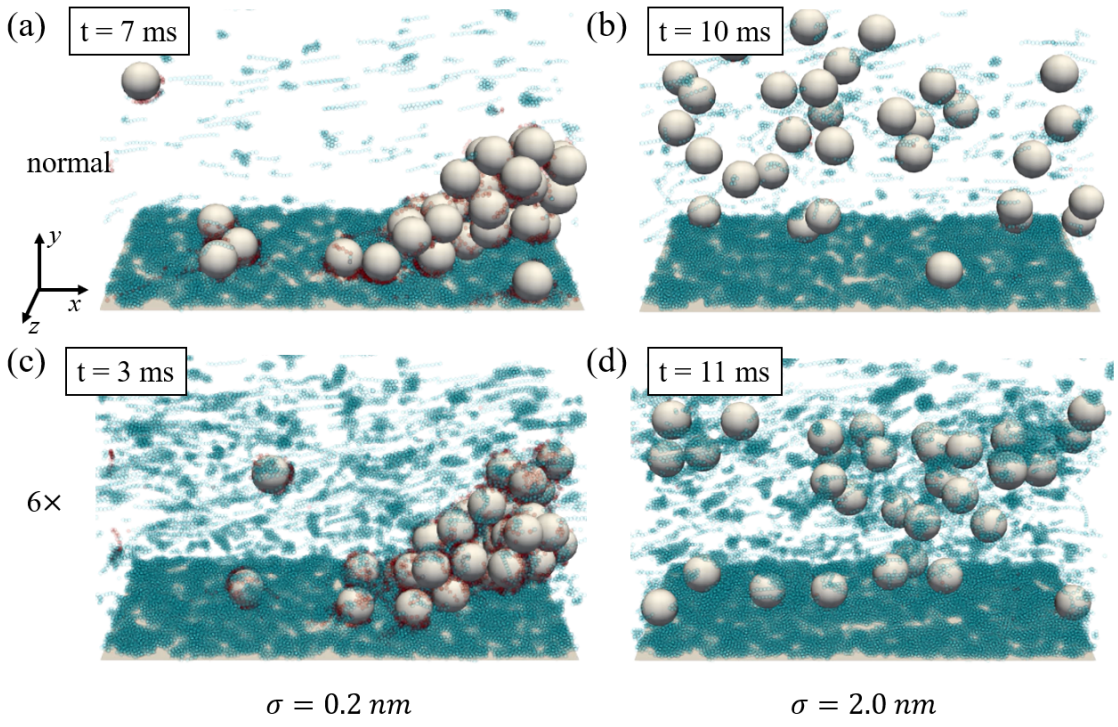

Figure 6.9: The platelet and VWF distribution during the SIPA process for two GP1b-A1 reactive compliance ($\sigma = 0.2$ and 2.0 nm) reported from single-molecule measurements at normal and elevated (6×normal) VWF concentrations. The time-point for each snapshot is indicated accordingly. (a, c) For small reactive compliance, aggregates form within 7ms. (b,d) For VWF with large reactive compliance, agglomeration does not occur.

6.3.4 Dependence of SIPA on VWF characteristics

The bioactivity of VWF heavily depends on its biological characteristics primarily including the VWF concentration (level) and VWF length (size). As already discussed in § 6.2.5, altering the VWF characteristics could lead to severe thrombotic and hemostatic diseases. Understanding how the alteration of VWF characteristics leads to the change of high-shear clot formation through SIPA may shed light on the pathology and potential treatment of relevant pathological complications.

Dependence on VWF concentration

To demonstrate the effect of changing VWF concentration on the microthrombi formation at the thrombi-blood interface, we simulate SIPA with the a wide range of sVWF concentrations changing from 0.1 to 18× normal concentrations at each specific VWF length. Here, we select the cases (Case NO. 3, 8, 13, 23 and 30) with intermediate-long VWFs (L_{VWF}=1.6 μm) for discussion.

As shown in Fig. 6.10 (a), increasing the sVWF concentration leads to a greater slope of the PAI curve, indicating the platelets agglomerates more rapidly. As a result, the time to capture the agglomerate deceases as indicated in Fig. 6.10b. For this particular intermediate-length VWF (L_{VWF}=1.6 μm), normal and elevated VWF concentrations (1∼18× normal concentration) lead to a firm capture of the agglomerate (PMI∼0). Quantitatively, elevating the normal sVWF concentration by 6× shortens the capture time by about 2.7 fold; elevating concentration by 18× shortens the capture time by about 4 fold. Diluting VWF concentrations by 10% and 40% (0.1× and 0.4×) reduces agglomeration as well as preventing platelet aggregation, as the PMI maintains around 1 (Fig. 6.10(b)).

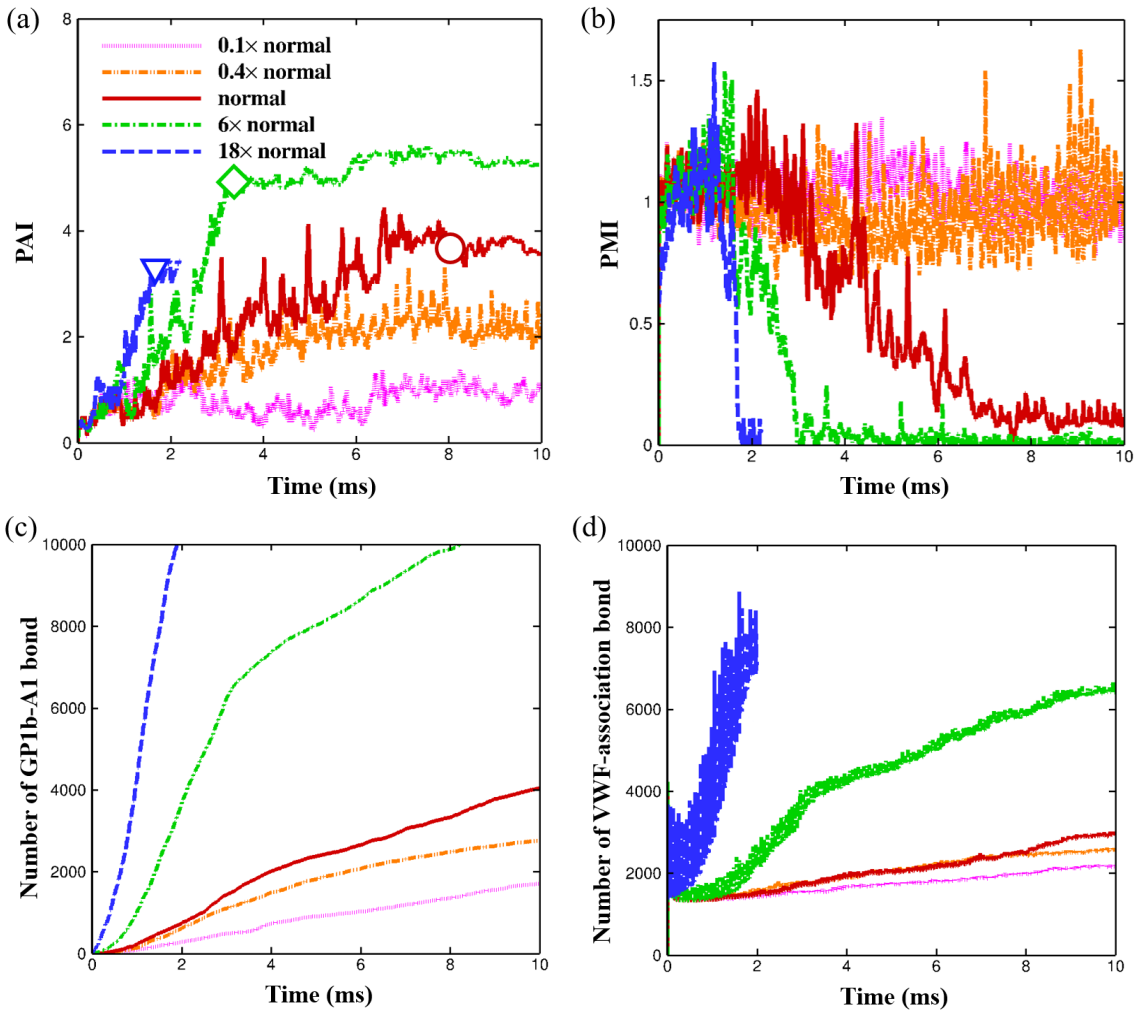

Figure 6.10: The time course of (a) platelet agglomeration index (PAI), (b) platelet mobility index (PMI), (c) the number of GP1b-A1 bonds and (d) the number of VWF-association bonds for different VWF concentrations. For this set of simulations, the shear rate is 10,000 s^{-1}. The platelets are set to 3×normal concentration to account for the margination effect. The VWF length is set at 1.6 μm.

The temporal change of bond numbers provides further insights to the SIPA process. As shown in Fig. 6.10c, the formation rate of GP1b-A1 bonds increases considerably with the elevation of sVWF concentration despite the platelet concentration remaining constant. This suggests the finite number of platelets can provide abundant binding sites to support an elevated level of GP1b-A1 binding events and platelet number is generally not the critical

limiting factor [226]. This is consistent with the experimental observation that each platelet on average contains more than 15000 GP1b receptors that is sufficiently high to support excessive binding events [257, 258]. The formation of VWF-association bonds in general follows the same trend as the GP1b-A1 bonds, which is aligned with the hypothesis that VWF-association depends on the GP1b-A1 bond formation during SIPA as speculated in § 6.3.3.

Fig. 6.11 depicts the platelet-VWF distributions in the long-time asymptotic limit. The dilute VWF concentration (0.4×) clearly manifests a cell-free layer between the adhered platelet mono-layer and the platelet aggregate suspended in the flow. In contrast, normal or elevated VWF concentrations show firmly captured platelet aggregates.

The captured aggregates also features a non-monotonic dependence on the VWF concentration, as the normal and severely elevated (18×normal) VWF concentration has a more elongated morphology (with PAI ranging from 3∼4) compared to the moderately elevated (6×normal) VWF concentration (with PAI around 5). Such non-monotonic change in the aggregate compactness can be explained by the synergy between GP1b-A1 bonds and VWF-association bonds. While moderate elevation in VWF concentration leads to more compact aggregates due to more GP1b-A1 bonds ((Fig. 6.10c) agglomerating the platelets, further elevation in VWF concentration could lead to excessive VWF association (Fig. 6.10d) between platelets which separates platelets through volume exclusion effect and through an increase in effective VWF from attached VWF strands.

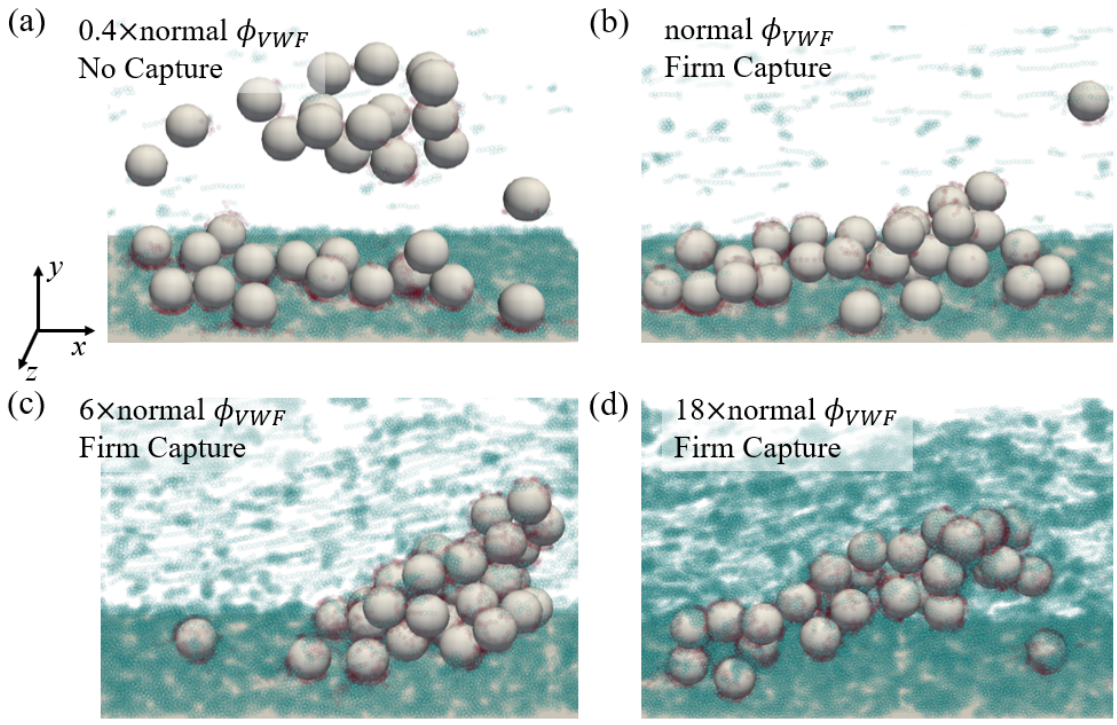

Figure 6.11: Platelet agglomeration and capture at (a) dilute (0.4×), (b) normal, (c) moderately elevated (6×) and (d) severely elevated (18×) sVWF concentrations. An intermediate-length (1.6 μm) VWF is selected for all the cases here. For this specific VWF length, diluting sVWF to 40% prevents the aggregate from being captured (a). Normal and elevated sVWF concentration can lead to firm capture (b−d).

Dependence on VWF length

To understand how VWF length alters the microthrombi formation, we simulated SIPA with various VWF length changing from 0.32 to 16 μm for each specific VWF concentration. Note that two dimers is 0.32 μm and ULVWF can be $>$16 μm (100 dimers). Here, we select the cases with normal VWF concentration (Case NO. $11-15$) and shear rates of 10,000 s^{-1} for this section.

The platelet agglomeration proceeds with various VWF lengths and are plotted as platelet agglomeration index (PAI) in Fig. 6.12(a). All PAI curves plateau after about 8 ms, indicating the agglomeration forms quickly and the system reaches equilibrium. As the VWF length increases, the platelet agglomeration rate (slope of the PAI curves before plateau) changes less than with concentration. Specifically, increasing VWF length from short (2 dimers or 0.32 μm) to long (40 dimers or 6.4 μm) enhances the agglomeration rate. In contrast, further increasing the VWF length to ultra-long (100 dimers or 16 μm) lowers the agglomeration rate.

The platelet capture processes are depicted in Fig. 6.12b as the platelet mobility index (PMI). With short VWF length (0.32 μm), the PMI oscillates around 1 even after the system reaching equilibrium. Correspondingly, the platelet aggregate remains suspended without being captured. Similar to the dilute VWF concentration case shown in previous section, a cell-free layer persists between the flowing aggregate and the surface of platelet monolayer (formed by platelet adhesion) as shown in Fig. 6.13(a). As the length of VWF increases to an intermediate regime (0.64 μm), the PMI at equilibrium decreases to 0.5. Such reduced level of PMI corresponds to a marginal capture of the aggregate onto the thrombotic surface, which exhibits a periodic "catch and release" adhesion between the aggregate and the adhered platelet monolayer, as shown in Fig. 6.13b. Further increasing VWF length to above 1 μm leads to the firm capture of the platelet aggregates. The capture time for $1.6-6.4$ μm VWF is about 8 ms, while it can be shorten to 6 ms with ULVWF (16 μm).

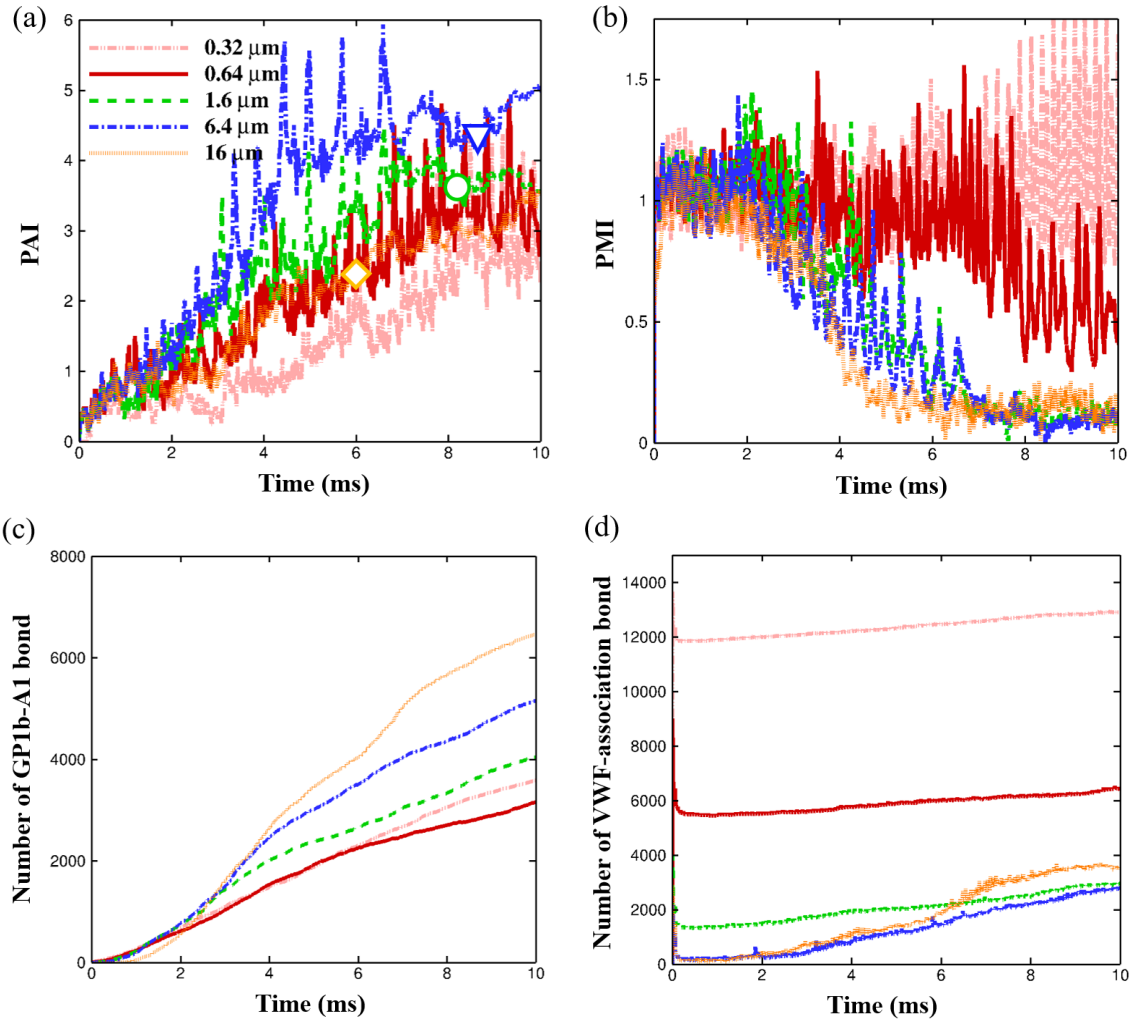

Figure 6.12: The time course of (a) platelet agglomeration index (PAI), (b) platelet mobility index (PMI), (c) the number of GP1b-A1 bonds and (d) the number of VWF-association bonds at different VWF length. For the VWF length, 0.32 μm corresponds to 2 dimers and 16 μm corresponds to 100 dimers. The symbols in (a) denotes the point when the aggregate becomes captured. For the set of simulations, the shear rate is set to 10,000 s^{-1}. Platelets is 3$\times$normal concentration and VWF has a normal plasma concentration.

Since the agglomeration rate with ULVWF is significantly lower than that with long VWFs, the shorter capture time in ULVWF suggests ULVWF is capable of arresting a rather loose aggregate, as demonstrated in Fig. 6.13(d). The PAI for the captured aggregates is denoted by symbols in Fig. 6.12, where the PAI upon Capture for ULVWF is about 2.5

and the PAI for longer VWFs is greater than 3.5.

Decreasing VWF length (with the same volume fraction) increases the level of VWF association (more VWF-association bonds) but reduces the rate of GP1b-A1 bond formation, as indicated in Fig. 6.13(c) and Fig. 6.13(d), respectively. The VWF length induced change in the number of VWF-association bond is more prominent compared to that of the GP1b-A1 bond. In particular, short VWF (0.32 μm) yields $\sim 6\times$ more VWF-association bonds compared to ULVWFs; while its number of GP1b-A1 bond is reduced by 50 %. This implies the platelet agglomeration occurred with short VWFs may be more supported by the VWF-association bonds, where with ULVWF the agglomeration is more driven by the GP1b-A1 bond.

Referring back to Fig. 6.12(a), the orange 16 μm ULVWF case features a persistent increase of PAI even after the capture event, while with green normal 1.6 μm case, the agglomeration level typically remains unchanged after the capture event. This behavior in PAI with ULVWF is associated with a post-capture compaction of the loose aggregate. During the aggregate compaction process ($6-7$ ms), the increase of VWF-association bond shows a rapid increase by 50% (orange curve Fig. 6.12(d)), while the GP1b-A1 bond curve roughly maintains the same slope (accumulation rate) (orange curve Fig. 6.12(c)). This suggests the post-capture compaction of the aggregate observed with ULVWF may be caused by the VWF association.

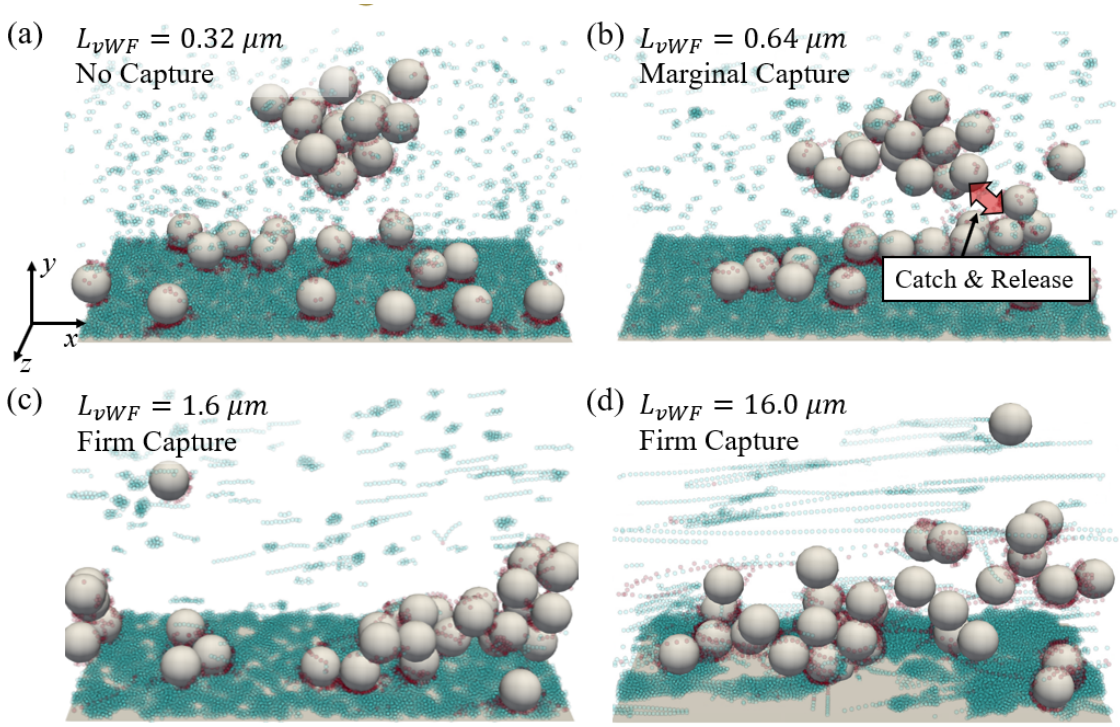

Figure 6.13: Platelet agglomeration and capture at normal VWF concentration with various VWF length. (a) Short VWF forms loose aggregate in the flow. The aggregate remains to be suspended without being captured onto the wall. (b) Average plasma VWF length leads to marginal capture of the aggregate. Marginal capture refers to a periodic ”catch and release” adhesion between the in-flow agglomerate and the adhered platelet monolayer. (c) Long VWF firmly captures the aggregate. (d) ULVWF can firmly capture the aggregate at a loose morphology.

Morphology and structure of captured platelet aggregate

The captured platelet aggregates that form under different VWF conditions show different morphological and structural characteristics. To understand how VWF length and concentration alters the aggregate morphology and structure, we summarize the PAIs of all 14 captured platelet aggregates and categorize the aggregate morphology observed in our simulations under different VWF conditions.

As shown in Fig. 6.14a, three aggregate morphological states can be classified based on the PAI levels. For PAI$\gtrapprox$4.5, the aggregates feature a $compact$ morphology where the platelets are densely packed into a spherical shape. Such compact aggregates mostly occur under moderately elevated (6$\times$) VWF concentration with intermediate VWFs that are typically available in normal plasma (NP). For 3$\lessapprox$PAI$\lessapprox$4.5, the aggregates exhibit an $elongated$ morphology with platelets packed primarily along the streamwise direction. Such elongated aggregates are commonly observable with NP-VWF under either normal VWF concentration or severely elevated VWF concentration. For PAI$\lessapprox$3, the aggregates feature a $loose$ morphology, where platelets are entangled by VWF nets without contacting each other. These loose aggregates mainly occurs with ULVWF or sometimes with long VWF under severely elevated concentrations. For visual demonstration purpose, the snapshots of aggregates for representative cases (A$-$F) are selected and depicted in Fig. 6.14a, which cover all three aggregate morphological states.

The PAI (average coordination number) can be experimentally related to its corresponding porosity and permeability in the context of a packed bed of spherical particles. Specifically, the porosity of the platelet aggregate can be estimated based on an empirical correlation by Lagemaat $et\ al.$ [259] as

$$\Omega_{PLT} = \frac{3.08}{\mathbf{PAI} + 1.13}. \tag{6.13}$$

With the calculated porosity, the permeability of the aggregate can be further calculated

based on the semi-empirical Kozeny-Carman (KC) correlation [260] as

$$k_{PLT} = \frac{2a_{PLT}^2 \Omega_{PLT}^3}{75(1-\Omega_{PLT})^2}, \tag{6.14}$$

where a_{PLT} is the radius of platelets with a value of 1 micron. The KC model is generally applicable to the porosity range of $0.26 < \Omega_{PLT} < 0.8$. The calculated aggregate porosity and permeability is also annotated in Fig. 6.14a. The compact aggregate has a porosity between $40-55\%$, corresponding to a permeability between $0.005-0.01$ μm^2. Elongated aggregate show a porosity between $55-75\%$, which corresponds to a permeability between $0.04-0.2$ μm^2. Loose aggregate in general has a porosity above 80%, where the permeability is much greater than 0.2 μm^2. In general, the platelet aggregates are at least 40% porous, which can affect the hydrodynamic drag it experiences and allow firm capture of such aggregates even under elevated shear.

Blood has a range of VWF size and concentrations. Processes such as cell release as discussed in § 6.2.5 could further alter the local concentration and size of VWFs in blood. It is expected that the three representative states of the platelet aggregate morphology being present in the vascular environment. In fact, previous $in\ vitro$ experiments have also observed the three states of mural aggregate morphology with NP-VWF [210] or EC-VWF (rich in ULVWF) [261], as demonstrated in Fig. 6.14(b). The aggregate morphology predicted by our $in\ silico$ approach compares qualitatively well with the $in\ vitro$ counterparts.

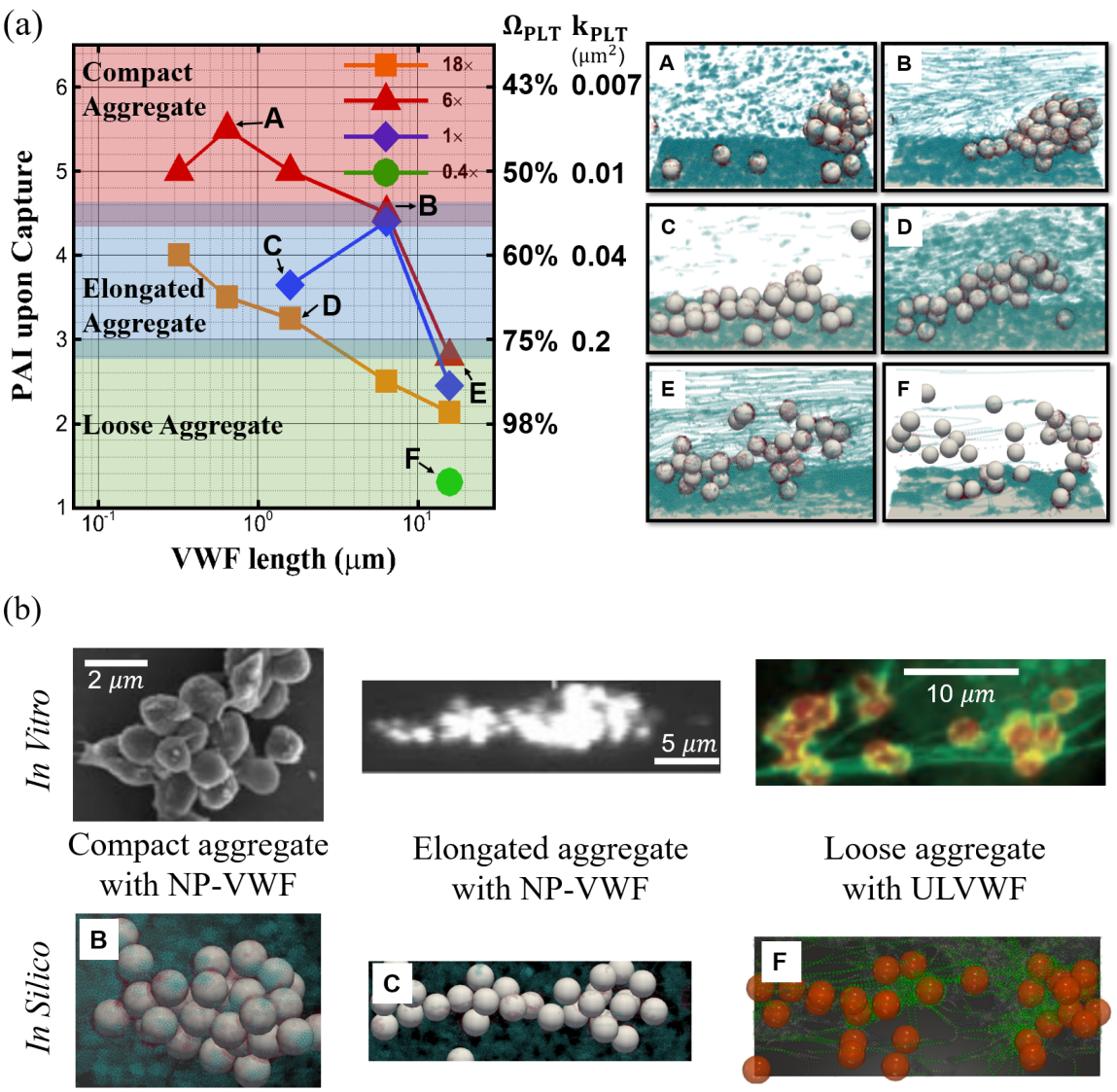

Figure 6.14: (a) Platelet agglomeration index of captured platelet aggregates as a function of VWF length and VWF concentration. The aggregate porosity (Ω_{PLT}) and permeability (k_{PLT}) are estimated and denoted based on the PAI values. The aggregate morphology for selective VWF conditions is denoted in alphabetical order and depicted on the right. (b) Top views of the morphology of captured platelet aggregates observed *in vitro* [210, 261] versus *in silico*. For all three cases, the flow direction is from left to right. The platelet color in the simulation is rendered similar to the experiment.

Phase diagrams of SIPA

SIPA can occur from several factors intersecting in complex ways. It is illustrative to create a phase diagram between VWF concentration and VWF length to show the boundaries between different behaviors of agglomeration and capture. To describe the rate of platelet agglomeration in the flow through VWF entanglement, we define an agglomeration rate as the slope of the best-linear fit to the PAI curve before reaching the long-time equilibrium plateau of the PAI ($t < t_{eq}$). Based on this definition, the agglomeration rate can be expressed as,

$$Agglomeration\ rate = \frac{\mathrm{d}[\mathbf{PAI}]_{t \leq t_{eq}}}{\mathrm{d}t}, \tag{6.15}$$

where the braket denotes the linear fit of the PAI curve when $t \leq t_{eq}$. Note that the platelet agglomeration rate does not necessarily determine how fast the platelet aggregates become captured onto the wall. To further describe the rate for aggregate capture, we define a capture rate based on the reciprocal of the aggregate capture time (t_{cap}) as follows,

$$Capture\ rate = 1/t_{cap}, \tag{6.16}$$

where the capture time is defined as the time needed for PMI to reach the long-time equilibrium plateau, provided PMI is less than 0.2 indicating a firm capture. The capture rate is set to zero ($i.e.$, $t_{cap} \to \infty$) when marginal or no capture (PMI>0.2) is observed. Based on the above definitions, we calculate the platelet agglomeration and capture rate specific to various VWF lengths and concentrations.

Fig. 6.15 plots the contour of agglomeration rate as a function of VWF length and concentration. Short VWF (<0.32 μm) and ULVWF (>10 μm) show relatively lower agglomeration rates compared to NP-level VWF length (0.64−6.4 μm). Diluting the VWF concentration to 10% eliminates the VWF-entanglement induced agglomeration, yielding an agglomeration rate below 0.1 ms^{-1} similar to the case without VWF. In other words,

we would expect that a large thrombus would NOT occur for these conditions.

Agglomeration rate shows a strong dependence on VWF concentration while only secondarily depends on the VWF length. Specifically, elevating the concentration of normal plasma (NP) VWF ($0.64-6.4\ \mu m$) by $6\times$ increase the agglomeration rate by 3 fold. With the intermediate VWF length ($0.64-1.6\ \mu m$), increasing the VWF concentration to $18\times$ increases the agglomeration rate by 5 fold, the fastest rate in the diagram. The primacy of the agglomeration dependence on VWF concentrations stresses the importance of local high concentration of VWF for effective hemostasis.

Overall, the platelet agglomeration under elevated shear is fast ($>0.4\ ms^{-1}$) in majority of the parameter space. As an example, based on the $0.4\ ms^{-1}$ agglomeration rate, an elongated aggregate (PAI=4) may form in less than 10 ms, provided the local VWF concentration remaining at least 40% the NP level. The agglomeration rate can be further enhanced by up to 5 fold with elevated VWF concentrations. Patho-physiologically, the quick formation of in-flow (mobile) agglomerates through SIPA may be a defensive mechanism in case of hemorrhagic injury. Such mobile agglomerate may act as building blocks ready to be captured onto hyper-thrombotic surfaces to stop bleeding.

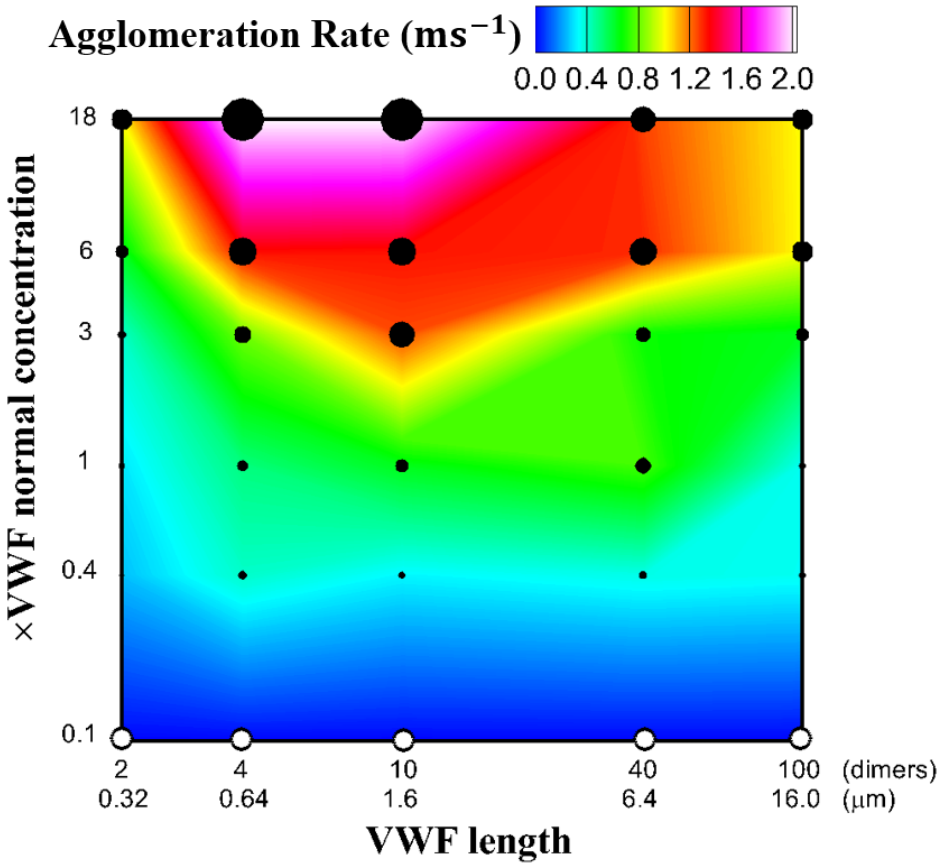

Figure 6.15: The rate of platelet agglomeration as a function of VWF length and VWF concentration. The filled symbols indicate an agglomeration rate that is above 0.1 ms^{-1} with the size of the symbol scales as the agglomeration rate. The empty symbols corresponds to an agglomeration rate below 0.1 ms^{-1}, which is comparable to the level of agglomeration in the absence of sVWF. The figure is plotted in log-log scale.

Fig. 6.16 plots the contour of capture rate with respect to VWF length and concentration. Three phases in terms of the aggregate capture characteristics can be observed. Short VWFs with diluted concentrations tend to cause no capture of the aggregate, which is indicated as the ”No Capture” phase. Increasing the VWF concentration and/or with long VWFs, a transitional phase featuring ”Marginal Capture” of platelet aggregates can be arrived. Further increasing the VWF concentration and length, the system transitions to the ”Firm Capture” phase.

Overall, the enhancement of the agglomerate capture is a strong function of concentration and secondarily by length. Increasing the VWF concentration from normal to $\sim 20\times$ with long VWF can leads to $5\times$ enhancement of capture rate. Increasing VWF length while maintaining VWF normal or slightly higher concentration ($3\times$) does not affect the capture as much. Alternatively, lowering the VWF concentration to sub-normal ($\sim 40\%$) can lead to no capture of agglomerate. Increasing VWF length does not alter the capture diagram as much. Nonetheless, ultra-long VWF lowers the VWF concentration (to $\sim 40\%$) required for capture.

Note that the normal blood condition with an average of 4 dimers of VWF will yield only marginal capture which is the balance that normal blood will want to maintain since blood should not clot in the normal vasculature. Some larger lengths of VWF in the blood can be on "reserve" to quickly stop blood loss when shear rates become elevated as in hemorrhage.

The corresponding long-time configurations of platelet-VWF complexes specific to different VWF conditions are summarized in Fig. 6.17, which schematically shows the transition from the no capture to the firm capture regime. Within the no capture regime, platelets are either uniformly dispersed or loose agglomerate in the flow, although near-wall platelet adhesion can still occur. Within the marginal capture regime, the aggregate loosely interacts with the surface through VWF tethers without being firmly captured. Within the firm capture regime, either loosely or compactly packed aggregates are firmly captured on the thrombotic surface.

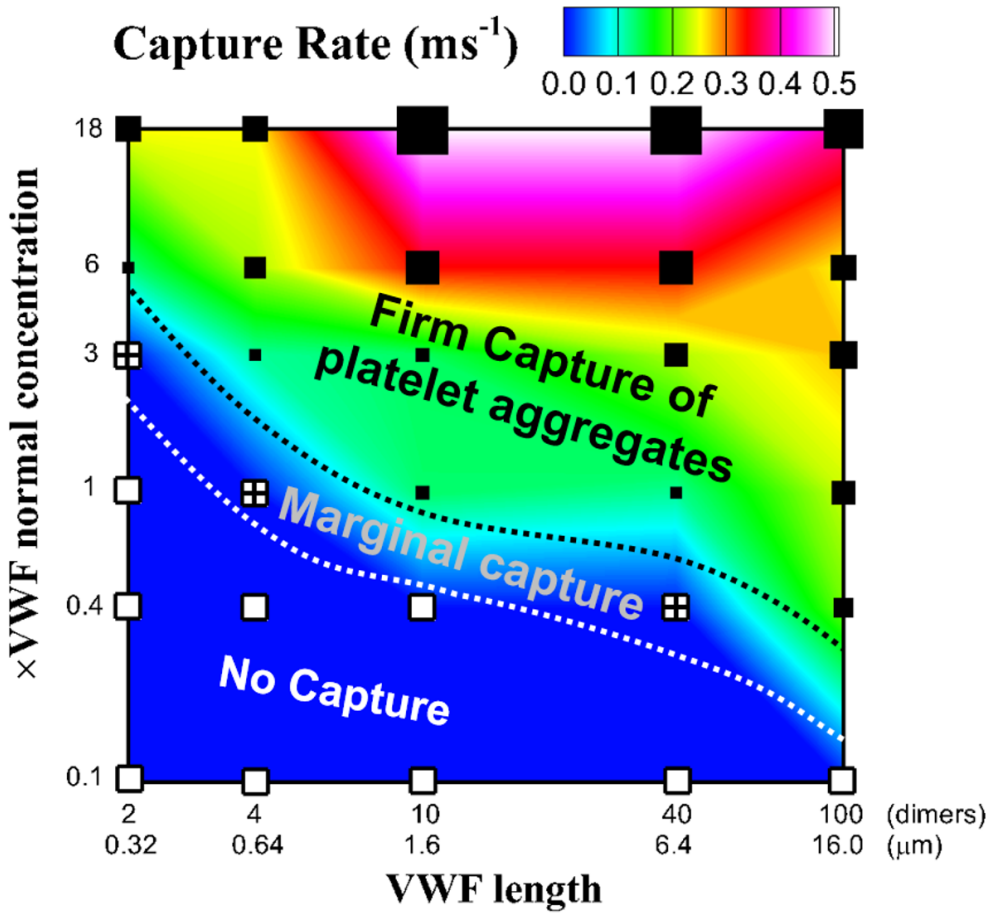

Figure 6.16: The rate of forming murally captured aggregate as a function of VWF length and VWF concentration. The filled, partially filled and empty symbols indicate the firm capture, marginal capture and no capture regime, respectively. The dashed lines qualitatively seperates the different regimes. The capture rate for the no capture and marginal capture regime is set to zero, as no firm capture of aggregates can be observed in the long-time asymptotic regime (when PAI reaches plateau). The figure is plotted in log-log scale.

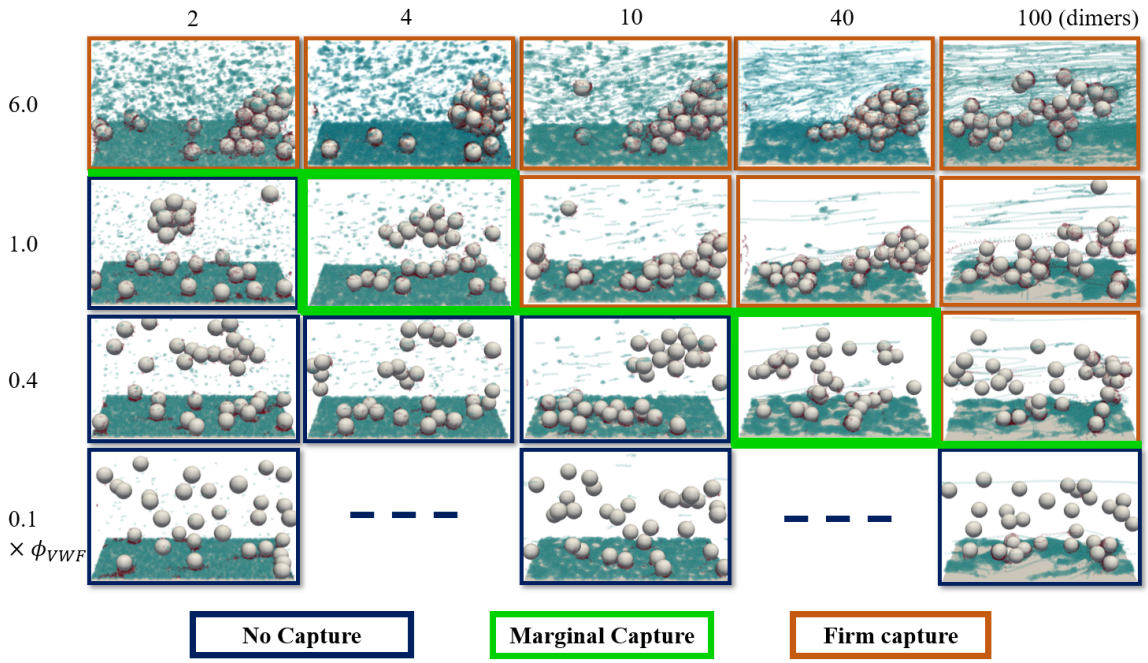

Figure 6.17: The long-time distribution of platelet and VWF under elevated shear with specific VWF lengths and concentrations. Elevating the VWF concentration or increasing the VWF at normal concentration leads the transition from no capture, to marginal capture and to firm capture of platelet aggregates.

6.4 Discussion

6.4.1 In-flow aggregate formation

Our results demonstrate the physics of platelet agglomerates in the flow through entanglement of VWF under elevated shear precedent to the mural capture of the platelet aggregate (if which occurs). Note that this is different from the existing viewpoint of platelet aggregation in the field of thrombosis and hemostasis, which generally regards the platelet aggregation as a surface phenomenon of discrete platelets attaching to pre-adhered mural platelets [256, 215].

Our findings define a new paradigm that the mural thrombi formation under elevated

shear is a two-stage process, where flowing platelets first agglomerate into micro-aggregates in the flow through entanglement by sVWF and then the preformed agglomerates are captured onto the thrombotic surface by iVWF (forming so-called platelet aggregates). Such in-flow pre-agglomeration through VWF entanglement facilitates the capture of platelets that are further away from the wall to increase the efficiency of thrombus formation.

6.4.2 Lag capture distance

Our $in\ silico$ approach quantitatively show that there should exist a lag capture distance (defined in 6.3.1) that is a few hundred microns ($\sim$200 μm) along the stream-wise direction, within which few platelet agglomerates can be captured on the thrombotic surface. Studies performed by our group using stenosis with wider throat (500$-$1000 μm) [30, 32, 262] show thrombi accumulation primarily occurs at the stenotic throat region where the shear rate peaks.

This capture distance may have relevance to studies with stenosis geometries that typically features a narrow throat (10$-$100 μm). Nesbitt $et\ al.$ [215, 216] observed thrombi accumulation primarily distal to the stenosis. Based on that, they proposed the thrombi formation is triggered by the large shear-gradient at the channel expansion region. The insignificant thrombus growth at the stenotic throat observed by Nesbitt $et\ al.$ may stem from their throat being much narrower than the lag capture distance such that few agglomerates could be captured at the peak of the stenosis. The platelet aggregates seen distal to the stenoses in their systems may have formed as agglomerates under high shear at the throat and then captured just downstream of the throat. We would predict that the agglomerates would then continually be captured and grow in the area $>$100 μm downstream as observed in their videos. Atherosclerotic stenoses typically have streamwise dimensions greater than 1 mm [263, 204, 264], so occlusive thrombosis would be expected to accumulate within the throat [263]. However, aortic valves that are stenotic but not thickened ($\sim$100 μm) may exhibit platelet aggregates downstream of the valve tips instead of on the leaflet edge as

seen clinically [265, 266].

Overall, the finding of lag capture distance using our computational approach aids in clarifying the controversy in terms of where the micro-thrombi initiates and grows. Besides, this lag capture distance could be an important geometric lower-bound constraint when designing thrombotic fluidic assays that are clinically relevant.

6.4.3 Microthrombi formation in milliseconds

Our study discovers that the microthrombi formation through VWF entanglement occurs on the millisecond timescale ($\sim 10^{-3}$ s). This is much shorter than the minimal time for shear-induced platelet activation ($1-10^{4}$ s) [255] and the typical GP1b-A1 bond lifetime (0.1−10 s) [219, 220, 221]. Such rapid process is made possible through both the ultra-fast intrinsic on rate of GP1b-A1 ($\sim 10^{5}\ s^{-1}$) and the elevated high shear rate ($>10\ 000\ s^{-1}$), as an effective synergy of both kinetics and transport that drives SIPA. Moreover, such millisecond-timescale SIPA process is fast enough to form mural aggregates within the short platelet transit time through high-shear stenosis (also in millisecond timescale), enabling the rapid platelet accumulation and the subsequent occlusion.

6.4.4 Controversies in GP1b-A1 off-rate measurements

Our results show that SIPA under elevated shear requires a relatively low GP1b-A1 bond reactive compliance ($\sigma = 0.2\ nm$) in order to withstand the high shear stresses, which support the single-molecule measurements of GP1b-A1 bond lifetime reported by Li Group [220] and Zhu Group [221]. The bond reactive compliance ($\sigma = 2.0\ nm$) reported by Springer Group [219] seems too high and would prevent occlusive SIPA from occurring based on our bottom-up computational approach. This is, however, contradictory to the $in\ vitro$ and $in\ vivo$ observations that SIPA occurs with normal blood under elevated high shear [30, 217, 262].

The difference in the measurement of GP1b-A1 bond lifetime may be attributed to

the different single-molecule force measurement technique used in these studies. As recently demonstrated by Chen $et\ al.$ [221], the force-ramp technique primarily used in Kim $et\ al.$ [219] tends to disrupt the bond stability. In contrast, the force-clamp technique adopted in Chen $et\ al.$ [221] is shown to better retain the bond stability. The laser optical tweezers used in Zhang $et\ al.$ [220] generally has higher force and temporal resolution compared to the other two techniques.

6.4.5 ULVWF enhances SIPA efficiency

Our study shows ULVWF can capture platelet agglomerates in a loose morphology even with a moderately diluted VWF concentration, while maintaining the capture time still around millisecond-scale. Such high efficiency of ULVWF in causing SIPA can be demonstrated by defining a dimensionless SIPA efficiency coefficient as

$$\textbf{SIPA Efficiency} = \frac{Capture\ Rate}{Agglomeration\ Rate}, \tag{6.17}$$

which describes how fast the capture event could occur at the corresponding agglomeration rate of the phase diagram. Based on this definition, the resulting heat map shown in Fig. 6.18 shows a peak efficiency at the ULVWF regime around the NP-level concentration. Thus, SIPA efficiency (Fig. 6.18) points to VWF length as primary over concentration, in contrast to just agglomeration (Fig. 6.15). Such high SIPA efficiency with ULVWF may explain the clinical thrombotic complications such as TTP and TMA, where an extravagant number of platelets can be sequestered by ULVWF through forming micro-aggregates throughout the microvasculatures where shear rates are elevated [213].

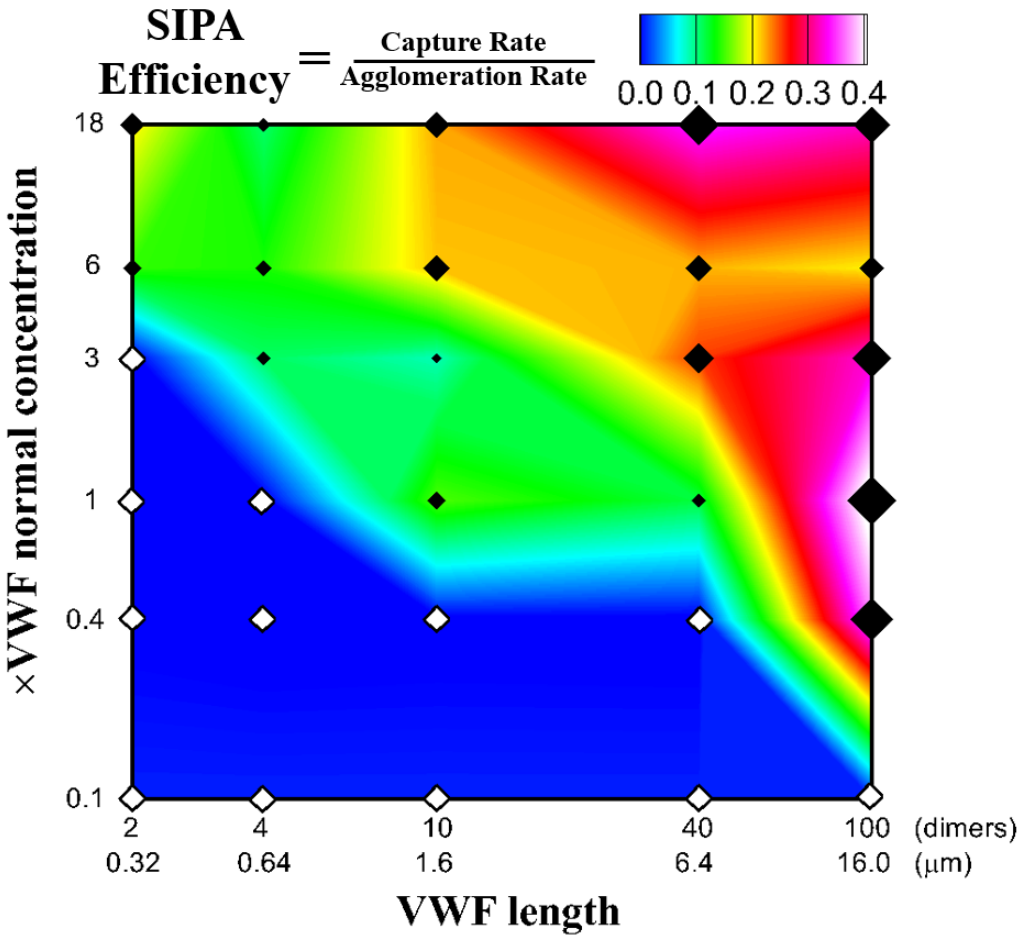

Figure 6.18: The SIPA efficiency as a function of VWF length and VWF concentration. The ULVWF at normal plasma concentration shows the peak efficiency.

6.4.6 Quantitative or qualitative deficiency in VWF prevents SIPA

Our results show short VWF ($<$0.64 μm) does not form captured aggregates even with mildly elevated VWF concentration ($\sim$3$\times$normal). This is consistent with the experimental observation by Ruggeri $et\ al.$ [210] that dimeric VWF-A1 always led to rolling aggregates while normal length VWF could sometimes form adhered aggregates. Clinically, this is also consistent with the bleeding complications observed in patients with VWD type 2A/2B and aVWS, where their blood plasma shows a substantial deficiency in intermediate and long VWF [211, 212, 242, 243].

Casa $et\ al.$ [226] show that healthy human blood after 90% dilution and restoration of normal platelet concentration leads to no occlusion (3 out of 5 cases), indicating the necessity of sufficient VWF concentration for thrombi formation. Our results show that lowering the VWF concentration to 40% NP-level with normal length should prevent capture, which can explain why no occlusion was observed by Casa $et\ al.$ [226]. Clinically, this also explains the excessive bleeding disorders observed in patients with VWD type 1/3, who systematically carry a lower-level or no plasma VWF compared to healthy population [213, 239].

6.4.7 Elevation in VWF concentration and length causes transition from LT to RPA

Previous studies using $ex\ vivo$ [204] and $in\ vitro$ [203] flow-through systems demonstrate the high-shear occlusive thrombus forms by three phases. Phase I is the lag time (LT) phase, which features mainly platelet adhesion with limited thrombus growth. Phase II is the rapid platelet accumulation (RPA) phase, which shows an explosive growth of the thrombus. Phase III is the occlusion phase which causes the cessation of blood flow. Para $et\ al.$ [30] have shown the thrombi growth rate during RPA phase is $4-6$ times the rate within the LT phase. Before this study, the mechanism that governs this elevation of growth rate from LT to RPA remains unexplained.

As shown by our phase diagram of capture rate (Fig. 6.16), normal plasma (NP)-VWF at normal concentration primarily leads platelet adhesion with only marginal capture of aggregates, which is consistent with the LT phenomenon observed experimentally [226, 11]. Quantitatively, the aggregate capture rate with NP-VWF at normal concentration is about 0.1 ms^{-1} based on our rate metric (Eqn. 6.16). Elevating the VWF concentration by $18\times$ while shifting the VWF average size to the high-end ($10-40$ dimers), the capture rate can be enhanced by $\sim$5 times ($\sim$0.5 ms^{-1}), which agrees well with the experimentally measured enhancement of thrombi growth rate from LT to RPA [30]. Furthermore, platelet upon activation can locally supply long VWFs at up to $50\times$ NP concentration [246]. Such

local supplement of long VWF through platelet α-granule release should be sufficient to support the $5\times$ elevation in thrombus growth rate. Therefore, our results suggest the driving mechanism for the LT-to-RPA transition during occlusive high-shear thrombosis may be the α-granule release through platelet activation that locally supports elevated VWF concentration at large multimer sizes. Using knock-out mice that genetically lack α-granule, Kim $et\ al.$ [218] recently show α-granule release is required for occlusive high-shear thrombosis. This supports our hypothesis for the LT-RPA transition mechanism.

Based on our capture rate diagram, the theoretical microthrombi accumulation rate during RPA can be calculated to be about $2.5 \times 10^3\ um^3/s$ in terms of platelet volume, which is $2-3$ orders of magnitude greater than the macroscale RPA rates ($50-80\ um^3/s$) [30, 33, 11]. The rate discrepancy between the microthrombi formation and macrothrombi formation is likely due to a rate-limiting effect imposed by the shear-induced platelet activation, which generally operates at second-scale and can take up to minutes under elevated shear (i.e, at least 3 orders of magnitude slower compared to the millisecond-scale microthrombi formation) [255].

The down-regulation of SIPA growth by platelet activation could be through two pathways. On one hand, platelet activation supplies long VWF at a high local concentration through α-granule release to support the (millisecond-scale) microthrombi formation [246]. One the other hand, platelet activation activates the GPIIb/IIIa-associated bonds to reinforce the pre-formed thrombi avoiding large embolization [11]. Nevertheless, ultra-fast aggregate capture in milliseconds is required for the macroscale RPA rate.

Major thrombotic events or complications related to the alteration of VWF length and concentration can be summarized and denoted in our SIPA capture-rate phase diagram, as shown in Fig. 6.19. VWD type 2A/B and aVWS occurs with excessive short VWFs, which features no capture of agglomerates. Normal plasma (NP) primarily leads to platelet adhesion with marginal capture of agglomerates, which is LT phenomenon. VWD type 1/3 has low concentration of VWF, which can be characterized by the no capture phenomenon.

TTP and TMA features excessive capture of platelet aggregates with ULVWF. Elevation in VWF concentrations at intermediate length leads to substantial increase of agglomerate capture rate, which causes the transition from LT to RPA. Similarly, hemostasis can be explained by the local release of long VWF in the neighborhood of an arterial wound to move from NP to the top right corner to stop bleeding as soon as possible. The consistency between the agglomerate capture behavior and the pathological symptoms/observations illustrates the reach of our theory to clinical relevance by our SIPA capture rate diagram.

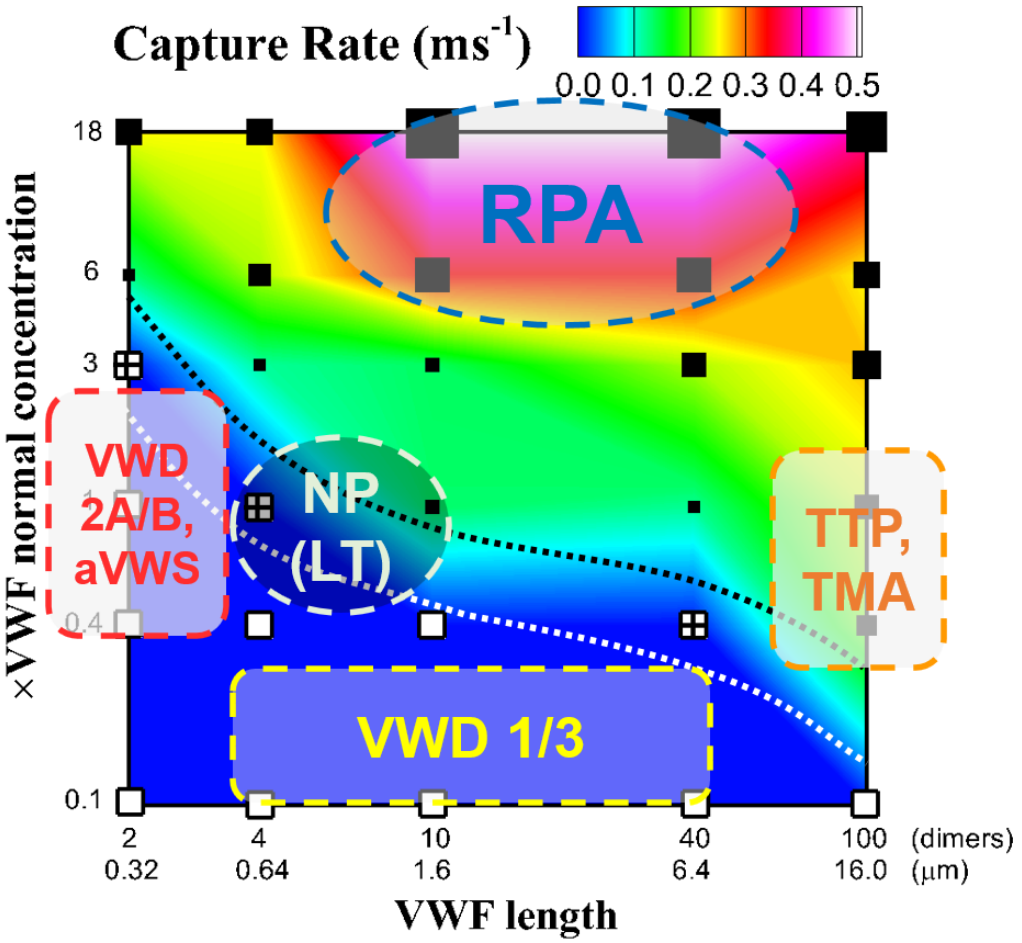

Figure 6.19: The clinical relevance of the SIPA capture diagram. VWD type 2A/B and aVWS occurs with excessive short VWFs, which features no capture of platelet agglomerates. Normal plasma (NP) primarily leads to platelet adhesion with marginal capture of agglomerates, which is LT phenomenon. VWD type 1/3 has low concentration of VWF, which can be characterized by the no capture phenomenon. TTP and TMA features excessive capture of platelet agglomerates with ULVWF. Elevation in VWF concentrations at intermediate length leads to substantial increase of the capture rate, which causes the transition from LT to RPA.

6.4.8 Multiscale hierarchy of occlusive thrombosis

As we have identified the plausible spatio-temporal scales associated with critical biological events for building up a high-shear thrombus, a multiscale hierarchy scaling up from molecular-level to cellular-level to tissue-level can be mapped out to better delineate the RPA process of acute arterial thrombosis leading to thrombotic occlusion, as shown in Fig. 6.20.

At the molecular-level, the GP1b-A1 formation features ultra-fast intrinsic on-rates ($\sim 10^5\ s^{-1}$), which can occur as fast as a few micro-seconds. Depending on the bond force, the GP1b-A1 bond lifetime varies from seconds to milliseconds, which is generally much longer than the time for bond formation. Such rate disparity between GP1b-A1 bond formation and rupture allows for the rapid accumulation of sufficient GP1b-A1 bonds in the elevated shear-rate environment.

As both the length- and time-scale move to the cellular-level, micro-thrombi start to appear in milliseconds, which is made possible through the microsecond-scale GP1b-A1 formation. The microthrombi is formed by SIPA, which is through VWF entanglement only and does not require platelet activation. Such pure physical mechanism make it just fast enough to form and capture the platelet aggregates within the short platelet transit time through stenosis (also in millisecond-scale depending on the shear rate). Note with normal plasma VWF, micro-thrombi would occur infrequently (as the platelet aggregates marginally captured) and only with platelet adhesion near the wall, which would not be sufficient to form occlusive thrombi at tissue-level. This should be the case with normal physiology.

To transition from the cellular-level to the tissue-level quickly, more sustained micro-thrombi formation is needed. This can be created by the shear-induced activation of pre-adhered platelets that occurs in second-scale. During this process, platelet activation plays at least two crucial roles. On one hand, it releases α-granule contents which contain HMWMs at high concentrations (up to 50$\times$ NP concentration) [246], thus supplying nec-

essary VWF levels for firm capture of aggregates. On the other hand, it activates the slower but stronger GPIIb/IIIa-VWF/fibrinogen bonds [209] to reinforce the microthrombi attachment so that the thrombi can grow against the elevating shear stresses. Thus, platelet activation is indeed necessary for thrombus formation, but not prior to platelet aggregation.

Such meticulous arrangement of multi-level bioactivities macroscopically gives rise to the RPA phase that is responsible for the arterial thrombotic occlusion with subsequent clinically strokes or heart-attacks. On the other hand, this elaborate mechanism could be life saving for hemostasis. The findings based on our bottom-up computational approach provide us a multiscale understanding of the occlusive arterial thrombosis.

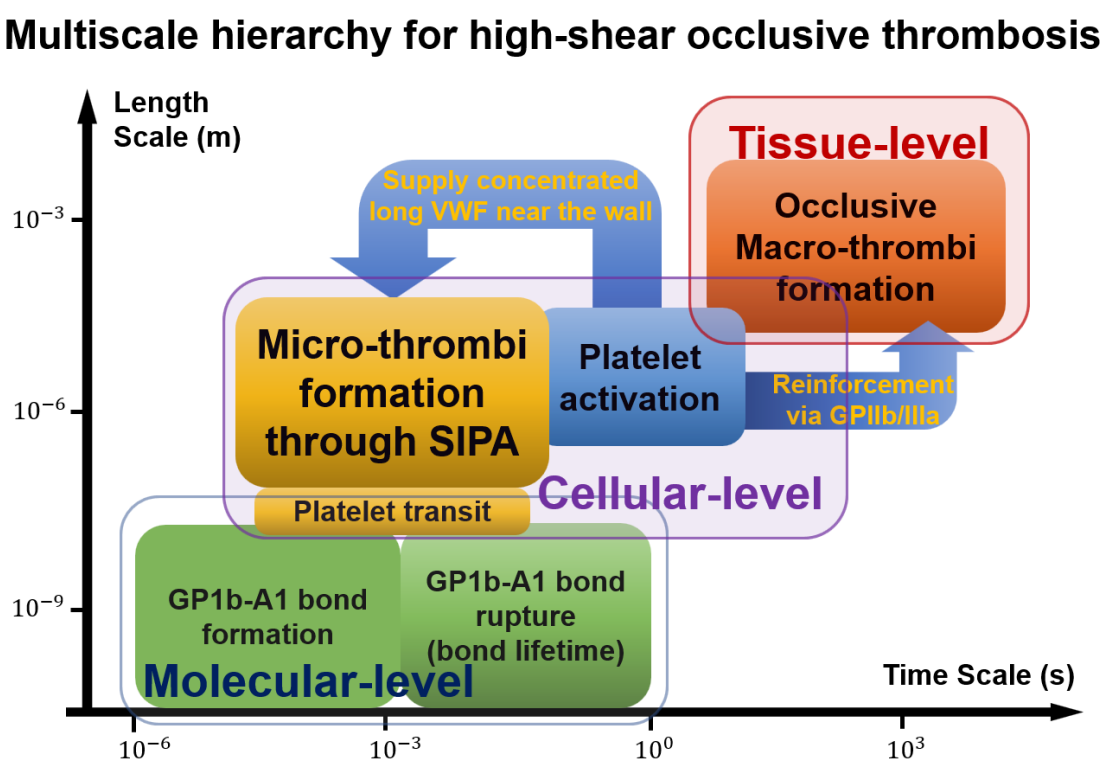

Figure 6.20: Occlusive arterial thrombosis is the outcome of a spatiotemporally multi-scale hierarchay of bio-chem-phyiscal processes. The ultra-fast GP1b-A1 bond formation within micro-seconds allows the rapid micro-thrombi formation through SIPA that occurs in milliseconds. The activation of captured platelets locally supplies elevated concentration of VWF through α-granule release, which provides necessary environment for rapid microthrombi formation and further bridges micro-thrombi formation to macro-thrombi accumulation. The entire multiscale procedure gives rise the RPA phase that directly leads to occlusion.

6.5 Concluding Remarks

In this chapter, we have developed a multiscale computational model that incorporates the necessary molecular and cellular ingredients for SIPA under elevated shear that is relevant to occlusive arterial thrombosis. By theoretically decomposing the macroscopic kinetics into the transport component and the intrinsic-kinetics component, an experiment-informed platelet-VWF GP1b-A1 binding kinetic model has been developed to specify the intrinsic role of GP1b-A1 bond formation and rupture. The intricate VWF polymer suspension dynamics are directly resolved through a well-validated LB-LD nanocale pariculate suspension flow method [225, 104].

Using this multiscale and multiphysics computational approach, the mechanobiology of SIPA has been interrogated $in\ silico$ by directly incorporating cellular and molecular biophysical information. The $in\ silico$ results show relevance and consistency with clinical and experimental observations. Multiple biophysical mechanisms regarding the high-shear occlusive thrombosis from spatio-temporally multiscale perspectives has been discovered, as listed below:

- SIPA under elevated shear is a two-stage process involving platelet agglomeration and agglomerate capture, where the agglomeration occurs in flow and agglomerate capture to the wall occurs subsequent to the agglomeration.

- The time-scale for micro-thrombi formation through SIPA is in milliseconds, which is comparable to the platelet transit time through high-shear stenosis.

- A lag capture distance of a few hundred micrometers (200$\sim$400 μm) is required before the platelet aggregate forms and becomes murally attached.

- The reactive compliance of GP1b-A1 bond needs to be in the order of $\sim\mathcal{O}(0.1)\ nm$ in order to give rise to macroscopic SIPA.

- The captured platelet aggregates typically show three morphological states, including compact state, elongated state and loose state.
- ULVWF can efficiently form mural microthrombi by forming loose aggregates with a porosity above $\sim$80%.
- Shortening VWF average size to below 4 dimers or lowering the VWF concentration to $<$40% prevents SIPA.
- Elevating the VWF concentration by $\sim 20\times$ and/or extending the average multimer size ($10-40$ dimers) accelerates SIPA by $\sim$5 times, and can be the mechanism transitioning LT (lag time) regime to RPA (rapid platelet accumulation) regime.

This work, for the first time, bridges the single-molecule bond force measurements to the microthrombi formation, and provides possible bio-physico-chemical explanations to clinical thrombosis or bleeding complications. The developed $in\ silico$ multiscale high-shear thrombosis simulator provides a cross-scale tool for exploring novel biophysical mechanisms that are typically inaccessible to only single-molecule measurements and micro-/marcro-fluidic assays. Such new perspectives could lead to the discovery of novel anti-thrombotic therapies.

Appendix

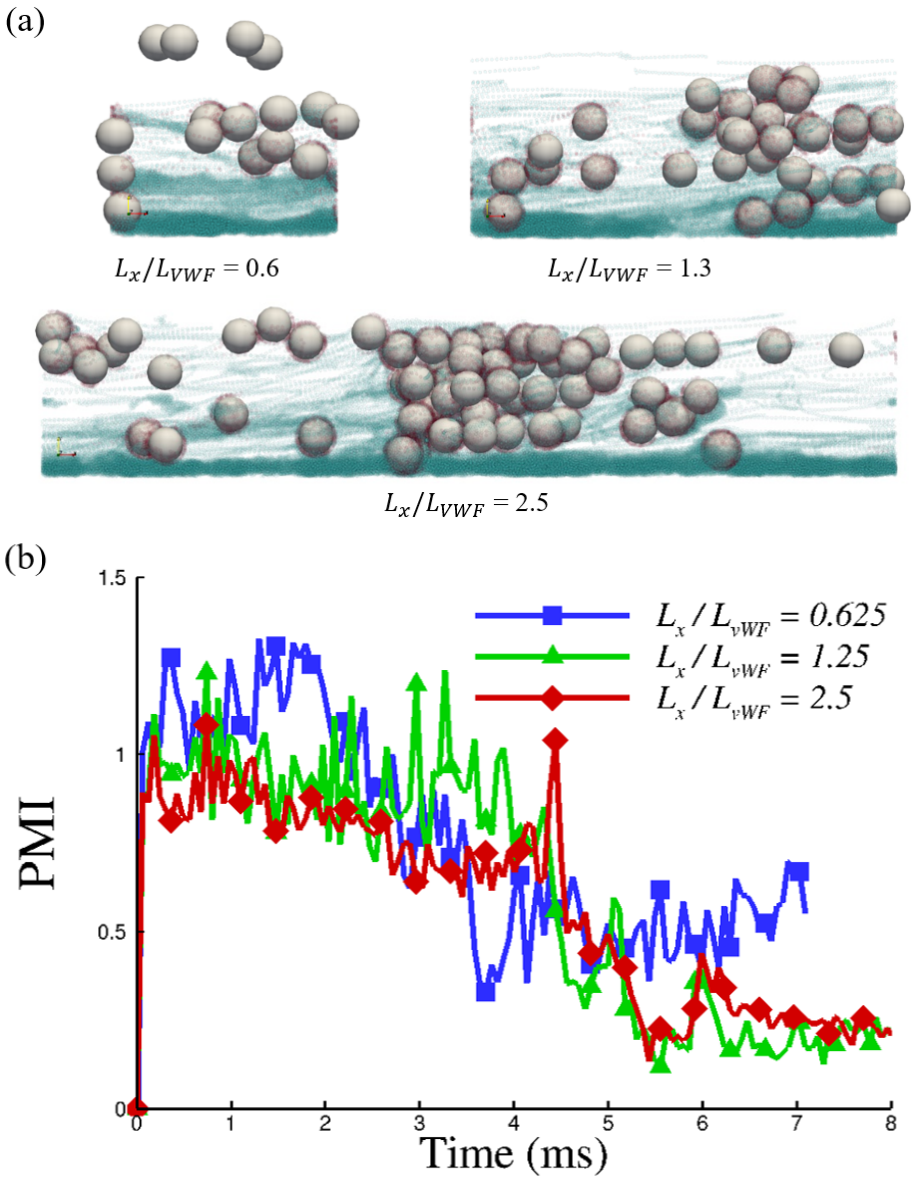

Figure 6.21: The numerical sensitivity of the platelet mobility index to the variation of the streamwise domain size. The results indicate the ratio $L_x/L_{VWF} = 1.25$ is a cost-effective resolution for simulating microthrombi formation in the current setting.

Table 6.1: Table of parameters simulated in the current study. Parameters are varied selectively to study the effect of VWF length, VWF concentration and GP1b-A1 off-rate, etc. Three domain sizes are considered to minimize the numeric artifacts of the periodic boundary conditions in the streamwise direction. The platelet volume fraction is set to ϕ_{PLT}=3% to match the physiologic level in the presence of platelet margination. The zero-bond-force intrinsic rate for GP1b-A1 is set to k_{-}^{0}=1 s^{-1}.

Case NO.	$\dot{\gamma}$	ϕ_{sVWF}	S_{iVWF}	L_{VWF}	N_{dimer}	σ	Domain size
-	$[s^{-1}]$	[%]	$[ng/mm^2]$	$[\mu m]$	-	$[nm]$	$[\mu m^3]$
1	10 000	0.05	0.1	0.32	2	0.2	20×20×10
2	10 000	0.05	0.1	0.64	4	0.2	20×20×10
3	10 000	0.05	0.1	1.6	10	0.2	20×20×10
4	10 000	0.05	0.1	6.4	40	0.2	20×20×10
5	10 000	0.05	0.1	16.0	100	0.2	20×20×10
6	10 000	0.2	0.1	0.32	2	0.2	20×20×10
7	10 000	0.2	0.1	0.64	4	0.2	20×20×10
8	10 000	0.2	0.1	1.6	10	0.2	20×20×10
9	10 000	0.2	0.1	6.4	40	0.2	20×20×10
10	10 000	0.2	0.1	16.0	100	0.2	20×20×10
11	10 000	0.5	0.1	0.32	2	0.2	20×20×10
12	10 000	0.5	0.1	0.64	4	0.2	20×20×10
13	10 000	0.5	0.1	1.6	10	0.2	20×20×10
14	10 000	0.5	0.1	6.4	40	0.2	20×20×10
15	10 000	0.5	0.1	16.0	100	0.2	20×20×10
16	10 000	1.5	0.1	0.32	2	0.2	20×20×10
17	10 000	1.5	0.1	0.64	4	0.2	20×20×10
18	10 000	1.5	0.1	1.6	10	0.2	20×20×10
19	10 000	1.5	0.1	6.4	40	0.2	20×20×10
20	10 000	1.5	0.1	16.0	100	0.2	20×20×10
21	10 000	3.0	0.1	0.32	2	0.2	20×20×10
22	10 000	3.0	0.1	0.64	4	0.2	20×20×10
23	10 000	3.0	0.1	1.6	10	0.2	20×20×10
24	10 000	3.0	0.1	6.4	40	0.2	20×20×10
25	10 000	3.0	0.1	16.0	100	0.2	10×20×10
26	10 000	3.0	0.1	16.0	100	0.2	20×20×10
27	10 000	3.0	0.1	16.0	100	0.2	40×20×10
28	10 000	9.0	0.1	0.32	2	0.2	20×20×10
29	10 000	9.0	0.1	0.64	4	0.2	20×20×10
30	10 000	9.0	0.1	1.6	10	0.2	20×20×10
31	10 000	9.0	0.1	6.4	40	0.2	20×20×10
32	10 000	9.0	0.1	16.0	100	0.2	20×20×10
33	20 000	1.0	0.1	1.6	10	0.2	20×20×10
34	20 000	1.0	0.1	3.2	20	0.2	20×20×10
35	20 000	1.0	0.1	6.4	40	0.2	20×20×10
36	10 000	0	0	1.6	10	0.2	20×20×10
37	10 000	0.5	0	1.6	10	0.2	20×20×10
38	10 000	0	0.1	1.6	10	0.2	20×20×10
39	10 000	0.5	0.1	1.6	10	2.0	20×20×10
40	10 000	3.0	0.1	1.6	10	2.0	20×20×10

CHAPTER 7
CONTRIBUTIONS AND RECOMMENDATIONS

The research described in this thesis is focused on multiscale modeling of blood flow and clotting by incorporating both molecular- and cellular-level particle/polymer suspension dynamics and biological details. This work is to address the urgency for better understanding blood biorheology across both molecular level and cellular level, so as to provide biophysical insights and understanding of vascular patho-physiological processes such as nanoscale solutes transport in blood and occlusive arterial thrombosis.

7.1 Original contributions

A number of original scientific contributions have been made from the thesis, as listed in the following:

1. We developed a coupled lattice-Boltzmann/Langevin-dynamics (LB-LD) method for simulating nanoscale particle/polymer suspensions [24, 225]. By coupling the non-fluctuating LB method with the LD method through momentum exchange, this method can effectively capture Brownian motion and long-distance hydrodynamics interactions without empirical renormalization. The coupling operation is local, therefore convenient for parallelization. This method can be used to study various polymeric fluids and soft matter physics.

2. The LB-LD method was further coupled with a course-grained spectrin-link (SL) based cellular blood flow solver [225]. The opens up a new area of studying blood flow and vascular diseases by incorporating both molecular- and cellular-level biophysical details, allowing for studying .

3. We developed of a general particulate suspension inflow and outflow boundary condition (PSIO-BC) [267]. This PSIO-BC can be applied to particulate flows where particle number is not conserved and/or periodic boundary condition is not applicable. Areas can be used including branching flows, cross-channel flows, flows with arbitrary inlet/outlet geometries and reactive flows, etc.

4. A single-molecule-measurement-informed binding kinetic model was developed for modeling GP1b-A1 bond formation and rupture in the presence of hydrodynamic influences. This binding kinetic model combines the classic equilibrium binding kinetic theory with the single-molecule level force/kinetics measurements, enabling us to obtain the intrinsic kinetic rates that is decoupled from the transport effect.

5. The abrupt transition from nanoparticle dispersion to platelet marginationin in microvesels was captured and found to be attributed to the RBC-enhanced diffusion overcoming the Brownian diffusion [24, 153].

6. We discovered a heterogeneous partitioning pattern of cellular-blood borne nanoparticles through microvascular bifurcations in response to the well-know Zweifach-Fung (ZF) effect [267]. This new phenomenon can be used for manipulating or separating nano-solute/molecule from blood.

7. The complete diffusion tensor of nano-solute in sheared cellular blood was fully characterized based on an $in\ silico$ rheometer [104]. This provides a major update of the shear-augmented diffusivity theories since 1980s' (by Zydney and Colton [178], etc.). The multiscale-simulation informed theory extends the scalar diffusivity to a diffusion tensorial form to account for the anisotropy of blood microstructure. It provides a more accurate constitutive law for solute transport in blood flows at continuum-scale.

8. We delineated the sub-second dynamic process of shear-induced platelet aggregation

(SIPA) as a two-stage process. The flowing platelets first agglomerate into micro-agglomerates in the flow through soluble VWF, and then the pre-formed agglomerates are captured onto the thrombotic surface by immobilized VWF. This provides a new perspective for the understanding of SIPA that is different from the existing paradigm regarding SIPA as a surface accumulation of platelets.

9. We discovered a lag capture distance of a few hundred microns is needed in order for the agglomerate to form and be captured on the thrombotic surface. This aids in clarifying the controversy in terms of where the micro-thrombi initiates and grows, and quantitatively provides a geometric constraint for designing fluidic thrombotic assays with better clinical relevance.

10. We demonstrated a relatively low GP1b-A1 bond reactive compliance ($\sigma = 0.2\ nm$) is required in order to yield SIPA. This aids in addressing the variations in measurements of GP1b-A1 bond lifetime performed by various researcher using different single-molecule measurements, recommending force-clamp and optical-tweezer assays over force-ramp assay.

11. The transitioning from lag time to rapid platelet accumulation (LT-to-RPA) during occlusive arterial thrombosis was attributed to the local elevation of VWF concentration at intermediate VWF sizes. This local elevation in VWF bioactivity can lead to the formation and firm capture of platelet agglomerates in milliseconds.

12. Biophysical explanation of the pathology regarding various thrombotic or hemostatic complications, such as von Willebrand disease (VWD) type 1/2B/2A/3, thrombotic microangiopathies (TMA) or thrombotic thrombocytopenic purpura (TTP), were provided with regard to various VWF length and concentration.

13. Three characteristic morphological states for the mural captured platelet micro-aggregates, including compact aggregate, elongated aggregate and loose aggregate, were ob-

served and summarized in terms of different VWF lengths and concentrations.

7.2 Publications in peer-reviewed articles

The above original contributions have so far led/contributed to the following articles published or to appear in peer-reviewed journals:

1. Z. Liu, C. K. Aidun, D. N. Ku, "*Controlling shear-induced platelet aggregation (SIPA) through altering von Willebrand factor characteristics under elevated shear*", Annals of Biomedical Engineering (in submission)

2. Z. Liu, C. K. Aidun, D. N. Ku, "*Shear-induced platelet aggregation (SIPA) under elevated shear depends on low reactive compliance of GP1b-A1 bonds*", Biophysical Journal (in submission)

3. Z. Liu, C. K. Aidun, D. N. Ku, "*Mechanobiology of shear-induced platelet aggregation (SIPA): an in silico perspective*", Journal of Biomechanics (invited perspectives, in submission)

4. Z. Liu, J. R. Clausen, J. Wagner, K. S. Butler, D. S. Bolintineanu, J. B. Lechman, R. R. Rao, and C. K. Aidun, "*Heterogeneous partition of cellular blood-borne nanoparticles through microvascular bifurcations*", Physical Review E, 102 (1), 013310, 2020 (selected as Editor's Suggestions)

5. Z. Liu, J. R. Clausen, R. R. Rao, C. K. Aidun, "*A unified analysis of nano-to-microscale particle dispersion in tubular blood flow*", Physics of Fluids, 31, 081903, 2019 (selected as Featured Article)

6. Z. Liu, J. R. Clausen, R. R. Rao, C. K. Aidun, "*Nanoparticle diffusion in sheared cellular blood flow*", Journal of Fluid Mechanics, 871, 636-667, 2019

7. Z. Liu, J. R. Clausen, Y. Zhu, J. B. Lechman, R. R. Rao, C. K. Aidun, "*Multiscale method based on coupled lattice-Boltzmann and Langevin-dynamics for direct simulation of nanoscale particle/polymer suspensions in complex flows*", International Journal for Numerical Methods in Fluids, 91: 228–246, 2019 (selected as Cover)

8. Z. Liu, Y. Zhu, R. R. Rao, J. R. Clausen, C. K. Aidun, "*Nanoparticle transport in cellular blood flow*", Computers & Fluids, 172, 609-620, 2018

9. D. Kim, C. Bresette, Z. Liu, D. N. Ku, "*Occlusive thrombosis in arteries*", APL Bioengineering, 3 (4), 041502, 2019 (selected as Featured Article)

10. M. T. Griffin, Y. Zhu, Z. Liu, C. K. Aidun, D. N. Ku, "*Inhibition of high shear arterial thrombosis by charged nanoparticles*", Biomicrofluidics 12 (4), 042210, 2018

11. F. Ahmed, M. Mehrabadi, Z. Liu, G. A. Barabino, C. K. Aidun, "*Internal viscosity dependent margination of red blood cells in microfluidic channels*", Journal of Biomechanical Engineering 140 (6), 061013, 2018

7.3 Future recommendations

The next step for nano-drug delivery after the drug reaching the vascular wall requires extravasation. Besides, the clearance of nanomedicine through renal filtration also requires the understanding of the extravasation process. Current studies on extravasation focuses on either single particle through single vascular fenestration using molecular dynamics (MD)-type techniques or continuum-level quantification using Starling's laws. To better understand the extravasation process at a relatively large scale while preserving the particle-scale characteristics, a mesoscale approach based on the Langevin-dynamics can be developed. This approach would help in designing optimal nano-pariticle/polymer for efficient extravasation and understanding the drug clearance process through renal filtration.

The hemodynamics studies within patient-specific geometries mostly neglect the presence of RBCs given its excessive computational cost. As we have fully characterized the nanoparticle diffusion in sheared cellular blood, an augmented Langevin-dynamics method can be developed to account for the drift diffusion of nano-solutes induced by the presence of RBC as an extra stochastic forcing term in the Langevin equation. This would further reduce the computational expenses imposed by the RBC membrane dynamics, and allow for interrogation of drug delivery problems within patient-specific geometries while implicitly resolving the effect of RBCs.

Due the presence of RBCs, the von Willebrand factor naturally shows a non-uniform distribution in microvessels. Recent studies have reported the both the margination as well as demargination behaviors of VWF in sheared cellular blood flows, therefore posing controversies in terms of the VWF migration in blood. An important aspect that was overlooked is that the VWF conformational change under shear is sensitive to certain shear-rate threshold. Therefore, a systematic study considering different shear regimes would be beneficial in fully understanding VWF migration behavior in cellular blood flow. Besides, as VWF is an important clotting factor that often adheres with platelets when necessary, it is of

clinical implication to understand its margination propensity relative to platelet to estimate the local stoichiometric ratio of VWF versus platelet for SIPA.

During occlusive arterial thrombosis, the formed platelet-rich clot is highly porous with "mountains-and-valleys" pattern. Understanding the emergence of such structure is of great importance to fully understanding the rapid growth of high-shear thrombus. To tackle this problem with computations, a continuum model augmented with constitutive relations through particle-scale methods (e.g., the method developed in Chapter 6) can be developed. This method would allow for capturing the microstructure with both efficiency and particle-scale relevance. Phase-field method may be a good candidate for such studies.

Thrombolysis is an important therapy which allows recanalization of an acutely occluded vessel in an invasive manner. Current thrombolytic agents such as recombinant ADAMTS13 and N-acetyl cysteine (NAC) are still lack efficiency partly because the lack of understanding of the drug penetration and reaction within the thrombotic porous media. The hindered diffusion of passive nanoparticles or active swimmers within the specific thrombus-like polymeric structure can be studied to provide guidance to the design of high-penetration, highly-reactive drugs for more effective thrombolytic therapies.

REFERENCES

[1] D. A. Fedosov, B. Caswell, and G. E. Karniadakis, "A multiscale red blood cell model with accurate mechanics, rheology, and dynamics," *Biophys. J.*, vol. 98, no. 10, pp. 2215–25, 2010.

[2] C. K. Aidun and J. R. Clausen, "Lattice-boltzmann method for complex flows," *Annu. Rev. Fluid Mech.*, vol. 42, no. 1, pp. 439–472, 2010.

[3] D. A. Reasor, J. R. Clausen, and C. K. Aidun, "Coupling the lattice-boltzmann and spectrin-link methods for the direct numerical simulation of cellular blood flow," *Int. J. Numer. Methods Fluids*, vol. 68, no. 6, pp. 767–781, 2012.

[4] J. R. Clausen, D. A. Reasor, and C. K. Aidun, "Parallel performance of a lattice-boltzmann/finite element cellular blood flow solver on the ibm blue gene/p architecture," *Comput. Phys. Commun.*, vol. 181, no. 6, pp. 1013–1020, 2010.

[5] H. Lei, D. A. Fedosov, B. Caswell, and G. E. Karniadakis, "Blood flow in small tubes: Quantifying the transition to the non-continuum regime," *Journal of fluid mechanics*, vol. 722, pp. 214–239, 2013.

[6] I. V. Pivkin and G. E. Karniadakis, "Accurate coarse-grained modeling of red blood cells," *Phys. Rev. Lett.*, vol. 101, no. 11, p. 118 105, 2008.

[7] D. A. Reasor, J. R. Clausen, and C. K. Aidun, "Rheological characterization of cellular blood in shear," *J. Fluid Mech.*, vol. 726, pp. 497–516, 2013.

[8] R. M. MacMeccan, J. R. Clausen, G. P. Neitzel, and C. K. Aidun, "Simulating deformable particle suspensions using a coupled lattice-boltzmann and finite-element method," *J. Fluid Mech.*, vol. 618, pp. 13–13, 2009.

[9] D. A. Fedosov, W. Pan, B. Caswell, G. Gompper, and G. E. Karniadakis, "Predicting human blood viscosity in silico," *Proc. Natl. Acad. Sci. U. S. A.*, vol. 108, no. 29, pp. 11 772–7, 2011.

[10] Y. Liu, L. Zhang, X. Wang, and W. K. Liu, "Coupling of Navier-Stokes equations with protein molecular dynamics and its application to hemodynamics," *Int. J. Numer. Methods Fluids*, vol. 46, no. 12, pp. 1237–1252, 2004.

[11] L. D. C. Casa and D. N. Ku, "Thrombus formation at high shear rates," *Annu. Rev. Biomed. Eng.*, vol. 19, no. 1, pp. 415–433, 2017.

[12] E. F. Grabowski, L. I. Friedman, and E. F. Leonard, "Effects of shear rate on the diffusion and adhesion of blood platelets to a foreign surface," *Ind. Eng. Chem. Res.*, vol. 11, no. 2, pp. 224–232, 1972.

[13] F. Ahmed, M. Mehrabadi, Z. Liu, G. A. Barabino, and C. K. Aidun, "Internal viscosity-dependent margination of red blood cells in microfluidic channels," *J. Biomech. Eng.*, vol. 140, no. 6, pp. 061 013–061013–7, 2018.

[14] E. Eckstein and F. Belgacem, "Model of platelet transport in flowing blood with drift and diffusion terms," *Biophys. J*, vol. 60, no. 1, pp. 53–69, 1991.

[15] M. Mehrabadi, D. N. Ku, and C. K. Aidun, "A continuum model for platelet transport in flowing blood based on direct numerical simulations of cellular blood flow," *Ann. Biomed. Eng.*, vol. 43, no. 6, pp. 1410–21, 2015.

[16] L. CROWL and A. L. FOGELSON, "Analysis of mechanisms for platelet near-wall excess under arterial blood flow conditions," *Journal of Fluid Mechanics*, vol. 676, 348–375, 2011.

[17] H. Zhao and E. S. G. Shaqfeh, "Shear-induced platelet margination in a microchannel," *Phys. Rev. E*, vol. 83, p. 061 924, 6 2011.

[18] H. Zhao, E. S. G. Shaqfeh, and V. Narsimhan, "Shear-induced particle migration and margination in a cellular suspension," *Phys. Fluids*, vol. 24, no. 1, p. 011 902, 2012.

[19] D. A. Reasor, M. Mehrabadi, D. N. Ku, and C. K. Aidun, "Determination of critical parameters in platelet margination," *Ann. Biomed. Eng.*, vol. 41, no. 2, pp. 238–49, 2013.

[20] T. Krüger, "Effect of tube diameter and capillary number on platelet margination and near-wall dynamics," *Rheologica Acta*, vol. 55, no. 6, pp. 511–526, 2016.

[21] J. Tan, S. Shah, A. Thomas, H. D. Ou-Yang, and Y. Liu, "The influence of size, shape and vessel geometry on nanoparticle distribution," *Microfluidics and nanofluidics*, vol. 14, no. 1-2, pp. 77–87, 2013.

[22] K. Muller, D. A. Fedosov, and G. Gompper, "Margination of micro- and nanoparticles in blood flow and its effect on drug delivery," *Sci. Rep.*, vol. 4, p. 4871, 2014.

[23] T. R. Lee, M. Choi, A. M. Kopacz, S. H. Yun, W. K. Liu, and P. Decuzzi, "On the near-wall accumulation of injectable particles in the microcirculation: Smaller is not better," *Sci. Rep.*, vol. 3, p. 2079, 2013.

[24] Z. Liu, Y. Zhu, R. R. Rao, J. R. Clausen, and C. K. Aidun, "Nanoparticle transport in cellular blood flow," *Comput. Fluids*, vol. 172, pp. 609–620, 2018.

[25] P. Decuzzi, B. Godin, T. Tanaka, S. Y. Lee, C. Chiappini, X. Liu, and M. Ferrari, "Size and shape effects in the biodistribution of intravascularly injected particles," *J. Control Release*, vol. 141, no. 3, pp. 320–7, 2010.

[26] S. P. Jackson, "The growing complexity of platelet aggregation," *Blood*, vol. 109, no. 12, pp. 5087–5095, 2007.

[27] D. L. Bark Jr and D. N. Ku, "Wall shear over high degree stenoses pertinent to atherothrombosis," *Journal of biomechanics*, vol. 43, no. 15, pp. 2970–2977, 2010.

[28] E. H. Ackerknecht *et al.*, "Rudolf virchow: Doctor, statesman, anthropologist.," *Rudolf Virchow: Doctor, Statesman, Anthropologist.*, 1953.

[29] L. D. Casa, D. H. Deaton, and D. N. Ku, "Role of high shear rate in thrombosis," *Journal of vascular surgery*, vol. 61, no. 4, pp. 1068–1080, 2015.

[30] A Para, D Bark, A Lin, and D. Ku, "Rapid platelet accumulation leading to thrombotic occlusion," *Annals of biomedical engineering*, vol. 39, no. 7, pp. 1961–1971, 2011.

[31] A. N. Para and D. N. Ku, "A low-volume, single pass in-vitro system of high shear thrombosis in a stenosis," *Thrombosis research*, vol. 131, no. 5, pp. 418–424, 2013.

[32] M. Mehrabadi, L. D. Casa, C. K. Aidun, and D. N. Ku, "A predictive model of high shear thrombus growth," *Annals of biomedical engineering*, vol. 44, no. 8, pp. 2339–2350, 2016.

[33] D. L. Bark Jr, A. N. Para, and D. N. Ku, "Correlation of thrombosis growth rate to pathological wall shear rate during platelet accumulation," *Biotechnology and bioengineering*, vol. 109, no. 10, pp. 2642–2650, 2012.

[34] W. Russel, "Brownian motion of small particles suspended in liquids," *Annual Review of Fluid Mechanics*, vol. 13, no. 1, pp. 425–455, 1981.

[35] A. J. C. Ladd and R Verberg, "Lattice-boltzmann simulations of particle-fluid suspensions," *J. Stat. Phys.*, vol. 104, no. 5-6, pp. 1191–1251, 2001.

[36] B. Dünweg and K. Kremer, "Molecular dynamics simulation of a polymer chain in solution," *The Journal of Chemical Physics*, vol. 99, no. 9, pp. 6983–6997, 1993.

[37] R. D. Groot and P. B. Warren, "Dissipative particle dynamics: Bridging the gap between atomistic and mesoscopic simulation," *The Journal of Chemical Physics*, vol. 107, no. 11, pp. 4423–4435, 1997.

[38] D. L. Ermak and J. McCammon, "Brownian dynamics with hydrodynamic interactions," *The Journal of Chemical Physics*, vol. 69, no. 4, pp. 1352–1360, 1978.

[39] J. F. Brady and G. Bossis, "Stokesian dynamics," *Annual Review of Fluid Mechanics*, vol. 20, no. 1, pp. 111–157, 1988.

[40] D. R. Foss and J. F. Brady, "Self-diffusion in sheared suspensions by dynamic simulation," *J. Fluid Mech.*, vol. 401, pp. 243–274, 1999.

[41] ——, "Structure, diffusion and rheology of brownian suspensions by stokesian dynamics simulation," *J. Fluid Mech.*, vol. 407, pp. 167–200, 2000.

[42] A. Sierou and J. F. Brady, "Shear-induced self-diffusion in non-colloidal suspensions," *J. Fluid Mech.*, vol. 506, no. 506, pp. 285–314, 2004.

[43] A. J. Banchio and J. F. Brady, "Accelerated stokesian dynamics: Brownian motion," *The Journal of Chemical Physics*, vol. 118, no. 22, pp. 10 323–10 332, 2003.

[44] A. Sierou and J. F. Brady, "Accelerated stokesian dynamics simulations," *Journal of Fluid Mechanics*, vol. 448, pp. 115–146, 2001.

[45] Y. Zhang, J. J. de Pablo, and M. D. Graham, "An immersed boundary method for brownian dynamics simulation of polymers in complex geometries: Application to dna flowing through a nanoslit with embedded nanopits," *The Journal of Chemical Physics*, vol. 136, no. 1, p. 014 901, 2012.

[46] M. Wang and J. F. Brady, "Spectral ewald acceleration of stokesian dynamics for polydisperse suspensions," *Journal of Computational Physics*, vol. 306, pp. 443–477, 2016.

[47] L. D. Landau and E. M. Lifshitz, *Fluid mechanics, by LD Landau and EM Lifshitz*. Pergamon Press, 1959.

[48] E. H. Hauge and A. Martin-Löf, "Fluctuating hydrodynamics and brownian motion," *Journal of Statistical Physics*, vol. 7, no. 3, pp. 259–281, 1973.

[49] P. Mazur, "On the motion and Brownian motion of n spheres in a viscous fluid," *Physica A: Statistical Mechanics and its Applications*, vol. 110, no. 1-2, pp. 128–146, 1982.

[50] A. J. Ladd, "Short-time motion of colloidal particles: Numerical simulation via a fluctuating lattice-boltzmann equation," *Physical Review Letters*, vol. 70, no. 9, p. 1339, 1993.

[51] ——, "Numerical simulations of particulate suspensions via a discretized boltzmann equation. part 1. theoretical foundation," *Journal of Fluid Mechanics*, vol. 271, pp. 285–309, 1994.

[52] P. Ahlrichs and B. Dünweg, "Lattice boltzmann simulation of polymer-solvent systems," *International Journal of Modern Physics C*, pp. 1–10, 1998.

[53] ——, "Simulation of a single polymer chain in solution by combining lattice boltzmann and molecular dynamics," *The Journal of Chemical Physics*, vol. 111, no. 17, pp. 8225–8239, 1999.

[54] M. G. Fyta, S. Melchionna, E. Kaxiras, and S. Succi, "Multiscale coupling of molecular dynamics and hydrodynamics: Application to dna translocation through a nanopore," *Simulation*, vol. 5, pp. 18–18, 2007.

[55] M. Fyta, S. Melchionna, S. Succi, and E. Kaxiras, "Hydrodynamic correlations in the translocation of a biopolymer through a nanopore: Theory and multiscale simulations," *Physical review E*, vol. 78, no. 3, p. 036 704, 2008.

[56] M. Bernaschi, S. Melchionna, S. Succi, M. Fyta, E. Kaxiras, and J. K. Sircar, "Muphy: A parallel multi physics/scale code for high performance bio-fluidic simulations," *Computer Physics Communications*, vol. 180, no. 9, pp. 1495–1502, 2009.

[57] M. Mynam, P Sunthar, and S. Ansumali, "Efficient lattice Boltzmann algorithm for Brownian suspensions," *Philos. Trans. Royal Soc. A*, vol. 369, no. 1944, pp. 2237–2245, 2011.

[58] X. He, Q. Zou, L.-S. Luo, and M. Dembo, "Analytic solutions of simple flows and analysis of nonslip boundary conditions for the lattice boltzmann bgk model," *Journal of Statistical Physics*, vol. 87, no. 1-2, pp. 115–136, 1997.

[59] Z. Guo, C. Zheng, and B. Shi, "Discrete lattice effects on the forcing term in the lattice boltzmann method," *Phys. Rev. E*, vol. 65, p. 046 308, 4 2002.

[60] M. T. Griffin, Y. Zhu, Z. Liu, C. K. Aidun, and D. N. Ku, "Inhibition of high shear arterial thrombosis by charged nanoparticles," *Biomicrofluidics*, vol. 12, no. 4, p. 042 210, 2018.

[61] M. S. Aljaghtham, Z. L. Liu, J. J. Guo, J. He, and E. Celik, "Numerical simulations of cell flow and trapping within microfluidic channels for stiffness based cell isolation," *Journal of biomechanics*, vol. 85, pp. 43–49, 2019.

[62] J. Clausen, Z. Liu, D. Bolintineanu, J. Lechman, J. Wagner, K. Butler, R. Rao, and C. Aidun, "Analysis of nanoparticle transport in blood flow through microvascular bifurcations," *Bulletin of the American Physical Society*, 2018.

[63] C. K. Aidun and Y. Lu, "Lattice Boltzmann simulation of solid particles suspended in fluid," *J. Stat. Phys.*, vol. 81, no. 1-2, pp. 49–61, 1995.

[64] C. K. Aidun, Y. N. Lu, and E. J. Ding, "Direct analysis of particulate suspensions with inertia using the discrete boltzmann equation," *J. Fluid Mech.*, vol. 373, pp. 287–311, 1998.

[65] P. L. Bhatnagar, E. P. Gross, and M. Krook, "A model for collision processes in gases. i. small amplitude processes in charged and neutral one-component systems," *Physical Review*, vol. 94, no. 3, pp. 511–525, 1954.

[66] P. V. Coveney, S. Succi, D. d'Humières, I. Ginzburg, M. Krafczyk, P. Lallemand, and L.-S. Luo, "Multiple-relaxation-time lattice boltzmann models in three dimensions," *Philosophical Transactions of the Royal Society of London. Series A: Mathematical, Physical and Engineering Sciences*, vol. 360, no. 1792, pp. 437–451, 2002.

[67] B. M. Yun, L. Dasi, C. Aidun, and A. Yoganathan, "Highly resolved pulsatile flows through prosthetic heart valves using the entropic lattice-boltzmann method," *Journal of Fluid Mechanics*, vol. 754, pp. 122–160, 2014.

[68] ——, "Computational modelling of flow through prosthetic heart valves using the entropic lattice-boltzmann method," *Journal of Fluid Mechanics*, vol. 743, pp. 170–201, 2014.

[69] I. V. Karlin, F. Bösch, and S. S. Chikatamarla, "Gibbs' principle for the lattice-kinetic theory of fluid dynamics," *Phys. Rev. E*, vol. 90, p. 031 302, 3 2014.

[70] G. Di Ilio, B. Dorschner, G. Bella, S. Succi, and I. V. Karlin, "Simulation of turbulent flows with the entropic multirelaxation time lattice boltzmann method on body-fitted meshes," *Journal of Fluid Mechanics*, vol. 849, 35–56, 2018.

[71] M. Junk, A. Klar, and L.-S. Luo, "Asymptotic analysis of the lattice boltzmann equation," *Journal of Computational Physics*, vol. 210, no. 2, pp. 676–704, 2005.

[72] E. J. Ding and C. K. Aidun, "The dynamics and scaling law for particles suspended in shear flow with inertia," *J. Fluid Mech.*, vol. 423, pp. 317–344, 2000.

[73] C. K. Aidun and D. W. Qi, "A new method for analysis of the fluid interaction with a deformable membrane," *Journal of statistical physics*, vol. 90, no. 1-2, pp. 145–158, 1998.

[74] J. R. Clausen, D. A. Reasor, and C. K. Aidun, "The rheology and microstructure of concentrated non-colloidal suspensions of deformable capsules," *J. Fluid Mech.*, vol. 685, no. 2011, pp. 202–234, 2011.

[75] E. Guazzelli and J. F. Morris, *A physical introduction to suspension dynamics*. Cambridge University Press, 2011, vol. 45, ISBN: 1139503936.

[76] R Kubo, "The fluctuation-dissipation theorem," *Rep. Prog. Phys.*, vol. 29, no. 1, p. 306, 1966.

[77] O. B. Usta, A. J. Ladd, and J. E. Butler, "Lattice-boltzmann simulations of the dynamics of polymer solutions in periodic and confined geometries," *Journal of Chemical Physics*, vol. 122, no. 9, pp. 1–11, 2005.

[78] G. E. Box and M. E. Muller, "A note on the generation of random normal deviates," *The Annals of Mathematical Statistics*, vol. 29, no. 2, pp. 610–611, 1958.

[79] C. S. Peskin, "The immersed boundary method," *Acta Numerica*, vol. 11, pp. 479–517, 2002.

[80] J. Wu and C. K. Aidun, "Simulating 3d deformable particle suspensions using lattice boltzmann method with discrete external boundary force," *Int. J. Numer. Methods Fluids*, vol. 62, no. 7, pp. 765–783, 2010.

[81] R. Everaers and M. R. Ejtehadi, "Interaction potentials for soft and hard ellipsoids," *Phys. Rev. E*, vol. 67, p. 041 710, 4 2003.

[82] P. R. Schunk, F. Pierce, J. B. Lechman, A. M. Grillet, P. J. in't Veld, H. Weiss, C. Stoltz, and D. R. Heine, "Performance of mesoscale modeling methods for predicting rheological properties of charged polystyrene/water suspensions," *Journal of Rheology*, vol. 56, no. 2, pp. 353–384, 2012.

[83] H. Hamaker, "The london–van der waals attraction between spherical particles," *Physica*, vol. 4, no. 10, pp. 1058–1072, 1937.

[84] D. S. Bolintineanu, G. S. Grest, J. B. Lechman, · Flint, P. ·. Steven, J Plimpton, and ·. P. R. Schunk, "Particle dynamics modeling methods for colloid suspensions," *Comp. Part. Mech*, vol. 1, pp. 321–356, 2014.

[85] A Alexander-Katz, M. Schneider, S. Schneider, A Wixforth, and R. Netz, "Shear-flow-induced unfolding of polymeric globules," *Physical Review Letters*, vol. 97, no. 13, p. 138 101, 2006.

[86] K. Kremer and G. S. Grest, "Dynamics of entangled linear polymer melts: A molecular-dynamics simulation," *The Journal of Chemical Physics*, vol. 92, no. 8, pp. 5057–5086, 1990.

[87] S. Schneider, S. Nuschele, A. Wixforth, C Gorzelanny, A Alexander-Katz, R. Netz, and M. F. Schneider, "Shear-induced unfolding triggers adhesion of von willebrand factor fibers," *Proceedings of the National Academy of Sciences*, vol. 104, no. 19, pp. 7899–7903, 2007.

[88] L. Verlet, "Computer "experiments" on classical fluids. i. thermodynamical properties of lennard-jones molecules," *Physical Review*, vol. 159, no. 1, pp. 98–103, 1967.

[89] R. W. Hockney and J. W. Eastwood, *Computer Simulation Using Particles*. CRC Press, 1988, ISBN: 1439822050.

[90] B. J. Alder and T. E. Wainwright, "Decay of the velocity autocorrelation function," *Phys. Rev. A*, vol. 1, pp. 18–21, 1 1970.

[91] A. J. C. Ladd, "Hydrodynamic transport coefficients of random dispersions of hard spheres," *The Journal of Chemical Physics*, vol. 93, no. 5, pp. 3484–3494, 1990.

[92] W. Schaertl and H. Sillescu, "Brownian Dynamics of Polydisperse Colloidal Hard Spheres : Equilibrium Structures and Random," *Journal of Statistical Physics*, vol. 77, pp. 1007–1025, 1994.

[93] D. R. Foss and J. F. Brady, "Brownian dynamics simulation of hard-sphere colloidal dispersions," *J. Rheol.*, vol. 44, no. 3, pp. 629–651, 2000.

[94] A. Kasper, E. Bartsch, and H. Sillescu, "Self-Diffusion in Concentrated Colloid Suspensions Studied by Digital Video Microscopy of CoreShell Tracer Particles," *Langmuir*, vol. 14, no. 18, pp. 5004–5010, 1998.

[95] M. Tokuyama and I. Oppenheim, "Dynamics of hard-sphere suspensions," *Phys. Rev. E*, vol. 50, no. 1, R16–R19, 1994.

[96] B. Cichocki, M. L. Ekiel-Jeżewska, and E. Wajnryb, "Lubrication corrections for three-particle contribution to short-time self-diffusion coefficients in colloidal dispersions," *The Journal of Chemical Physics*, vol. 111, no. 7, pp. 3265–3273, 1999.

[97] R. G. Larson, "The rheology of dilute solutions of flexible polymers: Progress and problems," *Journal of Rheology*, vol. 49, no. 1, pp. 1–70, 2005.

[98] P. E. Rouse Jr, "A theory of the linear viscoelastic properties of dilute solutions of coiling polymers," *The Journal of Chemical Physics*, vol. 21, no. 7, pp. 1272–1280, 1953.

[99] B. H. Zimm, "Dynamics of polymer molecules in dilute solution: Viscoelasticity, flow birefringence and dielectric loss," *Journal of Chemical Physics*, vol. 24, no. 2, pp. 269–278, 1956.

[100] P. Szymczak and M. Cieplak, "Hydrodynamic effects in proteins," *Journal of Physics: Condensed Matter*, vol. 23, no. 3, p. 033 102, 2011.

[101] T. T. Perkins, D. E. Smith, and S. Chu, "Single polymer dynamics in an elongational flow," *Science*, vol. 276, no. 5321, pp. 2016–2021, 1997.

[102] A. W. Lees and S. F. Edwards, "The computer study of transport processes under extreme conditions," *J. Phys. C*, vol. 5, no. 15, p. 1921, 1972.

[103] T. A. Springer, "Review Article von Willebrand factor , Jedi knight of the bloodstream," *Blood*, vol. 124, no. 9, pp. 1412–1426, 2016.

[104] Z. Liu, J. R. Clausen, R. R. Rao, and C. K. Aidun, "Nanoparticle diffusion in sheared cellular blood flow," *Journal of Fluid Mechanics*, 2019.

[105] Y.-C. Fung, *Biomechanics: circulation*. Springer Science & Business Media, 2013.

[106] T. W. Secomb, "Blood flow in the microcirculation," *Annual Review of Fluid Mechanics*, vol. 49, no. 1, pp. 443–461, 2017.

[107] R. Fahraeus and T. Lindqvist, "The viscosity of the blood in narrow capillary tubes," *American Journal of Physiology-Legacy Content*, vol. 96, no. 3, pp. 562–568, 1931.

[108] P. A. Aarts, S. A. van den Broek, G. W. Prins, G. D. Kuiken, J. J. Sixma, and R. M. Heethaar, "Blood platelets are concentrated near the wall and red blood cells, in the center in flowing blood.," *Arteriosclerosis: An Official Journal of the American Heart Association, Inc.*, vol. 8, no. 6, pp. 819–824, 1988.

[109] E. C. Eckstein, D. L. Bilsker, C. M. Waters, J. S. Kippenhan, and A. W. Tilles, "Transport of platelets in flowing blooda," *Annals of the New York academy of sciences*, vol. 516, no. 1, pp. 442–452, 1987.

[110] D. A. Fedosov, J. Fornleitner, and G. Gompper, "Margination of white blood cells in microcapillary flow," *Phys. Rev. Lett.*, vol. 108, p. 028 104, 2 2012.

[111] M. Mehrabadi, D. N. Ku, and C. K. Aidun, "Effects of shear rate, confinement, and particle parameters on margination in blood flow," *Phys. Rev. E*, vol. 93, no. 2, p. 023 109, 2016.

[112] K. Vahidkhah and P. Bagchi, "Microparticle shape effects on margination, near-wall dynamics and adhesion in a three-dimensional simulation of red blood cell suspension," *Soft Matter*, vol. 11, no. 11, pp. 2097–2109, 2015.

[113] G. Závodszky, B. van Rooij, B. Czaja, V. Azizi, D. de Kanter, and A. G. Hoekstra, "Red blood cell and platelet diffusivity and margination in the presence of cross-stream gradients in blood flows," *Physics of Fluids*, vol. 31, no. 3, p. 031 903, 2019.

[114] Q. M. Qi and E. S. Shaqfeh, "Theory to predict particle migration and margination in the pressure-driven channel flow of blood," *Physical Review Fluids*, vol. 2, no. 9, p. 093 102, 2017.

[115] A. Albanese, P. S. Tang, and W. C. Chan, "The effect of nanoparticle size, shape, and surface chemistry on biological systems," *Annu. Rev. Biomed. Eng.*, vol. 14, pp. 1–16, 2012.

[116] T. E. Diller, B. B. Mikic, and P. A. Drinker, "Shear-induced augmentation of oxygen transfer in blood," *J. Biomech. Eng.*, vol. 102, no. 1, pp. 67–72, 1980.

[117] J. Tan, A. Thomas, and Y. Liu, "Influence of red blood cells on nanoparticle targeted delivery in microcirculation," *Soft Matter*, vol. 8, no. 6, pp. 1934–1946, 2011.

[118] Z. Liu, J. R. Clausen, R. R. Rao, and C. K. Aidun, "Nanoparticle diffusion in sheared cellular blood flow," *J. Fluid Mech.*, vol. 871, pp. 636–667, 2019.

[119] M. Cooley, A. Sarode, M. Hoore, D. A. Fedosov, S. Mitragotri, and A. S. Gupta, "Influence of particle size and shape on their margination and wall-adhesion: Implications in drug delivery vehicle design across nano-to-micro scale," *Nanoscale*, vol. 10, no. 32, pp. 15 350–15 364, 2018.

[120] Z. Liu, Y. Zhu, R. R. Rao, J. R. Clausen, and C. K. Aidun, "Simulating nanoscale suspension of particles and polymers using a coupled lattice-boltzmann and langevin-dynamics approach," *arXiv preprint arXiv:1801.02299*, 2018.

[121] D. A. Fedosov, B. Caswell, and G. E. Karniadakis, "A multiscale red blood cell model with accurate mechanics, rheology, and dynamics," *Biophys. J.*, vol. 98, no. 10, pp. 2215–25, 2010.

[122] M. Dao, J. Li, and S. Suresh, "Molecularly based analysis of deformation of spectrin network and human erythrocyte," *Mater. Sci. Eng. C*, vol. 26, no. 8, pp. 1232–1244, 2006.

[123] C. Bustamante, Z. Bryant, and S. B. Smith, "Ten years of tension: single-molecule DNA mechanics," *Nature*, vol. 421, no. 6921, pp. 423–427, 2003.

[124] H. H. Lipowsky, "Microvascular rheology and hemodynamics," *Microcirculation*, vol. 12, no. 1, pp. 5–15, 2005.

[125] C. Bächer, A. Kihm, L. Schrack, L. Kaestner, M. W. Laschke, C. Wagner, and S. Gekle, "Antimargination of microparticles and platelets in the vicinity of branching vessels," *Biophysical journal*, vol. 115, no. 2, pp. 411–425, 2018.

[126] P. Balogh and P. Bagchi, "Analysis of red blood cell partitioning at bifurcations in simulated microvascular networks," *Physics of Fluids*, vol. 30, no. 5, p. 051 902, 2018.

[127] J. Clausen, Z. Liu, D. Bolintineanu, J. Lechman, J. Wagner, K. Butler, R. Rao, and C. Aidun, "Analysis of nanoparticle transport in blood flow through microvascular bifurcations," *Bulletin of the American Physical Society*, 2018.

[128] E. Kaliviotis, J. M. Sherwood, and S. Balabani, "Local viscosity distribution in bifurcating microfluidic blood flows," *Physics of Fluids*, vol. 30, no. 3, p. 030 706, 2018.

[129] P. R. Nott, E. Guazzelli, and O. Pouliquen, "The suspension balance model revisited," *Physics of Fluids*, vol. 23, no. 4, p. 043 304, 2011.

[130] N. Takeishi and Y. Imai, "Capture of microparticles by bolus flow of red blood cells in capillaries," *Scientific reports*, vol. 7, no. 1, p. 5381, 2017.

[131] D. A. Fedosov, W. Pan, B. Caswell, G. Gompper, and G. E. Karniadakis, "Predicting human blood viscosity in silico," *Proc. Natl. Acad. Sci. U. S. A.*, vol. 108, no. 29, pp. 11 772–7, 2011.

[132] K. Namdee, A. J. Thompson, P. Charoenphol, and O. Eniola-Adefeso, "Margination propensity of vascular-targeted spheres from blood flow in a microfluidic model of human microvessels," *Langmuir*, vol. 29, no. 8, pp. 2530–2535, 2013.

[133] R. G. H. Rivera, X. Zhang, and M. D. Graham, "Mechanistic theory of margination and flow-induced segregation in confined multicomponent suspensions: Simple shear and poiseuille flows," *Physical Review Fluids*, vol. 1, no. 6, p. 060 501, 2016.

[134] L. Sherwood, *Human physiology: from cells to systems*. Cengage learning, 2015.

[135] A. R. Pries, T. W. Secomb, P Gaehtgens, and J. Gross, "Blood flow in microvascular networks. experiments and simulation.," *Circulation research*, vol. 67, no. 4, pp. 826–834, 1990.

[136] A. R. Pries and T. W. Secomb, "Blood flow in microvascular networks," in *Microcirculation*, Elsevier, 2008, pp. 3–36.

[137] T. W. Secomb, "Blood flow in the microcirculation," *Annual Review of Fluid Mechanics*, vol. 49, pp. 443–461, 2017.

[138] K Svanes and B. Zweifach, "Variations in small blood vessel hematocrits produced in hypothermic rats by micro-occlusion," *Microvascular Research*, vol. 1, no. 2, pp. 210–220, 1968.

[139] A. Pries, K Ley, M Claassen, and P Gaehtgens, "Red cell distribution at microvascular bifurcations," *Microvascular research*, vol. 38, no. 1, pp. 81–101, 1989.

[140] G. Bugliarello and G. C. Hsiao, "Phase separation in suspensions flowing through bifurcations: A simplified hemodynamic model," *Science*, vol. 143, no. 3605, pp. 469–471, 1964.

[141] Y.-C. Fung, "Stochastic flow in capillary blood vessels," *Microvascular research*, vol. 5, no. 1, pp. 34–48, 1973.

[142] Z.-Y. Yan, A. Acrivos, and S. Weinbaum, "A three-dimensional analysis of plasma skimming at microvascular bifurcations," *Microvascular research*, vol. 42, no. 1, pp. 17–38, 1991.

[143] P. C. Johnson, "Red cell separation in the mesenteric capillary network," *American Journal of Physiology-Legacy Content*, vol. 221, no. 1, pp. 99–104, 1971.

[144] G Kanzow, A. Pries, and P Gaehtgens, "Analysis of the hematocrit distribution in the mesenteric microcirculation.," *International journal of microcirculation, clinical and experimental*, vol. 1, no. 1, pp. 67–79, 1982.

[145] S. Yang, A. Ündar, and J. D. Zahn, "A microfluidic device for continuous, real time blood plasma separation," *Lab on a Chip*, vol. 6, no. 7, pp. 871–880, 2006.

[146] R. Fan, O. Vermesh, A. Srivastava, B. K. Yen, L. Qin, H. Ahmad, G. A. Kwong, C.-C. Liu, J. Gould, L. Hood, *et al.*, "Integrated barcode chips for rapid, multiplexed analysis of proteins in microliter quantities of blood," *Nature biotechnology*, vol. 26, no. 12, p. 1373, 2008.

[147] N. Tousi, B. Wang, K. Pant, M. F. Kiani, and B. Prabhakarpandian, "Preferential adhesion of leukocytes near bifurcations is endothelium independent," *Microvascular research*, vol. 80, no. 3, pp. 384–388, 2010.

[148] N. Doshi, B. Prabhakarpandian, A. Rea-Ramsey, K. Pant, S. Sundaram, and S. Mitragotri, "Flow and adhesion of drug carriers in blood vessels depend on their shape: A study using model synthetic microvascular networks," *Journal of Controlled Release*, vol. 146, no. 2, pp. 196–200, 2010.

[149] C. Bächer, A. Kihm, L. Schrack, L. Kaestner, M. W. Laschke, C. Wagner, and S. Gekle, "Antimargination of microparticles and platelets in the vicinity of branching vessels," *Biophysical journal*, vol. 115, no. 2, pp. 411–425, 2018.

[150] S. Sohrabi, S. Wang, J. Tan, J. Xu, J. Yang, and Y. Liu, "Nanoparticle transport and delivery in a heterogeneous pulmonary vasculature," *Journal of biomechanics*, vol. 50, pp. 240–247, 2017.

[151] R. K. Jain and T. Stylianopoulos, "Delivering nanomedicine to solid tumors," *Nature reviews Clinical oncology*, vol. 7, no. 11, p. 653, 2010.

[152] S. Wilhelm, A. J. Tavares, Q. Dai, S. Ohta, J. Audet, H. F. Dvorak, and W. C. Chan, "Analysis of nanoparticle delivery to tumours," *Nature reviews materials*, vol. 1, no. 5, pp. 1–12, 2016.

[153] Z. Liu, J. R. Clausen, R. R. Rao, and C. K. Aidun, "A unified analysis of nano-to-microscale particle dispersion in tubular blood flow," *Physics of Fluids*, vol. 31, no. 8, p. 081 903, 2019.

[154] P. Balogh and P. Bagchi, "A computational approach to modeling cellular-scale blood flow in complex geometry," *Journal of Computational Physics*, vol. 334, pp. 280–307, 2017.

[155] V. W. A. Tarksalooyeh, G. Závodszky, B. J. van Rooij, and A. G. Hoekstra, "Inflow and outflow boundary conditions for 2d suspension simulations with the immersed boundary lattice boltzmann method," *Computers & fluids*, vol. 172, pp. 312–317, 2018.

[156] G. Li, T. Ye, and X. Li, "Parallel modeling of cell suspension flow in complex micro-networks with inflow/outflow boundary conditions," *Journal of Computational Physics*, vol. 401, p. 109 031, 2020.

[157] K. Lykov, X. Li, H. Lei, I. V. Pivkin, and G. E. Karniadakis, "Inflow/outflow boundary conditions for particle-based blood flow simulations: Application to arterial bifurcations and trees," *PLoS computational biology*, vol. 11, no. 8, 2015.

[158] J. Latt and B. Chopard, "Lattice boltzmann method with regularized pre-collision distribution functions," *Mathematics and Computers in Simulation*, vol. 72, no. 2-6, pp. 165–168, 2006.

[159] J. Latt, B. Chopard, O. Malaspinas, M. Deville, and A. Michler, "Straight velocity boundaries in the lattice boltzmann method," *Physical Review E*, vol. 77, no. 5, p. 056 703, 2008.

[160] C. D. Murray, "The physiological principle of minimum work: I. the vascular system and the cost of blood volume," *Proceedings of the National Academy of Sciences of the United States of America*, vol. 12, no. 3, p. 207, 1926.

[161] T. F. Sherman, "On connecting large vessels to small. the meaning of murray's law.," *The Journal of general physiology*, vol. 78, no. 4, pp. 431–453, 1981.

[162] M Zamir, "Nonsymmetrical bifurcations in arterial branching.," *The Journal of general physiology*, vol. 72, no. 6, pp. 837–845, 1978.

[163] M Zamir, S. Wrigley, and B. Langille, "Arterial bifurcations in the cardiovascular system of a rat.," *The Journal of general physiology*, vol. 81, no. 3, pp. 325–335, 1983.

[164] T.-R. Lee, J.-A. Hong, S. S. Yoo, and D. W. Kim, "A computational modeling of blood flow in asymmetrically bifurcating microvessels and its experimental validation," *International journal for numerical methods in biomedical engineering*, vol. 34, no. 6, e2981, 2018.

[165] H. S. Leong, N. F. Steinmetz, A. Ablack, G. Destito, A. Zijlstra, H. Stuhlmann, M. Manchester, and J. D. Lewis, "Intravital imaging of embryonic and tumor neovasculature using viral nanoparticles," *Nature protocols*, vol. 5, no. 8, p. 1406, 2010.

[166] J. Y. Lee, H. S. Ji, and S. J. Lee, "Micro-piv measurements of blood flow in extraembryonic blood vessels of chicken embryos," *Physiological measurement*, vol. 28, no. 10, p. 1149, 2007.

[167] M. Maibier, B. Reglin, B. Nitzsche, W. Xiang, W. W. Rong, B. Hoffmann, V. Djonov, T. W. Secomb, and A. R. Pries, "Structure and hemodynamics of vascular networks in the chorioallantoic membrane of the chicken," *American journal of physiology-heart and circulatory physiology*, vol. 311, no. 4, H913–H926, 2016.

[168] P Gaehtgens, F Schmidt, and G Will, "Comparative rheology of nucleated and non-nucleated red blood cells," *Pflügers Archiv*, vol. 390, no. 3, pp. 278–282, 1981.

[169] M. Abkarian, C. Lartigue, and A. Viallat, "Tank treading and unbinding of deformable vesicles in shear flow: Determination of the lift force," *Physical review letters*, vol. 88, no. 6, p. 068 103, 2002.

[170] D. Kim, C. Bresette, Z. Liu, and D. N. Ku, "Occlusive thrombosis in arteries," *APL bioengineering*, vol. 3, no. 4, p. 041 502, 2019.

[171] A. Malysheva, E. Lombi, and N. H. Voelcker, "Bridging the divide between human and environmental nanotoxicology," *Nat. Nanotechnol.*, vol. 10, no. 10, pp. 835–844, 2015.

[172] J. W. Yoo, D. J. Irvine, D. E. Discher, and S. Mitragotri, "Bio-inspired, bioengineered and biomimetic drug delivery carriers," *Nat. Rev. Drug Discov.*, vol. 10, no. 7, pp. 521–35, 2011.

[173] E. Blanco, H. Shen, and M. Ferrari, "Principles of nanoparticle design for overcoming biological barriers to drug delivery," *Nat. Biotechnol.*, vol. 33, no. 9, pp. 941–51, 2015.

[174] R. D. Brook, S. Rajagopalan, r. Pope C. A., J. R. Brook, A. Bhatnagar, A. V. Diez-Roux, F. Holguin, Y. Hong, R. V. Luepker, M. A. Mittleman, A. Peters, D. Siscovick, J. Smith S. C., L. Whitsel, J. D. Kaufman, E. American Heart Association Council on, C. o. t. K. i. C. D. Prevention, P. A. Council on Nutrition, and Metabolism, "Particulate matter air pollution and cardiovascular disease: An update to the scientific statement from the american heart association," *Circulation*, vol. 121, no. 21, pp. 2331–78, 2010.

[175] D. E. Newby, P. M. Mannucci, G. S. Tell, A. A. Baccarelli, R. D. Brook, K. Donaldson, F. Forastiere, M. Franchini, O. H. Franco, I. Graham, G. Hoek, B. Hoffmann, M. F. Hoylaerts, N. Kunzli, N. Mills, J. Pekkanen, A. Peters, M. F. Piepoli, S. Rajagopalan, R. F. Storey, E. A. f. C. P. Esc Working Group on Thrombosis, Rehabilitation, and E. S. C. H. F. Association, "Expert position paper on air pollution and cardiovascular disease," *Eur. Heart J.*, vol. 36, no. 2, 83–93b, 2015.

[176] M. R. Miller, J. B. Raftis, J. P. Langrish, S. G. McLean, P. Samutrtai, S. P. Connell, S. Wilson, A. T. Vesey, P. H. B. Fokkens, A. J. F. Boere, P. Krystek, C. J. Campbell, P. W. F. Hadoke, K. Donaldson, F. R. Cassee, D. E. Newby, R. Duffin, and N. L. Mills, "Inhaled nanoparticles accumulate at sites of vascular disease," *ACS Nano*, vol. 11, no. 5, pp. 4542–4552, 2017.

[177] S. S. Hossain, Y. Zhang, X. Liang, F. Hussain, M. Ferrari, T. J. Hughes, and P. Decuzzi, "In silico vascular modeling for personalized nanoparticle delivery," *Nanomedicine*, vol. 8, no. 3, pp. 343–357, 2013.

[178] A. L. Zydney and C. K. Colton, "Augmented solute transport in the shear flow of a concentrated suspension," *PhysicoChemical Hydrodynamics*, vol. 10, no. 1, pp. 77–96, 1988.

[179] E. C. Eckstein, D. G. Bailey, and A. H. Shapiro, "Self-diffusion of particles in shear flow of a suspension," *J. Fluid Mech.*, vol. 79, no. 01, p. 191, 1977.

[180] V. Breedveld, D. Van den Ende, A. Tripathi, and A. Acrivos, "The measurement of the shear-induced particle and fluid tracer diffusivities in concentrated suspensions by a novel method," *J. Fluid Mech.*, vol. 375, pp. 297–318, 1998.

[181] N. H. L. Wang and K. H. Keller, "Augmented transport of extracellular solutes in concentrated erythrocyte suspensions in couette-flow," *J. Colloid Interf. Sci.*, vol. 103, no. 1, pp. 210–225, 1985.

[182] K. Yeo and M. R. Maxey, "Anomalous diffusion of wall-bounded non-colloidal suspensions in a steady shear flow," *Europhys. Lett.*, vol. 92, no. 2, pp. 24 008–24 008, 2010.

[183] M. Gross, T. Kruger, and F. Varnik, "Fluctuations and diffusion in sheared athermal suspensions of deformable particles," *Europhys. Lett.*, vol. 108, no. 6, pp. 68 006–68 006, 2014.

[184] A. Kumar and M. D. Graham, "Mechanism of Margination in Confined Flows of Blood and Other Multicomponent Suspensions," *Phys. Rev. Lett.*, vol. 109, no. 10, p. 108 102, 2012.

[185] C. K. Aidun and D. W. Qi, "A new method for analysis of the fluid interaction with a deformable membrane," *Journal of Statistical Physics*, vol. 90, no. 1, pp. 145–158, 1998.

[186] A. J. Wagner and I. Pagonabarraga, "Lees-edwards boundary conditions for lattice boltzmann," *J. Stat. Phys.*, vol. 107, no. 1/2, pp. 521–537, 2002.

[187] J. F. Morris and J. F. Brady, "Self-diffusion in sheared suspensions," *J. Fluid Mech.*, vol. 312, pp. 223–252, 1996.

[188] R. N. Zia and J. F. Brady, "Single-particle motion in colloids: Force-induced diffusion," *J. Fluid Mech.*, vol. 658, pp. 188–210, 2010.

[189] J. F. Brady and J. F. Morris, "Microstructure of strongly sheared suspensions and its impact on rheology and diffusion," *J. Fluid Mech.*, vol. 348, pp. 103–139, 1997.

[190] M. Wang and J. F. Brady, "Spectral ewald acceleration of stokesian dynamics for polydisperse suspensions," *J. Comput. Phys.*, vol. 306, pp. 443 –477, 2016.

[191] S. Pednekar, J. Chun, and J. F. Morris, "Bidisperse and polydisperse suspension rheology at large solid fraction," *Journal of Rheology*, vol. 62, no. 2, pp. 513–526, 2018. eprint: https://doi.org/10.1122/1.5011353.

[192] A. Kumar and J. J. L. Higdon, "Dynamics of the orientation behavior and its connection with rheology in sheared non-brownian suspensions of anisotropic dicolloidal particles," *Journal of Rheology*, vol. 55, no. 3, pp. 581–626, 2011.

[193] A. S. Popel and P. C. Johnson, "Microcirculation and hemorheology," *Annu. Rev. Fluid Mech.*, vol. 37, pp. 43–69, 2005.

[194] L. Mountrakis, E. Lorenz, and A. G. Hoekstra, "Scaling of shear-induced diffusion and clustering in a blood-like suspension," *Europhys. Lett.*, vol. 114, no. 1, pp. 14 002–14 002, 2016.

[195] W. Xue and G. S. Grest, "Shear-induced alignment of colloidal particles in the presence of a shear flow," *Phys. Rev. Lett.*, vol. 64, no. 4, pp. 419–422, 1990.

[196] A. Kumar and J. J. L. Higdon, "Origins of the anomalous stress behavior in charged colloidal suspensions under shear," *Phys. Rev. E*, vol. 82, p. 051 401, 5 2010.

[197] P. Siegle, I. Goychuk, and P. Hanggi, "Origin of hyperdiffusion in generalized brownian motion," *Phys. Rev. Lett.*, vol. 105, no. 10, p. 100 602, 2010.

[198] G Antonini, G Guiffant, D Quemada, and A. Dosne, "Estimation of platelet diffusivity in flowing blood," *Biorheology*, vol. 15, no. 2, pp. 111–117, 1978.

[199] F. R. Da Cunha and E. J. Hinch, "Shear-induced dispersion in a dilute suspension of rough spheres," *J. Fluid Mech.*, vol. 309, pp. 211–223, 1996.

[200] S. S. Virani, A. Alonso, E. J. Benjamin, M. S. Bittencourt, C. W. Callaway, A. P. Carson, A. M. Chamberlain, A. R. Chang, S. Cheng, F. N. Delling, *et al.*, "Heart disease and stroke statistics—2020 update: A report from the american heart association," *Circulation*, E139–E596, 2020.

[201] D. N. Ku, D. P. Giddens, C. K. Zarins, and S. Glagov, "Pulsatile flow and atherosclerosis in the human carotid bifurcation. positive correlation between plaque location and low oscillating shear stress.," *Arteriosclerosis: An Official Journal of the American Heart Association, Inc.*, vol. 5, no. 3, pp. 293–302, 1985.

[202] R. Virchow, *Gesammelte abhandlungen zur wissenschaftlichen medicin*. Grote, 1862.

[203] D. N. Ku and C. J. Flannery, "Development of a flow-through system to create occluding thrombus," *Biorheology*, vol. 44, no. 4, pp. 273–284, 2007.

[204] D. M. Wootton and D. N. Ku, "Fluid mechanics of vascular systems, diseases, and thrombosis," *Annual review of biomedical engineering*, vol. 1, no. 1, pp. 299–329, 1999.

[205] M. J. Davies and A. Thomas, "Thrombosis and acute coronary-artery lesions in sudden cardiac ischemic death," *New England Journal of Medicine*, vol. 310, no. 18, pp. 1137–1140, 1984.

[206] B. Savage, F. Almus-Jacobs, and Z. M. Ruggeri, "Specific synergy of multiple substrate–receptor interactions in platelet thrombus formation under flow," *Cell*, vol. 94, no. 5, pp. 657–666, 1998.

[207] P. J. Wellings and D. N. Ku, "Mechanisms of platelet capture under very high shear," *Cardiovascular Engineering and Technology*, vol. 3, no. 2, pp. 161–170, 2012.

[208] H. Fu, Y. Jiang, D. Yang, F. Scheiflinger, W. P. Wong, and T. A. Springer, "Flow-induced elongation of von willebrand factor precedes tension-dependent activation," *Nature communications*, vol. 8, no. 1, pp. 1–12, 2017.

[209] W. Huber, J. Hurst, D. Schlatter, R. Barner, J. Hübscher, W. C. Kouns, and B. Steiner, "Determination of kinetic constants for the interaction between the platelet glycoprotein iib-iiia and fibrinogen by means of surface plasmon resonance," *European journal of biochemistry*, vol. 227, no. 3, pp. 647–656, 1995.

[210] Z. M. Ruggeri, J. N. Orje, R. Habermann, A. B. Federici, and A. J. Reininger, "Activation-independent platelet adhesion and aggregation under elevated shear stress," *Blood*, vol. 108, no. 6, pp. 1903–1910, 2006.

[211] V. Huck, M. F. Schneider, C. Gorzelanny, and S. W. Schneider, "The various states of von willebrand factor and their function in physiology and pathophysiology," *Thrombosis and haemostasis*, vol. 111, no. 04, pp. 598–609, 2014.

[212] A. Casonato, V. Daidone, E. Galletta, and A. Bertomoro, "Type 2b von willebrand disease with or without large multimers: A distinction of the two sides of the disorder is long overdue," *PloS one*, vol. 12, no. 6, e0179566, 2017.

[213] M. Stockschlaeder, R. Schneppenheim, and U. Budde, "Update on von willebrand factor multimers: Focus on high-molecular-weight multimers and their role in hemostasis," *Blood Coagulation & Fibrinolysis*, vol. 25, no. 3, p. 206, 2014.

[214] D. D. Wagner, "Cell biology of von willebrand factor," *Annual review of cell biology*, vol. 6, no. 1, pp. 217–242, 1990.

[215] W. S. Nesbitt, E. Westein, F. J. Tovar-Lopez, E. Tolouei, A. Mitchell, J. Fu, J. Carberry, A. Fouras, and S. P. Jackson, "A shear gradient–dependent platelet aggregation mechanism drives thrombus formation," *Nature medicine*, vol. 15, no. 6, pp. 665–673, 2009.

[216] E. Westein, A. D. van der Meer, M. J. Kuijpers, J.-P. Frimat, A. van den Berg, and J. W. Heemskerk, "Atherosclerotic geometries exacerbate pathological thrombus formation poststenosis in a von willebrand factor-dependent manner," *Proceedings of the National Academy of Sciences*, vol. 110, no. 4, pp. 1357–1362, 2013.

[217] M. Li, D. N. Ku, and C. R. Forest, "Microfluidic system for simultaneous optical measurement of platelet aggregation at multiple shear rates in whole blood," *Lab on a Chip*, vol. 12, no. 7, pp. 1355–1362, 2012.

[218] D. A. Kim, K. J. Ashworth, J. Di Paola, and D. N. Ku, "Platelet α-granules are required for occlusive high-shear-rate thrombosis," *Blood Advances*, vol. 4, no. 14, pp. 3258–3267, 2020.

[219] J. Kim, C.-Z. Zhang, X. Zhang, and T. A. Springer, "A mechanically stabilized receptor–ligand flex-bond important in the vasculature," *Nature*, vol. 466, no. 7309, pp. 992–995, 2010.

[220] W. Zhang, W. Deng, L. Zhou, Y. Xu, W. Yang, X. Liang, Y. Wang, J. D. Kulman, X. F. Zhang, and R. Li, "Identification of a juxtamembrane mechanosensitive domain in the platelet mechanosensor glycoprotein ib-ix complex," *Blood, The Journal of the American Society of Hematology*, vol. 125, no. 3, pp. 562–569, 2015.

[221] Y. Chen, J. Liao, Y. Zhou, K. Li, B. Liu, L. A. Ju, and C. Zhu, "Fast force loading disrupts molecular binding stability in human and mouse cell adhesions," *Molecular & Cellular Biomechanics*, vol. 16, no. 3, p. 211, 2019.

[222] A. L. Fogelson and K. B. Neeves, "Fluid mechanics of blood clot formation," *Annual review of fluid mechanics*, vol. 47, pp. 377–403, 2015.

[223] A. Belyaev, J. L. Dunster, J. M. Gibbins, M. Panteleev, and V. Volpert, "Modeling thrombosis in silico: Frontiers, challenges, unresolved problems and milestones," *Physics of life reviews*, vol. 26, pp. 57–95, 2018.

[224] H. Chen, M. A. Fallah, V. Huck, J. I. Angerer, A. J. Reininger, S. W. Schneider, M. F. Schneider, and A. Alexander-Katz, "Blood-clotting-inspired reversible polymer–colloid composite assembly in flow," *Nature communications*, vol. 4, no. 1, pp. 1–7, 2013.

[225] Z. Liu, Y. Zhu, J. R. Clausen, J. B. Lechman, R. R. Rao, and C. K. Aidun, "Multiscale method based on coupled lattice-boltzmann and langevin-dynamics for direct

simulation of nanoscale particle/polymer suspensions in complex flows," *International Journal for Numerical Methods in Fluids*, vol. 91, no. 5, pp. 228–246, 2019.

[226] L. Casa, S. Gillespie, S. Meeks, and D. Ku, "Relative contributions of von willebrand factor and platelets in high shear thrombosis," *Journal of Hematology & Thromboembolic Diseases*, 2016.

[227] H. Yuan, N. Deng, S. Zhang, Y. Cao, Q. Wang, X. Liu, and Q. Zhang, "The unfolded von willebrand factor response in bloodstream: The self-association perspective," *Journal of hematology & oncology*, vol. 5, no. 1, pp. 1–10, 2012.

[228] T. Kragh, M. Napoleone, M. A. Fallah, H. Gritsch, M. F. Schneider, and A. J. Reininger, "High shear dependent von willebrand factor self-assembly fostered by platelet interaction and controlled by adamts13," *Thrombosis Research*, vol. 133, no. 6, pp. 1079–1087, 2014.

[229] H. Ulrichts, K. Vanhoorelbeke, J. Girma, P. Lenting, S Vauterin, and H. Deckmyn, "The von willebrand factor self-association is modulated by a multiple domain interaction," *Journal of Thrombosis and Haemostasis*, vol. 3, no. 3, pp. 552–561, 2005.

[230] Y. Li, H. Choi, Z. Zhou, L. Nolasco, H. J. Pownall, J. Voorberg, J. L. Moake, and J.-F. Dong, "Covalent regulation of ulvwf string formation and elongation on endothelial cells under flow conditions," *Journal of thrombosis and haemostasis*, vol. 6, no. 7, pp. 1135–1143, 2008.

[231] Wikipedia contributors, *Orders of magnitude (energy) — Wikipedia, the free encyclopedia*, [Online; accessed 30-August-2020], 2020.

[232] M. J. Maxwell, S. M. Dopheide, S. J. Turner, and S. P. Jackson, "Shear induces a unique series of morphological changes in translocating platelets: Effects of morphology on translocation dynamics," *Arteriosclerosis, thrombosis, and vascular biology*, vol. 26, no. 3, pp. 663–669, 2006.

[233] G. I. Bell, "Models for the specific adhesion of cells to cells," *Science*, vol. 200, no. 4342, pp. 618–627, 1978.

[234] D. A. Hammer and S. M. Apte, "Simulation of cell rolling and adhesion on surfaces in shear flow: General results and analysis of selectin-mediated neutrophil adhesion," *Biophysical journal*, vol. 63, no. 1, pp. 35–57, 1992.

[235] M Eigen, *Quantum statistical mechanics in the natural sciences*, 1974.

[236] M. Fernandez, M. H. Ginsberg, Z. M. Ruggeri, F. J. Batlle, and T. S. Zimmerman, "Multimeric structure of platelet factor viii/von willebrand factor: The presence of larger multimers and their reassociation with thrombin-stimulated platelets," 1982.

[237] M. Arya, B. Anvari, G. M. Romo, M. A. Cruz, J.-F. Dong, L. V. McIntire, J. L. Moake, and J. Lopez, "Ultralarge multimers of von willebrand factor form spontaneous high-strength bonds with the platelet glycoprotein ib-ix complex: Studies using optical tweezers," *Blood, The Journal of the American Society of Hematology*, vol. 99, no. 11, pp. 3971–3977, 2002.

[238] W. E. Fowler, L. J. Fretto, K. K. Hamilton, H. P. Erickson, P. A. McKee, *et al.*, "Substructure of human von willebrand factor.," *The Journal of clinical investigation*, vol. 76, no. 4, pp. 1491–1500, 1985.

[239] T. A. Springer, "Von willebrand factor, jedi knight of the bloodstream," *Blood, The Journal of the American Society of Hematology*, vol. 124, no. 9, pp. 1412–1425, 2014.

[240] S. Lippok, T. Obser, J. P. Müller, V. K. Stierle, M. Benoit, U. Budde, R. Schneppenheim, and J. O. Rädler, "Exponential size distribution of von willebrand factor," *Biophysical journal*, vol. 105, no. 5, pp. 1208–1216, 2013.

[241] H. W. Ott, A. Griesmacher, M. Schnapka-Koepf, G. Golderer, A. Sieberer, M. Spannagl, B. Scheibe, S. Perkhofer, K. Will, and U. Budde, "Analysis of von willebrand factor multimers by simultaneous high-and low-resolution vertical sds-agarose gel electrophoresis and cy5-labeled antibody high-sensitivity fluorescence detection," *American journal of clinical pathology*, vol. 133, no. 2, pp. 322–330, 2010.

[242] C. Heilmann, U. Geisen, F. Beyersdorf, L. Nakamura, C. Benk, G. Trummer, M. Berchtold-Herz, C. Schlensak, and B. Zieger, "Acquired von willebrand syndrome in patients with extracorporeal life support (ecls)," *Intensive care medicine*, vol. 38, no. 1, pp. 62–68, 2012.

[243] U. Geisen, K. Brehm, G. Trummer, M. Berchtold-Herz, C. Heilmann, F. Beyersdorf, J. Schelling, A. Schlagenhauf, and B. Zieger, "Platelet secretion defects and acquired von willebrand syndrome in patients with ventricular assist devices," *Journal of the American Heart Association*, vol. 7, no. 2, e006519, 2018.

[244] J. E. Sadler, "New concepts in von willebrand disease," *Annu. Rev. Med.*, vol. 56, pp. 173–191, 2005.

[245] C. Loirat, J.-P. Girma, C. Desconclois, P. Coppo, and A. Veyradier, "Thrombotic thrombocytopenic purpura related to severe adamts13 deficiency in children," *Pediatric Nephrology*, vol. 24, no. 1, p. 19, 2009.

[246] P Harrison and E. M. Cramer, "Platelet α-granules," *Blood reviews*, vol. 7, no. 1, pp. 52–62, 1993.

[247] J. M. Siegel, C. P. Markou, D. N. Ku, and S. Hanson, "A scaling law for wall shear rate through an arterial stenosis," 1994.

[248] D. Bluestein, L. Niu, R. T. Schoephoerster, and M. K. Dewanjee, "Fluid mechanics of arterial stenosis: Relationship to the development of mural thrombus," *Annals of biomedical engineering*, vol. 25, no. 2, p. 344, 1997.

[249] M. J. Maxwell, E. Westein, W. S. Nesbitt, S. Giuliano, S. M. Dopheide, and S. P. Jackson, "Identification of a 2-stage platelet aggregation process mediating shear-dependent thrombus formation," *Blood*, vol. 109, no. 2, pp. 566–576, 2007.

[250] M. Moroi, S. M. Jung, S. Nomura, S. Sekiguchi, A. Ordinas, and M. Diaz-Ricart, "Analysis of the involvement of the von willebrand factor–glycoprotein ib interaction in platelet adhesion to a collagen-coated surface under flow conditions," *Blood, The Journal of the American Society of Hematology*, vol. 90, no. 11, pp. 4413–4424, 1997.

[251] R. R. Hansen, A. A. Tipnis, T. C. White-Adams, J. A. Di Paola, and K. B. Neeves, "Characterization of collagen thin films for von willebrand factor binding and platelet adhesion," *Langmuir*, vol. 27, no. 22, pp. 13 648–13 658, 2011.

[252] P. Jouannot-Chesney, J.-P. Jernot, and C. Lantuéjoul, "Practical determination of the coordination number in granular media," *Image Analysis & Stereology*, vol. 25, no. 1, pp. 55–61, 2006.

[253] H. Chen and A. Alexander-Katz, "Structure and dynamics of blood-clotting-inspired polymer-colloid composites," *Soft Matter*, vol. 9, no. 43, pp. 10 381–10 390, 2013.

[254] O. McCarty, D Ku, M Sugimoto, M. King, J. Cosemans, K. Neeves, and T. S. O. BIORHEOLOGY, "Dimensional analysis and scaling relevant to flow models of thrombus formation: Communication from the ssc of the isth," *Journal of thrombosis and haemostasis: JTH*, vol. 14, no. 3, p. 619, 2016.

[255] J. Hellums, D. Peterson, N. Stathopoulos, J. Moake, and T. Giorgio, "Studies on the mechanisms of shear-induced platelet activation," in *Cerebral ischemia and hemorheology*, Springer, 1987, pp. 80–89.

[256] S. Kulkarni, S. M. Dopheide, C. L. Yap, C. Ravanat, M. Freund, P. Mangin, K. A. Heel, A. Street, I. S. Harper, F. Lanza, *et al.*, "A revised model of platelet aggregation," *The Journal of clinical investigation*, vol. 105, no. 6, pp. 783–791, 2000.

[257] B. S. Coller, E. I. Peerschke, L. E. Scudder, and C. A. Sullivan, "Studies with a murine monoclonal antibody that abolishes ristocetin-induced binding of von willebrand factor to platelets: Additional evidence in support of gpib as a platelet receptor for von willebrand factor," 1983.

[258] Z. M. Ruggeri, A. Zarpellon, J. R. Roberts, R. A. Mc Clintock, H. Jing, and G. L. Mendolicchio, "Unraveling mechanism and significance of thrombin binding to platelet glycoprotein ib," *Thrombosis and haemostasis*, vol. 104, no. 5, 2010.

[259] J. Van de Lagemaat, K. D. Benkstein, and A. J. Frank, "Relation between particle coordination number and porosity in nanoparticle films: Implications to dye-sensitized solar cells," *The Journal of Physical Chemistry B*, vol. 105, no. 50, pp. 12 433–12 436, 2001.

[260] J. Happel and H. Brenner, *Low Reynolds number hydrodynamics: with special applications to particulate media*. Springer Science & Business Media, 2012, vol. 1.

[261] A. K. Chauhan, T Goerge, S. Schneider, and D. Wagner, "Formation of platelet strings and microthrombi in the presence of adamts-13 inhibitor does not require p-selectin or β3 integrin," *Journal of Thrombosis and Haemostasis*, vol. 5, no. 3, pp. 583–589, 2007.

[262] M. T. Griffin, D. Kim, and D. N. Ku, "Shear-induced platelet aggregation: 3d-grayscale microfluidics for repeatable and localized occlusive thrombosis," *Biomicrofluidics*, vol. 13, no. 5, p. 054 106, 2019.

[263] E. Falk, "Morphologic features of unstable atherothrombotic plaques underlying acute coronary syndromes," *The American journal of cardiology*, vol. 63, no. 10, E114–E120, 1989.

[264] M. Markl, F. Wegent, T. Zech, S. Bauer, C. Strecker, M. Schumacher, C. Weiller, J. Hennig, and A. Harloff, "In vivo wall shear stress distribution in the carotid artery: Effect of bifurcation geometry, internal carotid artery stenosis, and recanalization therapy," *Circulation: Cardiovascular Imaging*, vol. 3, no. 6, pp. 647–655, 2010.

[265] Y. Sahasakul, W. D. Edwards, J. M. Naessens, and A. J. Tajik, "Age-related changes in aortic and mitral valve thickness: Implications for two-dimensional echocardiography based on an autopsy study of 200 normal human hearts," *The American journal of cardiology*, vol. 62, no. 7, pp. 424–430, 1988.

[266] A. C. Egbe, S. V. Pislaru, P. A. Pellikka, J. T. Poterucha, H. V. Schaff, J. J. Maleszewski, and H. M. Connolly, "Bioprosthetic valve thrombosis versus structural failure: Clinical and echocardiographic predictors," *Journal of the American College of Cardiology*, vol. 66, no. 21, pp. 2285–2294, 2015.

[267] Z. L. Liu, J. R. Clausen, J. L. Wagner, K. S. Butler, D. S. Bolintineanu, J. B. Lechman, R. R. Rao, and C. K. Aidun, "Heterogeneous partition of cellular blood-borne nanoparticles through microvascular bifurcations," *Physical Review E*, vol. 102, no. 1, p. 013 310, 2020.

VITA

Zixiang Leo Liu was born in Pingxiang, a small city in the Jiangxi province of southern China. He obtained his bachelor's degree in Aeronautics from Beihang University in 2012. He obtained his master's degree in Aerospace Engineering from University of Florida in 2013. Before Leo joined the Woodruff School of Mechanical Engineering at Georgia Tech for PhD in 2016, he spent two years in industry working on engineering consultancy using computational fluid dynamics (CFD). His current research interest includes complex fluids, soft matter physics, rheology and thrombosis.